The Design, Fabrication and Testing of Micro-fabricated Linear and Planar Colloid Thruster Arrays

by

Luis Fernando Velásquez-García

Ingeniero Mecánico, Magna Cum Laude en Ingeniería Mecánica, Los Andes University, 1998
Ingeniero Civil, Magna Cum Laude en Ingeniería Civil, Los Andes University, Dec. 1999
S.M., Aeronautics and Astronautics, Massachusetts Institute of Technology, June 2001

SUBMITTED TO THE DEPARTMENT OF AERONAUTICS AND ASTRONAUTICS
IN PARTIAL FULFILLMENT OF THE DEGREE OF

DOCTOR OF PHILOSOPHY

at the
MASSACHUSETTS INSTITUTE OF TECHNOLOGY

May 2004

Signature of Author_____
Department of Aeronautics and Astronautics
May 6^{th}, 2004

Certified by_____
Professor Manuel Martínez-Sánchez
Department of Aeronautics and Astronautics, Ph.D. Committee Chair

Certified by_____
Professor Akintunde Ibitayo Akinwande
Department of Electrical Engineering and Computer Science

Certified by_____
Professor Michael Brenner
Department of Applied Mathematics, Harvard University

Certified by_____
Professor Jack Kerrebrock
Department of Aeronautics and Astronautics

Certified by_____
Professor Markus Zahn
Department of Electrical Engineering and Computer Science

Accepted by_____
Professor Edward M. Greitzer
Chair, Committee on Graduate Students

It is a lovely thing to live with courage,
and to die leaving behind everlasting fame.

Alexander III of Macedonia, called The Great

Without our enemies we would be only a
shadow of who we are: clumsier, weaker,
more rustic, and even a fickle kid could deal
with us; love them in secret by recognizing
that you would have been no one without them.

Timur Leng, mongol conqueror, called Tamerlane

The Design, Fabrication and Testing of Micro-fabricated Linear and Planar Electrospray Thruster Arrays

by

Luis Fernando Velásquez-García

Submitted to the Department of Aeronautics and Astronautics
on April 30^{th}, 2004 in Partial Fulfillment of the Requirements for
the Degree of Doctor of Philosophy at
the Massachusetts Institute of Technology

ABSTRACT

Electrospray Thrusters are space propulsion electric engines that use as propulsive principle an electrohydrodynamic effect known as *Taylor Cone*. When this effect takes place, charged particles are expelled from the apex of a conductive liquid meniscus deformed into a conical shape product of the presence of a large enough electric field surrounding them. Electrospray Thrusters are well suited for scaling down and batch production because these engines do not require large pressure ratios to achieve high efficiency, or high temperatures or plasma phase ionization to operate. Electrospray Thrusters can deliver thrust in a very precise way. Furthermore, they are able to match the requirements of any conceivable mission that any of the other space propulsion electromagnetic engines can achieve because it is possible to use the same engine and propellant to span a wide range of I_{sp}'s and thrusts: this is due to the series of different regimes that the emitters could operate in (droplet emission, solvated ions and mixed regime).

The present work tackles the problem of how to fabricate a Colloid Engine with large emitter density, from the stand point of the micro-fabrication techniques available at the Micro-fabrication Technologies Laboratory, MTL, and demonstrates that highly packed Colloid Thruster Arrays are feasible.

The work is centered on two engine concepts: an internally fed Linear Colloid Thruster Array with highly doped formamide as propellant -intended to work in the droplet emission regime, and two variations of an externally fed Planar Electrospray Thruster Array with the ionic liquid $EMI-BF_4$ as propellant -intended to work in the solvated ion emission regime-.

In the case of the Colloid Thruster Linear Array the experimental results are diverse: on one hand from impact patterns there is demonstration of cumulative uniform-unsteady operation and demonstration of steady uniform emission of complete structural modules (an emitter set fed by the same manifold), both in agreement with theoretical models. In addition from the current versus flow rate dependence, steady and uniform emission was demonstrated, in agreement with the theoretical model of Single Cone - droplet emission and the assumption that the array of emitters is uniformly operating. The propellant doping level strongly influ-

ences its wettability with respect to the engine internal surface. As a consequence of this effect, engines that were brought to steady emission showed arcing because of bursting events during operation. The operation of the proposed flow control was experimentally verified.

In the case of the Colloid Thruster Planar Array, uniform steady emission of two kinds of emitter geometries was demonstrated from experimental impact traces and current measurements. It was also possible to demonstrate strong dependence of the emitted current on temperature. The emitted current-versus-extraction voltage can be described by a simple exponential fit, but there is uncertainty on the voltage exponent dependence.

In order to implement both engines several novel fabrication techniques were developed, particularly a process to generate black silicon, a process to generate meso-scale uniform etching for silicon, plasma patterning of thick silicon oxide films, and emitter sharpening/construction of isotropic 3D features. Also, a novel precision substrate assembly based on displacement springs was developed and demonstrated.

The work concludes by pointing out potential areas of improvement of the engine concepts and research directions on this exciting propulsion topic.

Ph.D. Committee Chair:
Professor Manuel Martínez-Sánchez
Department of Aeronautics and Astronautics

ACKNOWLEDGEMENTS

This Ph.D. dissertation marks the end of my academic life as a student. I believe it is an important stage in my journey because until now my life had been centered in my preparation as a useful human being. It is then appropriate to say a few words about this accomplishment.

Many things have changed since the first recalls of reality that I have. Many things, as well as many people, have come and go during this transit, some of them leaving an everlasting memory. I feel compelled to give thanks to these people, for having helped me become who I am. The beings that enriched my life while I had the privilege to interact with them are well missed; the ones whose presence I still enjoy are invited to embrace me in my joy, to feel my victory as theirs, to remember and tell the tales that make our life worth-living. My gratitude to my parents and all my friends, both far and near, for being crucial in helping me withstand the tides, find certainty in times of uncertainty, keep hope where nothing else was left.

I will regard my graduate student MIT life in the years to come as a once-in-a-lifetime experience that allowed me to know me better, learn from people, and develop my potentiality. I would like to thank my Ph.D. committee: professors Tayo Akinwande (EECS), Michael Brenner (Applied Math, Harvard), Jack Kerrebrock (Aero/Astro), Manuel Martínez-Sánchez (Aero/Astro) and Marcus Zahn (EECS), for their vote of confidence and efficient guidance during my Ph.D. studies, and their inexhaustible patience with my thesis writing. I regard them as wise, admirable friends whom I had the privilege to work with. Only time will tell if I will honor their high expectations on me and my work becoming the man I was born to be.

I would also like to declare my profound admiration to my MIT professors because of their inspiring work and charisma. In particular, I would like to thank professors Dionisios Margetis and Hung Chen, from the Mathematics Department, for encouraging me to learn the ways of the mathematician; MEMS Master professor Steven Senturia, from the Electrical Engineering and Computer Science Department, for the fatherly conversations we held, as well as his undeserved compliments about my performance and strengths.

Finally, I would also like to thank a few people for their contributions to make this work possible: Timothy S. Glenn from the Space Systems Laboratory, for providing the templates to write this document; Jose Mariano Lopez-Urdiales from the Space Propulsion Laboratory, for his help in assembling the reference list of the previous work on Colloid Thrusters; Jorge Carretero Benigno from the Space Propulsion Laboratory, for his help in both setting the first testing facility and in carrying out some of the tests for the Colloid Linear Array; Fred Cote, manager of the Edgerton Student Shop for his help in the construction of the testing facilities; the staff of the Micro-fabrication Technologies Laboratory because of its invaluable support in tuning the engine fabrication processes.

Funding for this research was provided by the Air Force Office of Scientific Research under contract XXXXXXX, managed by Mitat Burkam.

Luis Fernando Velásquez-García
April 2004

TABLE OF CONTENTS

LIST OF FIGURES

LIST OF TABLES

Chapter 1

PROBLEM STATEMENT AND AN INTRODUCTION ON COLLOID THRUSTERS

This chapter addresses three key issues:

- To clearly state the goal of this Ph.D. dissertation.
- To briefly state why is important to carry out this investigation.
- To explain in general terms Colloid Thrusters and why is advantageous to agglomerate them into dense arrays. A deeper explanation on the physics involved with Colloid Thrusters is available in the following chapters of this dissertation.

1.1 Dissertation Goal

In a broad sense the goal of this dissertation is to explore the feasibility of highly packed Colloid thruster arrays. This statement implies the development one or more engine concepts to eventually validate them after a cycle of analysis, design and fabrication. The specific targeted devices are:

- An internally fed linear emitter array composed of 240 emitters that use doped formamide as propellant, activation voltage around 2000 V and a current versus flowrate dependence in agreement with single-cone droplet emission mode. This engine is able to provide specific impulse of the order of a few hundreds of seconds and thrust levels of the order of tenths of mili-Newtons while consuming a tenths of a watt. The propulsive efficiency is estimated at 90% or more [Lozano, 2003]. This engine is ideal for time-limited low-thrust precision-throtability missions such as changes in the orbit of small satellites.
- An externally fed planar emitter array that uses the ionic liquid $EMI-BF_4$ as propellant, activation voltage around 1500 V and solvated ion emission mode.

> The specific impulse of this engine falls in the 4500 - 8000 sec. range, with thrust levels of the order of a few tens of micro-Newtons. The propulsive efficiency is larger than 93% [Lozano, 2003]. This engine is ideal as main engine for micro-satellites where missions are not time-critical, such as orbital control and deep space. Smaller specific impulse values can be obtained with a decelerator electrode system.

The validation of these engines includes fabrication characterization, hydraulic tests, uniformity/stability tests and device characterization. The device characterization is compared with proposed models, and discrepancies are explained.

1.2 Research Importance

Colloid engines are electrical thrusters intended for space applications. Electrical engines use electromagnetic fields to accelerate an electrically charged stream to produce thrust. In space most propulsive effects are based on overall linear momentum conservation where every maneuver implies mass usage. Saving mass is a key objective in space; electrical engines are inherently mass efficient: in a chemically-based rocket the maximum speed of the stream coming out of the nozzle is limited by whatever energy-per-unit-of-mass is released in the chemical reaction; this limitation is not present in an electromagnetic propulsive scheme and in principle any speed smaller than the speed of light can be achieved with a large enough potential drop.

In order to reduce the absolute thrust magnitude while keeping the electrical engine efficient it is necessary to scale it down; to maintain the same efficiency, one has to keep constant the ratios of the different characteristic lengths involved in the engine. One of these characteristic lengths in the case of a plasma-based engine is the *ionization mean free path*. The mean free path is inversely proportional to the plasma number density; that is, decreasing the mean free path makes the plasma denser, with the corresponding increase in plasma chamber ion bombardment and life span reduction. Fortunately, unlike most other electric engines, Colloid Thrusters do not rely on a thermalized gas phase ionization and thus mean free-path scaling down does not take place. Also, the power levels / thrust per emitter in a Colloid Thruster are such that they do not require further reduction. The engine performance does not depend on the

actual emitter dimensions: smaller emitters are then an asset because they imply smaller evaporation losses and activation voltages. Therefore, Colloid Thrusters are well suited for scaling-down.

There is a key advantage in clustering many emitters of low current instead of a few of large current: low power emitters are more efficient, work with physics better understood, have smaller divergence angles and in general produce thrust in a cleaner way.

Colloid Thruster Technology is currently an important topic in electric propulsion because they are suitable for a technological niche not previously satisfied. Colloid Thrusters enjoy a renewed interest, because of the following reasons:

- New applications such as micro-satellites and orbit control (attitude control and station keeping) have created a demand for high-precision, low-thrust, efficient space engines. Other applications include the reduction of micro-accelerations that can perturb high precision experiments.
- Development of the field of spray ionization enabling the use of lower activation voltages. The work of professor Fenn on mass spectroscopy was crucial on this behalf [Fenn, 1989] as well as the work of professor de la Mora [de la Mora, 1994], both from Yale University.
- Maturation of the micro-fabrication procedures: the smaller the engine emitters the smaller the extractor voltage as well as the vaporization losses. The use of micro-fabrication techniques makes scaling-down a real possibility, as well as batch processing of many emitters with uniform characteristics.
- Colloid thrusters have low thrust cost, high thrust efficiency, moderate exhaust velocity, cold operation cycle and cheap working fluid, making this kind of engines attractive to long term missions were power constraints and mass saving are a must [Mueller, 1997].
- Colloid Thrusters can be self-neutralizing, as originally demonstrated by Perel [Perel, 1967]. This avoids the need for an external neutralizer, with the corresponding energy savings.
- Colloid Thruster power requirements per unit of thrust are much lower compared to the ones for FEEPs (Field Emission Electric Propulsion), the other technology in real competition for the same technological niche. FEEPs function under the same physical principle but they use liquid metals as propellant, substances that are not desirable in an spacecraft because of contamination issues.

The research carried out in this Ph.D. dissertation looks to develop engine concepts with corresponding fabrication techniques that achieve large emitter densities, small emitter dimensions, batch uniformity and low emitter activation voltage. Therefore, this work clearly addresses the motivation of the present interest in highly tunable - low thrust engines. In the next chapter a brief review of the state of the art in Colloid Thruster Technology is carried out where the proper place of this work is established as well as the existing deficiencies that the work corrects.

1.3 An introduction on Colloid Thrusters

Colloid Thrusters are electrostatic accelerators of charged particles. These particles can be either charged droplets, solvated ions or a mix of them. The exit stream is neutralized either by bipolar operation of the engine (modulation in space and/or time to achieve overall neutrality) or by a downstream electron stream (positively charged exit stream). Figure 1.1 shows a schematic of an emitter unit that is a part of a pressure-fed internally-fed Colloid Thruster Array working in the single-cone droplet emission mode.

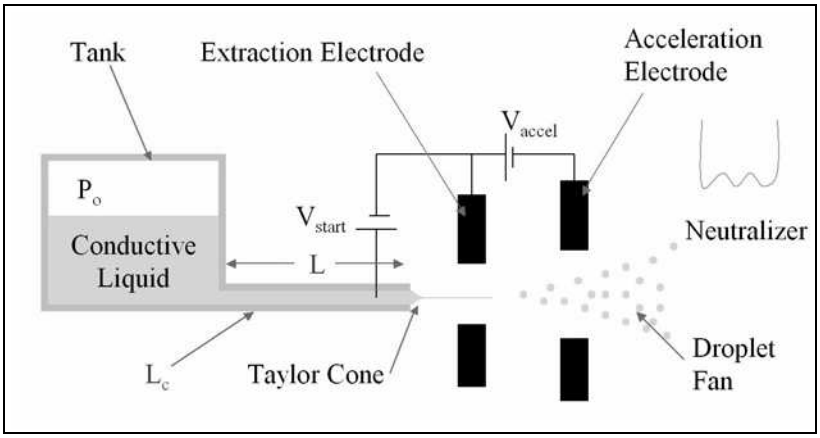

Figure 1.1 Schematic of a Colloid Thruster single hollow emitter.

In Figure 1.1, the engine tank has stored propellant at a stagnation pressure P_o, and this propellant flows through a hydraulic system to the emitters. The hydraulic system can be modeled as a hydraulic impedance. The hydraulic impedance is described by two quantities: a

hydraulic diameter L_c and an axial length L. Because L_c is quite small (micron-size range) the surface tension effects are important and thus it is desirable that the hydraulic system be wettable by the propellant. At the end of the hydraulic system there is an opening to the engine exterior, i.e., an emitter. There is a set of two electrodes in front of the spout, the first intended to extract charged particles form the emitter, and the second to accelerate the particles to the desired specific impulse. The specific impulse is defined as

$$I_{sp} = \frac{F}{\dot{m} \cdot g} \cong \frac{c}{g} \tag{1.1}$$

where F is the thrust, $\dot{m}$ is the mass flowrate, g is the gravitational acceleration constant, and c is the final particle speed. The emission from each spout can be described as a fan of charged particles where the fan divergence is the result of the particle production scheme (droplets from jet break-up or ion emission), the self-repelling forces acting on its constituent charged particles, and the physical properties of the propellant. In order to maintain the engine charge neutrality, a neutralizer may be placed downstream: the neutralizer provides particles with opposite charge that will mix with the exit stream. Because electron sources are far more practical to implement, positive charged particles are the default species of a monopolar Colloid Thruster. An alternative is *bipolar operation*, where two spouts are differentially connected to each other, both floating with respect to the extractor, so that ions of both polarities are emitted at exactly the same rate.

The spout is in reality a field-enhancer/confining vessel for the meniscus that is formed due to surface tension when the propellant gets through the hydraulic system and reaches the exterior as shown in Figure 1.2. Because it is desired to form a meniscus when the liquid comes outside the hydraulic system, it is ideal to have non-wettable surface on the exterior of the spout.

This meniscus is the equilibrium shape that balances the difference in pressure between the outside and the liquid interior. In reality this shape is perturbed by external sources, anything from vibrations to electromagnetic forces, and including thermal gradients and inertial forces.

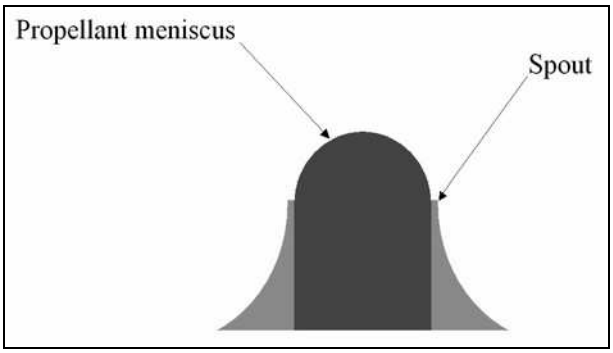

Figure 1.2 Cross-section of a Colloid Thruster spout confining the propellant meniscus.

It is possible to change the equilibrium shape if a voltage is applied between the meniscus and an external electrode called *extractor* as shown in Figure 1.3.

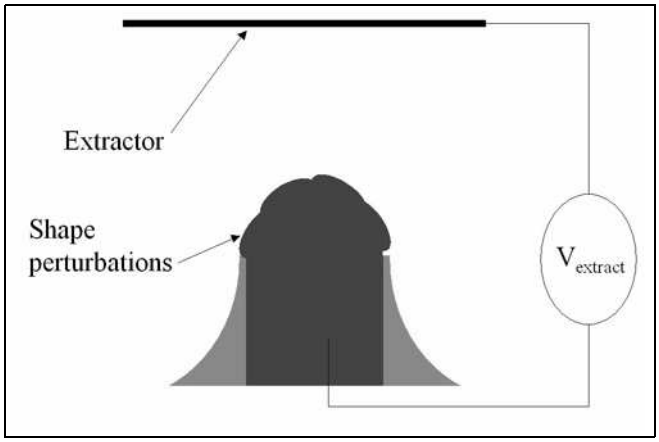

Figure 1.3 Shape perturbations and Extractor electrode.

The existence of a bias voltage between the meniscus and the extractor creates an electric field in the space between, in particular on the meniscus surface. The liquid is electrically conductive, but with a finite relaxation time, so the field will initially penetrate the liquid and force ionic charge to migrate to the meniscus surface. For polar liquids, the dipoles will also re-orient and contribute an additional polarization current to the surface. In equilibrium the internal and external fields will be related to the surface free charge, as predicted by Gauss' law. These electric fields will produce electrostatic pressure on the meniscus surface. Because the

electric field is normal to the meniscus surface (it is assumed here to be a constant potential contour) the electrostatic pressure will produce a net *suction* of the meniscus into the space right in front of it.

The surface tension of the liquid tends to counteract the effect of the electrostatic suction. Therefore, for small enough bias voltages the perturbation of the equilibrium shape remains small. If a bias voltage larger than a threshold value is applied then the meniscus shapes into a conic shape called a *Taylor Cone*. This Taylor cone becomes the equilibrium shape between the acting electrostatic pressure and the surface tension reaction, as shown in Figure 1.4. To first order the cone semi-angle has a universal value of $49.3°$ [Taylor, 1964].

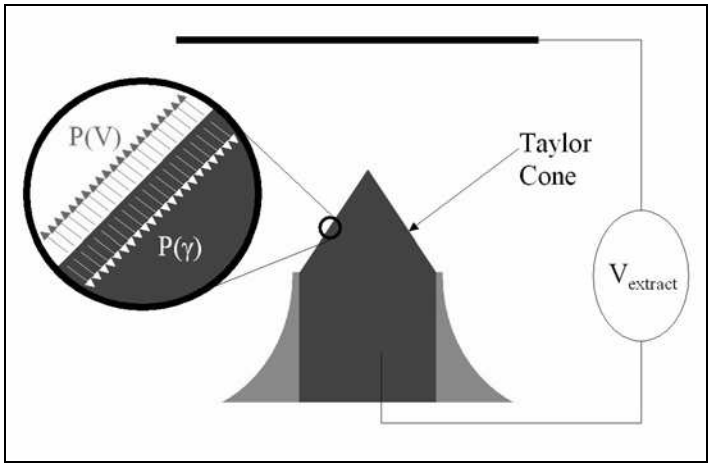

Figure 1.4 A Taylor Cone cross-section. A zoom of the equilibrium surface shows the two pressures interacting at the boundary.

Figure 1.5 shows a sequence of images taken from an actual cone formation where the change from spherical meniscus to conical meniscus is illustrated. The liquid used in this sequence is moderately doped formamide, expected to operate in the droplet emission mode.

The solution of the electrostatic problem predicts that the closer one gets to the cone apex the stronger the electric field. This in practice has two possible non-exclusive aftermaths: either a jet of liquid is expelled from the cone tip and/or ions are field-emitted from the cone tip. When a jet is formed it has an instability that follows a modified Rayleigh instability crite-

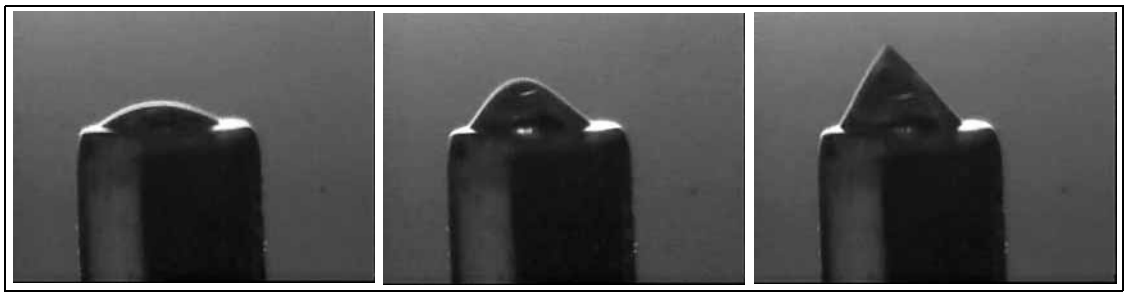

Figure 1.5 Sequence that illustrates the transition of an spherical meniscus into a Taylor Cone.

rion. Therefore, the jet eventually breaks into a set of charged droplets that conform a droplet fan. It is also possible to operate the emitter in an ions-only mode if the physical properties of the propellant are well suited and the flowrate is small enough. These charged droplets and ions provide the propulsive effect in a Colloid Thruster. Figure 1.6 illustrates the proceeding discussion.

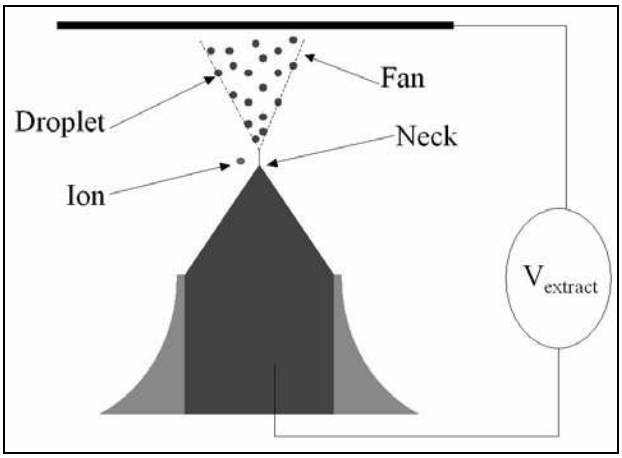

Figure 1.6 Charged particle emission schematic. A jet is emitted form the Taylor Cone to eventually break into a droplet fan. Solvated ions can be emitted from the jet neck.

Chapter 2

PREVIOUS WORK ON COLLOID THRUSTERS AND THRUSTER ARRAYS

The survey of previous work presented in this chapter is by no means exhaustive, but it is representative of the achievements and the state of the art of Colloid Thruster engine technology. The goal of this chapter is to establish some of the deficiencies of the state of the art of Colloid Thruster Technology as well as to highlight the place of this Ph.D. dissertation in the overall picture while providing answers to some of these deficiencies.

2.1 Previous work on Colloid Thrusters

2.1.1 The First Years (1914 - 1980)

Empirical documentation on electrospray emission can be tracked back to the beginning of the seventeenth century [Gilbert, 1600]. Probably the first person to report the emission of charged particles from a conductive liquid meniscus in recent times was Zeleny [Zeleny, 1914]. He studied as well the conditions for instability of the liquid droplets [Zeleny, 1915]. It was not until many years after his work that G. I. Taylor proposed a simple model to explain the conical shape of a meniscus under the influence of an electric stress larger than a critical value; this explanation has been adopted as the first-order explanation of what is has been known since then as a Taylor Cone effect [Taylor, 1964].

Within a few years after the publication of the work of Taylor, papers on Colloid Thrusters appeared. Hendricks in 1966 published a paper on the studies of electrohydrodynamic spray-

ing [Hendricks, 1966]. In his studies a metallic capillary of internal diameter equal to 50 μm was used; he proposed two bounds for the specific charge of the droplets produced by the Taylor Cone emission: a lower bound determined by the *minimum energy principle*, where for a fixed mass and charge the total energy (kinetic, potential, surface and interparticle) is minimized; the upper bound (twice as high) is termed the *Rayleigh limit* [Rayleigh, 1882], were the specific charge is the maximum that can be withstood by a droplet before breaking. Hendricks reports experimental results towards corroborating that the droplet specific charge is monodisperse and that it closely follows the minimum energy principle (More recently de la Mora reports specific charges following closely the Rayleigh criterion [de la Mora, 1994]).

In 1967 a work from Perel et al. appears on bipolar Colloid Thrusters [Perel, 1967] that was inspired by a work by Hunter [Hunter, 1965]. The work of Perel et al. was done with bias voltages that must have produced multiple cones in each meniscus of the 73 available in the engine (applied potentials ranged between 5 and 10 kV). The emitter is in 2-D configuration, with an approximated total substrate area of $5 \times 5\ cm^2$. Even though this emission regime is not the one this Ph.D. dissertation is aiming to implement in any of the engine versions, the work of Perel has several key features, among them:

- The exploration of the bipolar mode where charged droplets of both polarities are emitted at the same time, uniformly distributed in space so the spacecraft neutrality is achieved without the need of an external neutralizer. It is pointed out that in general propellants are tailored to work at only one polarity; thus, to get a bipolar operation two independent hydraulic systems must be implemented. Also the bias voltages are different to obtain the same current and this way achieve neutralization. The only exception that he found to the need of independent hydraulic systems / different operational voltages was using as propellant oleic acid doped with TEAC. Unfortunately his work uses propellants with small electrical conductivities, usually of the order of 10^{-4} to 10^{-2} Si/m. More recently Gamero has pointed out that formamide doped with NaI can be also worked in both polarities [Gamero, personal conversation].
- Large electrical conductivity, low vapor pressure, uniform molecular weight, non-corrosive and high solvation capability are identified as core features in an ideal Colloid Thruster Propellant profile.
- Use of large hydraulic impedances.

- The use of a pressure fed propellant system. The large dependence of the flow-rate on the temperature is mentioned as an argument to explore different feeding systems.
- Sharpened lips are advised for external emitter geometry. This is expected because it is needed to increase the electric field up to producing the Taylor Cone Threshold conditions. Some wettability issues might be present as well in this decision.
- Difficulties in emitter-to-emitter machining uniformity suggest the desirability of batch production for Colloid thrusters.
- The first 50 hour test was carried out, addressing issues on the survivability of the emitters due to backstreaming electrons. Because of this, refractory materials like Mo, Pt and W are advised for emitter / electrode formation (This was also to avoid electrochemical corrosion at the counter electrode).

Some time later Kenneth et al. wrote a NASA report on the research and development of Colloid Thrusters [Kenneth, 1969]. This report summarizes 8 years of work on Colloid Thrusters done under NASA funding. Some of the key features of this work are:

- Life tests of 1000 hours at an specific impulse of 800 seconds were carried out.
- Large electric potential drops are implemented between the emitters and the extractor: 6 - 25 kV. This electric potential implied multiple-cone regime.
- Some gravitational effect on the meniscus shape was pointed out; therefore, in multiple emitters it was advised to operate them vertically.
- Degassing the propellant thoroughly before operation is necessary to avoid erratic performance. Also it is indicated that is possible to obtain up to twice the non-degassed electrical conductivity if degassing is practiced.
- Propellant pressure feed systems with large hydraulic impedance are used in the series of tests.
- Some investigations on the emitter sharpening was done. It was found that either internal sharpening or external sharpening are needed for stable operation, giving support to the concept of field enhancement needed to produce the Taylor Cone instability.
- Stainless steel was found unfit for emitter material while a platinum-rhodium alloy was found as an excellent emitter raw material.
- Concerns were expressed about the electrochemical effects of the propellant on the emitters. Platinum and Rhodium emitters proved to be the best options to avoid electrochemical corrosion of the emitters under the influence of the propellant.

- The need of batch processing to reach suitable thrust levels in a feasible way is recognized.
- NaI doped propellants proved to operate the engine in a more stable way while the use of acids implied erratic peak currents. Glycerol is considered so far the best solvent candidate to be used as Colloid Thruster propellant.

Work on the testing facilities was also carried out during these years. In 1969 a paper from Zafran illustrates the design of a microthruster test stand based on a torsion pendulum, suitable for Colloid thruster thrust measurements [Zafran, 1969].

Later in 1970 Zafran published a paper on a Colloid Thruster system life test [Zafran, 1970]. In this paper a three-needle array was tested for 1792 hours. The engine uses about 5 W of power, three tungsten wire neutralizers and a bladderless blowdown propellant feed system. The engine supplied 8 micro-pounds ($\sim 35 \mu N$) of thrust at 950 seconds of I_{sp}. Acceleration and vibration tests to Titan III-C boosters were carried out to optimize the engine design. The engine used a mixture of 19.3% w/w NaI in Glycerol. The engine weighed 7.0 pounds, where 0.5 pounds were propellant. Apart from obtaining repeatable engine characteristics this work is important because it proposed as design a criterion to have manifolds and secondary plenums, although no reason is given for this choice. Large hydraulic impedances are also used in this work by Zafran.

In 1970 Perel et al. published a work on the analytical and experimental studies of Colloid Thrusters [Perel, 1970; Perel 1970-2]. This work is the first attempt to establish a set of design guidelines based on the following assumptions / experimental facts:

- There is a region of emitter operation at low mass flowrates where the beam current and the thrust are linear with the mass flowrate. This region was reported to be present with bias voltages above 10 kV. From these relationships there is a one-to-one linear relationship between thrust and mass flowrate.
- The current can get space charge limited. In this regime the current is characterized with a Child-Langmuir-like dependence where the current is related to the activation voltage (to the 3/2 power) via the space charge perveance.
- There are two regimes of operation: space charge saturation and emission limited. A function that smoothly connected the two extreme cases was suggested, based on a dimensionless parameter function of the mass flowrate.

Based on these elements a set of design plots were proposed where two *performance indices* are found: a constant that characterizes both the propellant properties and the emitter geometry and is related with charged particle generation (dimensions of this constant are $[A \cdot \text{sec.}/(Kg \cdot V)]^{0.5}$), and the *specific perveance*, related with particle acceleration, with dimensions $[A \cdot Kg \cdot (\text{sec.} \cdot V^3)]^{0.5}$. Experimental tests on this highly stressed emission regime seem to fit well these proposed design charts.

The work by Perel et al. on these papers uses annular emitters instead of capillary-like emitters, because in order to achieve practical thrust levels several hundred of these emitters must be used (clearly pointing towards batch fabrication). The working vacuum pressure of the engine tests was 10^{-6} Torr while spanning an I_{sp} between 500 and 1500 sec.

Experimentally it was determined that the control variables of the thruster are temperature, mass flowrate and emitter-to-extractor voltage drop.

The propellant was again heavily doped glycerol (NaI) and the operational voltage is 10 - 18 kV, working in the highly stressed multi-cone regime. Among the experimental conclusions of the work are:

- An increase in the mass flowrate at constant voltage drop decreases the specific charge and thus the I_{sp}.
- An increase of mass flowrate at constant voltage drop increases the thrust.
- An increase of mass flowrate at constant voltage drop increases the emitted current up to a saturation value (probably a space charge limitation effect).
- As a rule of thumb an increase of mass flowrate at constant voltage drop increases the divergence semi-angle, being in general larger than $28.5°$. At some larger voltages (~ 16 kV) the divergence semi-angle has a single global minimum at a certain mass flowrate. It is important to point out that in single Taylor Cone regime the divergence semi-angle is no larger than $20°$ [Lozano, 2003]. This corroborates that the multiple cone - highly stressed regime was present in operation.
- There is an exponential dependence of the mass flow rate on the temperature at constant voltage drop and tank pressure, directly related to fluid viscosity variation.

- It was verified experimentally that highly doped glycerol behaves as a Newtonian Liquid for fixed temperatures and voltage drop, over a wide temperature range.
- The specific charge decreased with increasing temperature at constant mass flowrate and voltage drop. An increase in conductivity due to more doping concentrations is believed to influence the engine performance in an stronger way than a similar increase due to higher temperature.
- It is suggested that for glycerol viscosity plays a major role in determining the droplet specific charge.
- As a rule of thumb, larger performance indices values imply higher thrust and specific impulse.

A few years later, in 1973, Perel et al. published a new paper on the development of the Colloid Thruster idea using annular emitters. In this case two emitter arrays, formed by three annular emitters with difference packing ratios, were designed, built and tested giving more experimental evidence of the feasibility of annular emitters in the highly stressed regime. The nominal thrust was 100 μlb. ($\sim 400 \mu N$), the I_{sp} was about 1400 sec. and the operational voltage 13 kV. The engines had individual heaters to provide thermal control to the mas flowrate. It was found that the beam emitted by the array had a larger divergence semi-angle than the single emitter case. In the case of the highly packed emitter array it was needed to bias a negative voltage (~ 400 V) to the engine screen so the backstream electrons would not hit the emitters (this electron current was probably made of secondary electrons).

In 1975 a work was published on the temperature and capillarity effects for Colloid Thrusters, specifically in surface tension driven propellant flow [Bailey, 1975]. This work is interesting because it explores in some detail the temperature influences on the capillary propellant transport, a method that seems not to have been researched in the USA before the publication time (the paper is from the UK). The propellant is glycerol with NaI doping. The paper argues that it is important to find a better candidate for propellant than the one mentioned because it has strong temperature dependence on its physical properties. The work concludes that capillary-fed engines can perform as well as positive pressure-fed engines, even in wide temperature variations, but that in order to operate at high thrust, large specific charge, the propellant temperature should be as low as possible. Also, whenever the engine was operated

at high current levels there were sudden thrust drops proportional to the capillary length. It is possible that this was due to the unmatched flowrate that is requested by the electrostatic pulling at the meniscus: the engine is then forced to emit in an intermittent way and several performance parameters of the engine that rely on a time-average sampling must fall.

One of the latest works on Colloid Thrusters in the 70's was again from Perel et al., a report on the mechanisms of surface damage [Perel, 1978]. In this reference Perel points out several core facts:

- Potential applications for the Colloid Thruster technology are attitude control and station keeping.
- Erosion traces in the annular emitters suggest the presence of 30 to 40 spraying sites, supporting the multiple cone regime of operation of these engines.
- Electric fields at the emitter tips are estimated to be on the order of 10^7 V/m. This value is substantially smaller than what would be expected for a highly stressed regime.
- Colloid Thrusters tend to show erosion damage after several thousands hours of testing.
- The droplet size distribution is not monodisperse but a gaussian distribution with a mean droplet size equal to 50 Å. The TOF (Time Of Flight) experiments also show the presence of solvated ions. Charged droplets, neutral droplets and electrons complete the kinds of particles that the fan has.
- Most erosion is produced by sputtering mechanisms and thus is concentrated near the emitter tip.
- Collisions between different particle species occur due to the large difference in velocities, which are proportional to the square root of the specific mass for a fixed voltage drop.
- Only collisions between solvated ions and charged droplets can produce droplet breakup.
- Most of the erosion is caused by back bombardment of the emitter by negative ions produced from the breakup of emitted droplets as a result of collisions with fast ions.
- Each negative ion hitting the emitter can sputter up to 10 atoms.
- Fragments of droplets have been detected in TOF experiments providing support to the erosion mechanism.

- Analyzing the erosion mechanism by assuming a monodisperse droplet size dispersion gives results close to the full model with the droplet size distribution, which is in good agreement with experimental data.
- Degradation of the emitter implies a decrease in its field enhancement capacity and thus a smaller performance.

Some of the recommendations of the work are:

- It is recommended to operate at lower voltages to reduce ion bombardment.
- Use of propellant doping with lower mass than iodine to reduce sputtering rate.
- Use of an emitter material with lower sputtering yield.
- Use of propellant with no molecules or atoms with large electron affinity to avoid negative ion production.
- Elimination of the positive ion production at the emitters in order to reduce the ion-to-charged droplet collision rate. This is achieved by lowering the extractor voltage and operating with flowrates larger than the critical value that would emit solvated ions even from the neck of a single Taylor Cone.

Curiously enough, these recommendations point towards what eventually became some of the paradigms of the new Colloid Thruster generation: this is ironic because the reasons given to make the changes were not the actual ones pondered for the renaissance of Colloid Thruster Technology during the last decade.

After the end of the 70's the interest on Colloid Thrusters faded away: the battle against the other electric propulsion engines for the high-I_{sp} technological niche had been lost, specially against the Kauffman engine, a.k.a. ion engine. Among the reasons for this aftermath one can point out the smaller net thrusts obtained with Colloid Thrusters, bulkiness of the engines, complexity of the engine architecture and batch production difficulties amplified by the lack of good understanding on the physics that described the phenomena involved.

2.1.2 The Second Colloid Thruster Technology Wave (1996 - present)

As pointed out in the previous chapter the new breath of Colloid Thruster Technology came mainly because of the appearance of new space applications that require scaled-down efficient space engines and the advance in several fields during the 80's and early 90's, in particular

micro-fabrication and spray ionization, that made feasible low-activation-voltage, bath uniform Colloid Thruster arrays.

In 1996 a paper from the Russians appears [Shtyrlin, 1996] describing the state of the art of the Colloidal propulsion technology developed by the Moscow Aviation Institute for 35 years. In this work the author explains that the Moscow Aviation Institute has been developing a Colloid Thruster that operates in the highly stressed regime, with thrust levels of the order of 0.5 - 1 mN, 30 W DC of power consumption and operational voltage of 15 - 25 kV. Missions such as main propulsion for satellites between 25 and 250 kilograms of mass, 1W/Kg onboard power and missions of $\Delta V \sim$ 40-400 m/s are well suited for this kind of engine. The reference finalizes to argue that Colloid Thruster technology can be transferred to other applications such as thin polymer coating and potable water generation.

In 1997 Mueller, from the Jet Propulsion Laboratory, wrote a paper on the thruster options for a Microspacecraft [Mueller, 1997]. Mueller addressed the problem of supplying thrust to satellites in the 1-20 Kg range: these satellites are or great importance at this moment because they will imply savings in the mission costs -proportional to the payload masses. A mission can be accomplished by a fleet of micro-satellites where the distribution will reduce mission risk. These spacecraft need to miniaturize all its components without reducing its operational range, and also to reduce as much as possible losses that in more powerful systems are not even taken into account when doing an energy balance.

Colloid thrusters are seen, with FEEPs, as the most promising candidate main engine for this kind of missions. Colloid Thrusters have a clear advantage because they can be self-neutralizing, have power requirements are much lower than the ones for FEEP and do not use liquid metals as propellant. The only drawback pointed out in the work by Mueller is its rather small I_{sp} for interplanetary missions, a definite attention focus for future propellant research. MEMS technology was identified as one of the key technologies to develop Colloid Thrusters for its new application range of missions.

In 1999, Martínez-Sánchez et al. publish a paper on micro-propulsion where it is proposed to resurrect the research on Colloid Thrusters [Martínez-Sánchez, 1999]. In this reference Colloid Propulsion is identified as applicable for two kinds of missions: precise attitude or position control, and high I_{sp} / efficient engines. It is also argued that the flexibility of choice in solvents, doping species and cluster configuration suggests a broad mission requirement matching. Finally, it is suggested that micro-fabrication technologies should be used to implement densely packed arrays.

Also in 1999 Stanford University published a paper on its work on Colloid Thrusters [Pranajaya, 1999]. This work is part of the Emerald Nanosatellite project that was intended to promote and support distributed space systems. Stanford university developed a 1 emitter engine and a 100 emitter array, both made of stainless steel capillary, that worked at atmospheric pressure with undoped glycerol and undoped isopropyl alcohol. Collected currents of the order of pA were reported. No mention of the stability of the engine or the correlation between the two engines is mentioned. The reference also points out that one of the strengths of Colloid Thrusters is the lack of complex systems, moving parts and some other complicating factors.

In 1999 the technology development of micro-fabricated Colloid thruster Arrays started at MIT. The first person to start the field development was Paine with his MS Thesis [Paine, 1999]. He tackled with some success the problem of developing a fabrication procedure to assemble a 100-emitter array. Even though his efforts towards contributing to the just born Colloid Thruster Technology Development program at MIT are acknowledged by this author Paine's work had a few flaws, among them:

- The proposal of a non-realistic fabrication procedure. Too many unnecessary steps, the use of wet etching as carving agent for sensitive dimensions, the misunderstanding of the alignment capabilities of MEMS, etc. made this specific process unfeasible.
- The miscalculation of the hydraulic diameter needed for pressure feeding the engine: The expected flow of the whole emitter array was assigned to each individual emitter and an underestimation of 100 times the required hydraulic impedance was made. This evolved into the impossibility to pattern the holes

with the desired geometry with the state of the art of the micro-fabrication capabilities at MIT, then and now.

- No micro-fabrication process tuning was carried out.

In 2000 Khayms publishes his Ph.D. dissertation [Khayms, 2000]. In this work he tackles the problem of efficiently scaling-down electric engines. After some analysis he proposes that both Hall Thrusters and Colloid Thrusters were well suited for the operation. In the case of Colloid Thrusters he points out that the inherent low power consumption and low thrust levels are do not require further scaling down. Finally, he develops a numerical model that accurately predicts the meniscus shape under the influence of the electrostatic pulling, for emitter-to-jet diameter ratios up to 10000, but that fails to correctly map the jet structure.

2001 was a fairly busy year for Colloid Thruster publications. Paine, then at The University of Southampton, in the UK, published in 2001 a paper on his latest developments on Colloid Thruster Technology [Paine, 2001]. This work is intended to contribute to the LISA mission (Laser Interferometer Space Antenna) created by NASA and ESA. His design has the following features:

- The hydraulic impedance of the emitters is quite small: hydraulic diameters are in the 3 - 10 μm while the channel depth is 6 - 8 μm.
- It uses a KOH etch with a diffused boron layer etch stop and a SOI wafer to clearly define the channel length.
- The electrodes are made of Aluminum.
- The electrical insulation is provided by vacuum and by 2 μm of silicon dioxide, either CVD or thermal. He expects not to use more than 1 kV to operate the engine.
- The propellant is pressure fed.

It is the opinion of the present author that this design has several issues that should be revised to produce a successful engine. The following are the most relevant:

- The electrode configuration is prone to produce electrical breakdown because an emitter spill directly creates a short circuit path.
- Electrode-to-emitter separation of 15 μm is not realistic because locally the pressure surrounding the emitters is closer to the vapor pressure of the propel-

lant instead of to hard vacuum; therefore, the probability of breakdown is quite large.

- Most experimental evidence, both from our laboratory experimentation and from other researchers, shows that high hydraulic impedance is needed. The smallest known value of a device that has ever worked is 30:1 [Tang, 2001] but values 1000:1 and above are widely used. This hydraulic impedance is needed to dampen de transients of the turning on of the engine, and in operation provides negative feedback to control the engine, both hydraulically and electrically as being a resistor in series with the emitters. Whenever no hydraulic impedance is present in an emitter array one of the emitters eventually kills the other ones by concentrating the emitted flow.
- It is not a good idea to pressure control something based on a poorly defined hydraulic impedance: a short pipe does not have the distance to fully develop the flow and thus the assumption of a Poiseuille flow is untenable for a length-to-diameter ratio so small. Also, a hydraulic impedance whose characteristic dimensions are closer to the fabrication dimensional uncertainty will invariably imply harder-to-predict characteristics and batch non-uniformity.
- It would be better if the electrodes were made of a more resistant material, such as *Mo, Pt* or *W*. The selection of a more suitable material for the electrodes would increase the engine life.

Also in 2001 an interesting work on Colloid Thruster system development is published by Hruby et al., from the company Busek [Hruby, 2001]. This paper talks about the development and testing of a Colloid Thruster for a flight application (STS-7). The system is composed of a 57 emitter engine, a field emission cathode neutralizer, feed system with propellant storage and a power processor. The whole system fits inside a box $9'' \times 5'' \times 5''$ and weights 2,5 Kg. The emitters are stainless needles of internal diameter equal to 30 μm with a length-to-diameter ratio of 333.3:1 plus a large length of capillary ahead of the needles. The neutralization is carried out with a CNT (Carbon Nano Tube) electron emitter; the feed system is composed of a propellant storage, a micro latching valve and a pressurization system based on zeolite crystals. This engine was delivered to JPL and it is expected to be able to participate in missions such as LISA, Earth Science Experimental Mission 5 (EX-5) and Laser Interplanetary Ranging Experiment (LIRE). The goal of the engine was to provide thrust in the range 1 - 20 μN with 0.1 μN precision for at least 1000 hrs. It demonstrated 20 - 89 μN with a maximum

I_{sp} of 400 sec.; stability of a single emitter was better than 0.01 μN, all this with doped formamide as propellant, with an electrical conductivity of 0.5 Si/m.

In 2001 as well a study on the micropropulsion system selection for formation flight satellites was published [Reichbach, 2001]. This paper addresses the usual claim that Colloid Thruster would fare well enough in this kind of application against the other propulsion options (FEEP, PPT, cold gas thrusters). The missions that this work contemplated are scientific interferometry, as the one mentioned before, such as LISA, ST-3, Terrestrial Planet Finder, Micro-arcsecond X-ray Imaging Mission and Sub-millimeter Probe of the Evolution of Cosmic Structure. The metrics used to evaluated the different propulsion options included performance (the ability to meet specified mission requirements), cost (hardware manufacturing, launch and development) and technical feasibility. Colloid Thrusters were found to be with FEEPs the best propulsion system option for the mentioned missions because of their inherent very fine thrust controlability. For example in PPTs the fact that its operation is pulsed means that the precision of the engine in cancelling disturbances is constrained by the minimum impulse and the maximum pulse repetition frequency the engine can deliver; on the other hand Colloid thrusters have two levels of thrust control: a coarser level that determines how many manifolds are activated at a given time and a finer level that determines the acceleration voltage of each manifold. Because the operation of a Colloid Thruster is continuous and the absolute magnitude of the thrust it delivers is small, this allows the engine to cancel disturbances almost exactly. Unlike Colloid Thrusters FEEPs have a well known noise level inherent to its steady state operation; this noise level is a few percent of the nominal thrust. The clustering potential of Colloid Thrusters allows the engine to span a larger thrust range without changes in propulsion efficiency or I_{sp}. The report ends by urging the future development of FEEPs and Colloid Thruster technologies.

Also on 2001 the present author wrote his MS thesis [Velásquez, 2001]. In this work several design conceptual points were proposed:

- The engine propellant feeding should be pressure controlled and electrically activated. This means that the stagnation pressure at the engine plenum must

be smaller than the maximum pressure withstood by the meniscus by surface tension means.

- This idea implies for most propellants a large length-to-diameter ratio. This automatically supplies large hydraulic impedance for dampening the transients as well as electrical resistance in series to the Taylor Cones to produce negative feedback.
- The engine should operate near the minimum flowrate for single cone stable operation in order to maximize the specific charge.
- The engine should be micro-fabricated to be able to batch process the emitters with good uniformity.
- Given the state of the art of the micro-fabrication technology it is not possible to pattern through channels with such large length to diameter ratio. It was proposed to pattern the channels *along* the wafer surface, that is, running parallel to the top surface.
- It was proposed to pattern the channels in halves, so two wafers are used to produce the hydraulic features.
- The hydraulic system inside the engine should consist of a plenum (tank), a manifold system and a set of channels.
- Silicon oxide and vacuum would provide electrical insulation to the engine; silicon would be the substrate material for the engine as 4" wafers 400 μm thick.
- An operational voltage to turn on the engine equal to 1200 V and a second stage for acceleration was proposed.
- The electrodes would be part of the hydraulics substrates.
- The emitters were proposed to be formed on the substrate edge, that is in a surface whose normal falls inside the plane defined by the channels.
- Some fabrication tuning was carried out but a working device was not finished.

This design had several problems when the time to fabricate the engine came:

- It was proposed to use wet etching to pattern the channels. This proved to be untenable because of etching-non-uniformities and lack of good control, because the etching is time-controlled. Therefore, it was decided to use plasma etching to pattern the channels. The idea of plasma etching cycling was proposed with successful results since then.
- The electrodes were meant to be patterned on a previously patterned surface; in other words the electrodes had to be transferred to an isotropic carving. The limitations of this technique were explored during the summer after the writing of the MS thesis and it was found that it is possible to transfer lines 10 μm wide

20 μm apart in isotropic trenches up to 20 - 25 μm deep. Because the engine needed 40 - 50 μm deep electrode trenches to take care of the droplet fan divergence angle this fact made it unfeasible to produce the electrical system. Some time later, based on the experiences of isotropic nested etching masks, it was found that a shadow-like mask could work well to pattern the electrode beds into the isotropic trenches.

- The vacuum gap needed to be too small (20 μm) because the larger the gap the deeper the isotropic carvings that would receive the electrodes should be. This problem got compounded with the one previously mentioned making the electrical system of the engine not possible to build in a satisfactory way.
- The field enhancement issue was not addressed. The emitters were then unsharpened with the consequent increase in the operational voltage and possibly wetting problems.

The last chapter of the MS thesis included a new design were the hydraulic impedance was supplied in the traditional way of long channels with a characteristic cross-sectional length but with the emitters *perpendicular* to the channel's axis so sharpening of the emitters was feasible with isotropic etching and photolithographic techniques. Fabrication development of the engine in its MS version with some exploration of the isotropic nested mask approach for the emitters is available in several reports to AFOSR and in a conference paper [Velásquez, 2002]. This idea of having a Linear array is corrected, improved and developed in this Ph.D. dissertation, as well as in several other conference papers [Velásquez, 2002-2; Velásquez, 2003; Velásquez, 2003-2] where the first experimental data of the Linear Colloid Thruster Array appear [Velásquez, 2003-2].

In 2001 as well a paper published on one of the American Chemical Society journals claimed the fabrication and testing of a nine-emitter system for mass spectrometry [Tang, 2001]. This work is not directly related to the conception and development of a propulsion system but it is quite interesting in the sense that it harnesses the same kind of technology required for Colloid thrusters with positive results. The emitters were patterned with a laser ablation system on a 1 mm thick polycarbonate substrate. The emitters were about 1.1 mm apart, with internal diameter equal to 30 μm. The surface of the emitters were treated with a CF_4 plasma (possibly to deposit polymers on the surface) to address wettability issues in the emitters and reach stable operation. The electrode was externally provided(5 mm apart) and the engine was

fed by a positive displacement pump. The working fluid was 50:50 methanol/water + 1% acetic acid. The experiments were done at atmospheric pressure. The experimental data of emitted current versus flowrate follows a power law with exponent equal to 0.44, close to the theoretical 0.5 from de la Mora's equations [de la Mora, 1994]. Probably the exponent is not exactly 0.5 because the tests were done at atmospheric pressure and this way the emitted particles had a chance to scatter/ be neutralized with the surrounding gas. The extraction voltage was 7 kV and a picture of 9 stable Taylor Cones is provided. The experimental data confirms that the emitted current (for a fixed total flow rate) is proportional to the square root of the number of emitters, a direct consequence of the de la Mora's laws.

In 2002 two papers from Xiong et al. appear on the fabrication and testing of a Colloid Thruster Array [Xiong, 2002; Xiong, 2002-2]. Both are interesting in the sense that it seems the authors manage to make two engine concepts work but unfortunately not enough rigor in the measurements and the proposed experiment to validate the engine make the paper lack true propulsion value. Lacking were for instance current versus flowrate measurements, a curve of thrust versus some relevant parameter, pictures of the external electrodes showing the impact marks of the engine exit stream as a proof of uniformity, or in any case stronger evidence than stating that the engine emitted this current at one operational point, so it works.

The first concept is, despite claims by the authors, a modification of the KOH-based emitter array proposed by Paine [Paine, 2001]. The electrode is made of aluminum as well but in this case the electrode substrate and the emitter substrate are separated by a glass gasket bonded with epoxy. The first question that arises is how they assured parallelism between the emitters and the electrode, a question that is not satisfactorily answered: as a matter of fact a non-uniformity in emission due to non-planarity has been seen in the 2-D engine test structures (see Chapter 6). The papers are poorly written, but it seems the hydraulic diameter is about 30 μm with a small length-to-diameter ratio. The authors show the SEM pictures of a 4-emitter array used to test the concept. Based on an indirect thrust measurement (the deflection of a cantilever beam due to the momentum transfer of the engine exit stream) the authors claim the

thrust measured at 1970 V is 6.8 μN which they conclude is in agreement with the prediction of four emitters delivering 1.9 μN of thrust with a flowrate of 1 nl/sec. (this thrust value is about right for a single emitter).

The paper makes two not well-corroborated claims:

- The authors claim the flowrate is 1 nl/sec. This flowrate is about 50 times the minimum flowrate for single cone stable operation ($2 \times 10^{-14} m^3$ /sec. for formamide of electrical conductivity equal to 2.1 Si/m) which implies an η value of about 7, a parameter believable for the stable droplet regime. There is not direct/indirect measurement of this flowrate but the assumption that somehow it occurs, not even the statement that a positive displacement pump or some other means was used to supply propellant. It is curious that the way the propellant was supplied to the engine was not mentioned in the paper.
- The authors measured the *total* thrust produced by the engine and the *total* flowrate fed into the engine. Then the issue that the engine is an array comes into play: de la Mora's law between the emitted current I and flowrate Q *per emitter* gives

$$I = f(\varepsilon) \cdot \left(\frac{K \cdot \gamma \cdot Q}{\varepsilon} \right)^{1/2} \tag{2.1}$$

where $f(\varepsilon)$ is an experimental fit function, K is the electrical conductivity of the propellant, ε is the relative electrical permittivity and γ is the surface tension of the liquid. If we assume that the engine uniformly emits the current and the flowrate through n-emitters then the following equation holds:

$$I_{total} = \sqrt{n} \cdot f(\varepsilon) \cdot \left(\frac{K \cdot \gamma \cdot Q_{total}}{\varepsilon} \right)^{1/2} \tag{2.2}$$

where there is a correction of the original formula given by the square root of the number of emitters. The thrust F is then (for one emitter)

$$F = \sqrt{2 \cdot V \cdot \rho \cdot f(\varepsilon)} \cdot \left(\frac{K \cdot \gamma \cdot Q^3}{\varepsilon} \right)^{1/4} \tag{2.3}$$

where V is the total voltage drop and ρ is the liquid mass density. With the same argument the equation for thrust gets corrected into

$$F_{total} = \sqrt[4]{n} \cdot \sqrt{2 \cdot V \cdot \rho \cdot f(\varepsilon)} \cdot \left(\frac{K \cdot \gamma \cdot Q_{total}^3}{\varepsilon} \right)^{1/4} \tag{2.4}$$

where the correction factor is then the number of emitters to the 0.25 power. It would have been really interesting to state that the de la Mora's law gets corrected for uniformly operating arrays and test this behavior experimentally, as was the case with the current versus flowrate measurements in the paper written by Tang [Tang, 2001].

In any case the authors do not support the claim of simultaneous operation of all the emitters with some direct evidence. What is fair to say about their engine is that it emitted some current while energized at 2000 V. The stability claim does not support engine emitter uniformity because you can have a situation where the engine is stable but only a few of the emitters emitting. The oscillations of the signal shown in the paper probably come from some noise source, like the vacuum pump oscillations as stated in their paper (50 Hz).

The second paper discusses an engine made with printed circuit board-based technology as Colloid Thruster, and a micropump made of two valves, a pump chamber and PZT as piezoelectric actuator. The thrust is measured by the displacement of a cantilever due to the thrust of the engine. The experiment is done in air with a starting voltage above 3.5 kV. A displacement curve of the cantilever tip made of narrow peaks is shown. The thrust measurement is analogous to the one used in the first paper; in this case it is at most a coarse estimate since it assumes perfectly elastic scattering of the emitted jet, some non-measured bouncing angle for the momentum transfer (presumably $90°$) and does not mention the fact that to emit in atmospheric pressure implies to lose some of the emitted current. The plot shows that the engine is not stable (as is acknowledged in the paper), in other words that it functions in bursts. It is possible that the reason for this behavior is related to the fact that the emitters do not have large hydraulic impedance and never make it through the transients (the length to diameter ratio is about 13.3:1). No proof of spatially-uniform emission is provided but in any case it is interesting to see that a simple, cheap fabrication process can produce engines that can actually work, not to satisfaction but work anyhow.

In 2002 a paper from Mueller et al. is published describing the research activities of JPL in micro-propulsion [Mueller, 2002]. This paper points out that both FEEP and Colloid thrust-

ers look attractive for the thrust range 1 - 20 μN with I_{sp} > 500 sec. where these parameter ranges capture a number of missions that also require engine mass reduction to become feasible. Among the missions pointed out there is the Magnetic Constellation where 50 - 100 spacecraft would be deployed to map Earth's magnetic field: large constellations are possible only if very small spacecraft are used to make launching costs affordable; another application is the use of pico-satellites for Earth observation, a mission contemplated by the Department of Defense. The paper discusses several other engine technologies such as FEEPs, micro-ion engines, Vaporizing Liquid Micro-thrusters (VLM) and gives some interesting information on the development of micro-fabricated Colloid thrusters: JPL was then developing a 36 emitter array with length-to-diameter ratio of 30:1 on SOI (Silicon On Insulator) wafers. This concept uses DRIE (Deep Reactive Ion Etching) to pattern the channels vertically on the silicon substrate. Gold bonding is used to join the extractor electrodes to the emitters and a second electrode stage was envisioned to further increase the exit velocity of the jets. The characteristic hydraulic diameter is about 8 μm. A picture of an emitter and electrode array is supplied in the paper, unfortunately with not enough magnification for providing information of the actual geometries used in the emitters, electrode, emitter-to-emitter separation, etc. The electrode-to-emitter gap is 20 μm and the electrode grid holes are between 40 and 200 μm. If the engine uses a highly doped solvent with non-zero vapor pressure even the wider electrode grid hole size could imply electrical breakdown because of the reasons previously pointed out in this chapter.

In 2002 M. Fife and D. Kirtley published a paper on a Colloid Thruster Acceleration Concept [Fife, 2002]. The idea introduced in this paper is to use the very same hydraulics as any other Colloid Thruster but to change the electrode system into an electrodynamic linear accelerator. A set of gates with varying spacing distances would be placed in front of the emitters in order to accelerate the charged droplets that conform the exit stream. The bias voltage would be AC, substantially smaller than the DC voltages that are implied in Colloid Thruster operation. Among the benefits of using this approach to accelerate the exit jets are a potentially larger I_{sp}, higher acceleration efficiency, simple acceleration physics, the fact that it would not require a CD rectifier and the absence of large voltages. The Colloid linear accelerator would

still have the same problems related to all Colloid Thrusters such as its complicated flow system, potential gate clogging, beam neutralization -if not operated in a bipolar mode-. Another critical disadvantage is related to the dispersion of the specific charge of the droplet population: if there is more than one specific charge the electrode gate system will not work properly. The main comment to this concept by this author is that to use fully reversed AC voltage signals, that is a voltage signal whose AC amplitude is larger than its mean value -presumably zero-, could imply large losses, up to 50% [Senturia, 2000]. Therefore, the efficiency gained in some parts of the engine performance can be lost if the power supply is not well selected.

The summary about the state of the art in Colloid Thruster technology just presented can serve as a good introduction and contrast background to the technology developments made in this Ph.D. dissertation, namely the exploration of Colloid Thruster Arrays in Linear and Planar geometries. Chapter 3 will cover the development of an internally fed, pressure controlled, micro-fabricated Colloid Thruster Array where the emitters are organized in a dotted line and use doped formamide as propellant. Chapters 4 will discuss the development of an externally fed micro-fabricated Colloid Thruster Array where the emitters are organized in a planar array that uses ionic liquid as propellant. Finally, Chapter 5 contains the conclusions and suggestions from the two engine concept validation are provided, as well as some future research directions on Colloid Thruster Technology: polymer arrays, internally fed planar arrays and holey fiber based engines.

This research survey finishes with a few references that inspire the work on Planar Colloid Thrusters done in this Ph.D. dissertation. Since some time it has been known that if the propellant is conductive enough, and the flow rate is small enough, the Taylor Cone can emit solvated ions in a mixed regime [Martinez-Sanchez, 2001]. In the last year it has been demonstrated experimentally that it is possible to extract only ions from electrospray sources that use ionic liquids [de la Mora, 2003; Dressler, 2003; Lozano, 2003]. Ionic liquids are virtually molted salts that have no solvent. On one hand to extract only ions increases the propulsive efficiency (compared to the mixed regime) and it allows to build efficient engines with a different specific impulse and thrust range compared to electrospray engines based on drop-

let emission; on the other hand to emit net charge particles implies to leave in the counter-electrode reactive species that can produce electrochemical effects if enough voltage is build up. Recent work has preliminary demonstrated that AC operation of electrospray sources using ionic liquids solves both the problem of the engine charge neutrality and the electrochemical effects making the concept of using ionic liquids in electrospray engines feasible [Lozano, unpublished work]. It is important to mention that externally fed electrospray engines are not a true novelty because FEEPs (Field Emission Electric Propulsion) and LMIS (Liquid Metal Ion Sources) use this engine architecture [Mair, 1991].

2.2 A brief statement on the way this Ph.D. dissertation expands the state of the art in Colloid Thruster Technology

This author believes that the research carried out in his Ph.D. dissertation is useful for the advance of the field of Colloid Thruster Technology because it expands the current state of the art. In particular Colloid Thruster Technology is benefited from the research work because of the following reasons:

- The research proposes fabrication processes that involve state of the art and novel micro-fabrication procedures. In other words, it not only tackles the problem of producing high emitter density Colloid Thruster Arrays with some of the best fabrication techniques available to date, but the bounds of what is feasible to produce using micro-fabrication techniques have been moved with the introduction of new processing chemistries, sequences and strategies. As a matter of fact most micro-fabricated Colloid Thruster Arrays proposed to date involve surface micro-machining instead of a combination of bulk and surface micro-machining, substantially constraining the range of dimensions that the different engine parts can get.
- The micro-fabricated Colloid thruster Arrays proposed before this dissertation implement emitter sets either composed of a small number of emitters or made of emitters with rather large dimensions, not taking full advantage of the clustering potential of micro-fabrication.
- Two key engineering decisions have been proposed and validated: to produce in different substrates the engine hydraulics and the electrodes without losing high alignment precision, and to *time-control* the etchings to produce uniform features. The first decision allows to optimize the susbtrate choice for the engine hydraulics and electrodes. The second decision implies the reduction of the

number of wafers to be bonded down to the minimum, while the former allowed to produce electrodes with large electrical safety. These two decisions translate in larger engine production yields and better performance.

- It is the first time that direct uniformity emission tests have been provided, in particular using the impact marks of the engine exit streams. On one hand an approach to validate uniform emission that was implemented in this dissertation is to measure overall emitted quantities, like currents and flowrates, and compare them to per-emitter characterization values -this strategy was carried out as well in previous works [Tang, 2001]-; on the other hand to provide impact pictures allows a far better corroboration on uniform emission.
- To the best of the knowledge of this author it is the first time current versus flowrate values in agreement with reduced-order models have been provided for large emitter arrays operating in vacuum. The other result of this kind known to this author operated at atmospheric pressure [Tang, 2001].
- The work gives experimental evidence towards demonstrating that in single Cone emission mode the charge distribution of the jet / charged particle fan is uniform, without the presence of a thermalized tail, as predicted from modeling [Lozano, 2003]. Furthermore, divergence angles shown this way are in agreement with the magnitude values reported for single emitter experiments both in droplet regime and solvated ion regime [Lozano, 2003]. This is an important issue because one of the strengths of Colloid Thrusters is their inherent low divergence that translates into smaller voltage optics and reduction of engine degradation from exit stream impacts.
- It is the first time a planar open architecture using an ionic liquid is proposed, implemented and tested; nonetheless, the first demonstration of external wetting ion emission was made by Lozano [Lozano, unpublished work]. The two key contributions are then the development of a silicon surface treatment and methods to making dense arrays of needles to make silicon-based planar arrays feasible. A preliminary test that demonstrates the feasibility of varying orders of magnitude the emitted current via thermal control was successfully carried out. As many as a thousand emitters in less than $0.64 cm^2$ has been demonstrated.
- It is the first time a reasonable answer to the problems on electrical breakdown that micro-fabricated Colloid Thruster Arrays face because of the small gap dimensions and insulating layer thicknesses has been provided, in particular by using micro-fabrication technologies as well. The solution provided here is two-fold: on one hand it involves the deposition and patterning of thick SiO_2 layers with plasma and the use of micro-fabricated displacement springs for the tasks of alignment and clamping while assembling. This solution has been demonstrated to be able to space the electrodes with respect to the emitters with resolution in the micron-size range. This way the fabrication clustering potential is not affected by the interaction with macro-sized interfaces.

- It is the fist time that an electrode system for a micro-fabricated Colloid Thruster whose conductive parts are made of refractory metal is proposed, fabricated and validated. The electrodes produced in this work used Tungsten as conductive material but the procedure allows to deposit any CMOS compatible metal including Molybdenum and some other good anti-sputtering candidates.
- In a broader sense the research work proposes design concepts applicable to many other propellants, substrates and operation modes: flowrate matching, electrical control and clustering architectures. Therefore, one of its strengths is its inherent adaptability.

Chapter 3

PRELIMINARY DEVELOPMENT OF A LINEAR COLLOID THRUSTER ARRAY

This chapter illustrates the development of an electrically controlled, internally fed Linear Colloid Thruster Array that uses doped formamide as propellant and sharpened spouts as field enhancers. The engine operates in the droplet emission regime. The exposition is concentrated in three key topics:

- Explanation of the engine design concept and design decisions.
- Device fabrication.
- Device results, analysis and discussion.

The conclusions that arise from the validation of the proposed Linear Colloid Thruster Array appear in Chapter 7.

3.1 Engine design concept

The proposed Linear Colloid Thruster Array is the result of pondering considerations about the propellant selection, flowrate control, engine architecture, emission mode, electrical losses and electrical issues. The following paragraphs will briefly comment each one of these design criteria.

3.1.1 Propellant selection

The engine uses doped formamide as propellant. Ionic salt doping is needed to increase the electrical conductivity of the propellant, directly related with the engine I_{sp}. The propellant

choice comes from considerations on the physics of Taylor Cone emission in droplet mode, as well as the engine architecture: in an internally fed engine it is possible to use propellants with moderate vapor pressure because most of the time the liquid will be shielded from vacuum making the vaporization losses inherent of the spout exits.

The total current emitted by a Taylor cone as a droplet fan drifting from the cone apex is [de la Mora, 1994]

$$I = f(\varepsilon) \cdot \left[\frac{\gamma \cdot K \cdot Q}{\varepsilon}\right]^{1/2} \tag{3.1}$$

where γ is the surface tension, K is the electrical conductivity, Q is the flowrate emitted by the taylor Cone, ε is the relative electrical permittivity, and $f(\varepsilon)$ is a function of ε. When the dielectric constant is large the function $f(\varepsilon)$ tends to a limit value experimentally found to be near 20 for ε values larger than about 40; for smaller ε values the experimental coefficient functional dependence can be roughly described as a straight line passing through the origin.

Equation 3.1 is independent of voltage, but it applies only as long as the single cone jet regime holds, which, for a fixed flow rate, is in a narrow voltage range near the start-up voltage. When the voltage is increased enough the current emitted goes through several step-like increases and eventually shows an exponential behavior [Hruby, 2001].

The specific charge δ is defined as

$$\begin{aligned} \delta &= \frac{q}{m} = \frac{I}{\rho \cdot Q} \\ \delta &= \left[\frac{\gamma \cdot K}{\varepsilon \cdot Q}\right]^{1/2} \cdot \frac{f(\varepsilon)}{\rho} \end{aligned} \tag{3.2}$$

where q is the net charge of the emitted particle and m its mass. In a Colloid Thruster it is desired to increase as much as possible the specific charge because this implies larger I_{sp} values for a fixed potential drop. From equation 3.1 it is clear that in order to achieve large I_{sp} it is required to use a propellant that has a ε value larger than 40 and as large as possible electri-

cal conductivity. Also, the engine would use as little flowrate as possible, down to a minimum flowrate Q_{min} needed for steady-sate operation

$$Q_{min} = \eta_{min}^2 \cdot \frac{\gamma \cdot \varepsilon \cdot \varepsilon_o}{\rho \cdot K} \tag{3.3}$$

where η_{min} is the minimum value the dimensionless parameter η can be for stable Taylor cone operation. The dimentionless para meter η is the square root of the ratio between inertial and capillary forces evaluated at the point where the electric field is maximum (at the neck). Experimentally it is known the minimum value for η is about 1.

Formamide has a large electrical permittivity ($\varepsilon = 111$), large electrical conductivity -when doped- (conductivities up to 2.9 Si/m were used in the device testing) and low vapor pressure, a combination of physical values that makes formamide well suited for Colloid Thrusters. Formamide is a solvent with proven cancerigenous effects; therefore, care is advised in handling this substance.

3.1.2 Engine propellant feed and Electrical Control

In the case of the Linear Colloid thruster Array the concept behind the engine operation can be summarized in the following points:

- There is a non-zero pressure difference between the engine tank and the external atmosphere surrounding the engine: this pressure difference is used to feed the propellant to the emitters. The pressure difference between the tank and the exterior is such that, given the hydraulic impedance of the system, it provides a flow-rate matching the flow-rate steadily pumped by the Taylor cones when the electrodes are activated. This flow rate is a few times the minimum for stable operation if it is intended to maximize the I_{sp}. The literature illustrates that pressure feeding a Colloid Thruster yields a smoother, more controllable and repeatable operation than other alternatives such as a displacement pump fed engine.
- The pressure difference between the engine tank and the outside is smaller than the maximum pressure the meniscus at the emitters tips can withstand by surface tension before breaking/producing flow. Therefore, no flow is possible unless the extractor electrodes are activated. The fraction of the maximum pressure that is actually applied in the engine tank is arbitrarily defined: frac-

tions closer to unity will produce a meniscus with a smaller radius of curvature. A highly curved meniscus is a good idea to lower the threshold activation voltage; on the other hand curvatures closer to zero will be more robust to variations on the propellant physical properties which depend on parameters such as doping concentration, temperature, etc.

- The extra pressure needed to break the meniscus and produce flow is externally supplied as electrostatic pressure by the extractor electrode. The applied voltage between the emitters and the extractor electrode will induce charge at the surface of the meniscus that will set an electric field at the meniscus surface, responsible for the electric suction at the interface that will eventually generate the flow.
- Under operating conditions (flow already established), the internal pressure in the meniscus is much less than the stagnation pressure or the surface tension pressure -which are of the same order of magnitude-. Most of the stagnation pressure at the reservoir is lost as viscous losses in the hydraulic system (mainly at the channels); the electrostatic pressure and surface tension effects balance each other leaving a pressure difference between the meniscus interior and exterior close to zero [Taylor, 1964; Carretero, 2003].
- The flow field in the channels is assumed to be fully developed, and is described by the Navier-Stokes equations. The volumetric flowrate through the square channel of axial length L and square cross section of side L_c is

$$Q = 0.42173 \cdot \frac{L_c^4}{12 \cdot \mu} \cdot \frac{\Delta P}{L} \tag{3.4}$$

where ΔP is the available pressure difference and μ the liquid viscosity.

- Once a fraction of the maximum pressure that can be applied to the engine has been selected, the channel hydraulic diameter is obtained by equating the hydraulic loss to the fraction of the maximum meniscus capillary pressure. The maximum pressure withstood by a meniscus at the end of a channel of square cross-section is [Leonomand, 1981]

$$\Delta P = \frac{3.77 \cdot \gamma}{L_c} \tag{3.5}$$

For a given value f of the ratio of the maximum pressure withstood by the meniscus before breaking to the available stagnation pressure at the engine tank, the engine hydraulic system length-to-diameter ratio is expressed in the case of a channel with circular cross-section as

$$\frac{L}{L_c} = \left[\frac{0.1326 \cdot \gamma \cdot f \cdot L^2}{Q \cdot \mu}\right]^{1/3} \tag{3.6}$$

This gives for most electrolytes a large length-to-hydraulic diameter ratio, i.e., large hydraulic impedance. Given the state of the art of the micro-fabrication procedures, a good way to obtain a high length-to-characteristic cross-sectional length ratio for a cross-section that can be dimensionally controlled is by carving the feed channels along the top surface of the wafer.

- When working with moderate vapor pressure propellants the hydraulic diameter should be as small as possible to avoid evaporation losses because they scale as the square of the hydraulic diameter and evaporation losses can produce emitter clogging. A small hydraulic diameter also implies a smaller start-up voltage because it scales as the square root of the hydraulic diameter. It is advisable to design engines with a hydraulic diameter substantially larger than D^* (the minimum), due to inherent variations in the engine dimensions from fabrication and the physical properties of the propellant. If the propellant is a highly doped solvent and its physical properties are not determined then this design choice gives some room for variation. Figure 3.1 shows the propellant tank stagnation pressure (A) and several percentages of the maximum reservoir pressure before producing flow, all vs. hydraulic diameter, for a fixed flow rate - three times the minimum flow rate- (100% (B), 75% (C), 50% (D), 25% (E)). It is also assumed that the channel axial length has been fixed: this makes sense due to space constrains in the wafer set up that arise in practice. D^* occurs when the line of 100% and the stagnation pressure line meet. Figure 3.1 was obtained for NaI-doped formamide with an electrical conductivity of 2.3 Si/m. For Formamide of such conductivity D^* is around 7 μm when the channel axial length is 15 mm.
- The mode of operation proposed for the Linear Colloid Thruster Array can be easily adapted to many other propellants.
- To reach the desired I_{sp} a second electrode, the accelerator, is placed with a bias voltage with respect to the extractor. The purpose of a second electrode is to maintain a low-enough voltage to assure that just one Taylor cone is produced in each emitter, regardless of the voltage needed to reach the I_{sp} /thrust goal.

There are several other advantages for implementing this concept for a Colloid engine. The author also believes a Colloid Thruster based on this approach is operationally more robust than one with a low hydraulic impedance feed, even though it implies a more complicated micro-fabrication process, because it is able to better dampen instabilities that might arise while functioning. The Space Propulsion Laboratory has substantial evidence to believe that Colloid Thruster Arrays with low hydraulic impedance tend to function with just a fraction of the emitters turned on: a possible explanation of this behavior is that the emitters end up killing the emission of the neighboring partners by stealing the flow rate intended for them.

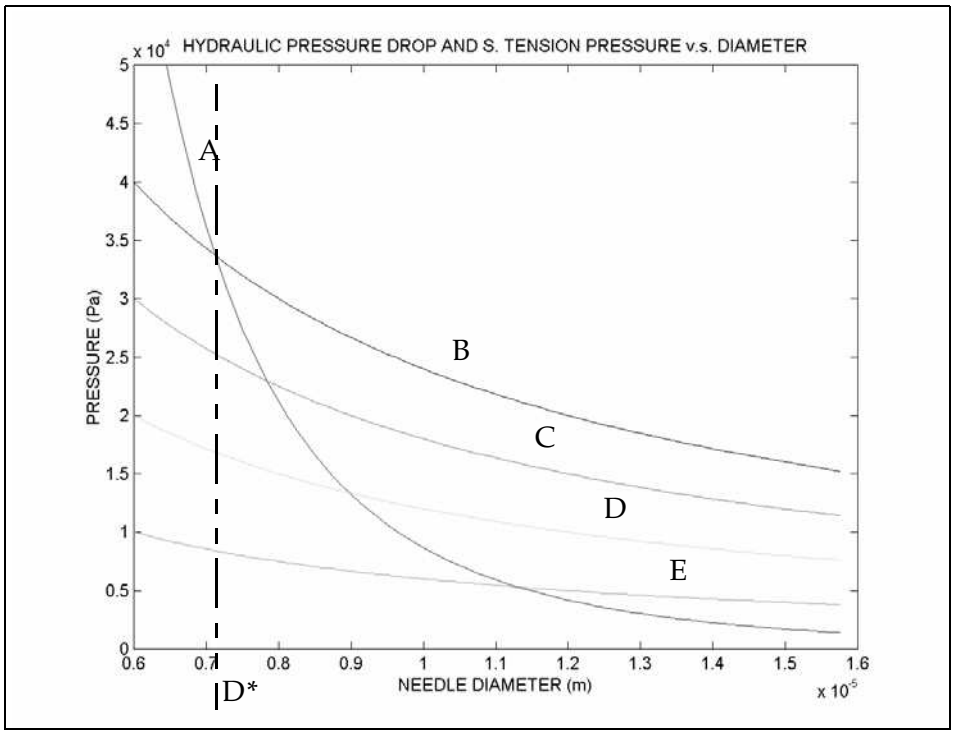

Figure 3.1 Stagnation pressure at the 1-D Colloid Thruster tank (A), and fractions (100% (B), 75% (C), 50% (D), 25% (E)) of the maximum pressure withstood by the meniscus at the emitter before flow versus characteristic cross-sectional length for NaI-doped formamide, 2.3 Si/m, for a fixed flowrate (three times the minimum flow rate), temperature and channel length. The channel cross-section is a square.

Occasionally, we might want to control the temperature of the engine, for example to change the physical properties of the propellant in order to tune either the I_{sp} or the thrust by changing the operational point of the engine or even its regime (droplet emission, solvated ion emission or a mix of them). In this case a large hydraulic impedance makes room to locally place heat controllers and extend the residence time of the propellant in the heated area.

Finally, the validity of using a continuum approach to model the fluid dynamics is determined by the non-dimensional *Knudsen number* K_n, which is the ratio between the liquid molecular mean free path and the characteristic cross-sectional length: for Knudsen values smaller than 0.1 the zero slip condition at the solid boundary is accurate; for Knudsen numbers larger than 0.1 the zero slip condition at the solid boundaries is no longer true; the particles near the solid interface resemble particles bouncing over a solid wall while conserving at least part of their

tangential momentum, i.e., sliding along the solid interface. Among the several corrections that can be implemented the effective viscosity -a reduction of the original viscosity- defined as

$$\mu_{eff} = \frac{\mu}{1 + 6 \cdot K_n} \tag{3.7}$$

is the easiest to implement and gives good integral results (predicts with good accuracy integral results of the flow field such as flow rate [Senturia, 2000]). The correction of the viscosity is important for MEMS that interact with rarefied gases in micron-size gaps. In the case of liquids inside channels with diameters equal to several microns the Knudsen number is far smaller than 0.1 and the effective viscosity is for practical purposes identical to the unchanged viscosity.

3.1.3 Engine architecture and structural considerations

Based on the propellant selection, electrical flowrate control, and available micro-fabrication methods, an internally fed architecture is proposed. The device uses silicon wafers as substrates, while the electrical insulation is provided by thick CMOS-grade silicon oxide films and vacuum. The use of thick oxide films required to implement stress compensation fabrication procedures for both intrinsic and thermal stresses [Velásquez, 2003-3].

The engine has a hydraulic system that aims to both enable efficient / more uniform engine propellant filling-in, and supply hydraulic impedance to achieve flowrate matching.

The other two key architectural design decisions are the use of uniform time controlled etchings to generate critical engine features, and fabricating the electrodes and the hydraulics in different substrates:

- Implementing time control etchings requires a tight control of the fabrication procedures. With time control etching it is possible to have several etch depth features in the same substrate, opposed to defining the critical depths by the substrate thickness. The benefit of implementing time controlled etching is to gain an overall simpler fabrication process because less substrates are needed.

- To decouple the hydraulics and electrode susbtrates needs some precision assembly strategy. Therefore, the engine fabrication includes a suitable assembly system based on displacement springs.

Most of the hydraulic system is carved in a single substrate to avoid alignment problems. There is a sealing wafer to allow pressurization of the engine hydraulics. The hydraulic system of the Linear Colloid Thruster Array has the following architecture:

- A plenum or propellant tank that locally stores the propellant. The propellant tank is reachable from the exterior by an inlet.
- A set of twelve manifolds intended to distribute the propellant to the channels.
- A set of channels, twenty per manifold, that provide most of the hydraulic impedance. The channels have a square cross-section to facilitate its fabrication and to reduce property variations from time-controlled etching.
- For each channel there is a spout, responsible for addressing wettability issues, and electric field enhancement.

The author believes that an engine with manifolds and plenums is stiffer, more resistant to pressure differences in the plenums and in general with better performance in structural terms. Also, grouping the emitters in manifolds allows us to leave pads of unperturbed surface to enhance wafer bonding quality. The tank has a set of columns to avoid excessive deflection or collapse when pressurized. The other role of the columns is to provide physical support to attach the fluidic nanoport to the inlet.

The electric system of the engine has the following architecture:

- An extractor electrode, responsible for generating the Taylor Cone from the propellant meniscus formed by the existence of pressure difference between the engine tank and the exterior.
- An accelerator electrode, responsible for providing to the exit stream the intended velocity.

An schematic of the engine architecture is shown in Figure 3.2 (the electrodes from the conceptual point of view are identical; therefore, only one electrode schematic appears). The engine hydraulics is seen without the sealing substrate in order to illustrate the different parts of the hydraulics. The dimensions shown in the schematic are in μm.

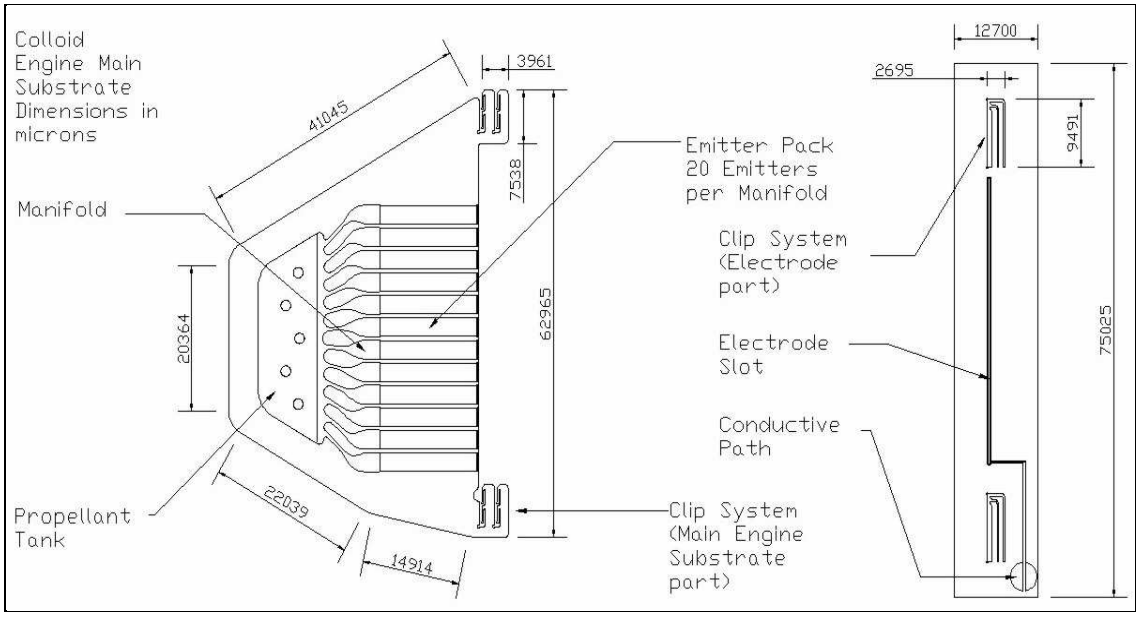

Figure 3.2 1-D Colloid Thruster Array schematic.

Three spout geometries are proposed as a trade-off between fabrication complexity and field enhancement capabilities (more area reduction provides better field enhancement).

- *Non-sharpened* emitters that have emitter-to-emitter separations but not out-of-plane area reduction.
- Emitters with emitter-to-emitter separations and one out-of-plane sharpening, i.e., *half-sharpened.*
- Fully sharpened emitters.

The spout geometries are shown in Figure 3.3. The emitter-to-extractor separation is dominated by propellant vapor pressure considerations, instead of the jet divergence. The way the engine hydraulics and electrodes are assembled is shown in Figure 3.4 and Figure 3.5.

The spring system that carries out the electrode - hydraulic assembly is designed considering silicon as a linear isotropic material [Senturia, 2000] with an allowed tensile stress equal to 1GPa [Spearing, 2000; Rice, 1981], with the following design premises:

- It should be possible to assemble the engine by hand to the electrodes while preserving good alignment, by taking advantage of the absolute precision uncertainty of the micro-fabrication techniques, specifically contact photolithography and DRIE (Deep Reactive Ion Etching).

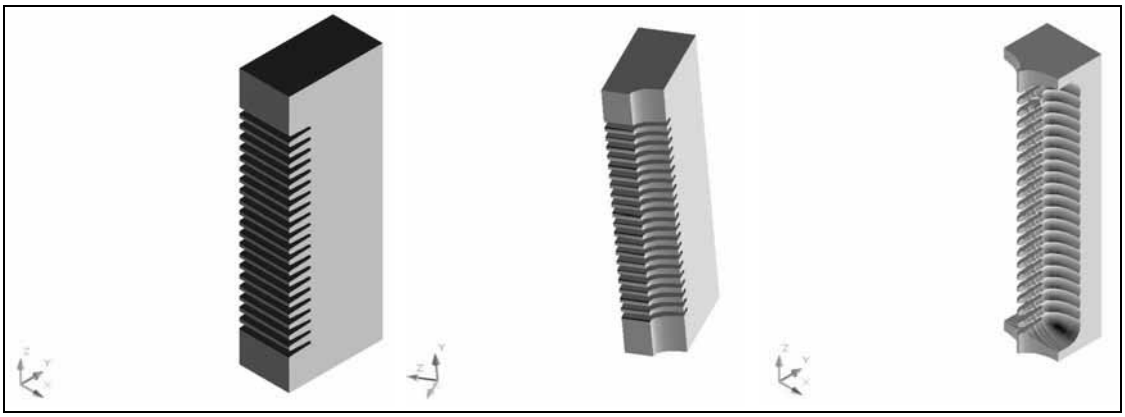

Figure 3.3 Schematics of the proposed spout geometries: unsharpened spouts *(left)*, half sharpened *(center)*, and fully sharpened *(right)*. The emitters are placed at the middle of the substrate, at the center of each finger-like structure.

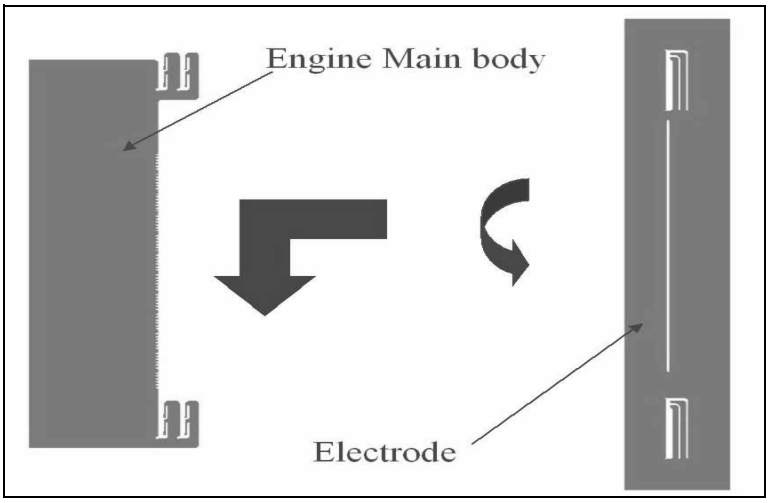

Figure 3.4 Schematic to illustrate the way the hydraulic and electric system of the 1-D engine are hand assembled via a set of springs to self align the two structures while having acceptable misalignment levels.

- The assembly should tolerate as much misalignment as possible, including beam divergence.
- The springs should be activated with the smallest expected wafer thickness and when acting on the maximum expected thickness wafers, they should not to fail

The assembly concept is fully explained and validated in a paper in preparation by the author [Velásquez, unpublished work]. The design was optimized using the commercial finite Element Software Ansys. The following are some of the highlights of the assembly: each spring

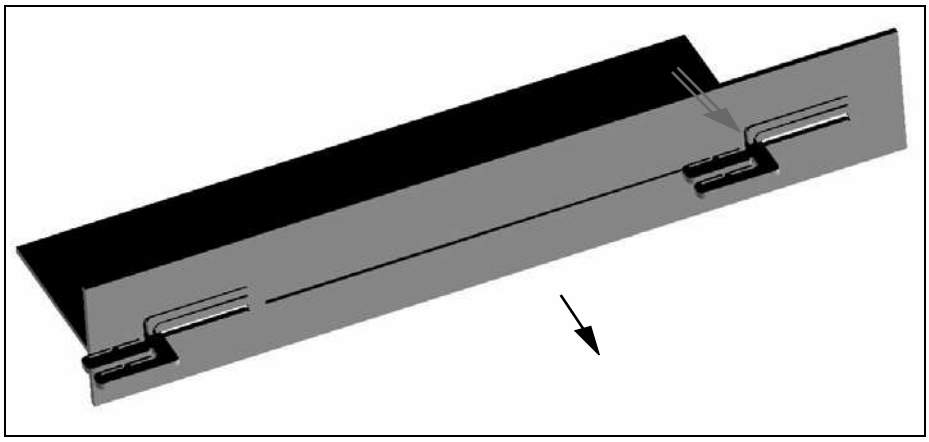

Figure 3.5 Computer-generated model of a hydraulic substrate and an extractor electrode in assembly. The single tailed arrow shows the direction of the emitted droplets. The doubly tailed arrow indicates the view direction of the SEM pictures that illustrate the assembly tests in page 110.

exerts a force of the order of 1 N when deformed; the misalignment was estimated at about 15 μm in either direction, with a misalignment floor estimated at 5 μm; the misalignment value is substantially smaller than the maximum misalignment allowed by the assembly: 120 μm; some safety factor to spring misuse is provided in the design; because the springs are in *tension* when the electrodes are assembled buckling does not take place.

There are two clip geometries, one for each substrate that takes part in the union, as shown in Figure 3.6 and Figure 3.7. The principal reason for this difference was the available room on each of the substrates. Both figures show the geometries in their true proportions: as a guideline the substrate thickness shown in the drawing is 700 μm.

3.1.4 Operational Mode

The engine is intended to operate in the single Taylor Cone mode because the highly stressed regime is not as well understood as the former, and also because a single cone yields lower beam divergence.

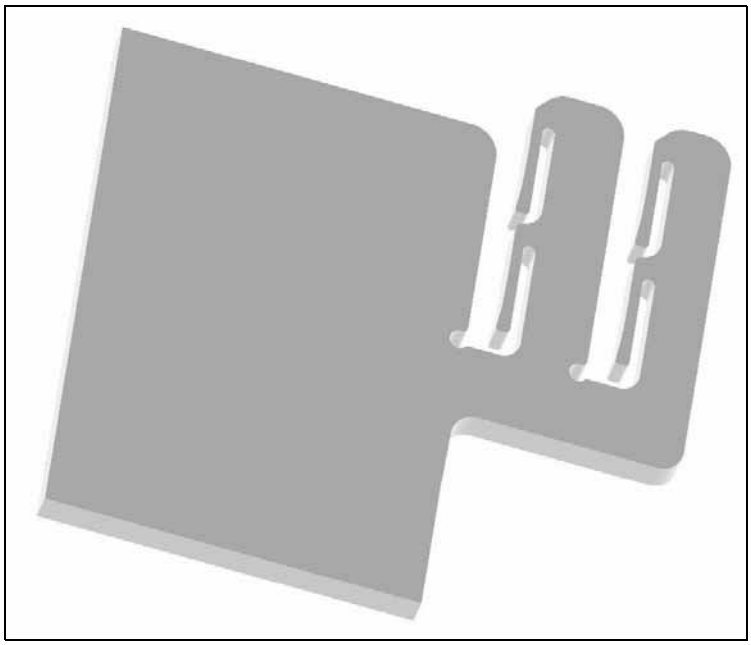

Figure 3.6 3-D schematic of the clips system carved on the engine main substrate. The drawing is to scale. The inner spring pair clamps the extractor electrode while the other pair plays the same role for the accelerator electrode.

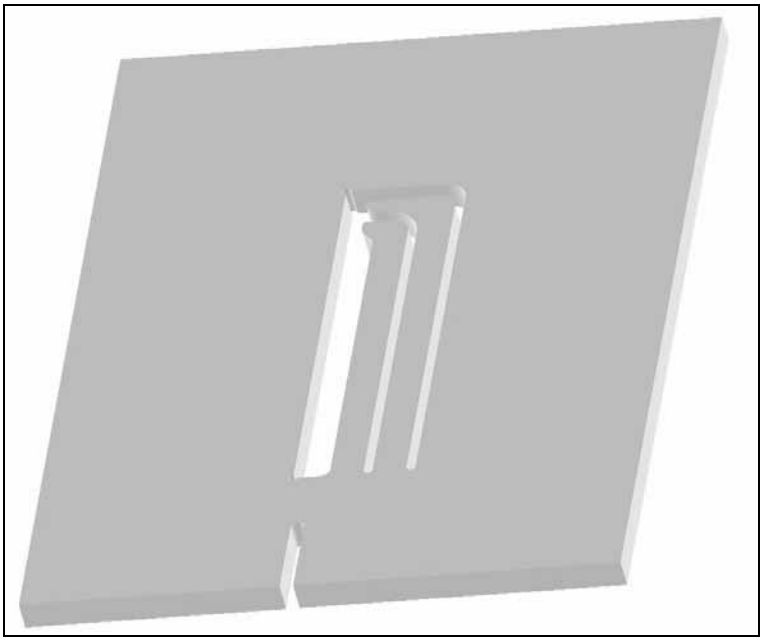

Figure 3.7 3-D schematic of the clip system carved on the electrode substrates. The drawing is to scale. The spring pair clamps the engine main substrate at the clips. The cavity below the spring roots is the electrode slot that allows the droplets to pass through without hitting the electrode substrate.

One of the key considerations to make to select the operational mode in a Colloid Thruster is its propulsive efficiency η_p, defined as the power that would be required to produce a thrust F if the whole mass flow $\dot{m}$ were accelerated to a common speed, divided to the actual power:

$$\eta_p = \frac{F^2}{2 \cdot \dot{m} \cdot I \cdot V} \tag{3.8}$$

where V is the total potential drop (extraction plus acceleration potentials). In the droplet regime the droplet population is basically mono-energetic. If the normal electric field at the neck is larger than $10^9 V/m$ solvated ions can be emitted directly from the liquid; therefore, two particle species (ions and droplets) would coexist in the exit stream of the Colloid Thruster nozzle. It is then possible to define a dimensionless specific charge δ^*

$$\delta^* = \frac{\delta_D}{\delta_I} \tag{3.9}$$

where the droplet specific charge is δ_D and the solvated ion specific charge is δ_I. If the current fraction delivered by the ion stream is denoted as β then it is possible to express the propulsive efficiency as

$$\eta_p = \frac{\left[1 - (1 - \sqrt{\delta^*}) \cdot \beta\right]^2}{1 - (1 - \delta^*) \cdot \beta} \tag{3.10}$$

Figure 3.8 shows the dependence of the propulsive efficiency on β and δ^*. The propulsive efficiency is 1 only when velocity non-uniformities are not present in the exit stream; in other words the energy implied in generating velocity differences does not pay back in the form of thrust. It is clear from Figure 3.8 that in order to operate with large propulsive efficiency, i.e., to have most of the input energy transformed into the exit stream, it is important to operate near single species emission. Within the range of achievable δ^*'s the minimum of the propulsive efficiency plot falls quite close to the 100% ion current fraction; therefore, near the pure solvated ion emission there is a strong dependence of the efficiency on the presence of droplets inside the exit stream. In a specific case of engine design it might be desirable to sacrifice some propulsive efficiency to get a given I_{sp}. The way to vary the ion current emission for a

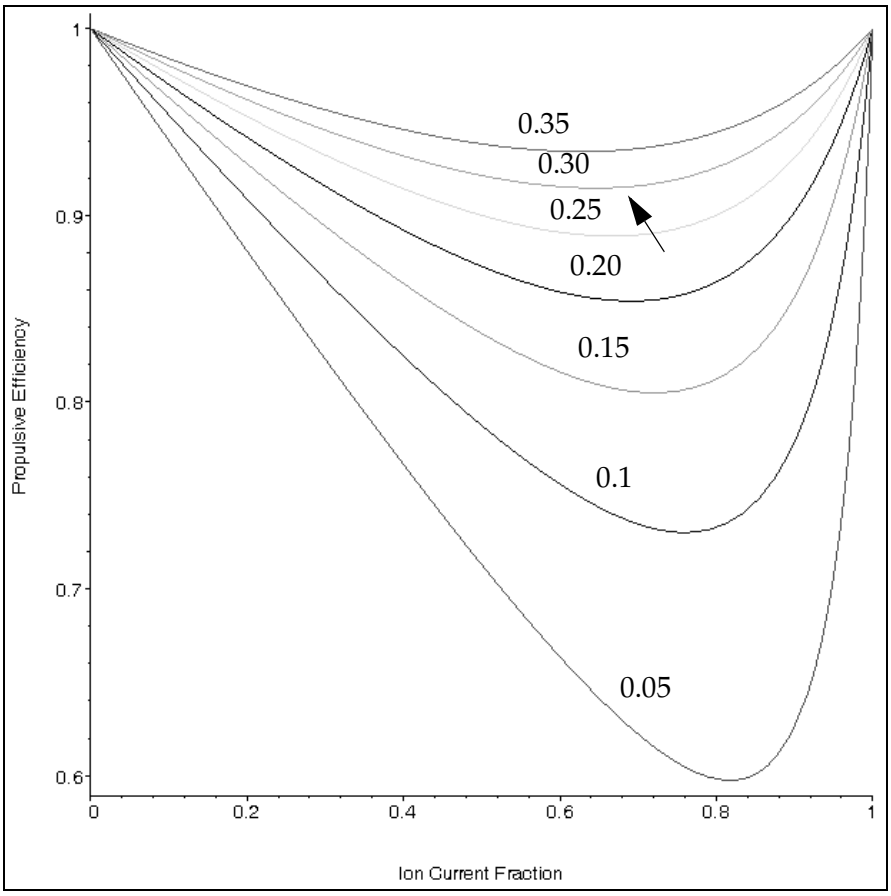

Figure 3.8 Propulsive Efficiency dependence on Ion current fraction and δ^*. Each contour has a fixed δ^*. The arrow points at the contour with a δ^* value about what the implemented Linear Array has, showing a lower bound of about 90% [Lozano, 2003].

given propellant would be to force the flowrate to fall near Q_{min} for force the normal electric field at the cone neck in order to reach field emission values.

3.1.5 Engine Losses

Using high conductivity propellants implies smaller electrical ohmic losses in the hydraulic system and Taylor Cone, but larger viscous losses. THe power invested in creating surface is inversely proportional to the dimensionless flowrate η. A small emitter internal diameter produces larger electrical losses because it increases the ohmic resistance; therefore a trade off may exist between starting voltage and evaporation losses versus electrical losses. For the particular case of Linear Colloid Thruster that was implemented the losses are rather small com-

pared to the kinetic energy of the exit stream because of the physical constants for formamide; therefore, it would be safe as a first order approximation (if lacking TOF experiments) to assume all the available electrical power is invested in accelerating the engine exit stream. Most of the losses are represented in the convective acceleration of the fluid inside the meniscus to reach the jet velocity (~ 5%); the second source of power losses are the ohmic heating due to charge conduction inside the hydraulics (~1.5%). It also takes about 4.5% of the power into surface creation, but this power is reversible.

The available pressure at the engine tank is used to pay for the viscous losses in the engine hydraulic system: while the meniscus is not broken the viscous losses are zero and because the pressure is unable to initiate flow by itself, no power is consumed. Once the meniscus is broken and the Taylor Cone is formed the stagnation pressure at the engine tank is used to move the flow through the hydraulic system down to the emitter tips.

The electrical input power is then spent through three main loss mechanisms:

- **Viscous losses in the jet that is emitted from the cone apex:** viscous dissipation scales as τ^2/μ where τ is the shear stress and μ is the viscosity. Most of the viscous dissipation comes from the stretching of the meniscus into a jet:

$$\tau = \mu \frac{\partial}{\partial z}(v_z) \tag{3.11}$$

  where the z-direction goes parallel to the streamlines. It is known from numerical simulations that the bulk of liquid accelerates up to the jet velocity in a distance of the order of a few times the characteristic length r^* [Carretero, 2003]

$$r^* = \left[\frac{\varepsilon \cdot \varepsilon_o \cdot Q}{K}\right]^{1/3} \tag{3.12}$$

  The ratio of the viscous power to the kinetic power is

$$\frac{\dfrac{\mu \cdot v^2 \cdot \beta_1 \cdot r^{*3}}{\beta_2^2 \cdot r^{*2}}}{\dfrac{\rho \cdot Q \cdot v^2}{2}} = \frac{2 \cdot \beta_1 \cdot \mu \cdot r^*}{\beta_2^2 \cdot \rho \cdot Q} \tag{3.13}$$

where β_2 is the scaling factor of the distance that it takes for the fluid to accelerate up to the jet velocity with respect to r^* (~ 3), β_1 is the scaling factor of the volume that is involved in most of the viscous dissipation to the cube of r^* (~1/2), ρ is the fluid density, and Q is the volumetric flow rate. From equation 3.3 the flowrate can be replaced and the equation 3.13 becomes

$$\frac{\mu}{9} \cdot \left[\frac{K}{\eta^4 \cdot \gamma^2 \cdot \rho \cdot \varepsilon \cdot \varepsilon_o} \right]^{1/3} \tag{3.14}$$

In other words, the viscous losses increase with the electrical conductivity and is inversely proportional to the surface tension. For the case of the formamide with K = 0.5 S/m, γ equal to 0.06 N/m, ρ equal to 1130 Kg/m^3, ε equal to 111, μ equal to 0.0038 Pa.s, and an η value of 3 the viscous loss is about 5%.

- **Surface creation:** The liquid is expelled from the cone apex and the creation of free surface per unit of time requires some energy. The surface creation loss has two possible bounds: the power spent in creating the jet and the energy spent in creating the free surface of the droplets. The power spent to create the jet free surface is

$$P_w = 2 \cdot \pi \cdot R_j \cdot \gamma \cdot v_j \tag{3.15}$$

where the jet radius R_j is (empirically [de la Mora, 1994])

$$R_j = 0.2 \cdot \left[\frac{\varepsilon \cdot \varepsilon_o \cdot Q}{K} \right]^{1/3} \tag{3.16}$$

and the jet velocity at the free boundary v_j for a flat flow profile is

$$v_{jet} = \frac{Q}{\pi \cdot R_j^2} \tag{3.17}$$

where Q is the flow rate delivered per emitter.

The energy per unit of time spent in generating the droplet free surface of k particle sizes is

$$P_w = \sum_{n=1}^{\kappa} \dot{N}_n \cdot 4 \cdot \pi \cdot R_D^2 \cdot \gamma \tag{3.18}$$

In the case of a monodisperse population made of droplets with droplet radius R_D given approximately by the Rayleigh relationship

$$R_D \cong 1.89 \cdot R_j \tag{3.19}$$

the number of droplets $\dot{N}$ expelled per emitter is given by

$$\dot{N} = \frac{3Q}{4\pi R_D^3} \tag{3.20}$$

therefore, the power invested in generating the jet is

$$P_w = 10 \cdot \gamma \cdot \sqrt[3]{\frac{Q^2 \cdot K}{\varepsilon \cdot \varepsilon_o}} \tag{3.21}$$

and the power invested in creating monodisperse droplets is

$$P_w = 15 \cdot \gamma \cdot \sqrt[3]{\frac{Q^2 \cdot K}{\varepsilon \cdot \varepsilon_o}} \tag{3.22}$$

The real surface generation loss is a weighted sum of the terms shown in equations 3.21 and 3.22. Both terms have the same functional dependence on the physical properties of the liquid and the flowrate. It can be shown that the ratio of the power used in surface creation to the kinetic power is

$$\frac{30 \cdot \gamma \cdot Q^{2/3} \cdot K^{1/3}}{\varepsilon^{1/3} \cdot \varepsilon_o^{1/3} \cdot \rho \cdot Q \cdot v^2} \approx \left[\frac{0.2 \cdot \pi}{\eta}\right]^2 \tag{3.23}$$

Independent of the fluid properties. For a typical η values of 3 the power invested in surface creation is about 4.5%, taking into account droplet formation. It is important to point out that this power is eversible, i.e., can be re-used later when the droplet gets destroyed. This result makes sense because it predicts that the more flow is emitted the less important the power spent in creating surface: the volume-to-surface ratio scales with the droplet diameter and therefore, more mass per droplet translated in less surface generation.

As a guideline, for a fixed flow rate smaller power losses will be obtained with large electrical permittivities and small electrical conductivities. The part of reducing the electrical conductivity is in disagreement with enhancing the I_{sp} and, as it will be seem later, with ohmic losses due to the finite electrical conductivity of the propellant. Therefore, a trade off should be made when selecting K.

- **Ohmic losses due to charge conduction:** Electrical energy is used in moving the charge through a medium with non-zero resistance. Given the large length-to-diameter most of the ohmic loss will occur at the channels but some loss will occur at the tank, manifolds, cone and jet. The power dissipated for an emitter expelling a current I is

$$P_w = I^2 \cdot R_\Omega \tag{3.24}$$

where R_Ω is the ohmic resistance of each channel, equal to

$$\int_0^L \frac{1}{K(x) \cdot A_{\perp}(x)} dx \tag{3.25}$$

where K is the electrical conductivity (a possible function of the position variable x) and $A_{\perp}$ is the cross sectional area. Reduction of ohmic losses calls for larger conductivities and cross-sections. For a constant cross-section channel this implies some trade-off when confronted to vaporization losses, activation voltages and emitter clustering potential. For a channel with non-constant cross-section (like the one proposed in Chapter 5 to improve engine fill-in control with non-wettable propellants) a suitable solution is to have the emitter tip substantially smaller than the channel cross-section: this way the ohmic losses and the aspects relevant to emitter activation and vaporization loss get decoupled thus being able to satisfy both in a more compelling way. The ratio of the ohmic losses due to charge conduction to the kinetic power is

$$\frac{I \cdot R_{\Omega}}{V} \tag{3.26}$$

A typical Linear Array emitter with L_c equal to 12 μm and an axial length equal to 15 mm, an activation voltage of 2000 V and a current emitted of 0.12 μA, using formamide with K = 0.6 S/m, gives a power ratio equal to 1.3%.

The energy implied in making the droplets go from the emitters to the accelerator electrode is not lost but is transformed into the kinetic energy of the exit stream:

$$\frac{1}{2} \cdot \rho \cdot Q \cdot v^2 \tag{3.27}$$

where v is the stream velocity whose upper bound (all available energy goes into kinetic energy of the exit stream) is

$$v = \sqrt{2 \cdot \delta \cdot V} \tag{3.28}$$

where V is the total potential drop and δ is the specific charge of the droplets. A time of flight (TOF) experiment will determine in practice the exit stream velocity, and hence δ.

3.1.6 Engine Electric Field Enhancers

The engine relies on spout area reduction / sharp spout slope change to effectively enhance the electric field near the propellant menisci. Local features, such as sharp turns in the contour of the emitter near the emitter tip, roughness and sharp corners of the channels, should help enhance the electric field. The engine spouts were designed using Finite Element analysis of the electric field surrounding the emitters. The conclusion from the Finite Element Analysis is that the spout system of the Linear Colloid Thruster Array does a good job in increasing the electric field around the spouts, but the emitters are close enough to produce some shadowing. The predicted activation voltages for the emitter-to-extractor separations that were implemented in the engine are sound. For the fully sharpened case the values fall within 28% from the predictions of one of the reduced order models.

There is a theoretical model of the electric potential surrounding an conic emitter with a blunt tip, facing a series of ring electrodes [Smythe, 1939; Hall, 1949; Akinwande, 2001; Akinwande, 2001-2; Velásquez, 2002-3]. No attempt to use the model was made, among other reasons because of the difficulty in determining the functional base of the solution, and the accessibility to good numerical tools; instead, Finite Element Simulations of the electric field in the space between the emitters and the extractor, using the commercial software Maxwell, was carried out to validate the spout geometries. For the numerical simulations the spouts and the extractor were considered equipotentials and the physical constraint that the field must decay away from the charge source was also enforced. The spouts were modeled as solid, that is, without any internal geometry. The analysis was done as if only the external structure of the emitter (no internal features) were responsible of enhancing the field, while the internal geometry of the emitter was setting the threshold electric field value for starting. The starting electric field for formamide, based on the expression [Martinez-Sanchez, 2001]

$$E_{TH} = \sqrt{\frac{\pi \cdot \gamma}{\varepsilon_o \cdot L_c}} \tag{3.29}$$

is equal to 3.85×10^7 V/m for 12 μm of L_c.

Simulations with different emitter-to-extractor separations for a fixed potential drop equal to 1000 volts were carried out. The minimum electric field at the exit plane of the emitter (minimum in magnitude) was compared to the minimum electric field to trigger the Taylor Cone formation (equation 3.29) and with the starting voltage criterion based on prolate spheroidal coordinates [Martinez-Sanchez, 2001]

$$V_E = \sqrt{\frac{\gamma \cdot L_c}{\varepsilon_o}} \ln\left(\frac{4 \cdot G}{L_c}\right) \tag{3.30}$$

where G is the emitter-to-extractor separation and L_c is a characteristic cross-sectional length, to first order the hydraulic diameter of the emitter.

A correction of the starting voltage predicted by equation 3.30 is proposed, based on a reference [Thompson, 1984]. This corrected model was also compared to the results from finite element analysis in the case of the fully sharpened case. In this corrected model the balance of the electrostatic suction and surface tension pulling is done by taking into account the influence of L_c^o, the characteristic cross-sectional length of the spout exterior:

$$\frac{\varepsilon_o}{2} \cdot \left[\frac{V_E}{\beta_3 \cdot \sqrt{L_c \cdot L_c^o}}\right]^2 \geq \frac{2 \cdot \gamma}{L_c} \tag{3.31}$$

where β_3 is a scaling factor presumably of order one. Equation3.30 then becomes

$$V_E = \sqrt{\frac{\gamma \cdot L_c^o}{\varepsilon_o}} \ln\left(\frac{4 \cdot G}{\sqrt{L_c \cdot L_c^o}}\right) \tag{3.32}$$

Equation 3.32 predicts that the true figure of merit to calculate the starting voltage is the external dimension of the spout. The surface tension value used in both equations 3.30 and 3.32 is 0.06 N/m.

The use of the minimum electric field at the spout exit plane allows us to dampen non-physical effects such as singularities, non-uniformities due to meshing coarseness, etc. It is well

known that as soon as the points of the domain are farther than the mesh size from the boundaries their solution is not strongly sensitive to the fine details of the boundary shape; unfortunately the electric field values that we are interested fall at the boundary and some noise is expected from the discretization of the domain geometry / boundaries.

Because this minimum electric field was visually determined there is some uncertainty on its value, added to the original uncertainty in the error of the energy that the finite element solver was generating (less than 1%).

Benchmarking of the Spout Electric Field Performance

A 2-D analysis of the spout - electrode system was performed where the electrode was modeled as an infinite slot facing the emitter from a given distance and the emitter was a continuous wedge. An axisymmetric model of the spout was also created, thus simulating the electrode as a ring surrounding from a distance the emitter. Then a 3-D simulation of the fully sharpened spout geometry, with the same electrode separation of both the 2-D and axisymmetric analyses, was carried out to compare it to the extreme cases. The characteristic length of the Linear Array spout system is 40 μm, which is the frontal dimension of the emitter tip.

Figure 3.9 shows the magnitude of the electric field for the 2-D analysis while Figure 3.10 shows the magnitude of the electric field for the axisymmetric analysis. For the 2-D case the minimum electric field is about $2.4 \times 10^7 \text{V/m}$ while for the axisymmetric case it was $4.2 \times 10^7 \text{V/m}$. As expected the axisymmetric geometry does better at enhancing locally the electric field than the 2-D geometry.Figure 3.11 shows the 3-D simulation of the electric field for the Linear Array and its ideal spout geometry. The characteristic electric field was found to be equal to $3.5 \times 10^7 \text{V/m}$, a value that clearly is closer to the axisymmetric case than the 2-D case and will imply savings in extraction voltage.

The numerical results show that there is some coupling among emitters (the field halfway between the emitters is not zero but about one order of magnitude less) large enough to generate a shadowing effect. This interference is small enough to avoid starting a spout if the adjacent spout is on.

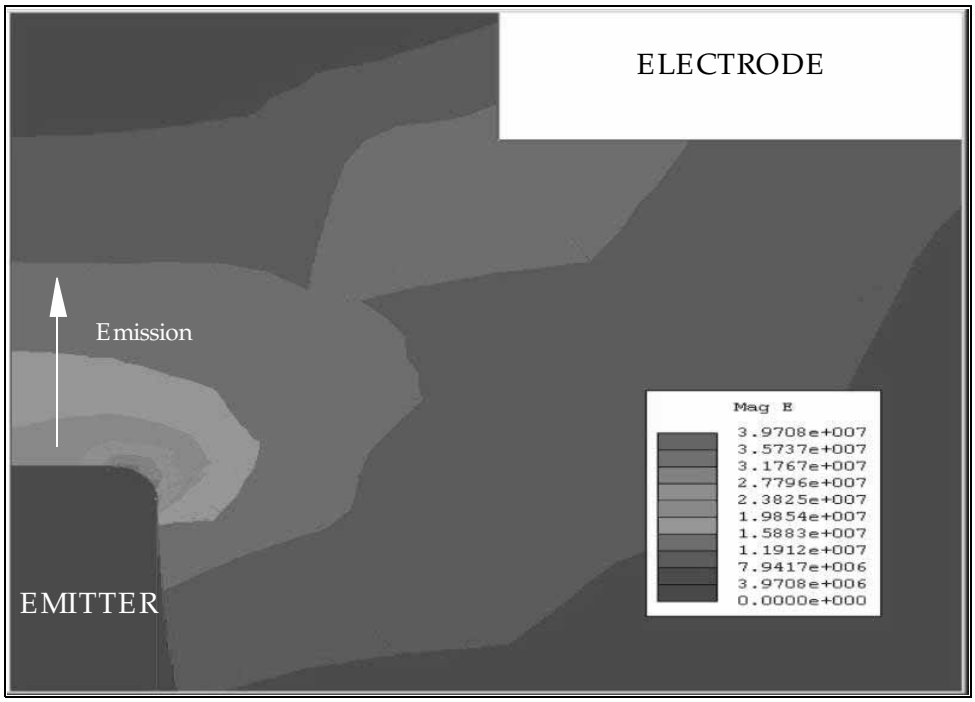

Figure 3.9 Magnitude contour of the electric field surrounding the Linear Array as modeled assuming a 2-D geometry. The characteristic electric field was estimated as 2.4×10^7 V/m .

Field Enhancement Spout Geometries in the Linear Colloid Thruster Array

It was found numerically that only the fully sharpened spouts of the Linear Array show a logarithmic dependence of the starting voltage on the emitter-to-extractor separations implemented on the actual engine. This logarithmic dependence is desirable because it would dampen the influence of the electrode misalignment with respect to the emitters on the starting voltage. The saturation values found in the finite element simulations are substantially closer to the values predicted by equation 3.32 than by equation 3.30, corroborating the claim of the corrected reduced order model that the electric field surrounding the meniscus is influenced by the external dimensions of the spout.

The author believes that the implemented finite element modeling was rather conservative compared to the potential field enhancing capabilities of the actual devices; in a way the finite element analysis sets an upper bound of the activation voltage. Among other reasons the following ones are the most relevant in support of this idea:

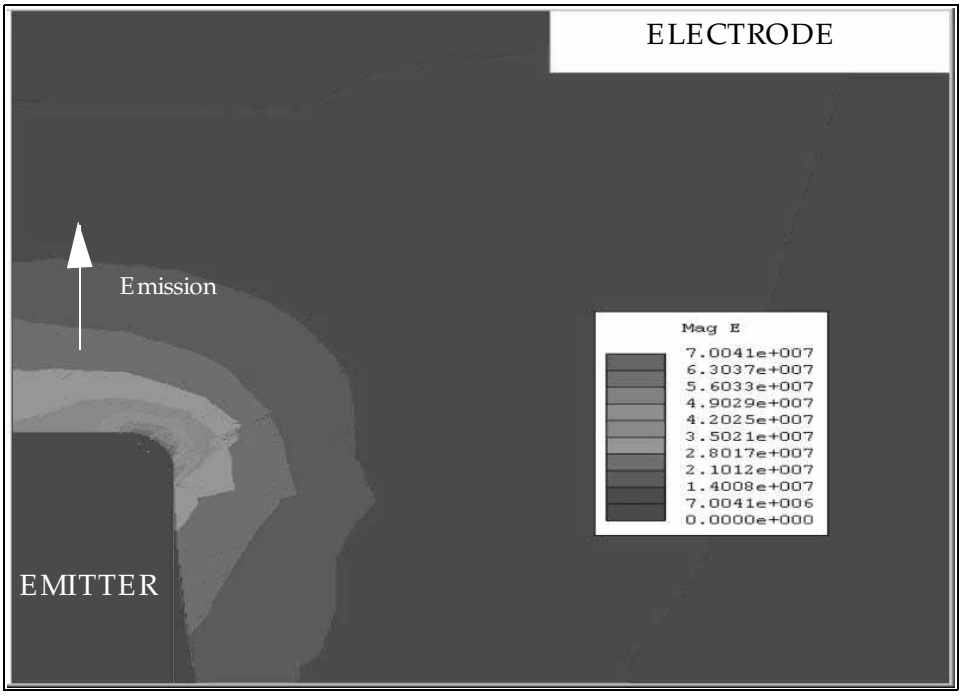

Figure 3.10 Magnitude contour of the electric field surrounding the Linear Array as modeled assuming a 2-D geometry. The characteristic electric field was estimated as 4.2×10^7 V/m .

- The spouts are plasma carved from a silicon substrate. Plasma etching inherently leaves roughness, specially DRIE (used to pattern the spouts) because of the way DRIE performs the etching. This roughness is easily of the order of a micron and can act as sharp points to locally help to enhance the electric field.
- The hydraulic system used in the Linear Array has a square cross section. It is known experimentally from work at the MIT Space Propulsion Laboratory that square needles turn on with slightly lower voltage [Lozano, unpublished work]. From equations 3.5 and 3.30 the starting voltage should be reduced by 3%. The author believes that the reason behind it is the presence of the sharp corner of the square that locally enhance the electric field. The hydraulic cross section enhances the electric field by itself so the net electric filed that surrounds the spouts in the case of the Linear engine is larger than predicted.
- Equation 3.30 does not rely on external electric enhancing structures but in a self collapsing dynamic system represented by the meniscus and its capacity to resist the deformation from the electrostatic pressure surrounding it. There is experimental evidence in the work of the MIT Space Propulsion Laboratory suggesting that for some designs the meniscus by itself can generate the instability without the help of the spouts, without excessive increments in the starting voltages. If this is true then the confining cross section of the meniscus will

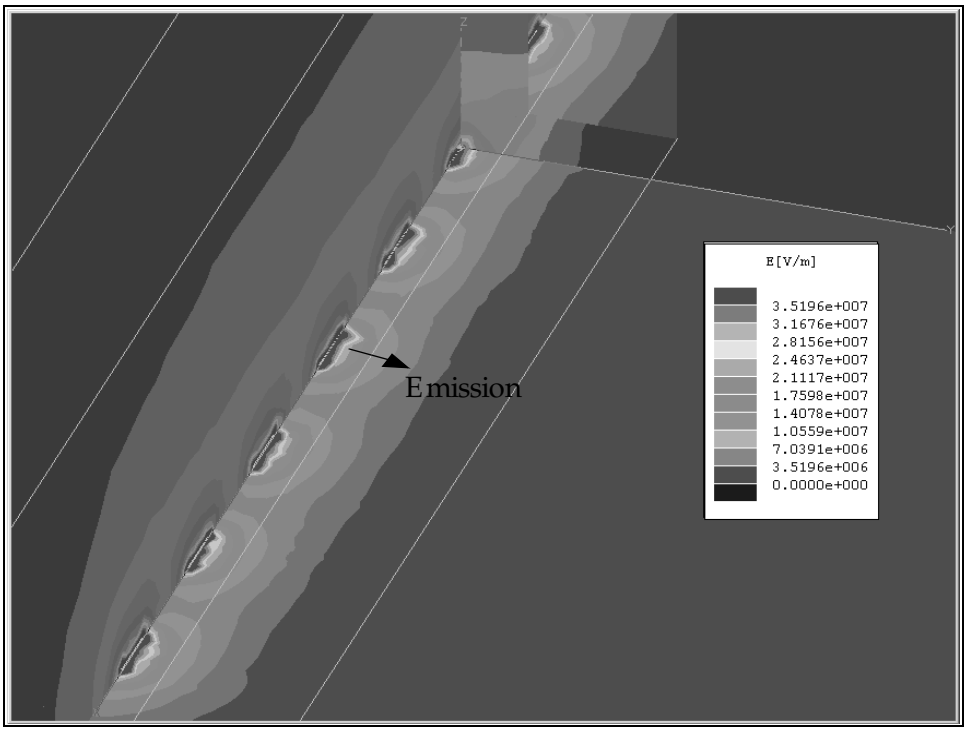

Figure 3.11 Magnitude contour of the electric field surrounding the Linear Array as modeled with its ideal 3-D geometry. The characteristic electric field was estimated as 3.5×10^7 V/m .

be the figure of merit for predicting the instability and the spouts will play a mere supporting role in the instability production.

- If the argument that the square needles turn on with smaller voltages compared to the circular needles because of the sharp corners of the cross section is basically true, then the figure of merit for the electric field is not the minimum electric field that surround the whole emitter tip but the *maximum* electric field locally available. In that sense, then the emitters should start with substantially less voltage; on the other hand predicting the starting voltage using finite elements can become quite tricky because maximum electric fields will invariably depend on the coarseness of the mesh.

The following is a more detailed exposure of the field enhancing capabilities found in the proposed spouts for the Linear Colloid thruster Array:

- **Non-Sharpened Emitters:** The conclusion of the series of numerical simulations is that these spouts substantially enhance the electric field compared to the parallel capacitor limit and therefore, are a valid choice of spout geometry. Figure 3.12 shows a typical result of simulating the electric field for an electrode-to-emitter separation between 50 μm and 200 μm using a flat electrode.

The summary of the relevant information from the finite element analysis is in

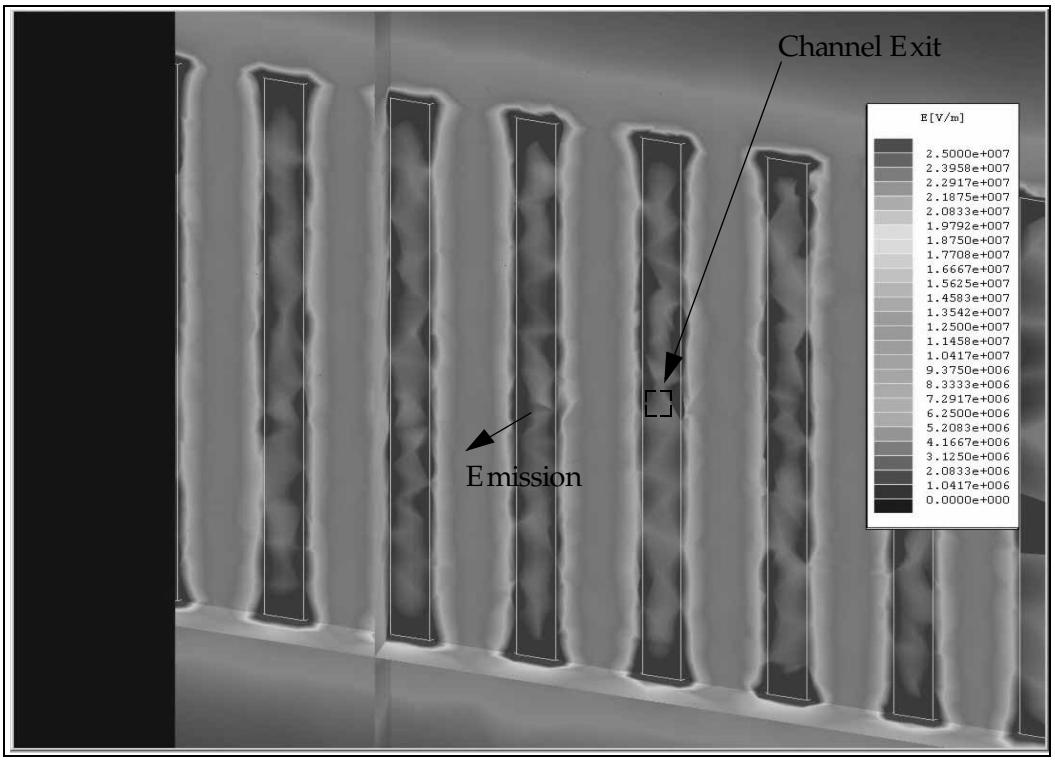

Figure 3.12 Typical 3-D Finite Element result of the electric field surrounding the Linear Array spout system with unsharpened spouts and a flat electrode. In the particular case the electrode-to-emitter separation is 50 μm and the applied voltage is 1000 V.

Table 3.1, including a starting voltage forecast for a spout geometry using formamide with a characteristic length of 12 μm. The starting voltage versus the

TABLE 3.1 Minimum electric field at the emitter's surface when biased at V = 1000 volts and predicted starting voltage for several electrode-to-emitter separations for the case of non-sharpened spouts, Linear Colloid Thruster Array.

Electrode-to-emitter separation (μm)	Minimum Electric Field @ 1000 V (V/ m)	Starting Voltage (V)
50	2.5×10^7	1540
100	1.35×10^7	2853
150	9.2×10^6	4186
200	7.0×10^6	5501

electrode-to-emitter distance is shown in Figure 3.13. No logarithmic dependence of the starting voltage on the electrode-to-emitter separation was found, but rather a linear dependence, as shown by the linear fit that was obtained from the data.

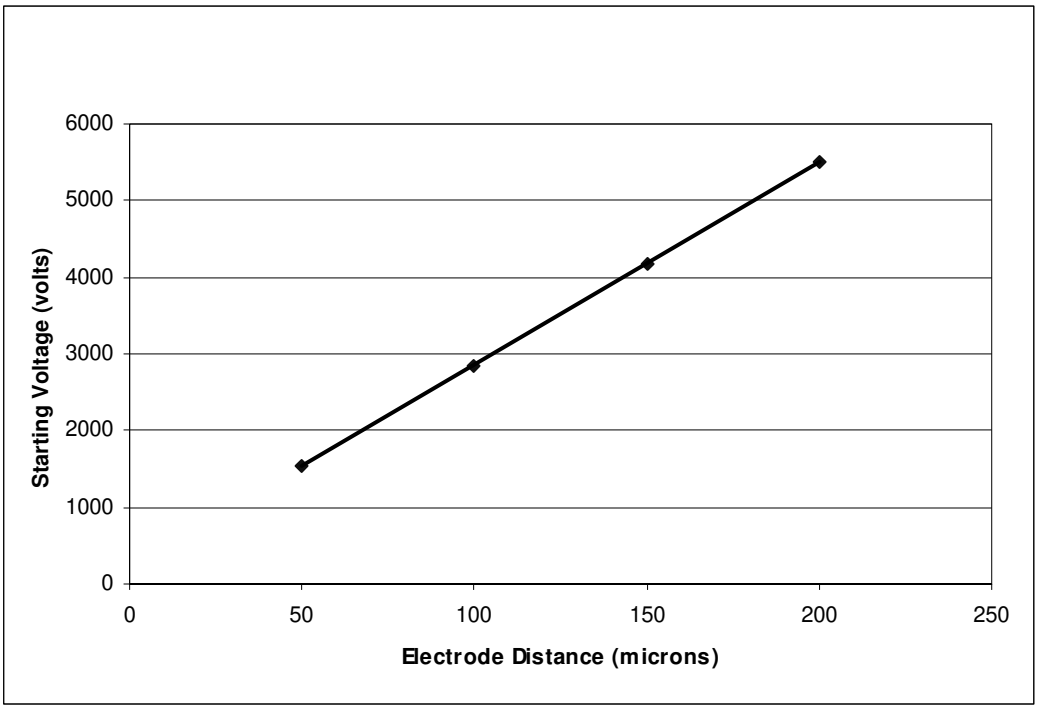

Figure 3.13 Starting Voltage versus Electrode-to-Emitter Distance for non-sharpened Spouts.

- **Half-sharpened Emitters:** The key result from the series of numerical simulations is that the starting voltage has been substantially reduced compared to the non-sharpened case, specially when the electrode-to-emitter separation is large. This result emphasizes the importance of locally enhancing the field to reduce starting voltages. The author believes that the reason behind the previous result is the fact that the exit of the hydraulic channels falls near a sharp geometrical feature of the spout (the part where the lip and the emitter tip meet) so this local field enhancer feature has an area of influence that affects the portion of the spout where we are interested in augmenting the electric field. Figure 3.14 presents a typical result of simulating the electric field for an electrode-to-emitter separation between 50 μm and 250 μm using a flat electrode. The summary of the characteristic electric fields at 1000 V from the FEA is in Table 3.2, where the predicted voltage from equation 3.29 is calculated using formamide with a square channel 12 μm wide, as in the unsharpened spout case. The starting voltage versus electrode-to-emitter distance is shown in Figure 3.15. A lin-

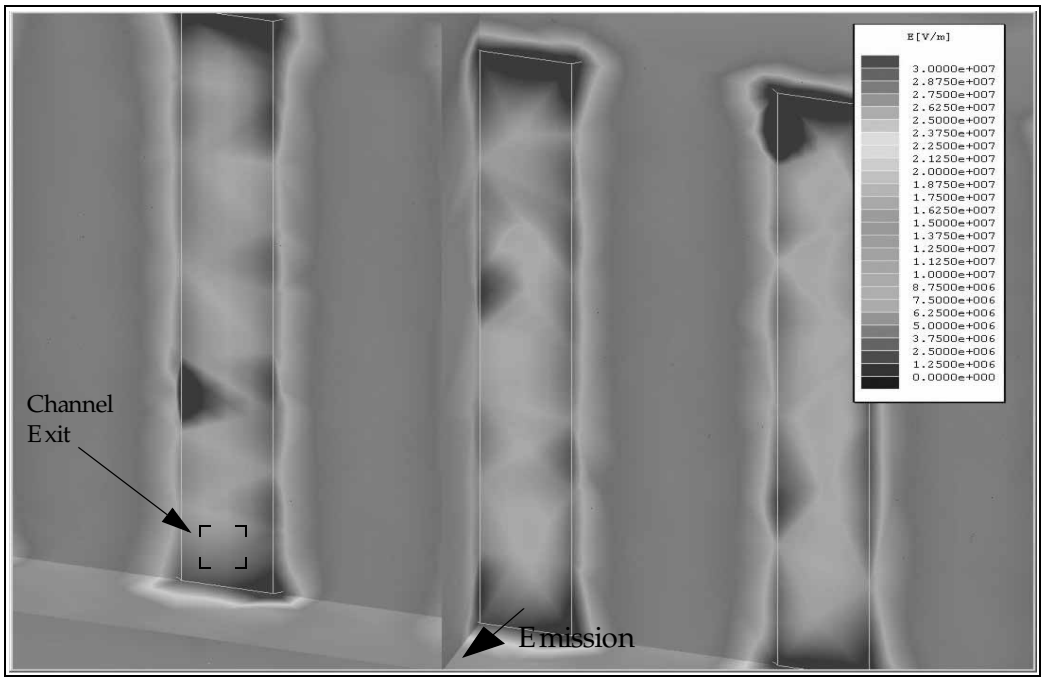

Figure 3.14 Typical 3-D Finite Element result of the electric field surrounding the Linear Array spout system with half-sharpened spouts. In the particular case the electrode-to-emitter separation is 50 μm and the applied voltage is 1000 V.

ear dependence of the starting voltage on the emitter-to-extractor separation in the range of interest, but unlike the non-sharpened case it seems the y-cut of the plot (when the distance is zero) is not the origin but some finite voltage value. The voltages are also lower by ~ 2/3.

TABLE 3.2 Minimum Electric field at the emitters surface when biased at V = 1000 volts, and predicted starting voltage versus several Electrode-to-emitter separation for the half-sharpened spouts.

Electrode-to-emitter separation (μm)	Minimum Electric Field @ 1000 V (V/ m)	Starting Voltage (V)
50	3.0×10^7	1284
100	1.95×10^7	1975
150	1.45×10^7	2656
200	1.15×10^7	3349
250	9.5×10^6	4054

- **Fully Sharpened Emitters, flat plate electrode:** The key results of the series of numerical simulations in this case are the logarithmic dependence of the starting voltage on the emitter-to-extractor separation, and that equation 3.32

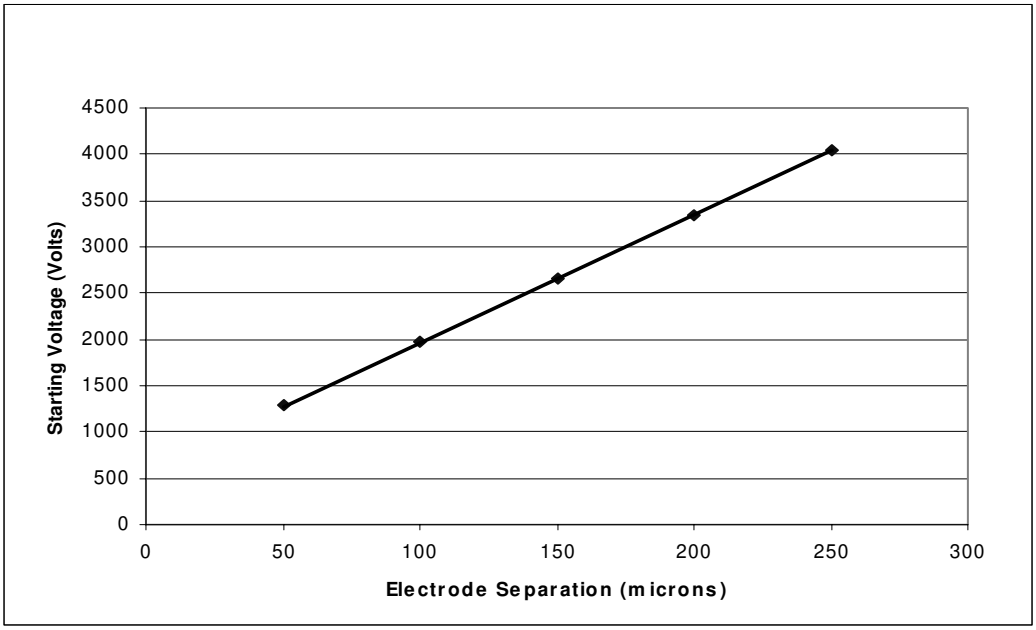

Figure 3.15 Starting Voltage versus Electrode Distance for half-sharpened spouts in the Linear Array.

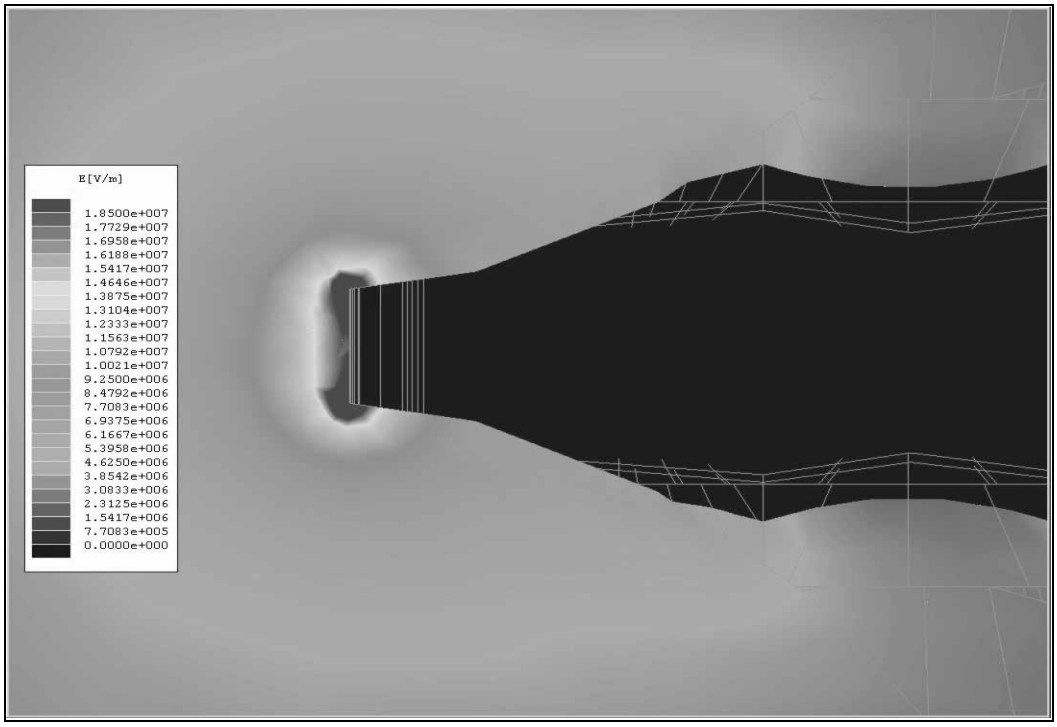

Figure 3.16 Typical 3-D Finite Element result of the electric field surrounding the Linear Array spout system with fully sharpened spouts and a flat electrode. In the particular case the electrode-to-emitter separation is 150 μm and the applied voltage is 1000 V.

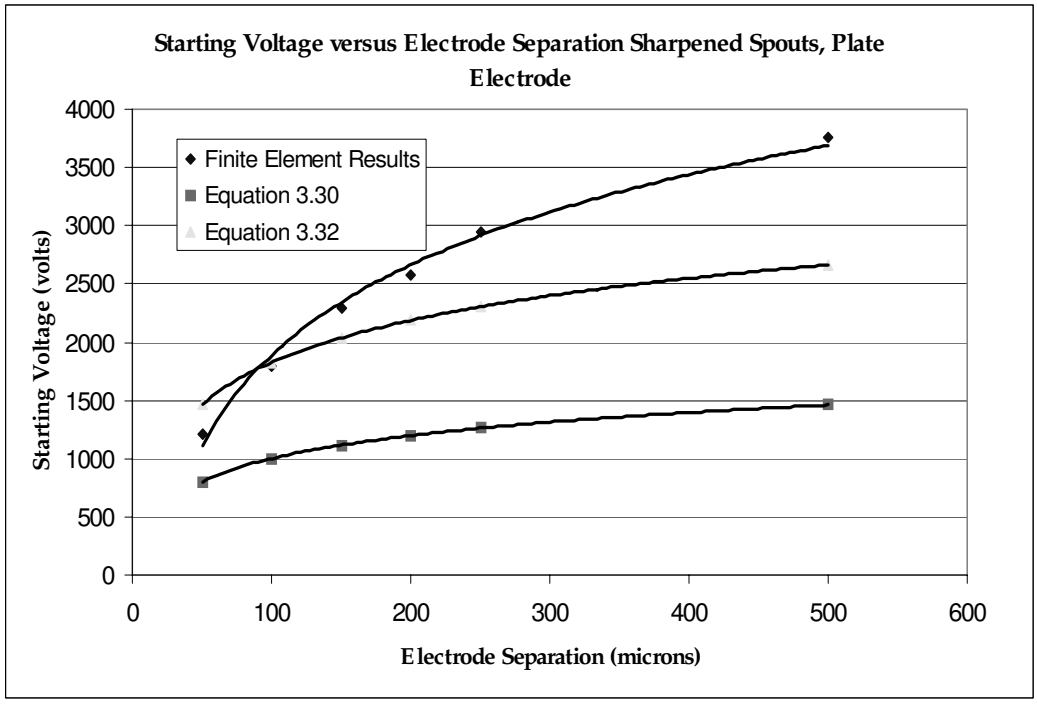

Figure 3.17 Starting Voltage versus Electrode Separation Sharpened Spouts, Plate Electrode. The higher curve corresponds to the finite element data while the other curve represents the prediction of the reduced order model based on prolate spheroidal coordinates.

has a better agreement with numerical results than equation 3.30 (the values from equation 3.32 are within 28% from the finite element results). From the finite element data points it can be seen that the slope diminishes as the electrode-to-emitter separation is increased. Equation 3.30 underestimates the starting voltage magnitude when the electrode-to-emitter separation is large enough. Also, the relative magnitude of the electric field at midpoints between emitters compared to the electric field at the emitter tips increases with the distance to the electrode: at large distances the FEA suggests that the emitters look like a 2-D wedge. The starting voltage in the case of the fully sharpened emitters is substantially reduced compared to the previous emitter geometries but if the electrode-to-emitter separation is kept small enough, a half-sharpened emitter requires only a few hundred volts more than a fully sharpened one. Figure 3.16 shows the typical results of simulating the electric field around the spouts for electrode-to-emitter separations between 50 μm and 500 μm using a flat electrode. The summary of the characteristic electric fields at V = 1000 Volts from the finite element analysis is in Table 3.3, including the starting voltage prediction for formamide with an L_c equal to 12 μm. The starting voltage versus the electrode-to-emitter distance is shown in Figure 3.17.

TABLE 3.3 Minimum Electric field surrounding the emitters when biased at 1000 V and predicted starting voltage from two reduced order models versus several Electrode-to-emitter separation for the fully sharpened spouts (solid electrode case)

Electrode separation (μm)	Minimum E. Field (V/ m)	Starting Voltage (V)	Voltage (V), equation 3.30	Voltage (V), equation 3.32
50	3.4×10^7	1216	802	1465
100	2.3×10^7	1797	1000	1826
150	1.8×10^7	2296	1116	2037
200	1.6×10^7	2583	1198	2187
250	1.4×10^7	2952	1262	2303
500	1.1×10^7	3758	1459	2664

- **Sharpened Emitters, slotted plate electrode:** The key result of the series of numerical simulations is that if the effective separation of emitter to electrode edge is used (distance from the emitter to the closest edge of the electrode slot) then finite element analyses with flat and with slotted electrodes match well. Therefore, the existence of a slot in the electrode diminish the effective electric field surrounding the emitters. A logarithmic fit seems to follow the data quite well. The saturation value is again substantially closer to the saturation value from equation 3.32 than to the saturation value from equation 3.30. The prediction from equation 3.32 are within 28% from the finite element simulation results. Figure 3.18 shows a typical result of the finite element simulation of the electric field in the space between the electrode and the emitters for electrode-to-emitter separations between 100 μm and 500 μm. The summary of this analysis is shown in Table 3.4 The starting voltage versus the electrode-to-emitter distance is shown in Figure 3.19

3.1.7 Electrode Pull-in

One of the design requirements on the electrodes was to assure structural integrity while the electrodes are energized. It is possible to generate a self-sustained collapse mechanism in an electrode-emitter configuration if the electrostatic suction is large enough to make it impossible for the system to recover from a displacement perturbation when the starting point of the perturbation (the steady-state deflection) is larger than a threshold value and the system experiences softening as deflection increases. After some modeling (see Appendix A) it was found that the criterion of structural collapse in the electrodes implemented in the Linear Array is

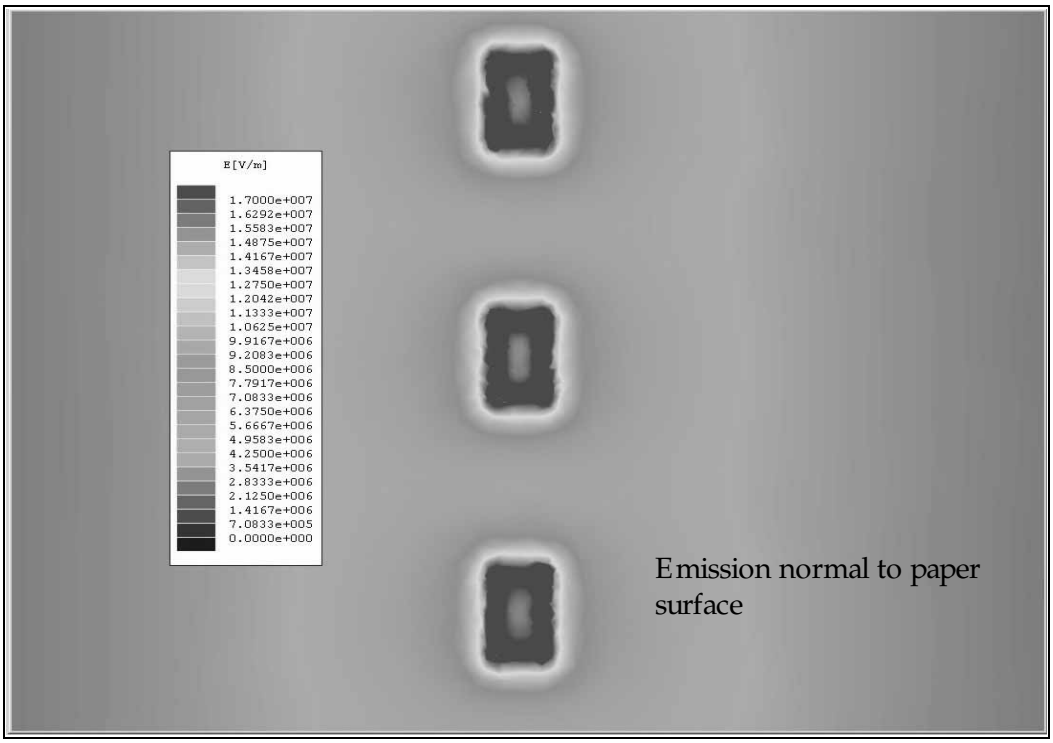

Figure 3.18 3-D Finite Element Analysis of the 1-D engine spout system with fully sharpened spouts (slotted electrode case). Electrode-to-emitter separation 100 μm . Applied voltage = 1000 V.

TABLE 3.4 Minimum Electric field at the emitters surface when biased at 1000 V and predicted starting voltage from two reduced order models versus Electrode-to-emitter separations for the fully sharpened spouts (slotted electrode case).

Electrode sep. (μm)	Corr. sep. (μm)	Minimum E. Field (V/ m)	Starting Voltage (V)	Voltage eq. 3.30 (V)	Voltage eq. 3.32 (V)
100	180	1.7×10^7	2431	1243	2270
150	212	1.5×10^7	2756	1273	2323
200	250	1.35×10^7	3062	1305	2383
300	335	1.25×10^7	3307	1371	2504
500	522	1.1×10^7	3758	1483	2707

$$V_{max} = \sqrt{\frac{8 \cdot E \cdot b \cdot H^3 \cdot G_o^3}{3 \cdot L^4 \cdot \upsilon \cdot \varepsilon_o}} \tag{3.33}$$

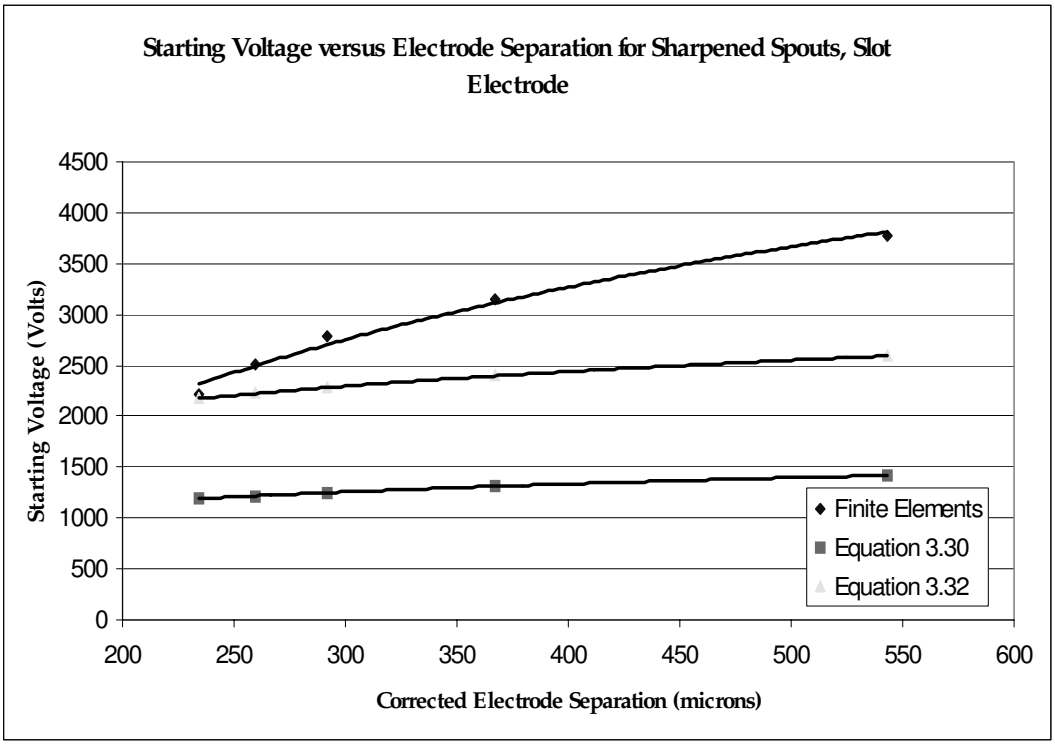

Figure 3.19 Starting Voltage versus Electrode Separation Sharpened Spouts, Slotted Electrode. The higher curve corresponds to the finite element data while the other curve represented the prediction of the reduced order model based on prolate spheroidal coordinates.

where H is the cross-section height, b is the cross-section width, E is Young's Modulus of the electrode ($145.5 \times 10^9 Pa$), G_o is the unperturbed emitter-to-extractor separation, υ is the width of the conductive lines in the electrode ($50 \mu m$), L is the effective electrode length (4.58 cm.) and ε_o is the electrical permittivity of free space.

The result of using equation 3.33 is summarized graphically in Figure 3.20.

Given the emitter-to-extractor separation, the logarithmic behavior of the starting voltage on G, and the voltages expected from the finite element simulations the author considers that this collapse will not take place.

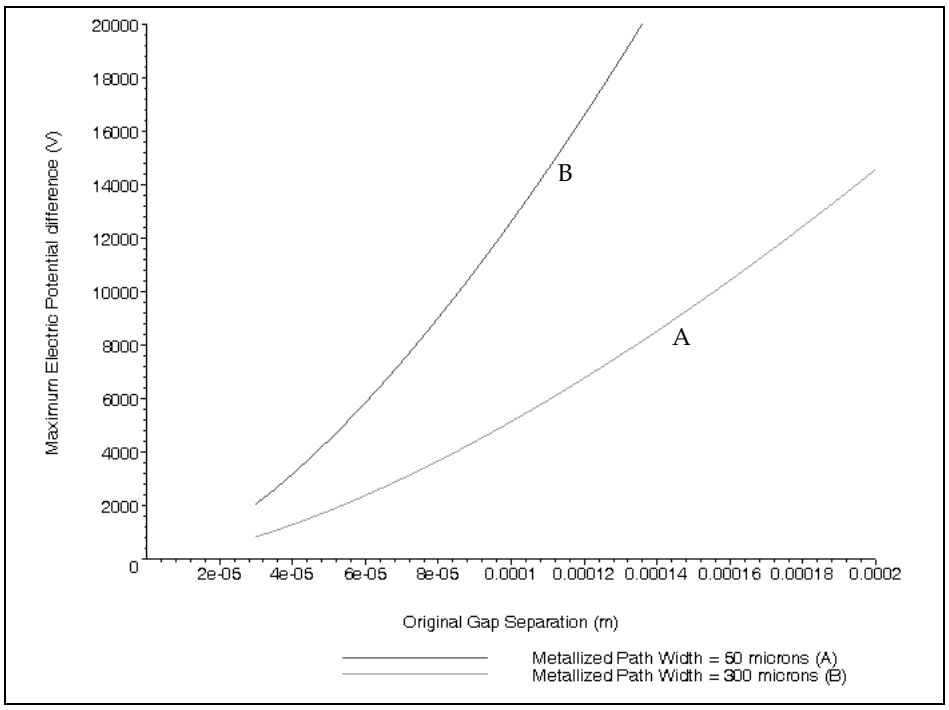

Figure 3.20 Maximum potential drop versus gap separation for the electrode geometry of the 1-D Colloid Thruster Array.

3.1.8 Space Charge Considerations

Space charge effects should be considered when analyzing space propulsion engines because they can highlight valuable theoretical limits to bound the engine performance and functional characteristics.A space charge saturated engine fully uses its potential for thrust density.

Based in first principles it is concluded that it is not possible to generate space charge saturation with the emitter diameters and emitter-to-electrode separation that are achievable in practice. Therefore, the proposed Linear Array does not fully use its area.

A model that combines the equations that describe the current emitted by single Taylor Cone emitters in droplet mode [de la Mora, 1994] with the Child-Langmuir space saturation model and equation 3.29 predicts that the necessary conditions for space charge limitation in Colloid Thruster Arrays are defined by the following expression [Appendix B]:

$$\frac{G}{S} = \sqrt{\frac{4\sqrt{2}\cdot\zeta}{9\cdot f(\varepsilon)\cdot\eta\cdot\gamma}}\cdot\sqrt[4]{\varepsilon_o\cdot\delta\cdot\rho\cdot\left[\sqrt{\frac{\gamma\cdot L_c}{\varepsilon_o}}\ln\left(\frac{4\cdot G}{L_c}\right)\right]^3} \tag{3.34}$$

where G is the emitter-to-extractor separation, S is the emitter-to-emitter separation, ζ is a dimensionless factor that takes into account the emitter packing and their relative distribution, η is a dimensionless number coming from dimensional analysis [de la Mora, 1994], γ is the surface tension of the liquid, δ is the specific charge of the droplets coming out of the emitters, ρ is the mass density, ε is the relative electrical permittivity, $f(\varepsilon)$ is a function that relates the current with the volumetric flowrate, and L_c is the hydraulic diameter of the emitter. There are then two relevant parameters that can be used to describe the emitter-to-emitter spacing S: L_c and G. Therefore, the full dependence can be shown as a series of contours in a 2-D plot.

Figure 3.21 shows the uniform spacing needed between emitters to achieve space charge saturation as a function of both the emitter diameter and the electrode gap for a Colloid thruster Array using formamide 30% w/w NaI doped with an electrical conductivity equal to 2.3 Si/m , mass density equal to 1289 Kg/m^3, relative electrical permittivity equal to 111, surface tension equal to 0.06 N/m. Also, $\eta = 1$, the specific charge is equal to $3950 C/Kg$ and $\zeta = 1$. In this plot the electrode-to-emitter distance increases in steps of 30 μm starting at 30 μm, and the gap G increases upwards in the plot.

For practical purposes it is desired to avoid starting voltages above a few thousands of volts; therefore, the extractor electrode - to - emitter spacing should not be larger than a fraction of a millimeter, less than two millimeters at most. Therefore, just a few more contours should be added to the figure, contours that do not change the conclusion extracted from those already appearing.

Any values that falls below the 45° curve cannot be obtained in practice because they imply an emitter-to-emitter separation smaller than L_c. Usually L_c is smaller than the actual length that defines the dimension of unit cell that is repeated in the array. Furthermore, in order to

enhance locally the electric field a substantial change in cross sectional area of the emitter, from its base to its tip, must take place. Therefore, the line $S = 10 \cdot L_c$ is a better estimate of the physical limit for the emitter spacing: in the actual case of the Linear Colloid Thruster Array that is described in this work the emitter spacing is 10.8 times L_c; in the case of a Planar Colloid Thruster Array described in Chapter 4 the lower bound for this ratio is about 8:1 and it can get as large as 130:1; for field emitters the ratio is about 50:1 for emitters 20 nm sharp, 1 μm wide [Akinwande, 2002].

The lower bound of L_c is either the minimum feature size of the photolithography transferal process or D^*, the minimum hydraulic diameter needed to implement electrical control. In any case, working with highly doped solvents with emitters smaller than 5 μm in diameter can be quite prone to clogging, reducing the region of feasible space charge saturation in Figure 3.21.

From Figure 3.21 it is not possible to generate space charge saturation with the diameters and electrode separation that are achievable in practice: all the contours fall below the physical limit line of $S = 10 \cdot L_c$. Each contour eventually crosses the physical limit line but by the time they do it the assumption that was used to estimate the starting voltage ($L_c \ll G$) does not hold.

If we use a simpler reduced order model to estimate the electric field that triggers the electrical instability and we use the fact that most of the potential drop occurs within a diameter's length [Carretero, 2003], then the criterion for starting voltage, free from electrode separation dependence, is [Velásquez, 2001]

$$V_E = \sqrt{\frac{\pi \cdot \gamma \cdot L_c}{\varepsilon_o}} \tag{3.35}$$

then Figure 3.22 is obtained. The result is the same: it is not possible for the proposed Linear Array to space the emitters close enough for space charge saturation to take place when the actual fabrication limits are taken into account.

One might be tempted to say then that the thrust per unit of area in a Colloid engine is smaller than the thrust densities for an ion engine. This is not necessarily true because the gap G in a Colloid Thruster can be made smaller than in an ion engine, so that a Colloid engine below its own space charge limit can have a higher current density than a space charge limited ion engine. In other words, one may not need to get near space charge saturation conditions to achieve the thrust density and thrust level for the mission under consideration. I_{sp} is, of course, not limited by space charge.

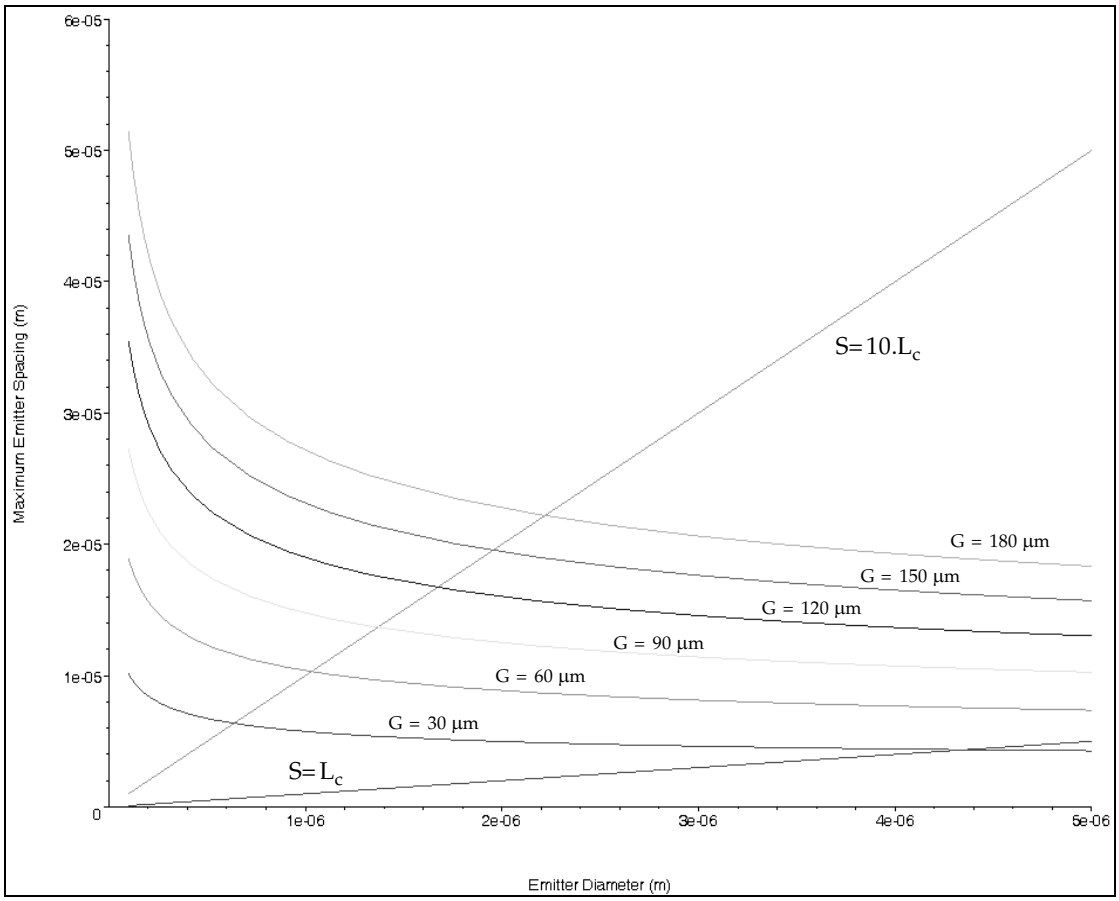

Figure 3.21 Maximum emitter spacing versus Emitter L_c to achieve Space Charge Saturation Conditions. In the plot $\delta = 3950$ C/Kg, $\zeta = 1$ and $\eta = 1$.

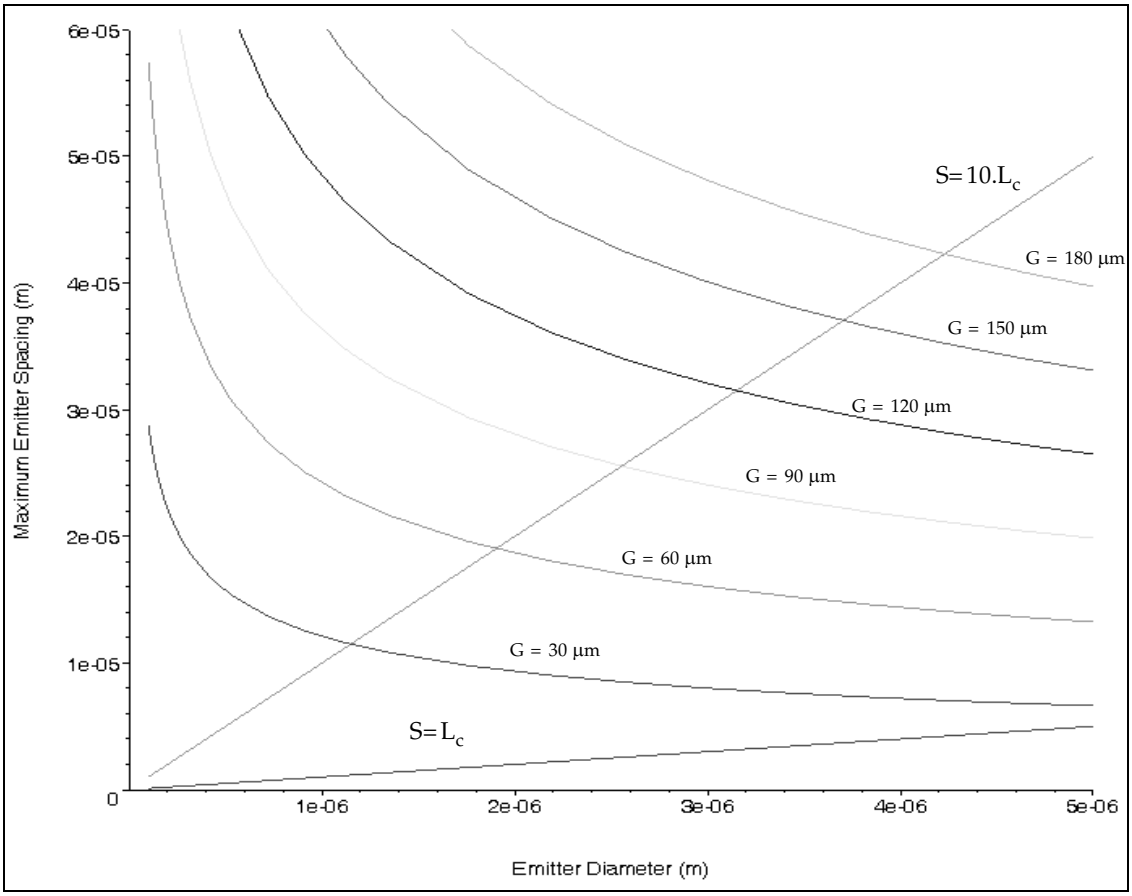

Figure 3.22 Maximum emitter spacing versus Emitter Diameter achieve Space Charge Saturation Conditions, simpler reduced order model to estimate the threshold voltage to generate the electrical instability. In the plot $\delta = 3950$ C/Kg, $\zeta = 1$ and $\eta = 1$.

3.2 Device Fabrication

Figure 3.23 shows a series of pictures of a fully assembled Linear Colloid thruster Array. The engine uses four silicon substrates, two for the hydraulics and one for each electrode. The engine is entirely patterned using plasma etching using RIE and DRIE. To elaborate the hydraulic system 7 optical masks, 12 photolithographic processes, and more than 130 fabrication steps are needed. To elaborate the electrodes 4 Optical Masks, 5 Photolithographic processes, and more than 60 fabrication processes are required. The electrode has a conductive path made of W/Ti on top of a PECVD silicon oxide layer 10 μm thick used as insulating layer. The electrodes have a slot to allow the charged droplets to get through the electrode

and also some substrate removal to avoid substrate impact by the droplet fan.The electrodes and the hydraulics are hand assembled with the spring system mentioned in the previous section.

Section 3.2.1 briefly refers to the fabrication considerations, Section 3.2.2 exposes the fabrication process flow, while Section 3.2.3 highlights the novel fabrication procedures developed to fabricate the Linear Colloid Thruster Array. In order to gain a better knowledge of the micro-fabrication techniques the author advises to go to general references [Campbell, 1996; Madou, 2002], or the brief summary included in his Master of Science Thesis [Velásquez, 2001].

3.2.1 Fabrication Considerations

The following is a summary of the key fabrication choices made to implement the Linear Array fabrication:

- **Photolithography:** positive tone contact photolithography was selected as the photolithographic transfer method. The selection was mainly based on the need to build large enough Linear Colloid Thruster Arrays, be able to use global alignment features, make the optical masks be invariant under reflection by the vertical axis, and acceptable MFS (minimum feature size) and resolution (contact photolithography has a MFS of $\sim 3\ \mu m\ \pm 0.5 \mu m$). The engine layout was designed to be invariant to reflections through the vertical axis to avoid keeping track of the sense the optical masks that are transferred to the substrates.
- **Etching and etch depth control:** Plasma time-controlled etching was selected to define the etch-depth of the features. The use of either a multi stack approach where each substrate thickness defines a key feature depth, or the implementation of etch stops, were found unfit for the fabrication process. Highly selective plasma etching recipes were favored in the fabrication tuning.
- **Nested Masks:** The engine has a set of manifolds and a plenum to supply propellant to the emitters. A nested mask approach was selected to transfer these features because they substantially overlap and contact photolithography cannot accurately transfer features that are not at the top surface level [Velásquez, 2002, Velásquez-2003].
- **Hydraulic system sealing using fusion wafer bonding:** Other alternatives, such as polymer molding, anodic bonding and epoxyc bonding do not provide the processing compatibility / resolution needed.

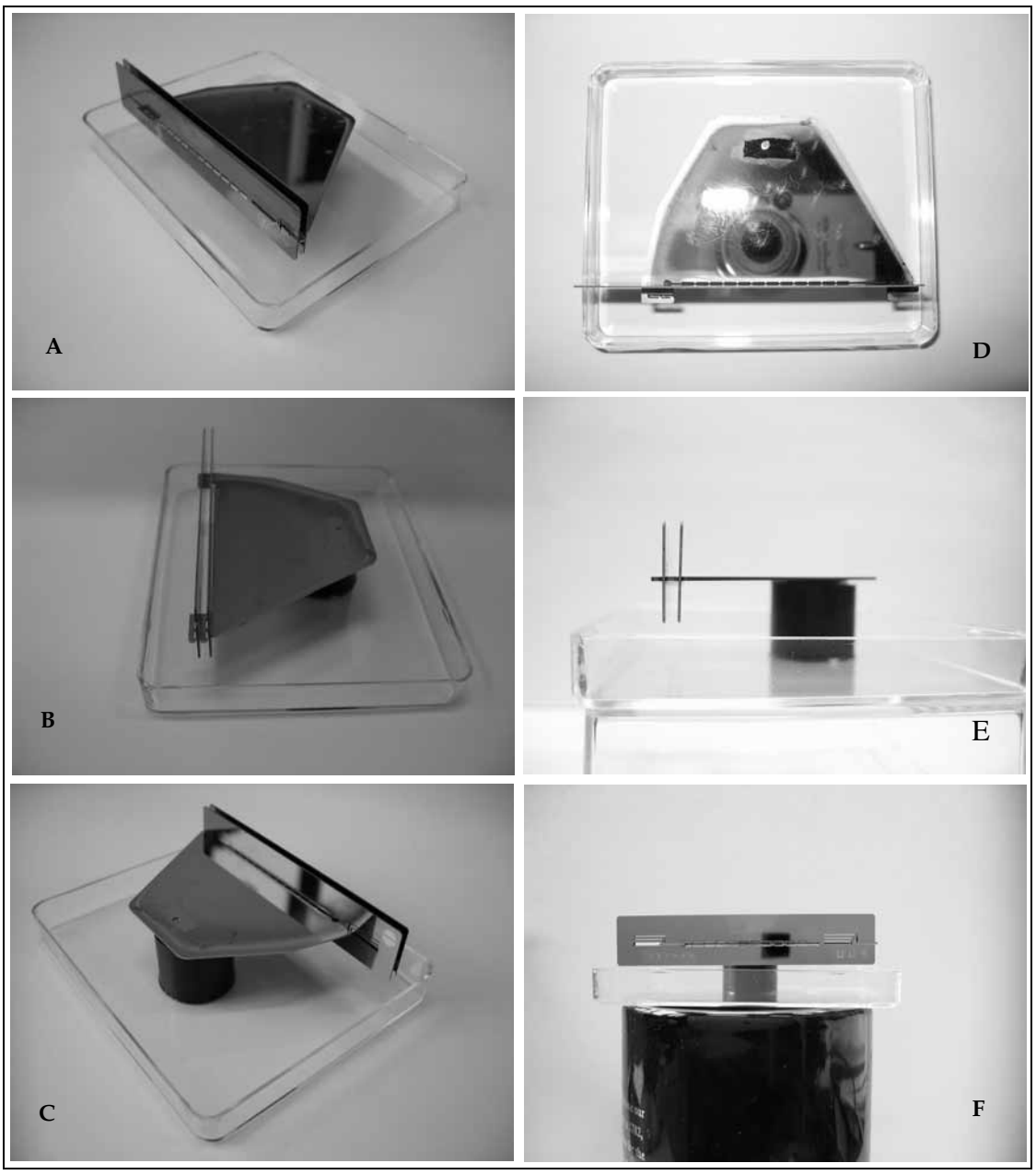

Figure 3.23 Series of pictures to describe the Linear Colloid Thruster Array: isometric views in different orientations *(A, B, C)*; top view, the camera flash was activated to better appreciate the extractor-to-emitter separation uniformity *(D)*; side view of showing the excellent parallelism of the electrodes *(E)*, front view showing the electrode exit expansions *(F)*.

- **Lightly doped DSP substrates:** The substrates chosen for the Linear Array are lightly doped (resistivities of the order of $30\Omega/cm$) because several silicon etching steps are done with highly selective recipes with respect to silicon oxide and native oxide growth is slower for these substrates. Also, the substrates are

double side polished because both wafer surfaces are used to transfer optical mask patterns.

3.2.2 Fabrication Process Flow

The Linear Colloid Thruster Array is composed of two process flows: one for the hydraulics and one for the electrodes. Each fabrication flow includes some steps to create the springs to later assemble the engine. In both cases 6" Si p<100> DSP, boron doped, 375 ± 5 μm thick substrates are used. At key stages of the fabrication procedure, pictures of the fabrication results are provided.

Fabrication Process of the Hydraulic system

The micro-fabrication procedure builds 6 engines per wafer set, where the engines are arranged in pairs with their spout arrays facing each other. The process of the most complex engine, i.e., with fully sharpened spouts, is provided here. In order to clarify the process flow a series of computer-generated concept views is included where only the processing of one engine is shown. In this concept views several of its relevant dimensions, such as the wafer thickness and etch depths, have been distorted. Also, only two emitters per manifold are carved on the model substrate.

- **Transfer on both sides of top and bottom wafers Mask 0 using a black silicon plasma etching recipe:** This procedure generates on the substrate the global aligning features, etch rate testers, and a set of features that allows doing in-plane metrology, including misalignment grids to estimate the relative positioning of the subsequent optical mask transfers with respect to the first patterning.The black silicon implementation allows excellent alignment in the subsequent photolithography transfer, even though several films tens of microns thick are placed between the optical mask template and the wafer substrate.
- **Transfer to bottom wafer the channels to the substrate using Mask 1:** A Deep silicon RIE is practiced using a PECVD silicon oxide hard mask. The channels have a square cross-section with a characteristic length equal to 12 μm. The channels have expansion inlets to smooth the hydraulics an thus avoid bubble trapping and stress concentrators. Figure 3.24 is a concept view of the substrate after patterning the channels. Figure 3.25 is a picture of the channel ends of a channel set fed by the same manifold were optical mask transfer uniformity is noticed.

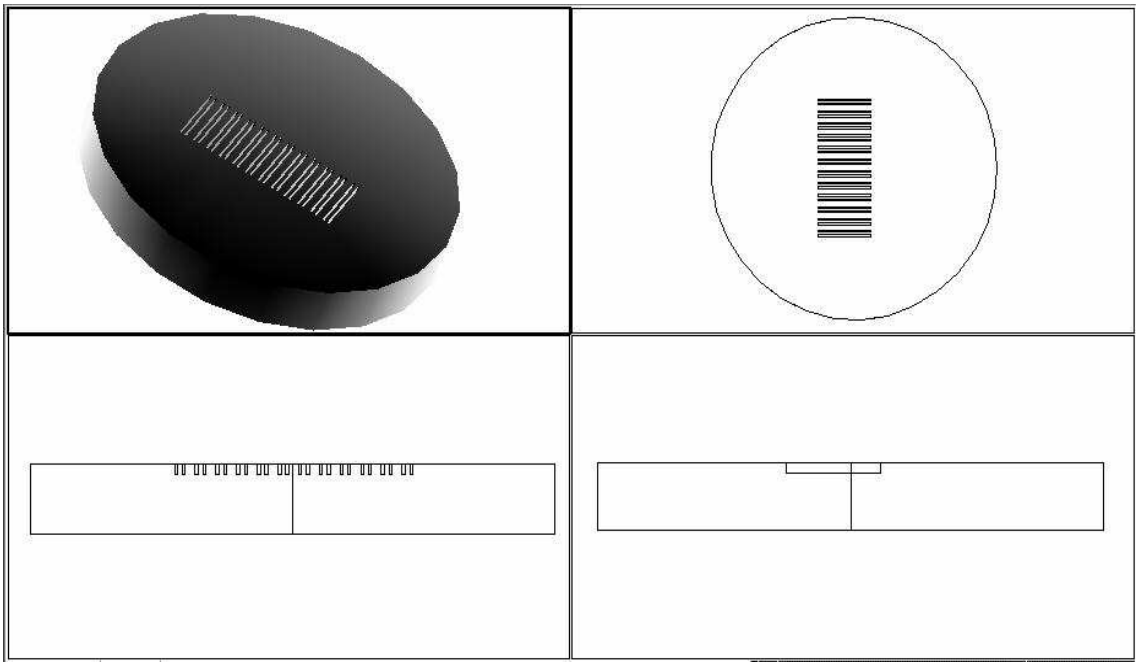

Figure 3.24 3-D view (upper left), top view (upper right), front view (lower left) and side view (lower right) of a substrate after transferring Mask 1.

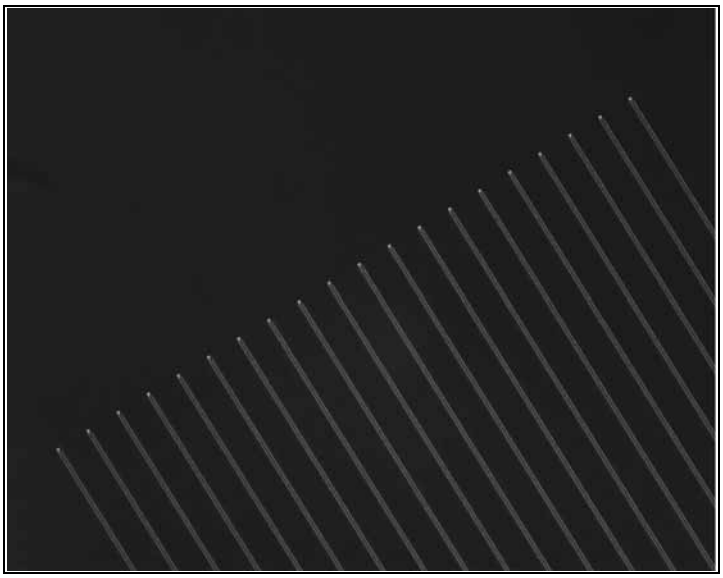

Figure 3.25 Optical microscope top view picture of a set of channels fed by the same manifold at their ends. Excellent uniformity and to some extent good anisotropy can be appreciated.

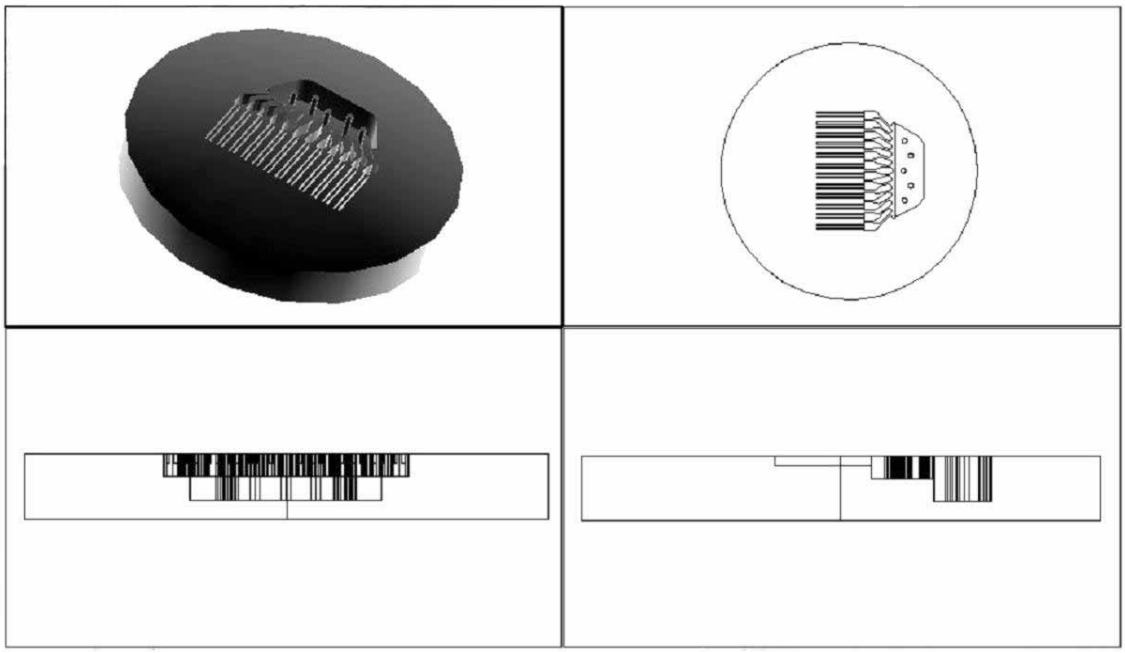

Figure 3.26 3-D view (upper left), top view (upper right), front view (lower left) and side view (lower right) of a substrate after transferring optical Masks 2 and 3.

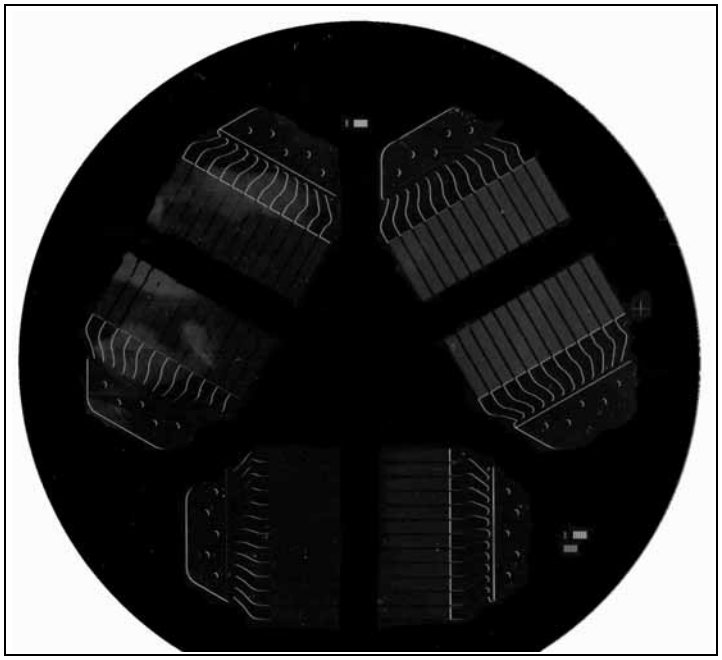

Figure 3.27 Picture of a wafer after the channels, manifolds and propellant tank are formed.

- **Pattern the engine manifolds and propellant tank in bottom wafer using DRIE without passivation phase and a nested mask approach:** The nested mask is composed of a hard mask made of 2.5 μm thick PECVD silicon oxide with the features of Mask 2 (manifolds plus propellant tank) and a thick resist film with the features of Mask 3 (propellant tank). A series of DRIE etch steps without passivation are used to leave smooth surfaces at the engine interior. In this step a set of columns is created to protect the propellant tank from excessive deflection. Figure 3.26 is a concept view of a substrate after transferring Masks 2 and 3 to the substrate. Figure 3.27 is a picture of a wafer at this stage in the process
- **Grow on both wafers a thin layer of thermal silicon oxide 0.275 μm thick:** This oxide layer has two key roles: to act as an etch stop for the spout generation and to enhance the wettability of the engine interior to formamide.
- **Transfer to both bottom and top wafers Mask 5A with a shallow anisotropic etch**: Mask 5A is transferred using DRIE creating 15 - 20 μm trenches to create the spout frontal surfaces. A RIE step to pattern the thermal oxide is carried out beforehand.
- **Fusion Bond bottom and top wafers:** Figure 3.28 is a concept view of the bonding process. Absolute cleanliness is required for this step to be successful.

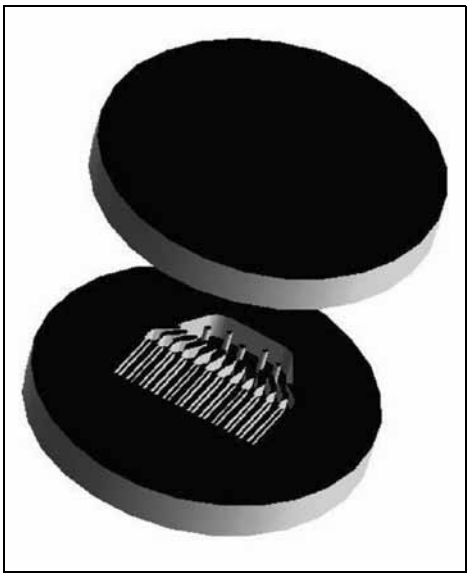

Figure 3.28 Top and bottom wafers are about to be bonded to seal the hydraulics.

The misalignment between the two wafers is about 1.5 μm. Figure 3.29 is a series of IR pictures of a wafer pair after annealing at $1050°C$ for one hour in a

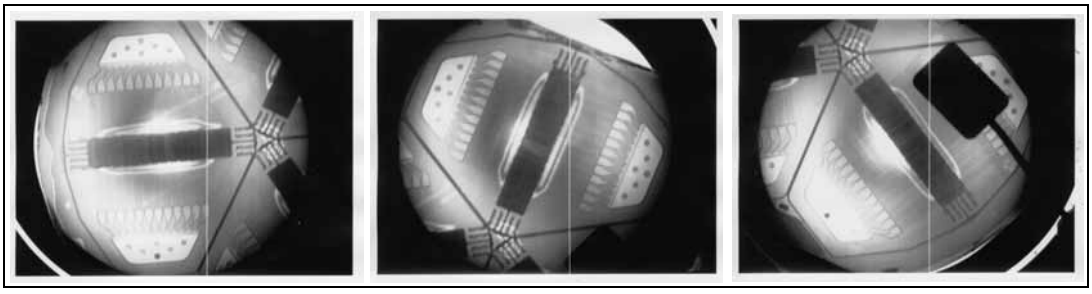

Figure 3.29 Series of IR pictures of a fully-sharpened engine set right before final device retrieval from the bonded substrate. The newton rings in the emitter area are due to the sudden change in height but are not related to bonding problems. Excellent bonding quality is seen in this particular wafer set.

nitrogen atmosphere. Two additional tricks are useful to increase the quality of the wafer bonding: one of them is to wait about *one day* between the time the wafer pair is bonded and the time the wafer pair is annealed to allow the interface energy to saturate; the other trick is to grow thermal oxide right after annealing the wafer pair to supply sealing material for features that have an opening to the exterior. Figure 3.30 is a series of pictures to evidence the good quality of the wafer bonding. The wafer bonding quality can be evidenced by two observations:

- The wafer pair interface is barely visible (something important to point out for a coarse/traumatic process like wafer die-sawing)
- The wafer pair union shows far smaller striations than for instance the free boundary of the *top* wafer. The die-saw striations on both original substrates are continuous, i.e., roughness lines transmit through the interface, evidencing a stiff bond.

- **Deposit on both sides of the wafer pair thick layers of PECVD silicon oxide.** These oxide films will be used as hard masks.
- **Transfer to one of the silicon oxide films Mask 4 and to the other one Mask 5A using Deep silicon oxide plasma etching:** These two masks have the features of the set of springs and the remaining part of the spouts.
- **Transfer to both sides of the wafer pair a thick layer of resist with the features of Mask 6A:** This mask has a set of pads to cover the spring clusters and thus it implements a nested mask with Mask 4 and Mask 5A.
- **Practice an isotropic etching until reaching the wafer pair mid interface:** The purpose of this etching is both to start releasing the engine form the substrate, and to produce the first out-of-plant spout sharpening.
- **Practice a deep etching to finish the engine:** This step can be done in two ways: if the resist pads covering the spring clusters are removed with an asher then a DRIE step can be done to both finish the spouts, the engine release and

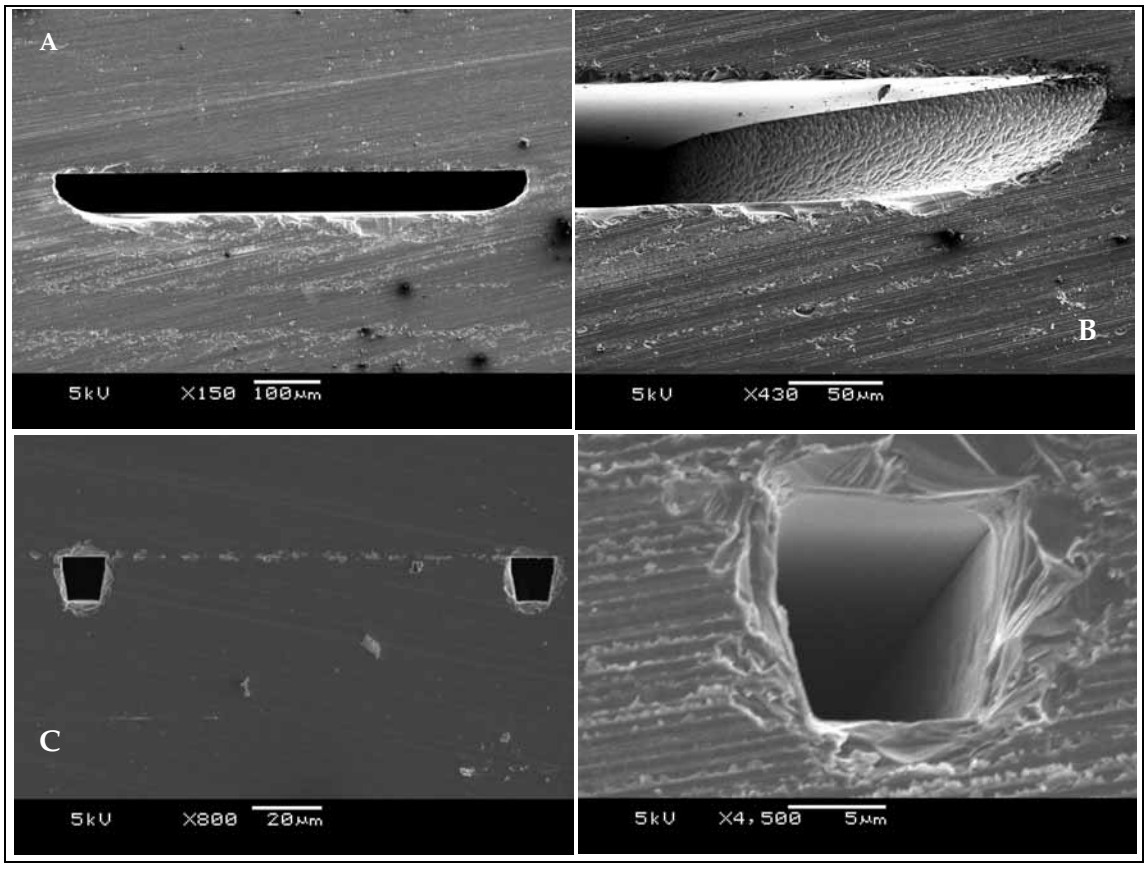

Figure 3.30 Series of pictures to evidence the wafer bonding quality of the Linear Array Hydraulics: SEM picture of the a manifold cross-section *(A)*; SEM picture of the unperturbed wafer pair interface *(B)*; SEM picture that shows a cross section of two consecutive channels *(C)*; SEM picture of a channel cross-section.

pattern the spring clusters. This way a half-sharpened engine is obtained. Figure 3.31 shows the emitters that are obtained this way. The other possibility is to practice another isotropic etching on the other side of the wafer pair to release the engine from the substrate and produce the second out-of-plant spout sharpening. Then an umbrella made of a piece of quartz is placed to protect the spouts while a DRIE step is carried out to generate the spring clusters. This way a Linear Array with Fully sharpened emitters is obtained. The result of this procedure is shown in Figure 3.32. In this step the fuel inlet is also formed.

- **Deposit a 1 μm thick teflon coating from the passivation phase of DRIE**: This film is intended to set the spout exterior non-wettable to help define the wetting front of the meniscus at each spout.

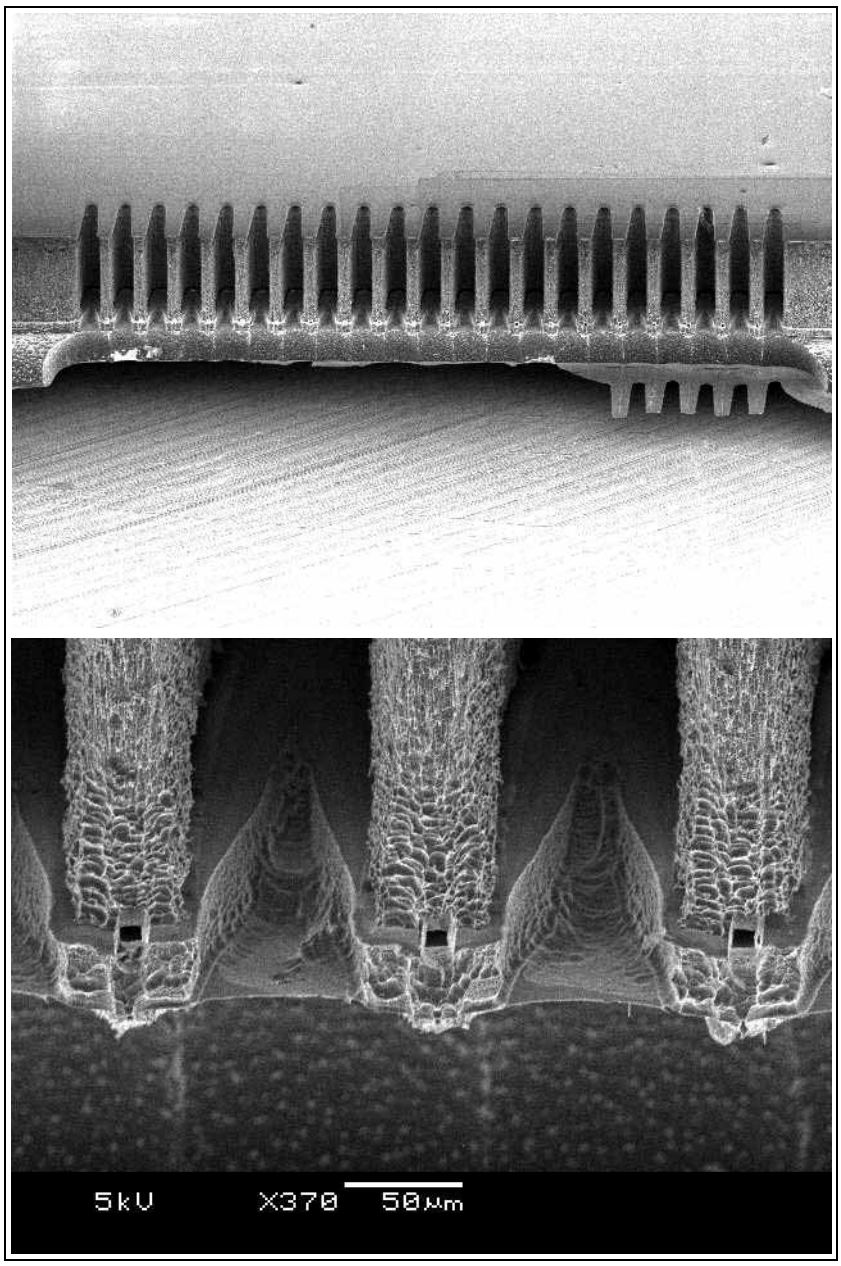

Figure 3.31 SEM picture of a half-sharpened spout system manifold set patterned on a real Linear Array Hydraulics substrate (above) and emitter detail (below). The emitter is placed near the intersection of the anisotropic etching and the lower lip. The emitter openings survived the patterning due to the high selectivity of silicon oxide over silicon of the plasma etching recipe used for DRIE. The alignment is excellent and the spouts seal quite well.

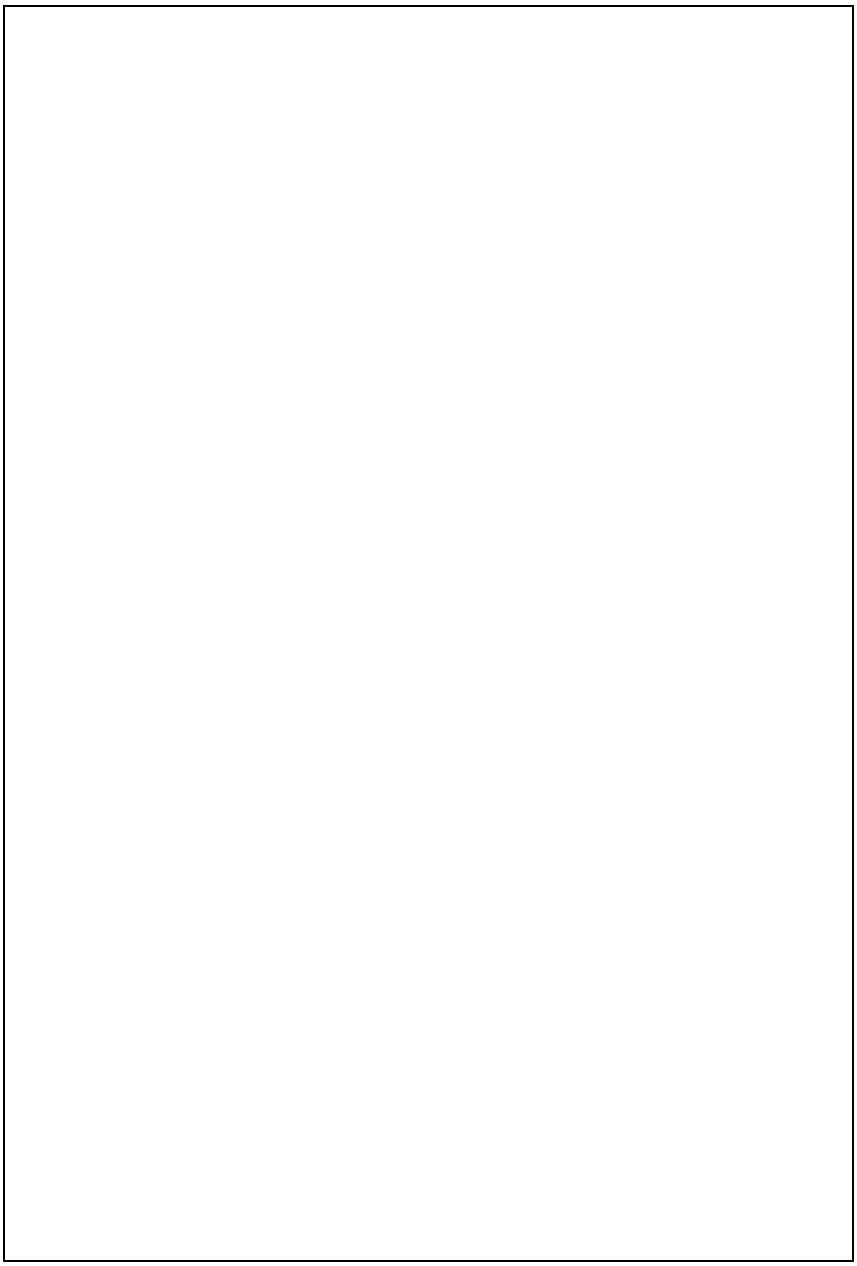

Figure 3.32 SEM picture of a fully-sharpened spout system manifold set patterned on a real Linear Array Hydraulics substrate (above) and emitter detail (below). One can see the emitters placed between the two lips and the emitter-to-emitter separations. The emitter openings survived the patterning because of the DRIE recipe implemented and the small exposure to the isotropic plasma.The emitter fronts are patterned before wafer bonding; when the lips are formed the etch is stopped as soon as an opening is seen.

Spring Clusters of the Linear Colloid Thruster Array

Between the electrodes and the spouts there must be a vacuum gap large enough to allow the propellant vapors to leave the spout area of influence so the breakdown voltage does not substantially decrease. A set of spring clusters allows to hand assemble with micron-size precision the electrodes and the hydraulic system. The alignment accuracy relies on the feasibility of patterning macro-scale features with micro-scale precision using micro-fabricating methods, structurally strong enough to allow hand assembly.

There are two version of spring clusters, shown in Figure 3.33 (spring cluster patterned in the hydraulics wafer pair) and Figure 3.34 (electrodes). The dimensions of the different features closely resemble the dimensions of the optical mask, to better than 4 μm.

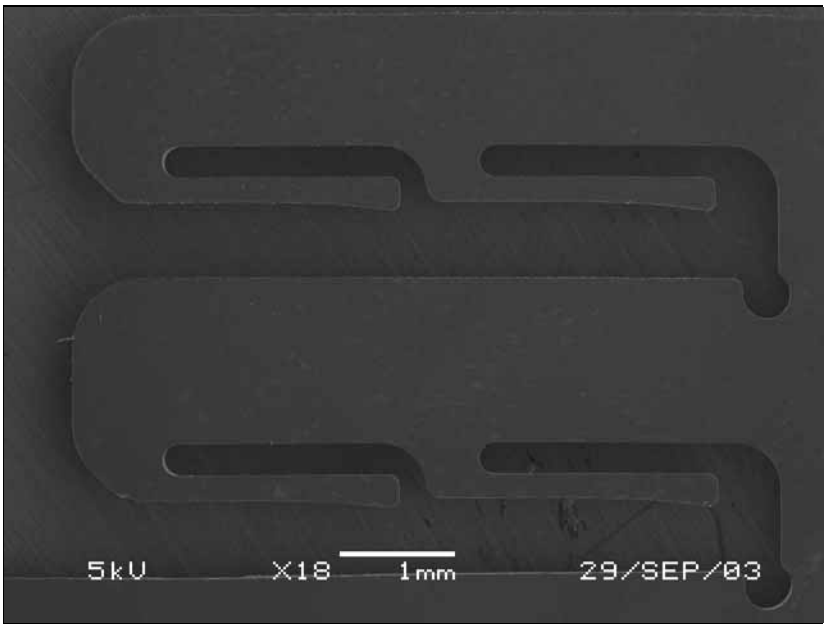

Figure 3.33 SEM picture showing a single spring and a cluster spring root on the hydraulics wafer pair. The picture evidences the smooth geometry of the spring to avoid stress concentrations.

Figure 3.35 through Figure 3.39 shows a series of SEM pictures of a hydraulics substrate assembled to an extractor electrode with the viewing direction pointed out in Figure 3.5. In this pictures the nominal deflection of the hydraulics spring clusters is 30 μm while the nomi-

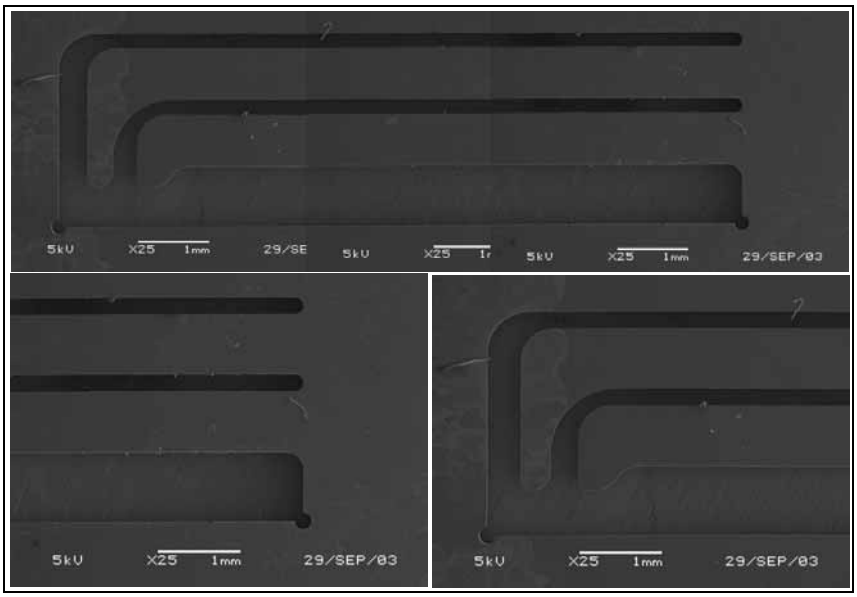

Figure 3.34 Set of SEM pictures of an electrode spring cluster. Some particle contamination / remnants of the etching mask (poly-Si + SiO_2) / residues of acetone - from cleaning- are visible *(above)*; SEM picture showing the spring roots, electrode slot and sliding path endpoint *(below, left)*; SEM showing a zoom of the spring tips *(below, right)*. The spring tips clearly show a sense of sliding movement (right to left) and have smooth geometry to decrease the probability of structural failure.

nal deflection of the electrode spring clusters is 60 μm. Several key issues can be seen in this set of pictures:

- The springs are deflected, i.e., there is a zero gap between the spring tips and the unperturbed reference surfaces. Therefore, the pieces are making physical contact.
- The physical contact between the springs and the clamped substrates is made exclusively at the spring tips. Given the etch sidewall taper this contact is made at a point instead of a line. This does not present a problem, because the springs manage to make a stiff assembly; also the union is controlled with 8 points of precision, enough to assure the control of the rotations and axial displacements [Slocum, 1992].
- It is always possible to slide the electrodes down to the spring cluster roots. The presence of a well defined stopping point at the spring cluster roots allows us to control the third degree of freedom not controlled by the springs.
- By comparing the deflected springs to the non-deflected springs in Figure 3.39 one can see the deformation / distortion of the spring geometries.

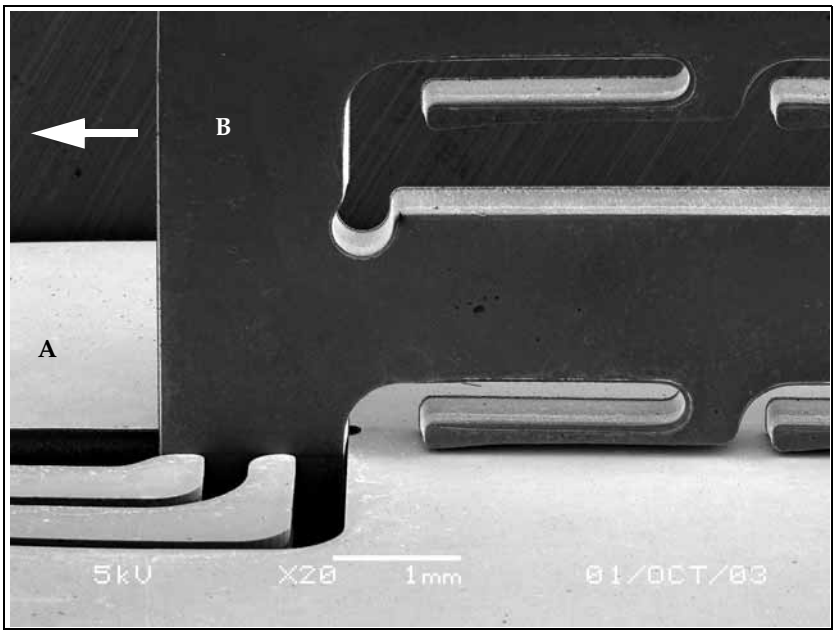

Figure 3.35 SEM picture showing the four electrode springs of one cluster in deflection. The electrode (**A**) is completely sled down to make physical contact with the corresponding root of the Hydraulics spring cluster (**B**). From this picture also excellent etching anisotropy can be evidenced. The arrow shows the relative sliding direction of the electrode respect to the Engine Main Body.

- There is no evidence of cracking in the spring structures. Because silicon is fragile this means that the stress levels of the springs are below failure values.
- Several test structures were assembled and the test structure never failed during assembly. This validates the proposal of hand assembly without any other auxiliary equipment aside from a tweezer (no sliding guides, other than the actual clusters, are needed).
- Experimentally it was found that the stiffness of the union is increased if the force exerted by the springs is increased; this implies to set larger nominal spring deflections.

Figure 3.40 is an picture of an assembled test structure as seen from the side: the virtually $90°$ orientation of the electrode with respect to the Linear Array main body is evident.

The alignment resolution depends on the optical mask resolution ($\sim 0.5\ \mu m$ for pattern generated masks) photolithography resolution (about 4 - 5 μm per sidewall for a typical thick resist film with a taper $\sim 64°$), etching taper (dependent on the etching window orientation and width, see Figure 3.41), etching roughness ($1.2\ \mu m$), and the wafer thickness.

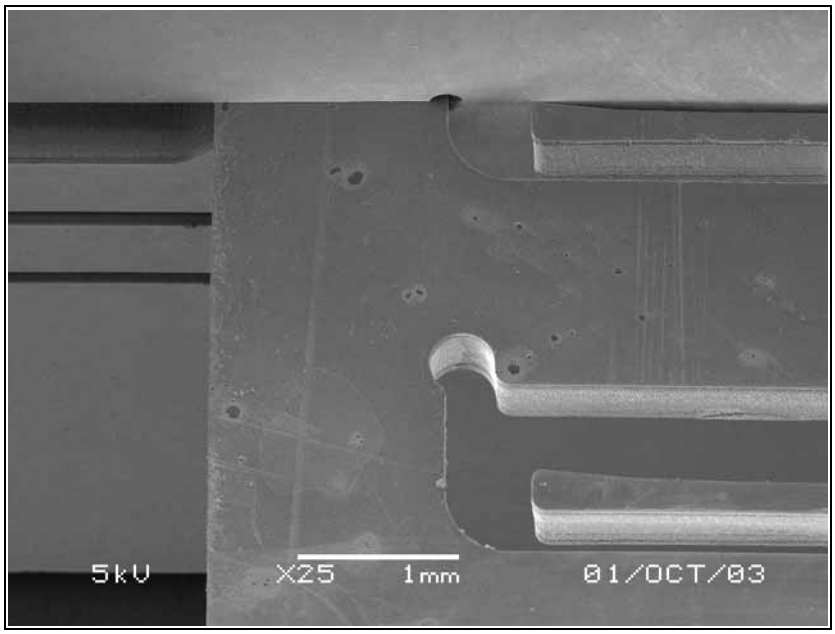

Figure 3.36 SEM picture showing the other spring cluster, activated from the opposite viewing point compared to the one in Figure 3.35. There is visible change in shape in the deflected spring (above) compare to the spring that is not activated (below). The excellent anisotropy of the DRIE recipe used is evidenced here.

The estimation of the alignment resolution of the assembly is based on the assumption of gaussian distribution of the different uncertainty sources and the definition of misalignment as the distance between a point in the middle of the substrate that has the spring cluster and the projection of this point onto the plane defined by the internal face of the unperturbed surface that it interacts with. If there were perfectly perpendicular sidewalls at the etched surfaces the distance between any middle thickness point and its projection would be zero. This definition is useful because what we are interested in diagnosing how much change the emitter position referenced to the electrodes gets due to non-idealities. Figure 3.42 might help to better understand the misalignment definition.

Based on the reference frame selected (Figure 3.43), the different misalignments produced by the two spring sets are estimated to be bounded by:

$$\Delta_X = 32.7\mu m \quad \Delta_Y = 16.9\mu m \quad \Delta_Z = 18.1\mu m \tag{3.36}$$

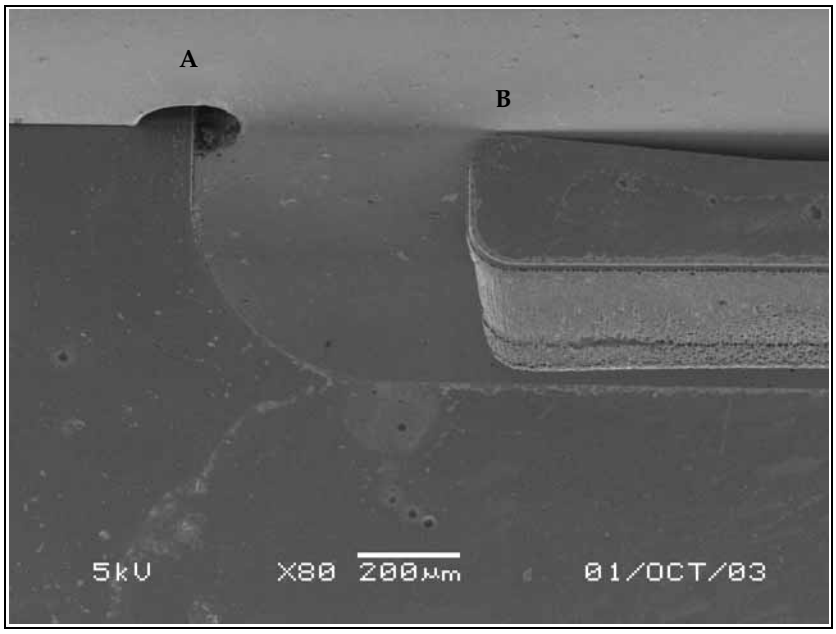

Figure 3.37 SEM picture showing an electrode spring cluster root, as well as the deflected tip of a spring from the corresponding a hydraulics spring cluster. Looking at the root notch (**A**) one can see a zero gap between the two substrates at the electrode spring cluster root in the two degrees of freedom. There is physical contact between the spring tips and the clamped substrate just at the spring tip (**B**).

These values are impressive coming from a hand assembled structure, and also compared to the resolution of standard machining (25 μm) or the bound for the misalignment of standard machining (35 - 40 μm).

The rotation control is achieved by a tight union and eight points of control. Based on the position of the emitters the influence of rotation on the misalignment calculations is to first order negligible.

Figure 3.44 is a pictorial summary of the different parts of the hydraulics wafer pair.

Fabrication Process for the Electrodes

- **Transfer to both sides of the substrate Mask A using a black silicon etching recipe:** Metrology features, back-to-top alignment guides, a macro-scale mark of the electrode slot width (300 μm, 500 μm, and 2600 μm are also formed.

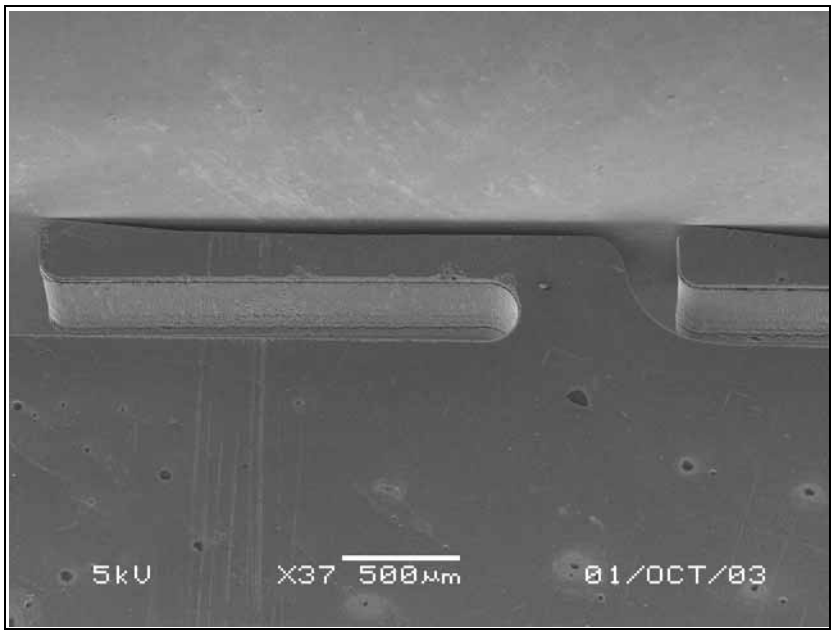

Figure 3.38 SEM picture showing two consecutive activated springs from the hydraulics spring clusters. The shadows evidence that the springs make contact to the clamped substrate only at their tips.

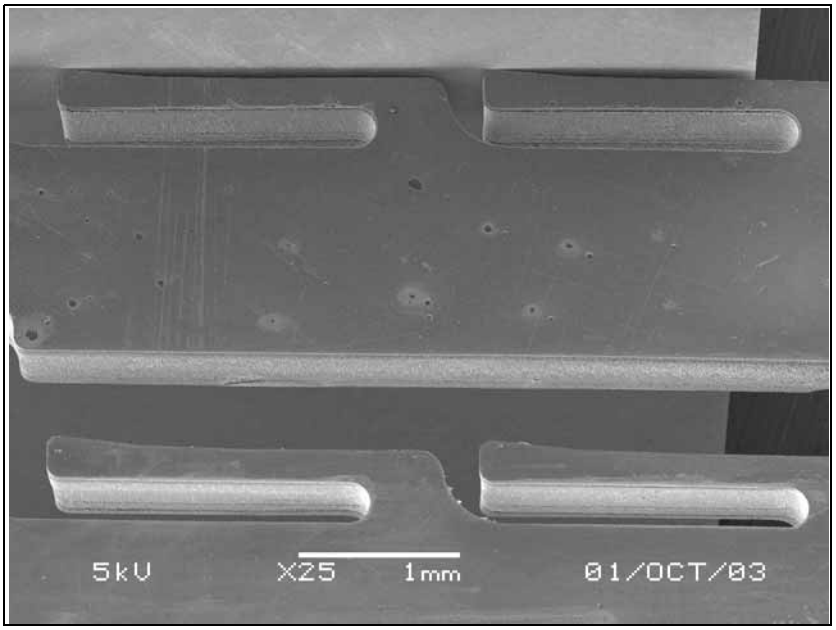

Figure 3.39 SEM picture of the complete set of springs of a hydraulics spring cluster. The lower spring couple is intended to clamp the accelerator while the upper spring pair is already clamping an extractor. The difference between the shapes of the deflected and non-deflected springs is visible, specially near the spring tips. This further corroborates the spring activation.

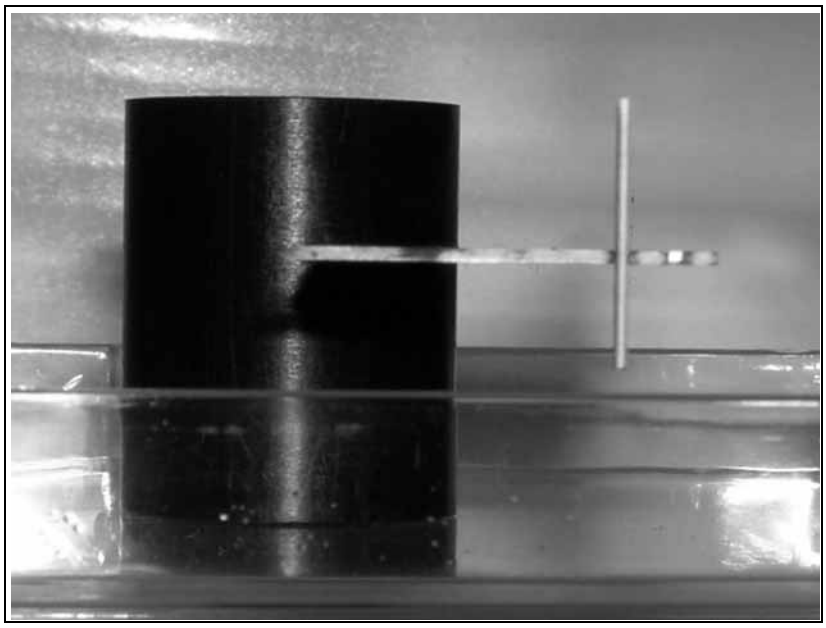

Figure 3.40 Picture showing an assembled test structure of the clip system idea. The test structure is seen from the side. The excellent perpendicularity of the electrode with respect to the main body can be appreciated.

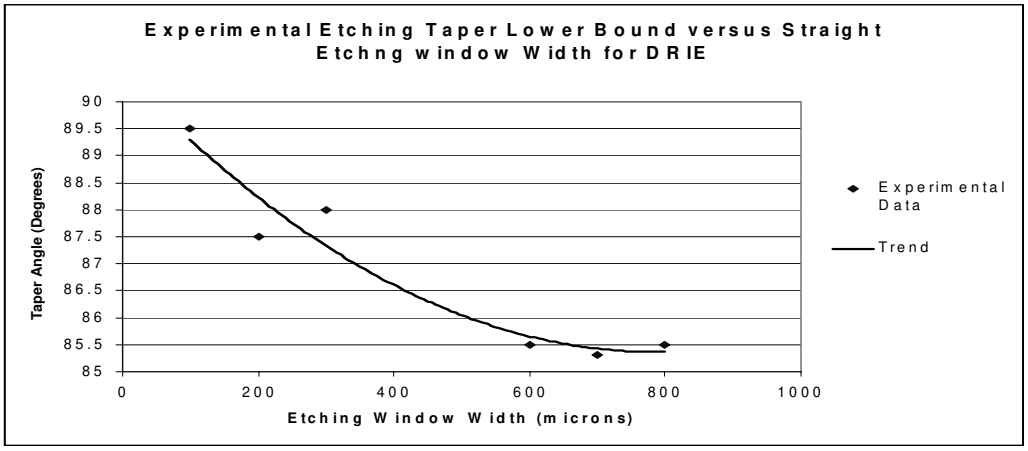

Figure 3.41 Dependence of the negative etching taper on the etching window for a straight etching mask fro DRIE. For a large - highly curved etching mask the taper is 82.3° ; for a collimated stratified nested mask with a large etching window the taper is 79.5° . The experimental data support a *plasma confinement effect,* in the sense that the smaller the etching window and less etching window curvature, the steeper the sidewall produced by DRIE.

- **Grow on both sides of the wafer thermal oxide 1.0 μm thick and then deposit PECVD silicon oxide + annealing 9.0 μm thick**: The film is intended to be used as hard mask and electrical insulation layer.

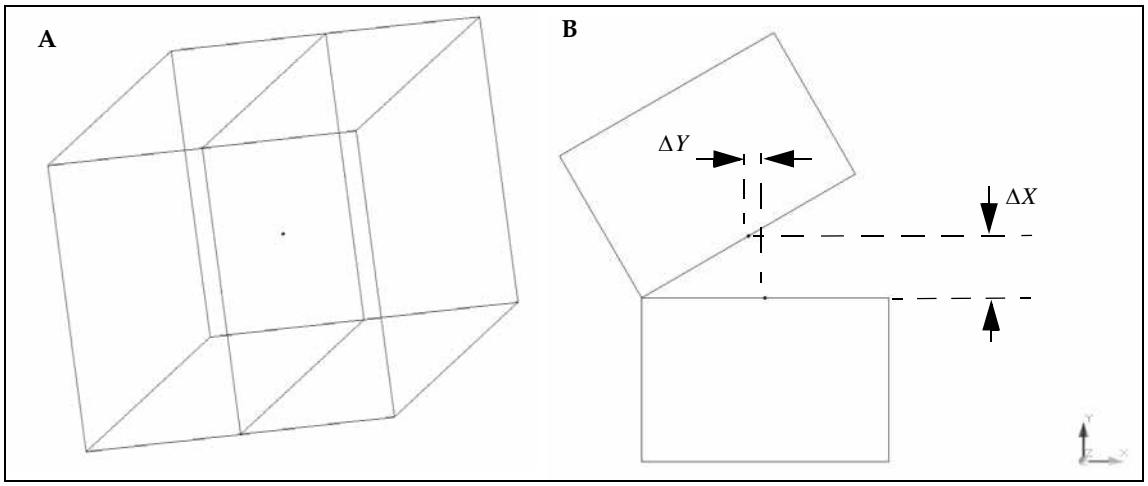

Figure 3.42 Schematic showing the proposed misalignment definition. There are two bodies making physical contact. If both contact surfaces are well-oriented, then the mid-points of the surfaces should touch (**A**); if the surfaces are not parallel then the mid-points will separate some measurable distance. One way to measure this mismatch is by using one of the contact surfaces as reference and see how much the mid-point of the other surface has moved (**B**).

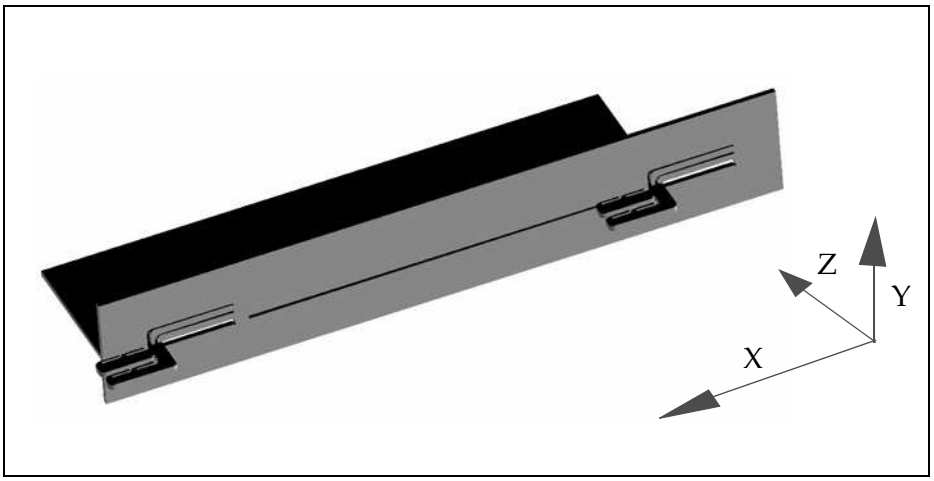

Figure 3.43 Schematic to define the coordinate system to analyze the misalignment produced by the clip system. The X-axis is in the direction of the sliding; the Y-axis controls the misalignment that is directly related to the beam hitting to the electrode; finally the Z-axis is in the direction of the emitter-to-electrode separation.

- **Deposit on the top surface of the substrate a thin layer of PVD** *Titanium* **and** *Tungsten*: Titanium acts as an adhesion layer between the silicon oxide film and the tungsten film. Tungsten is inherently resistant to ion sputtering. This processing step required to create a Tungsten melt and deposition proce-

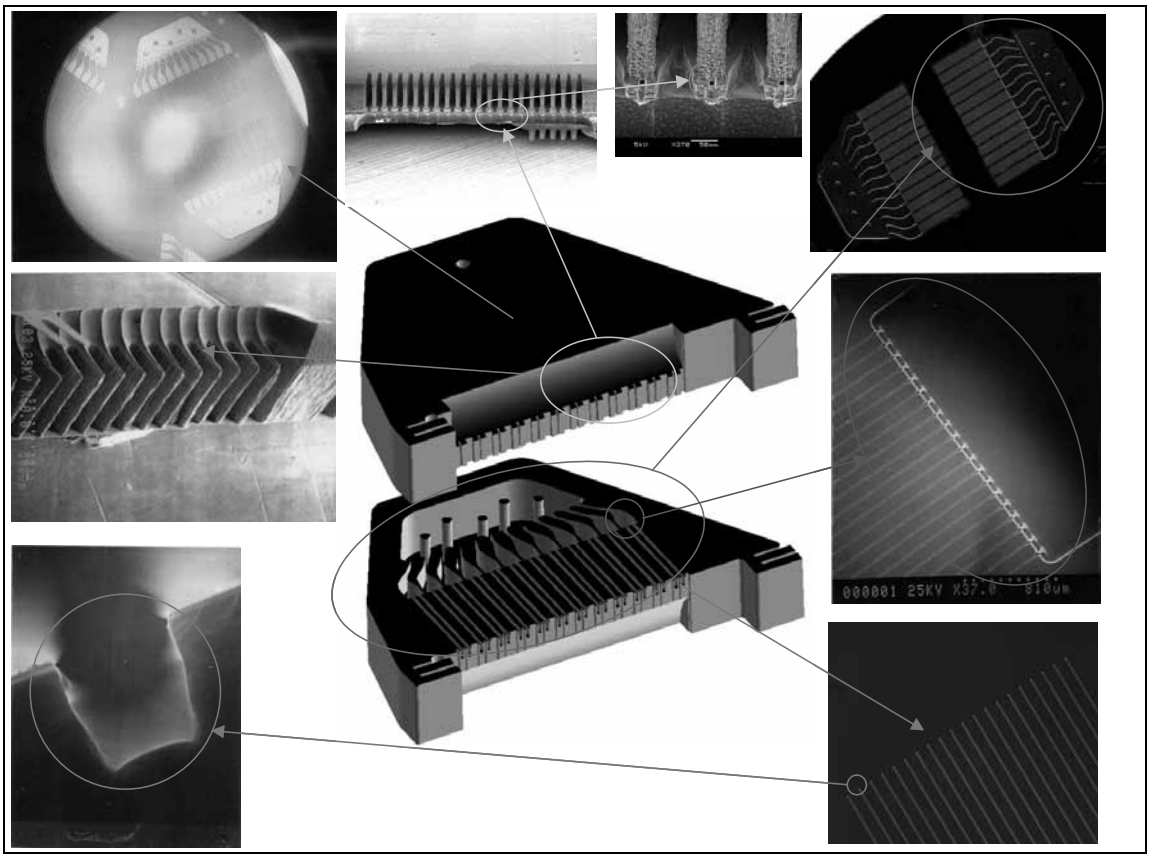

Figure 3.44 Set of pictures to illustrate the fabrication process carried out so far in the text to build the Linear Colloid Thruster Array. From bottom left in clockwise direction: SEM picture of a channel cross-section; SEM picture of half-sharpened spouts; IR picture of the wafer pair after bonding / annealing; SEM picture of a set of half sharpened emitters where the spout exit holes are visible; zoom of three emitters; optical microscope picture of a full engine hydraulics pair; SEM picture of a manifold evolving into a set of twenty channels; optical microscope picture of a set of channels evolved from the same manifold at their endpoints. Central figure: computer-generated exploded view of a Linear Colloid Thruster Array with its clip system patterned (the claw-like structures at either end of the emitter line). The clip system was discussed before.

dure that was not available before in the Micro-fabrication Technologies Laboratory at MIT.

- **Pattern the metal film with plasma using Mask C:** This patterning required to tune a novel SF_6-based plasma recipe for Tungsten. The recipe is novel in the sense that it was not available in the Micro-fabrication Technologies Laboratory at MIT. In this step the electrode pads are formed as well. Figure 3.45 is an SEM picture of the conductive paths obtained with this procedure.
- **Transfer Mask D to the silicon oxide film on the bottom surface of the substrate, using Deep Silicon oxide etching:** The hard mask for the electrode slot exit expansions is formed this way. Also, the layout of a set of ribs is transferred. The ribs will increase the stiffness of the electrode at the region

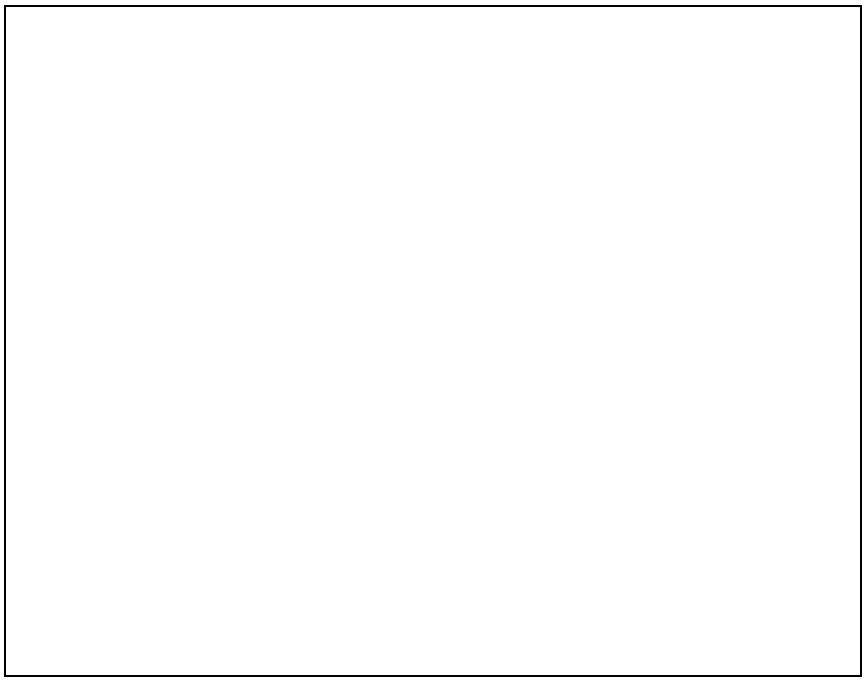

Figure 3.45 SEM picture of a conductive path produced by metal evaporation and plasma etching patterning. The cleanliness of the etching can be appreciated here. The etch stop for this wafer is 1 μm thermal oxide and not attack to the film is visible.

near the droplet fan. Figure 3.46 is an SEM picture of the silicon oxide patterning of the cellular pattern generation features.

- **Pattern the silicon oxide on the top surface of the substrate using Mask B and Deep Silicon oxide Etching:** This layout has the electrode slots, the electrode edges (to enable electrode extraction from the substrate in the last etching step) and the electrode spring clusters.For clarification, a cartoon of the state of the electrode fabrication up to this point is shown in Figure 3.47.
- **Generate the slot exit expansions by using a non-passivated DRIE recipe** (Figure 3.48)
- **Pattern with DRIE the features included in the silicon oxide layer that is on the top surface of the substrate:** Figure 3.49 is a cartoon of an electrode after this step.

Figure 3.50 is a picture of one of these electrodes completely fabricated. Figure 3.51 is a set of SEM pictures with some of the structural details of the electrode.

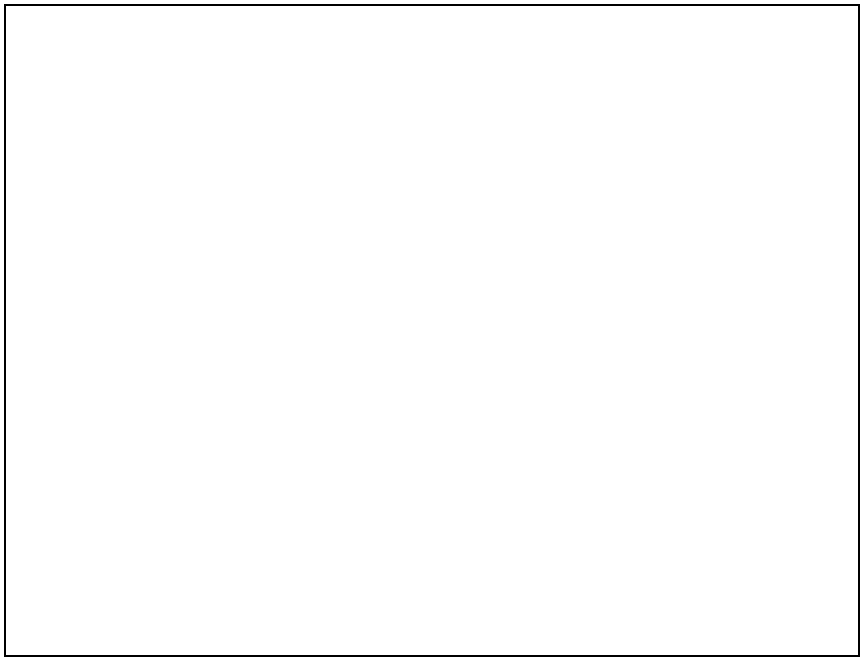

Figure 3.46 Picture of an electrode slot expansion on a 10 μm thick silicon oxide film.

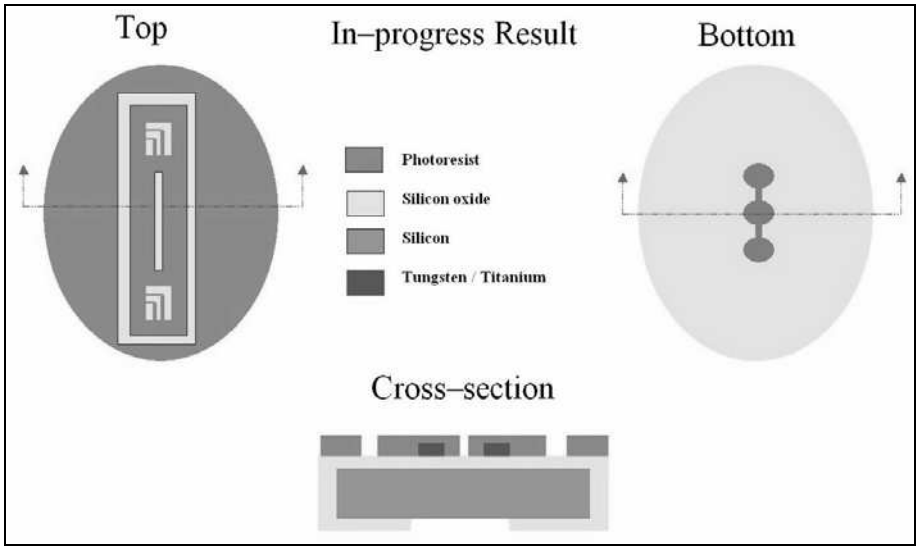

Figure 3.47 Cartoon that shows the state of progress of the electrode fabrication.

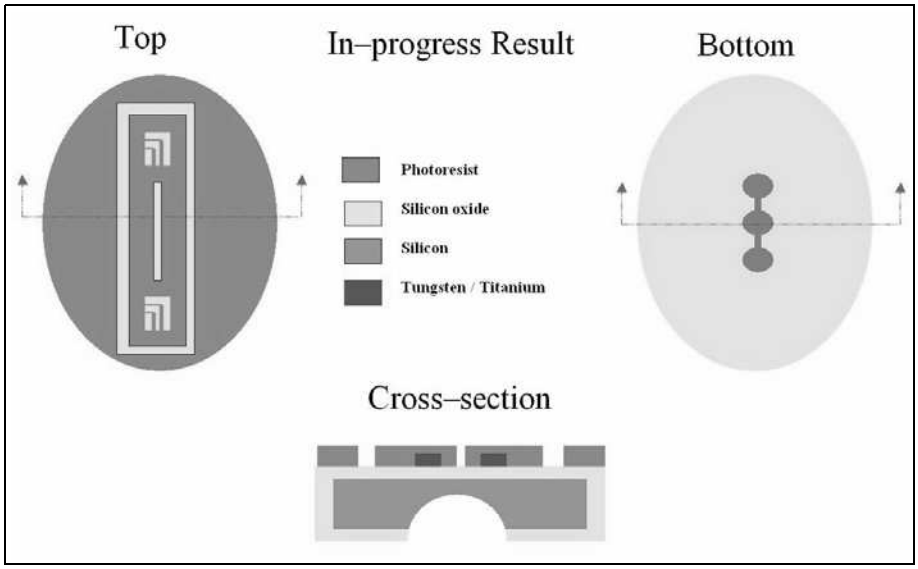

Figure 3.48 State of progress of the electrode micro-fabrication after the slot exit expansions are generated.

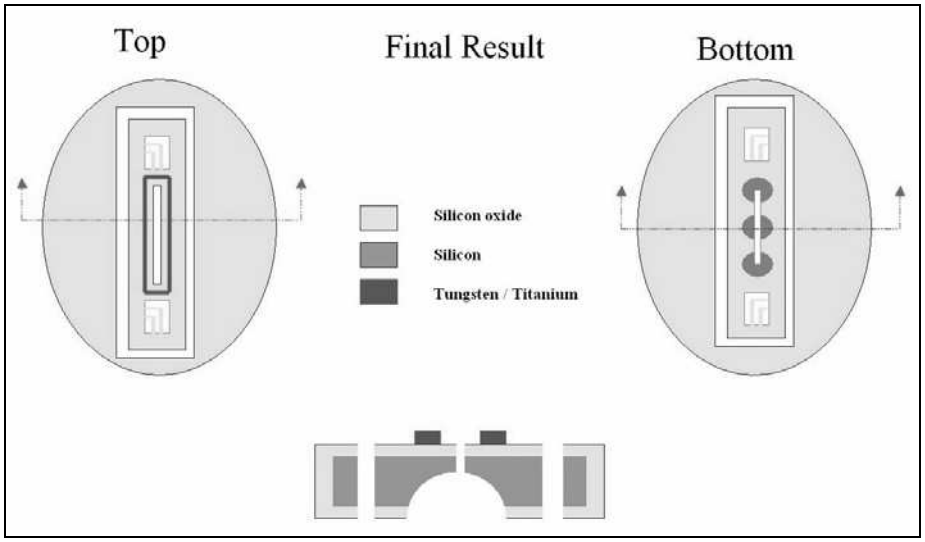

Figure 3.49 Cartoon that shows the electrode fabrication final result.

3.2.3 Novel Fabrication Steps

The fabrication procedure of the Linear Colloid thruster Array has the extra achievement that it was tuned while carrying out a 6" machine upgrade in the micro-fabrication facility of MIT (from 4" substrate machining capabilities). The author actively contributed in tuning from

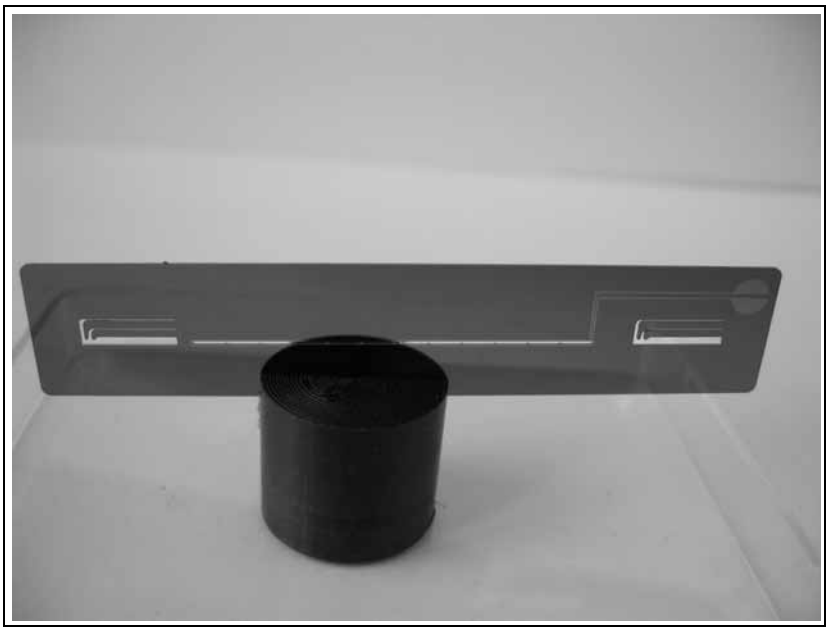

Figure 3.50 Picture of a terminated electrode.

scratch what are now considered standard fabrication steps there, including plasma etching, deposition and CMP. Parallel to this, several novel fabrication procedures such as Cycled deep silicon oxide etching, Cycled deep silicon RIE, chlorine-based black silicon generation and collimated stratified nested masks were developed to make the fabrication of the Linear Array a reality.

Cycled deep silicon RIE

With the exception of the DRIE tools, the micro-fabrication machinery in MTL was intended for shallow etches (up to 0.5 μm). Cycled deep silicon RIE (as developed for this Thesis) is based on a fabrication technique that makes feasible a number of applications that require middle-size etch depths (2 - 50 μm) with excellent uniformity. The technique has been used by several research groups such as Dr. Jeon's group (used in patterning PZT-driven actuators) professor Manalis' group (bioMEMS) and professor Slocum's group (micron precision concentric ring assemblies).

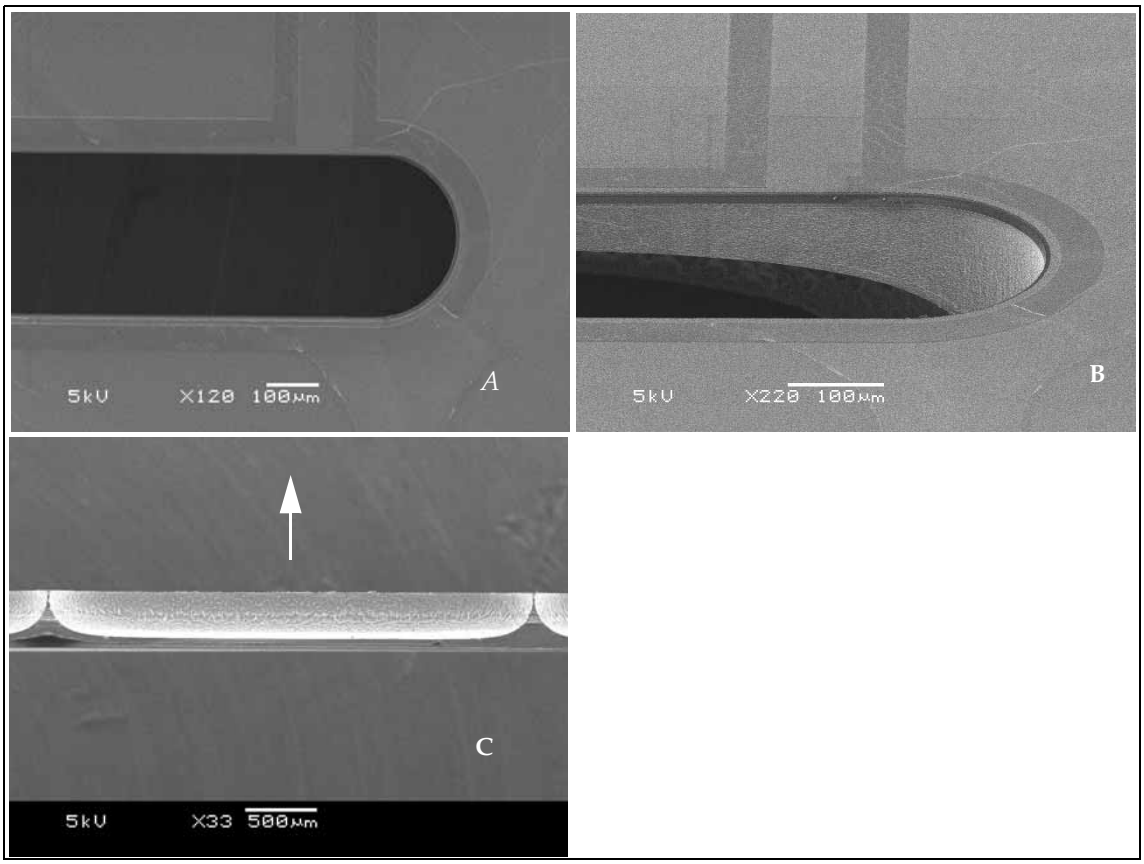

Figure 3.51 Series of SEM pictures that show structural details of the electrode: top view of a conductive path corner *(A)* and tilted view (below); tilted view of a slot corner where the conductive path, the silicon oxide layer, exit slot and the exit slot expansion can be seen *(B)*; electrode axial cross section *(C)* where the ribs are visible; electrode cross-section showing the electrode slot and the electrode slot exit expansion *(D)*. The arrows point in the direction of droplet motion.

The procedure to achieve deep etchings is based on tricking the plasma etcher into believing that instead of etching one wafer it is etching a series of wafers with partial etch depth smaller than the target depth. The summation of partial etch depths then will be equal to the etch depth target. The implementation of this strategy calls for etching as long as possible before either wafer damage or tool interlock activation, and then, turning off the plasma without stopping the gas flow. This way the wafer has the opportunity to cool down both by convection to the gas stream and by using the default helium cooling system present in the wafer chuck. If the cooling gases are reacting it is important to use the same gases present during the plasma-on phase in order to avoid the introduction of foreign species into the plasma

chemistry and therefore have the potential for a variation in the etch profile/uniformity. At a certain time after turning off the plasma, the wafer will reach a temperature similar to the one it had before the etching step; therefore, the plasma can be turned on again for a time span comparable to the one previously used, until the target etch depth is reached. During this cycle the gas flowrates/total pressure can be varied to make sure the plasma is not depleted (the plasma might run out of reacting species if the local exposed area exceeds a certain maximum: in this case the etching becomes species limited), or to increase to some extent the etch anisotropy. The Deep silicon RIE uses a chlorine plasma to pattern the substrate. Figure 3.52 is an SEM of a channel cross section, with an included parameterization of the channel cross-section morphology. In the case of deeper etchings the parameterization shown in Figure 3.52 still holds, as evidenced in Figure 3.53

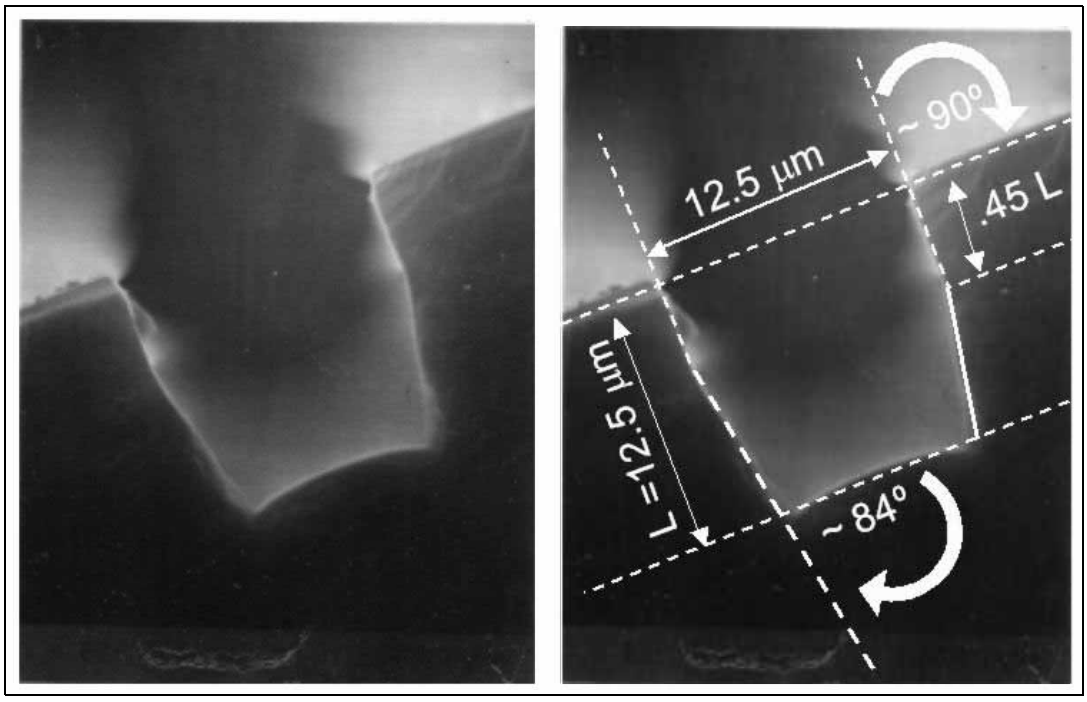

Figure 3.52 SEM picture of the channel cross section. To first order the cross section is a square with a little trenching at the lower corners (left); parameterization of the cross-section, described as an isosceles trapezoid-like cross-section with hydraulic diameter equal to 0.985 L, where L is the size of the upper horizontal boundary, in close agreement with the ideal L value (right).

Cycled deep silicon oxide etching

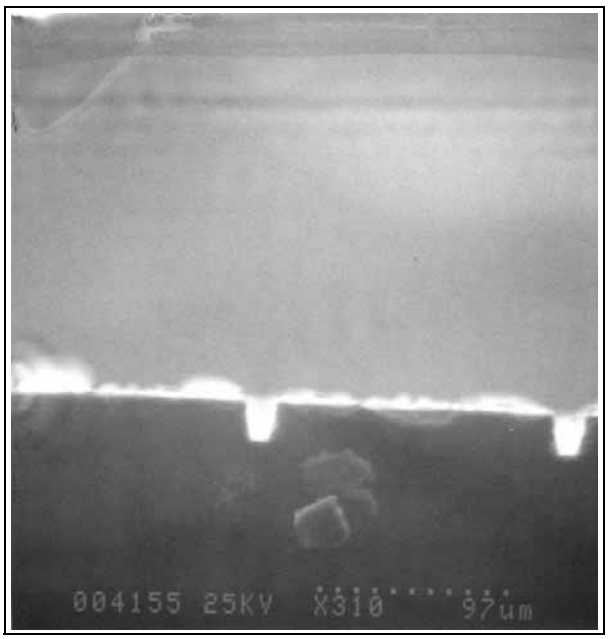

Figure 3.53 SEM picture of a test wafer with a channel formation 25 μm deep, showing the same cross-sectional parametrization of Figure 3.52. The ruler that appears on the picture is 1.1 - 1.2 times larger than in reality (a way to tune the ruler is check the 130 μm channel separation).

The plasma patterning of thick silicon oxide films is implemented with a cycling like the one used for the Deep silicon DRIE. Thick silicon oxide can be patterned with an etching mask made of either resist or LPCVD Poly-Si. At MTL currently there are two dielectric plasma etchers that can be used to pattern silicon oxide films: one of them (*Centura*) accepts LPCVD-Si etching masks because of its awesome selectivity, while the other (*AME 5000)* uses thick resists as etching mask.On both machines it was possible to tune a plasma recipe for silicon oxide patterning. Figure 3.54 and Figure 3.55 are SEM pictures of an 11.3 μm thick silicon oxide film, plasma patterned with different plasma etcher tools. There are tools that can do this kind of etching but they are quite expensive: it is a contribution to have found a way to pattern thick oxide films with tools that were not originally intended for that task. This process is currently used by Kimmerling's group (waveguides) and Schmidt's group (BioMEMS in quartz wafers)

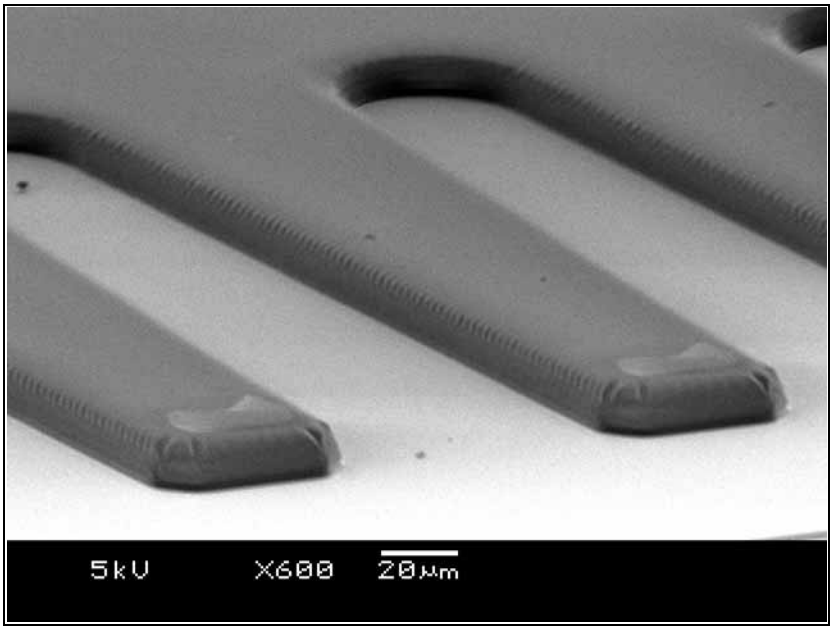

Figure 3.54 SEM picture of a silicon oxide layer 11.3 μm thick patterned with *AME 5000*. Excellent transfer resolution and etching anisotropy can be seen.

Black silicon generation

This plasma etching recipe roughens the silicon surface in a way that scatters most incident light while having etch depths smaller than 0.5 μm. It was developed by running a a battery of tests with a chlorine-based plasma in the free molecular flow regime (low pressure). The black silicon term was coined by the person that first developed the black silicon morphology [Jansen, 1995]. The novelty of the present author's etching recipe comes from the fact that Jansen used a different tool, plasma chemistry (SF_6), low yield for the procedure, while the present recipe has a large repeatability when etching times larger than 1.5 minutes are used. Figure 3.56 are SEM pictures of actual cross hairs patterned with this plasma etching recipe.

Collimated stratified nested masks

This procedure uses a nested mask approach were some of the etching steps are isotropic and some undercut is exerted. In some portion of the plasma etching cycle the mask is hanging from a fully constrained post in a cantilever-like fashion: then the etching mask acts like an umbrella to protect parts of the substrate from the ion flux accelerated by the plasma etcher

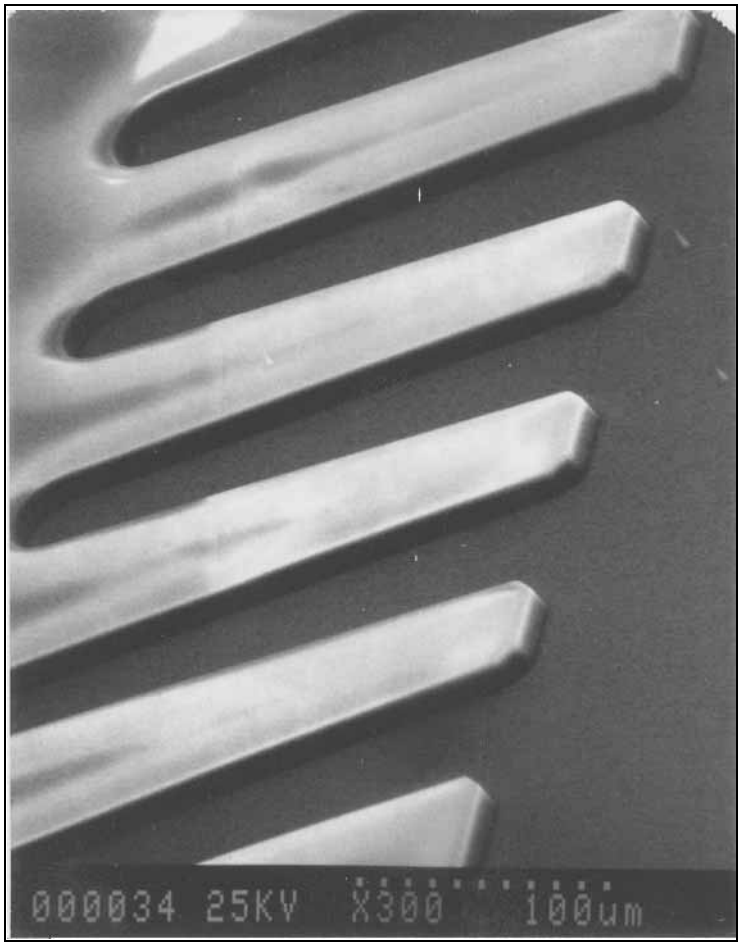

Figure 3.55 SEM picture of a silicon oxide layer 11.3 μm thick, patterned in *Centura*. The etching anisotropy is excellent as well as the resolution of the etching mask (see the sharp corners of the finger-like structures). The actual optical mask that was transferred in this picture contains the emitter-to-emitter separations (an emitter would be below each finger-like silicon oxide structure). Remains of the resist etching mask are still visible on top of the silicon oxide layer (the silicon oxide layer top is glowing due to charge accumulation)

bias power. Because the etching mask can be in cantilever for a good portion of the emitter formation it is also desirable to use silicon oxide film thickness up what is feasible, to augment its stiffness and thus reduce deflection.

This processing strategy is a novelty because it allows one to generate true 3D features using planar layouts such as sharp tip formation, and anisotropic features at the bottom of a previously formed bowl. Also, because it demonstrates that for some DRIE recipes a good

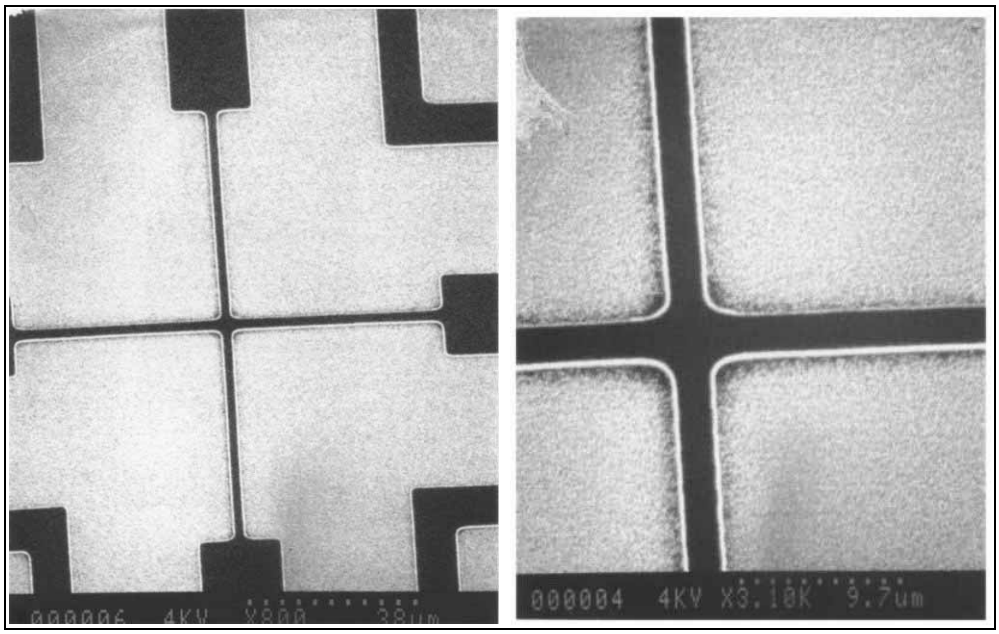

Figure 3.56 SEM picture of a hydraulic substrate cross-hair alignment system *(left)*, zoom of the central part of the cross-hair *(right)*. High contrast, even for electron sources, is achieved. The cross-hair width at its narrowest part is 3 μm .

amount of the anisotropy of DRIE is not given by the passivation cycle and the etch side-walls, but by the bias potential: the etching masks and the bias potential collimate the ion flux through gaps hundreds of microns deep, using the etching mask as a template even if it is not making direct physical contact to the substrate that is being etched. Finally, the nested mask is expanded: one etching mask can be used with different plasma recipes to produce the stratified etching.

Figure 3.57 is a series of SEM pictures that show how a hanging etching mask can be used to pattern features at the bottom of a bowl previously formed with the same etching mask.

Figure 3.58 demonstrates the validity of collimated stratified nested mask concept using the layouts to pattern the Linear Array Spouts: several key features can be appreciated:

- It is possible to pattern the emitter-to-emitter separation with this procedure.
- The roughness of the sidewalls of the anisotropic part of the process can be substantially large.

- Negative taper (the deeper the channel the larger its base) is common, as large as $11°$ with respect to the substrate upper surface normal. This taper is strongly influenced by the etching mask width and orientation: for straight etching windows 100 μm or smaller the negative taper can get as small as $0.5°$.

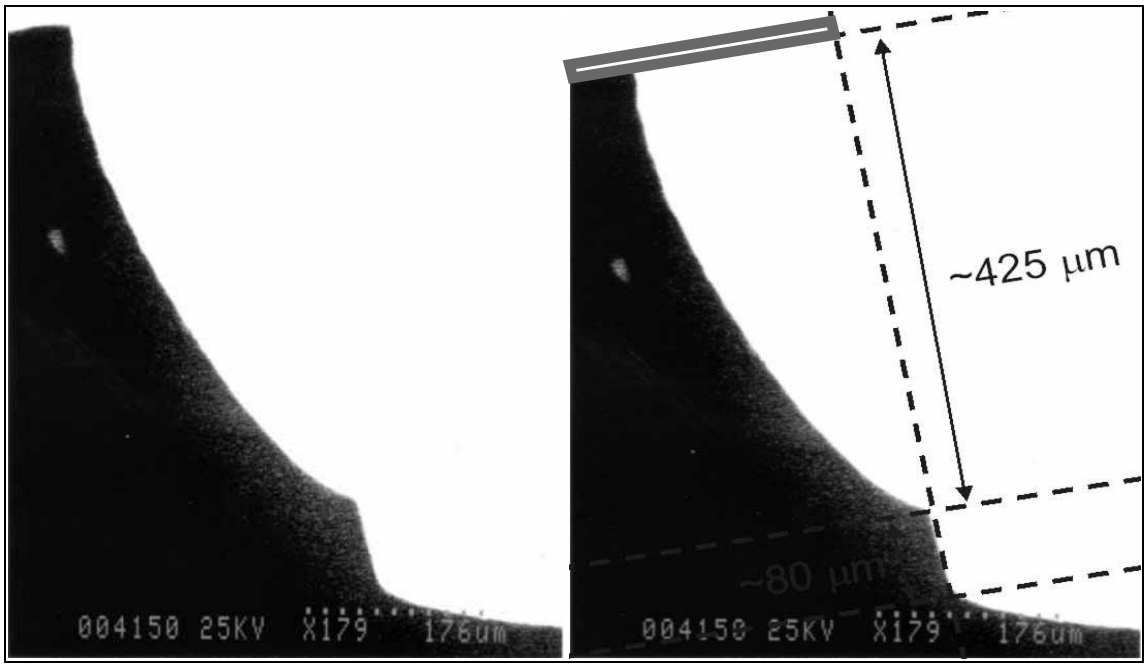

Figure 3.57 Series of SEM pictures an etch profile obtained with a collimated stratified nested mask approach: original etch profile (left) and metrology of the etch profile (right). The verticality of the anisotropic etch and the 2.5V:1H etch profile of SF6-14 is evident. The etching mask position is shown as rectangle on top of the trench.

3.3 Device Results

The feasibility of the Linear Array Concept was demonstrated through a series of tests. The goal was to demonstrate cumulative uniform emission of large arrays of emitters. The results from experimentation are

- The engine follows the model proposed by de la Mora for single Taylor Cone droplet emission [de la Mora, 1994], both as to the steady flowrate versus current dependence, and the minimum flowrate to reach steady operation.
- The impact traces of the droplet fan demonstrate a divergence angle of the order of what is predicted by models [Lozano, 2003]. It also demonstrates that the droplet fan does not have a thermalized tail, but has instead sharp boundaries.

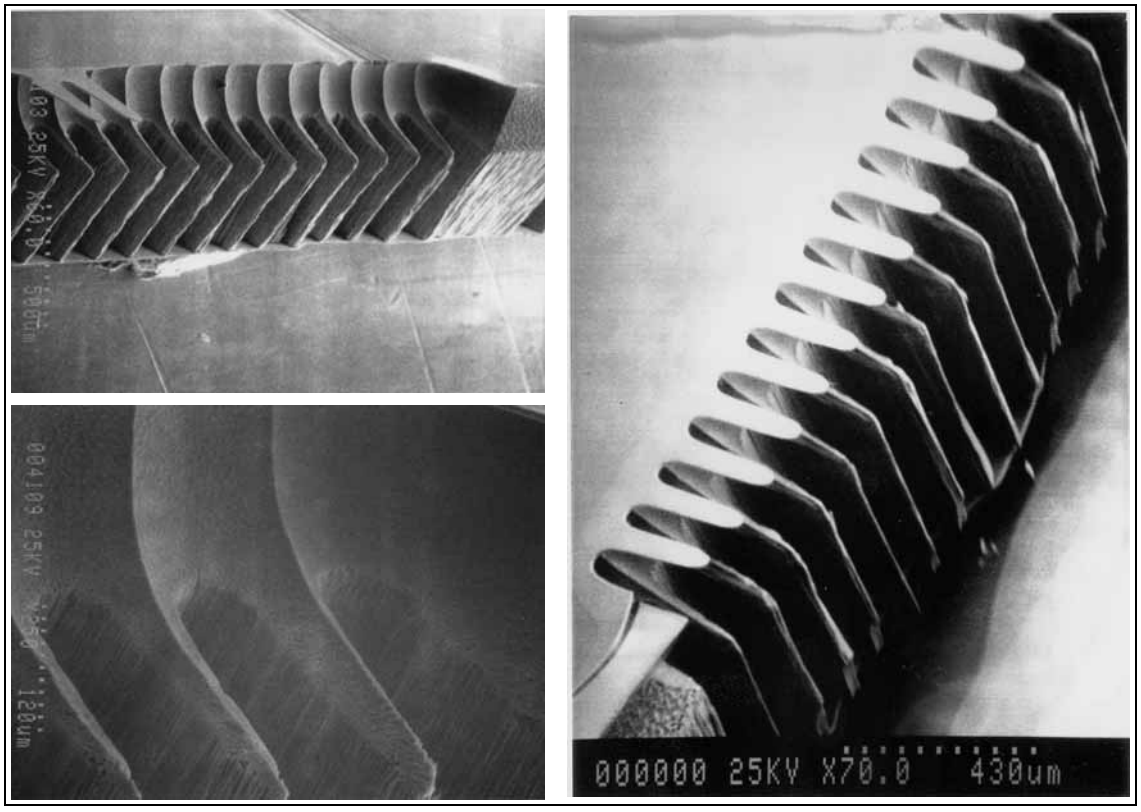

Figure 3.58 SEM pictures of a test wafer with the spouts patterned using a collimated nested mask process: the hanging etching masks still present (upper left), the etching mask was removed with low pressure nitrogen (right) showing no damage to the previously formed spouts, and detail of the upper lip morphology (lower left). The roughness of the emitter-to-emitter etching separations is striking compared to the smooth of the emitter lips.

- Several complete adjacent manifold sets were demonstrated to work.
- All the subsystems of the engine were demonstrated to work well, with the exception of the spout system. The hydraulic system and the electrical system work to satisfaction. The spouts enhance the electric field enough to turn on the engine, but depending on the doping level of the propellant they do not address well wettability issues.

It was not possible to show a clean trace of all the emitters because in order to reach stable operation we needed to use highly doped formamide. This produced wettability problems that generated propellant spilling and thus transient breakdown events. The author believes this does not invalidates the concept because of the operation of the independent modular unit (a set of emitters fed by the same manifold) was achieved, and the wettability issue can be corrected by applying some coating on the external surface of the spouts, thus cleanly defin-

ing the wetting fronts in the spouts. If the engine needs to change its wettability inside then a reaching gas can flow through. This process can take some time to tune but it looks feasible to implement.

A full engine with the electrodes mounted has not fired yet, because of the testing philosophy that was implemented: to tune the subsystems to eventually test the whole engine.

Finally, the neutralization problem was not tackled at all. It is expected that using the engine in bipolar mode, or using a hot cathode will solve the neutralization issue in a straightforward way. The way the engine was tested did not require a neutralizer because the droplets where part of a closed circuit. Also, space charge effects were minimal at the current levels attained.

3.3.1 Testing facility

The facility was designed to help us verify a number of issues, such as

- A safe emitter-to-electrode separation.
- Spatial uniformity of the engine emission.
- Emitted current versus flowrate curves to characterize the engine and show its operation in the single Taylor Cone droplet regime.
- Potential hydraulic tests like hydraulic impedance characterization (if needed).

The testing facility is composed of four parts:

- **An external electrode.**
- **A 1-DOF stage to set the electrode-to-emitter separation.** The Micrometric screw in the stage displaces about 300 μm per complete turn and it has a precision of about 10 μm (a division mark of the dial).
- **A mounting base.** This piece allows some visual inspection of the engine while inside the vacuum chamber.
- **A propellant supply system.** This system is somewhat inspired by the one used by Dr. Lozano in his Ph.D. studies [Lozano, 2003] which in turn is similar to the one Gamero used for his experimentation [Gamero, 2001]. The system uses mainly ultra-Torr unions that allow to easily modify the propellant supply. The system is composed of:
    - A nitrogen tank

- A mechanical pump
- A propellant tank
- A supply line.

In this system a decoupled two-flow pattern of propellant and gas is set. On one hand the nitrogen tank delivers a gas flowrate driven by a pressure difference between the nitrogen tank exit P_{gas} and the propellant tank P_{po}: this flowrate is equal to the flowrate drawn by the mechanical pump via the pressure difference between the propellant tank pressure and the pressure at the pump inlet P_{pump}. Once the propellant tank pressure is set the engine will receive propellant at the rate set by the pressure difference between the propellant tank and the vacuum chamber pressure (this latter pressure is to first order 0). The nitrogen and propellant flows are considered laminar. The pressure losses at the valves (when fully open) and connections are negligible because they scale with the dynamic head of the flows. Each channel is described by a hydraulic diameter and an axial length as shown in Figure 3.59. It can be shown from first principles assuming ideal gas behavior, constant temperature and average density for the nitrogen flow, that the propellant tank pressure can be approximated as

$$P_{po} = \sqrt{\frac{\left[\frac{D^4_{gas}}{L_{gas}} \cdot \left(\frac{L_{interm}}{D^4_{interm}} + \frac{L_{pump}}{D^4_{pump}}\right)\right]}{1 + \left[\frac{D^4_{gas}}{L_{gas}} \cdot \left(\frac{L_{interm}}{D^4_{interm}} + \frac{L_{pump}}{D^4_{pump}}\right)\right]}} \cdot P_{gas} \tag{3.37}$$

And for a fully developed incompressible propellant flow the pressure at the engine propellant inlet P_o is

$$P_o = \frac{P_{po} \cdot D_{inlet}^4}{L_{inlet} \cdot \left[343.66 \frac{L_c^4}{L} + \frac{D_{inlet}^4}{L_{inlet}}\right]} \tag{3.38}$$

Table 3.5 summarizes the actual values of the parameters of the propellant supply and the Linear Colloid Thruster Array hydraulic impedance.

- **Vacuum Chamber.** The vacuum chamber that was used in the series of experiments has an inner diameter about 1.5 m, a length of 1.6 m, and it can reach ultimate vacuum levels (no flow) down to 1×10^{-8} Torr, with a pumping speed of 7000 liters/sec. for Xenon. The chamber pressure is monitored using two gauges: a thermocouple gauge for pressure higher than 1×10^{-3} Torr. and a cold cathode gauge for lower pressures, up to 1×10^{-9} Torr.

TABLE 3.5 Hydraulic diameter and axial length for the different channels part of the propellant supply system of the Linear Colloid Thruster Array.

Propellant Supply Part	Hydraulic Diameter (μm)	Axial Length (cm)
Gas channel	63.5	100
Interm. channel	381	20
Pump Channel	3680	100
Inlet channel	500	200
Engine	12	1.5

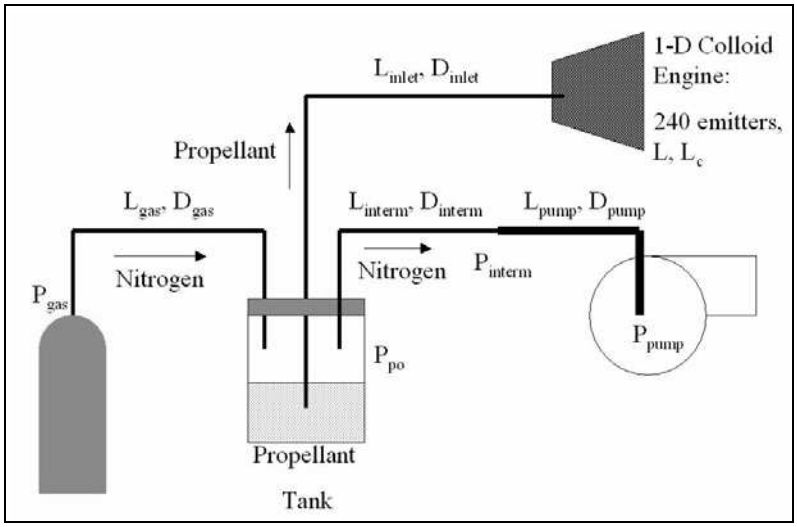

Figure 3.59 Schematic of the propellant supply system, part of the Linear Colloid Thruster Array Testing Facility. All channels are modeled as hydraulic impedances characterized by a hydraulic diameter and an axial length.

Figure 3.60 is a picture of the engine after receiving the propellant connection and with the testing facility fully assembled.Figure 3.61 shows a typical view of the engine while inside the vacuum chamber . Once the chamber pressure dropped down to 1×10^{-8} Torr the engine was energized and measurements were carried out of flowrate via pressure readings / bubble tracking, and of current collected by the electrode and generated by the power supply. During the tests the pressure inside the chamber was in the 1×10^{-6} Torr to 5×10^{-6} Torr range.

Figure 3.62 shows the final version of testing facility that was used to test the Linear Array. A previous version of the testing facility was designed in cooperation of Jorge Carretero, a Ph.D.

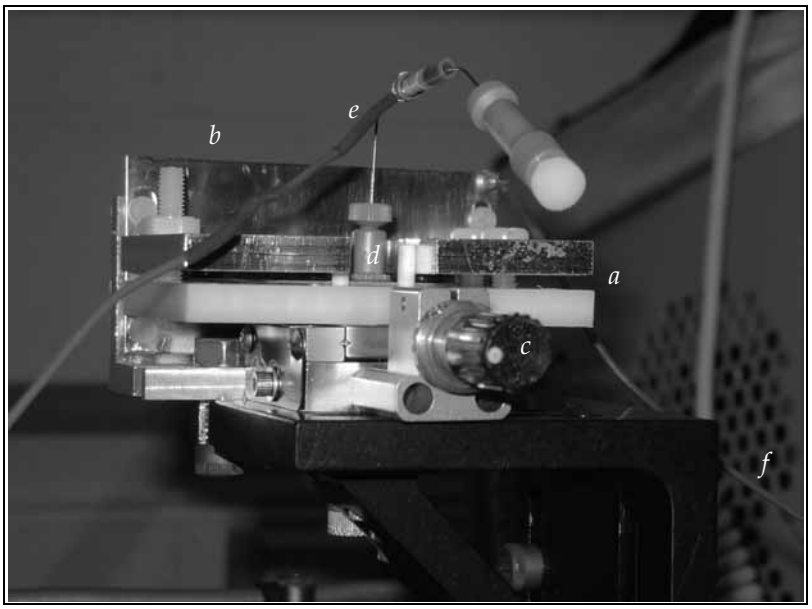

Figure 3.60 Linear Colloid Thruster Array with the fully assembled testing gear. The engine is inside the gap between two plates *(a)*; the engine is facing an external electrode *(b)* that is separated from the engine spouts using a micrometric screws *(c)*; the engine has a nanoport *(d)* connected to a metallic tube that receives an electrical connection *(e)*. The engine receives a bias voltage using the nanoport connection and a cable *(f)* connected to the electrode.

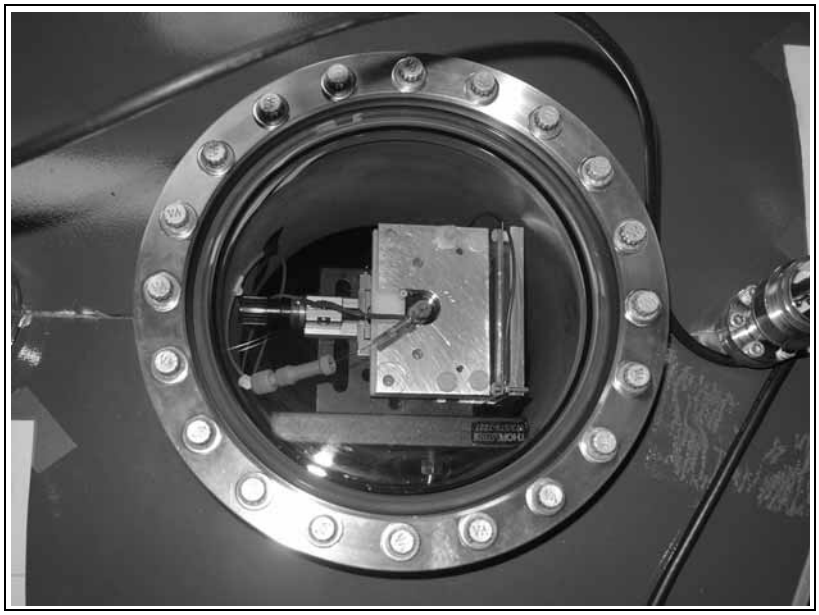

Figure 3.61 A view of a Linear Colloid Thruster Array inside the vacuum chamber.

Candidate in the Department of Mechanical Engineering, who built /conditioned the first version of the facility [Velásquez, 2003-2].

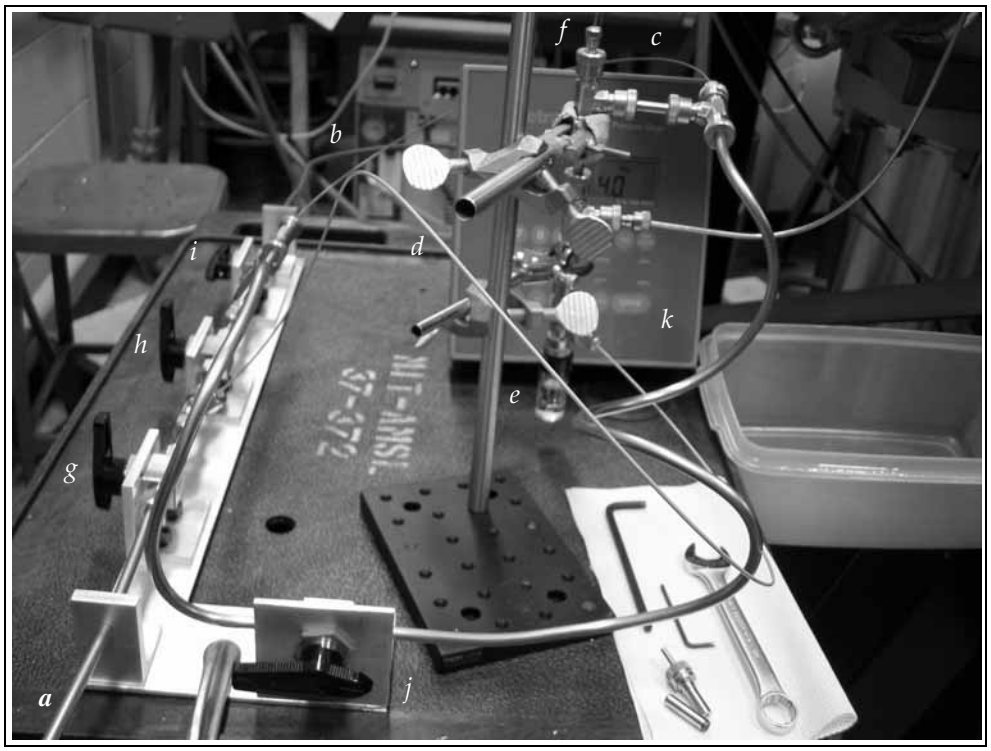

Figure 3.62 Picture of the propellant supply system for the Linear Colloid Thruster Array. The system has a pipe connected to a pressurized nitrogen tank *(a)* and a pipe that connects to the inlet of a roughing pump *(b)*; a set of two large hydraulic impedances *(c, d)* act as a pressure divider to set a certain pressure inside the propellant tank *(e)*. The propellant is then fed into the engine using a transparent pipe *(f)*. The system has a valve to isolate the tank from the rest of the system *(g)*, a valve to purge the high pressure line *(h)*, a valve to isolate the roughing pump from the rest of the system *(i)* and a bypass to outgass the propellant *(j)*. The pressure at the propellant tank is measured with a diaphragm pressure sensor *(k)*.

3.3.2 Results and discussion

Electrode characterization

The electrode system was validated through a series of three kinds of tests. Resistance values were sound compared to expected values. No test was carried out with propellant presence due to time constraints in the shared equipment. In the event the result of this test would be unsuccessful, this would not imply that the proposed electrode system is not feasible: a selec-

tion of a larger emitter-to-extractor separation and/or the use of an insulating material as electrode substrate would likely correct the problem.

The electrode resistance was measured with a probe station inside MTL. The resistance was found to fall in the range of 13.3 - 4.8 $k\Omega$, depending on the electrode path width, in agreement with expected values. An applied voltage of 1.5 KV between the silicon substrate and the electrode metallization did not generate current leak.The resistance value is adequate for our purposes because it would imply a small voltage change in the event some droplets hit the electrode, probably being at most a fraction of a μA (the total emitted current seldom exceeds ~ 20 μA); this current sets a voltage drop negligible compared to the extraction voltage (~ 2000 V).

A test of the electrodes assembled to a structure with exactly the same external features of a Linear Colloid Thruster Array was carried out under vacuum (1×10^{-7} Torr). The test was done in the absence of propellant. The decoy engine had only less than 5% of the silicon oxide film used in the real engine. Therefore the results are a lower bound of the performance of the electrode with the real engine.

The testing facility for this electrode test is composed of a vacuum pump, a Fluke 199 Scope Meter, a voltage divider (to avoid large current levels through the system, and be able to measure the current passing through the system by measuring the voltage drop on one of the resistors part of the voltage divider) and a special engine handler. The engine handler is made of PVC, a low-degassing material [Varian, 2004].

An schematic of the electrical circuit is shown in Figure 3.63. A series of pictures of the engine handler with the engine installed can be seen in Figure 3.64. The voltage divider is composed of a high-voltage resistor of 200 $M\Omega$ and a 100 $k\Omega$. The Fluke Scopemeter is connected in parallel to the smaller resistor of the voltage divider while the high-voltage resistor is held by the engine handler inside the vacuum chamber. If the extractor were to short to the engine then the voltage should be divided between the two resistors to be measurable by the Fluke equipment. If the voltage is in the order of thousands of volts the voltage across the

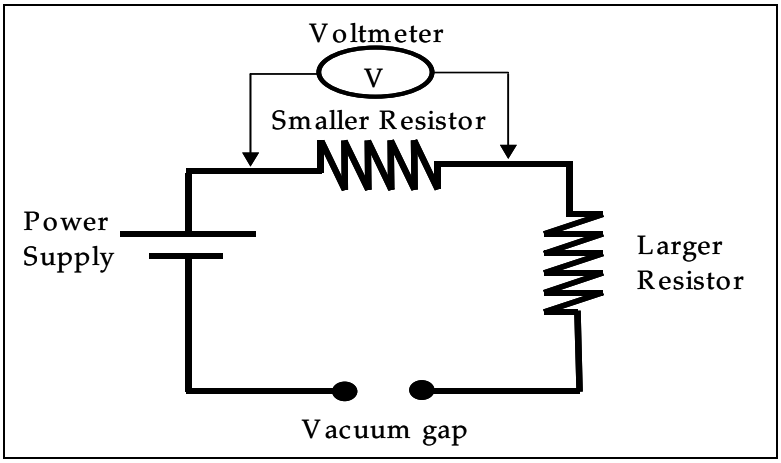

Figure 3.63 Schematic of the electrical system used to test the electrodes.

smaller resistor should be in the order of volts, above the noise level. The testing setup is shown in Figure 3.65.

Three tests were done:

- **Noise Level**: This test was done without energizing the engine in order to determine experimentally the kind of noise that is present in the experimental setup. Figure 3.66 is a picture of the screen of the Fluke equipment after almost one hour and twenty-one minutes of recording. Noise voltage levels of the order of millivolts where measured. The possible source of this noise is the induction of currents in the voltage divider due to electromagnetic waves.
- **Progressive test:** The engine was energized from 0 volts up to 2500 volts in steps of 500 volts. The step time was 15 minutes in each case. No measured signal in the Fluke equipment arguably related to breakdown of the gap was recorded. Sometimes it was found that the setup was making a short circuit presumably from zero voltage: surface contamination, wrong assembly, and non-ideal electrode yield are pointed out as the potential sources of this behavior.
- **Extended time test:** A bias voltage of 2.5 kV was applied between the Linear Array Hydraulics and the electrode metallization. This is more than the voltage needed to activate the engine in its half-sharpened emitter version. Figure 3.67 is a picture of the Fluke equipment screen after almost twelve hours of testing. If the gap would have made broken down, then a 1.25 volt constant reading would have been recorded. What was recorded is a zero-voltage reading, except for a few spikes that randomly occur, measuring at most 0.15 volts.

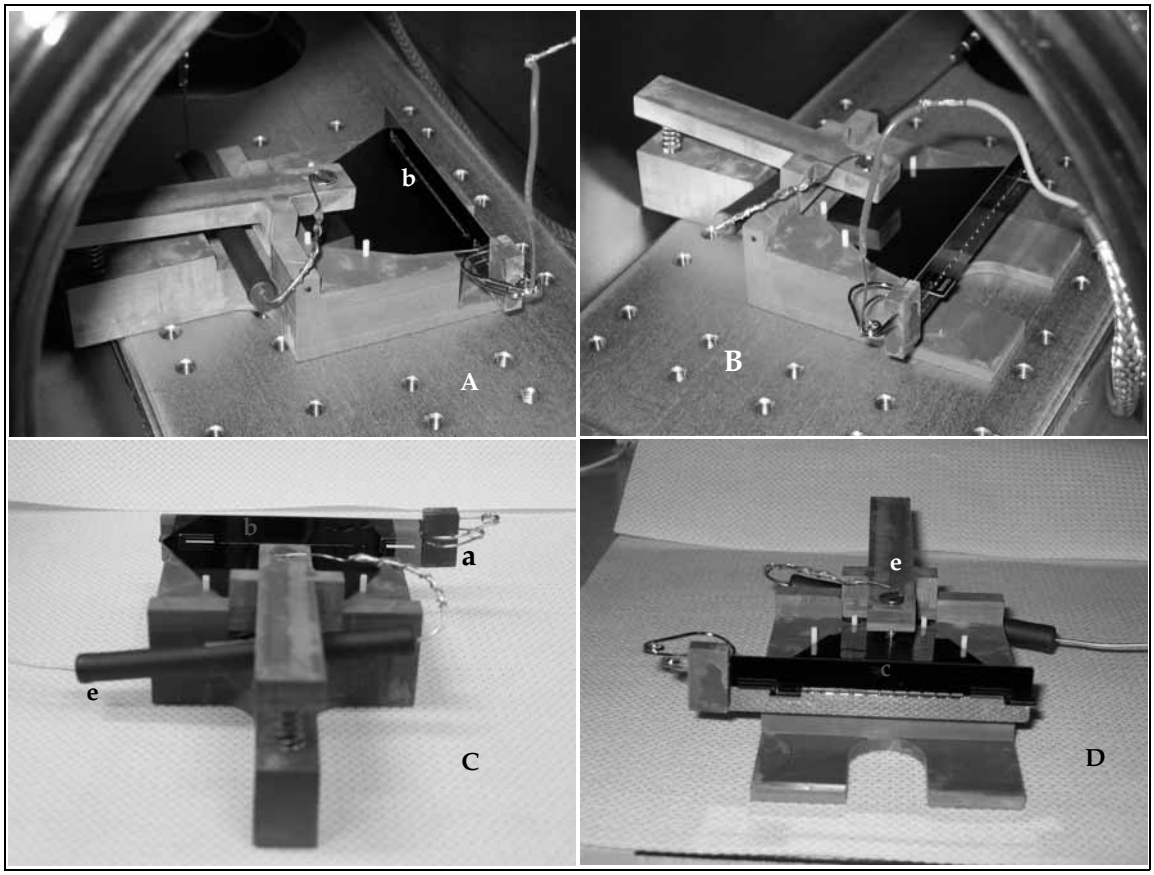

Figure 3.64 Pictures of the engine handler with an engine decoy assembled with an extractor electrode: top view from the back (**A**), top view from the front (**B**), detail of the electrode slot (**C**), front view (**D**). The engine handler includes a claw-like appendix (**a**) that allows to energize the electrode from both electrode pads (in case the electrode metal path is not continuous). The small separation between the engine and the electrode (**b**), the slot widening at the electrode front (**c**), and the high-voltage resistor used in testing (**d**) are visible in these pictures. The engine is energized by using the claw-like appendix and the engine body. The engine body is connected electrically with a probe that compresses the engine (**e**).

Engine characterization

The preliminary validation of the Linear Colloid Thruster concept was successfully carried out, with the notable exception of the spout performance. In other words the experimentation generated enough data to preliminarily validate cumulative uniformity, steady emission, and fan divergence. Several complete manifolds sets (the modular unit of the engine) where shown to work as expected from reduced order models. The spouts were showing wettability problems that created arcing events in the engine while operating when the propellant con-

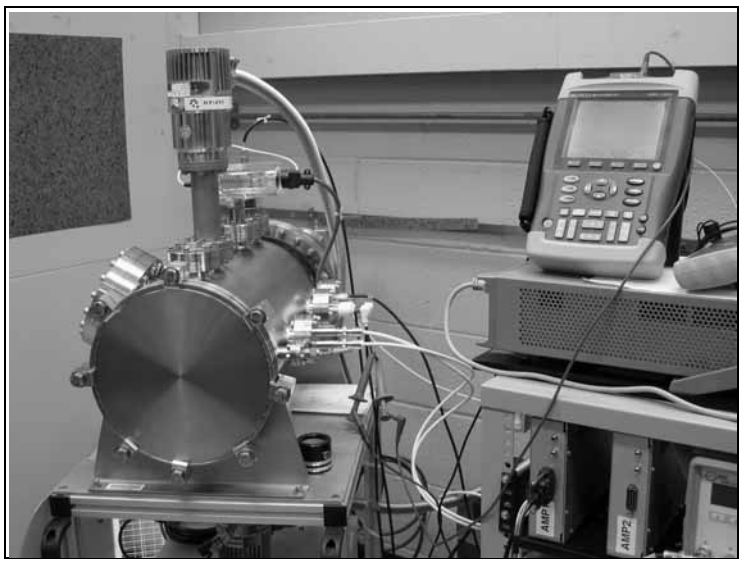

Figure 3.65 Test setup to characterize the electrodes.

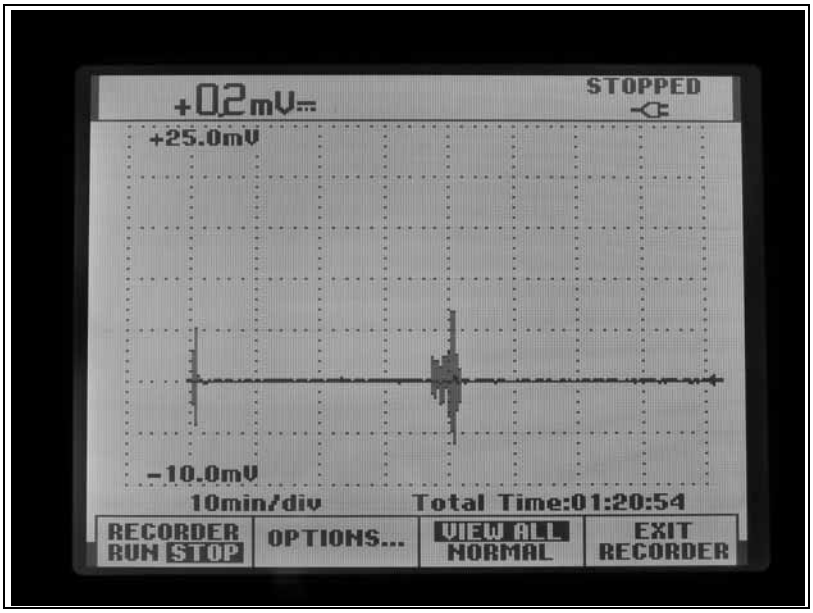

Figure 3.66 Picture of the Fluke Scopemeter screen after the noise level test. A small measurement of a random signal with maximum amplitude on the order of tens of millivolts is present.

ductivity was large. Finally, experimental verification of the range of validity of the de la Mora's equations was obtained.

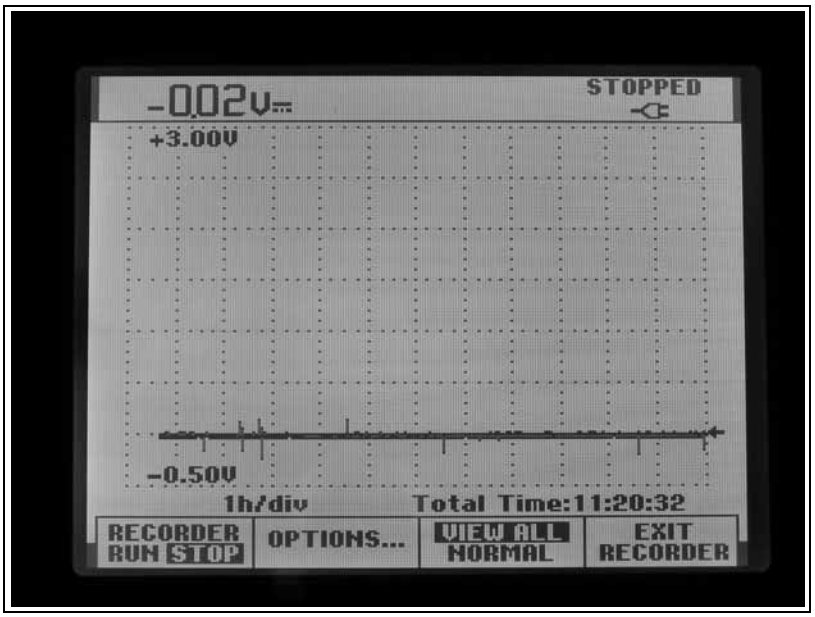

Figure 3.67 Picture of the Fluke Scopemeter after almost twelve hours of continuous testing.

A total of five experiments were done with different engine spouts, external electrodes and propellant electrical conductivities. The propellant conductivities were determined using a Jenway conductivity meter 4320. The experimental results of the engine can be summarized as:

Electrical control

The concept of electrical control proposed in this Ph.D. dissertation (no flow should be produced unless electrically assisted) was experimentally verified by sequentially turning on and off the power supply while having at the engine plenum less pressure than what the meniscus can resist. This was done for two engines, using formamide with an electrical conductivity of 0.007 Si/m. No leak was detected by optical inspection of the test stage or the engine. SEM inspection of the engines around the spouts did not show propellant traces way from the spout exits.

When propellants with electrical conductivities equal to 2.9 Si/m and 0.612 Si/m were used, then leaks were detected by visual inspection. The spills were near the spouts. In all cases after

cleaning the engine exterior and leaving the engines inside sealed beakers for days it was verified that the leak was not a product of bad wafer bonding: there is strong evidence that the propellant came out from the engine only through the spouts, because of their wettability problems. These wettability problems will be further discussed in a following section of this chapter.

Hydraulics integrity:

In all cases the good sealing of the hydraulic wafer pair shown in SEM pictures was corroborated both by SEM and visual inspection. The hydraulic system does not leak (except at the spouts in some cases when pressurized), fills-in well from a single propellant inlet source (validating the plenum / manifold / channel architecture) and in general has a performance that matches expectations when the propellant wets well the engine interior. The plasma retrieval of the engines from the substrate to avoid device die-sawing proved to be a good fabrication decision.

Starting voltage

When using engines with un-sharpened or half-sharpened emitters the experimental activation voltages fell midway between the predictions from the finite element analysis and the predicted values from equations 3.30 and 3.32. This is expected because of four key reasons:

- The electric field of any emitter has some shadowing due to the presence of the adjacent emitters, as shown by the finite element analysis.
- The criterion used to interpret the finite element simulations was to visually sample the minimum electric field at the spout exit. The criterion was adopted because even though for an instability to develop only a local value is needed electric field values at the boundary of the solution domain are prone to numerical error due to meshing / geometry idealization.
- Presence of non-idealitites in the real spouts: surface roughness, sharp corners.
- Equation 3.30 is an asymptotic expression for emitter diameters-to-electrode separation ratios substantially small.

When using emitters with some sharpening (half-sharpened, fully sharpened) the activation voltages showed good agreement with the values predicted by the finite element analysis the predicted value using equation 3.32, using a L_c equal to 12 μm and a L_c^o equal to 40 μm. The experimental values were closer to the equations than to the finite element results.

From the loss considerations done in the beginning of the chapter the estimated voltage drop across the engine in all experiments was very small compared to the activation voltages.

Uniformity validation

Cumulative uniform emission was demonstrated from the droplet impacts on the external electrode used to activate the engine:

- A test was run using Li-Cl doped formamide with an electrical conductivity equal to 0.007 Si/m., using an engine with unsharpened spouts, 500 μm of separation between the electrode and the spouts. Formamide of this conductivity wets the silicon / silicon oxide very well. The propellant inlet tube had an ID equal to 250 μm, and the activation voltage was set at 3500 V. The engine emitted unsteadily, showing frequent peaks of 1 μA, but also zero current values were registered. The engine emitted for about 30 minutes. The droplet fan impacts on the electrode are shown in Figure 3.68.

  Cumulative *uniform emission* can be seen from the pattern left although it is not clear whether it was uniform at any given instant. It is *unsteady* because the flowrate provided was not enough to reach the flowrate range that can generate stable Taylor Cones in single jet emission. The minimum flowrate that a Taylor Cone can emit in a steady way is given by

$$Q_{min} = \eta_{min}^2 \cdot \frac{\gamma \cdot \varepsilon \cdot \varepsilon_o}{\rho \cdot K} \tag{3.39}$$

  where γ is the surface tension, ε is the relative electrical permittivity, ε_o is the free-space electrical permittivity, ρ is the fluid density and K is the electrical conductivity. η_{min} is the minimum value η can get in steady operation (~1). When η is less than unity the inertial forces become smaller than the surface tension forces forcing the jet to collapse: the cone emits in a discrete pattern, expelling chunks of fluid from the cone apex. For the small conductivity propellant used, this minimum flow is equal to $7.32 \times 10^{-12}\ m^3/\text{sec.}$ per emitter, or a total of $1.76 \times 10^{-9}\ m^3/\text{sec.}$ for the whole engine (240 spouts). Figure 3.69 is a plot of the flowrate that the testing facility can deliver with a propellant inlet tube with an ID equal to 250 μm.

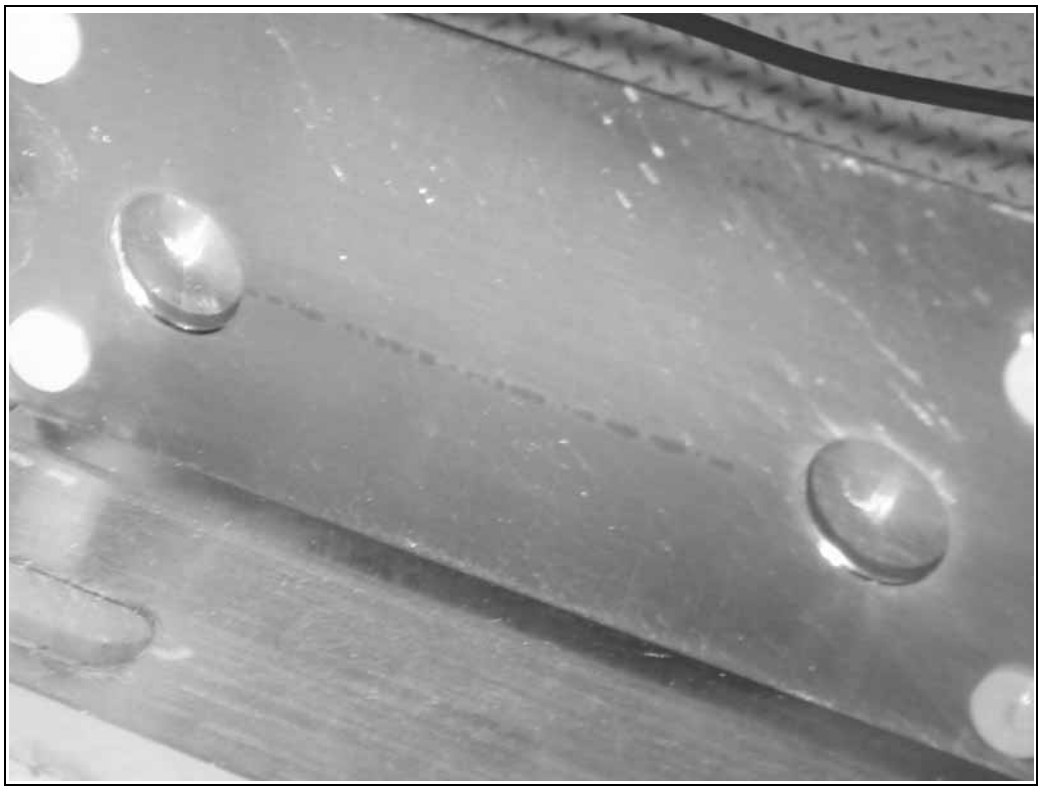

Figure 3.68 Picture of the external electrode after a test with lowly doped formamide using an engine with unsharpened spouts was carried out.

It is clear that we are over one order of magnitude below what we need to supply for stable operation (we can deliver up to $7.2 \times 10^{-11}\ m^3/\text{sec.}$ with the testing facility in its original configuration).The η that was obtained was about 0.2.

- A test using an engine with half-sharpened spouts was carried out. The test used the same propellant conductivity and electrode separation of the previous test, but the propellant inlet tube had an ID equal to 500 μm. The engine activation voltage was set to 2000 V. The engine emitted unsteady between 1 and 2 μA for about 60 minutes, while a flow rate of 75 nl/s ($7.5 \times 10^{-11}\ m^3/\text{sec.}$) was supplied to the engine. During the test the current was seen to fluctuate but no zero-current was measured. Therefore, it could be argued that at any time a number of emitters were on in an unsteady way. The droplet fan impacts on the electrode are shown in Figure 3.70.

  The trace is continuous, basically uniform suggesting that most of the emitters were operational and emitted about the same flow for long times. The trace has a little widening towards the midpoint of the electrode. The η that was obtained was about the same compared to the previous test, smaller than needed to reach steady operation.

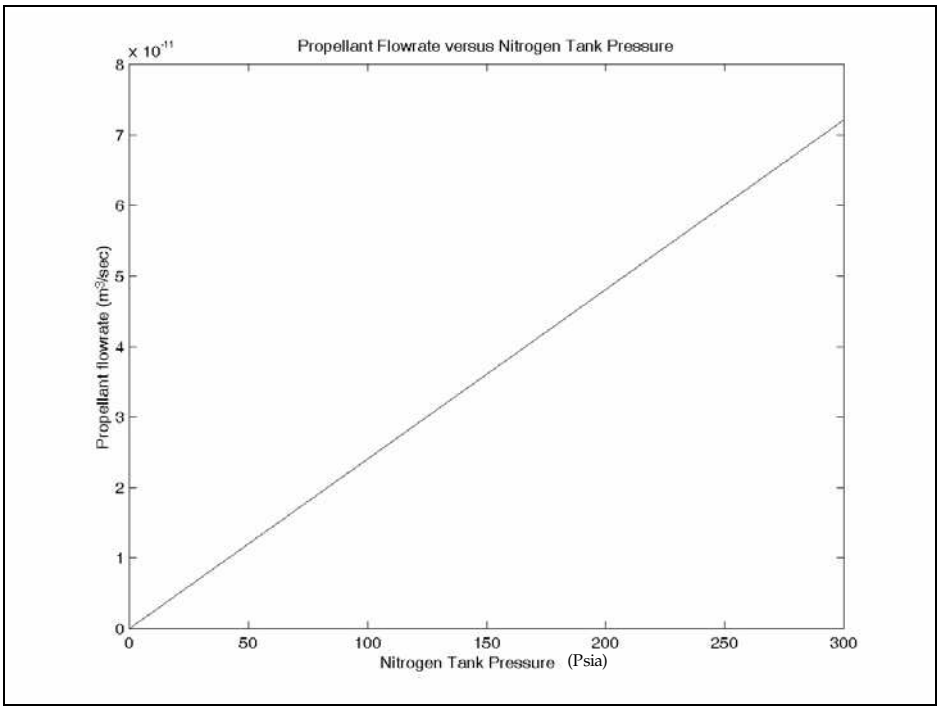

Figure 3.69 Propellant flowrate versus Nitrogen tank pressure

Steady-state validation

Two tests using doped formamide with an electrical conductivity equal to 2.9 Si/m. experimentally demonstrated cumulative uniform - steady operation for several complete manifold sets (a manifold set is the modular engine unit). A test made with formamide with an electrical conductivity equal to 2.9 Si/m, and one with 0.612 Si/m., showed a current versus flowrate behavior in agreement with the de la Mora equations, applied for steady single cone droplet emission mode.

The current emitted by a Taylor Cone in droplet emission mode is [de la Mora, 1994]

$$I = f(\varepsilon) \cdot \sqrt{\frac{\gamma \cdot K \cdot Q}{\varepsilon}} \tag{3.40}$$

If a total flowrate Q_{tot} is uniformly distributed into n equal emitters, then one can easily show that the total current I_{tot} emitted by the set of emitters is

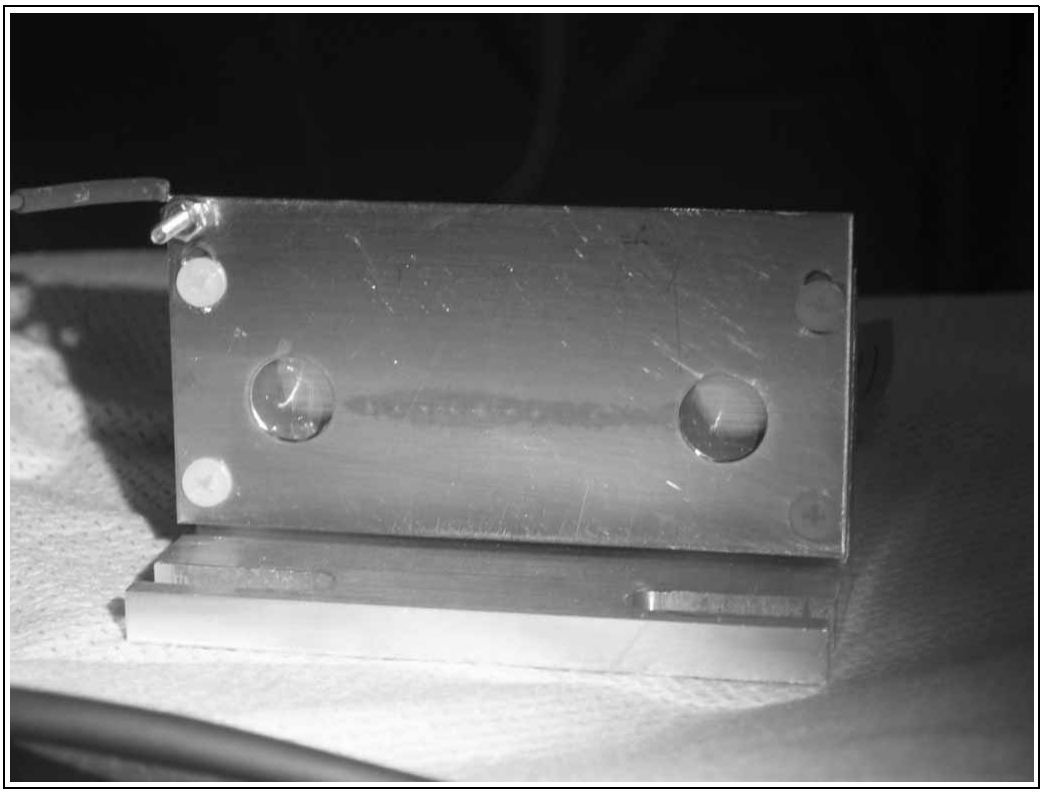

Figure 3.70 Picture of the external electrode used to test a Linear Colloid Thruster Array. Cumulative uniform emission is demonstrated from this picture. Some sharp marks are visible as well in the middle line of the propellant impact trace, probably from the manifold separators when aligning the engine.

$$I_{tot} = \sqrt{n} \cdot f(\varepsilon) \cdot \left(\frac{K \cdot \gamma \cdot Q_{tot}}{\varepsilon} \right)^{1/2} \tag{3.41}$$

The correction factor based on the number of emitters was verified in this work, as well as in the literature [Tang, 2001]. The experimental results on steady emission can be summarized in the following points:

- Two tests were carried out using formamide with K= 2.9 Si/m, electrode-to-emitter separation set at 500 μm, an engine with half-sharpened spouts and an activation voltage equal to 2000 V. While performing the test, breakdown transients occurred in some of the manifolds. Because of the continuous arcing problems only two data points were collected. SEM / optical microscope pictures of some of the complete manifold sets that were not destroyed by arcing are shown in Figure 3.71 while SEM pictures of these impacts are shown in Figure 3.72. In these pictures the emission is not only uniform emitter-to-emitter, but also in time, as judged from the size of the electrode impacts.

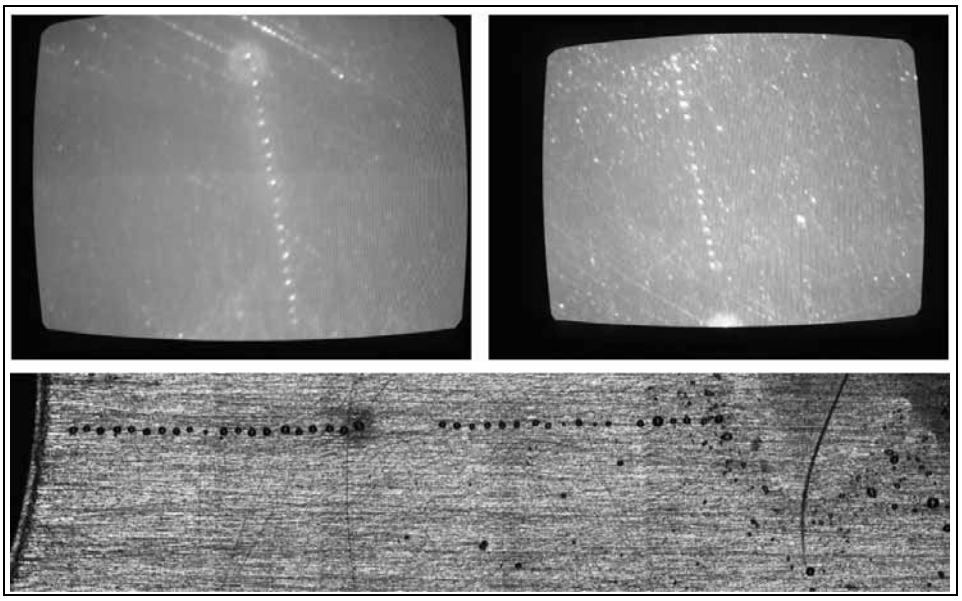

Figure 3.71 Set of optical microscope pictures of the impacts of emitters from complete manifolds surrounded by arcing. The sharp impacts demonstrated the uniform spray distribution as well as emitter-to-emitter uniformity. Pictures with the optical microscope in-site the vacuum chamber facility *(upper left, upper right)*; optical microscope collage obtained days later with the microscope of the Laboratory of Vacuum Microelectronics *(below)*.

These pictures demonstrate that stable cones were formed, current versus flowrate was measured but only a few manifolds (4 out of 12) kept their electrode impact traces free of arcing events.

- A test made with an engine with half-sharpened spouts, K=2.9 Si/m, activation voltage equal to 2000 V for an electrode separation equal to 500 mm, gave a current versus flowrate plot shown in Figure 3.73 If the semi-empirical equation of de la Mora is used with an $f(\varepsilon)$ equal to 21 then the experimental points show good agreement with the theoretical model.
- A test with half sharpened spouts, K = 0.612 Si/m, 3.5 kV of voltage activation and electrode separation of 1.2 mm gave a current versus flowrate plot shown in Figure 3.74. The error bar of the current comes from the minimum unit of the Ammeter dial, while the error bar of the flowrate measurements come form an estimation using Gauss' error propagation law on bubble measurements. If the semi-empirical equation of de la Mora is used with an $f(\varepsilon)$ equal to 21 then the experimental points show good agreement with the theoretical model.

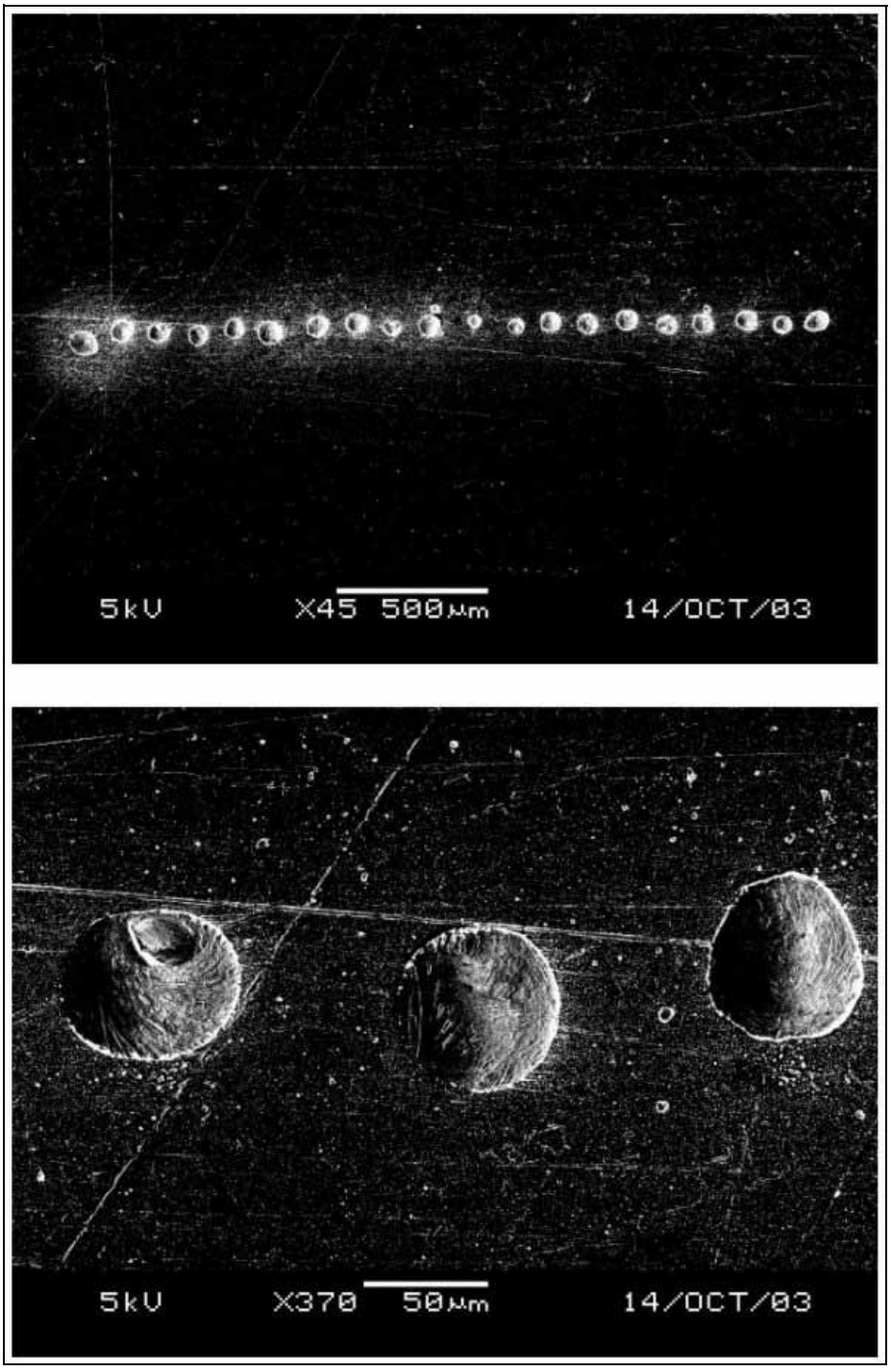

Figure 3.72 Set of SEM pictures of the impacts of emitters from complete manifolds (*above*) and detail of electrode impact (*below*). The sharp impacts demonstrate the uniform spray distribution as well as emitter-to-emitter uniformity. It is also important to point out that the emitter jets are *aligned*, that is the emitters fall in the same straight line. This validates the emitter uniform morphology.

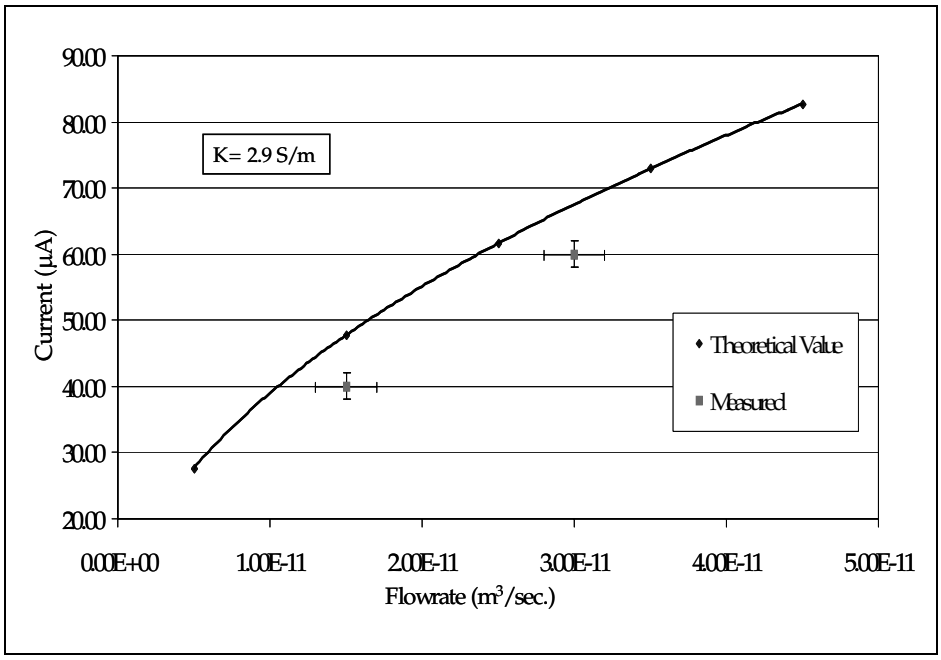

Figure 3.73 Experimental data points versus the theoretical model. The experimental emitted current is smaller than what the model predicts. This can be explained as scattering from high pressure surrounding the emitters and damage of several emitters because of arcing.

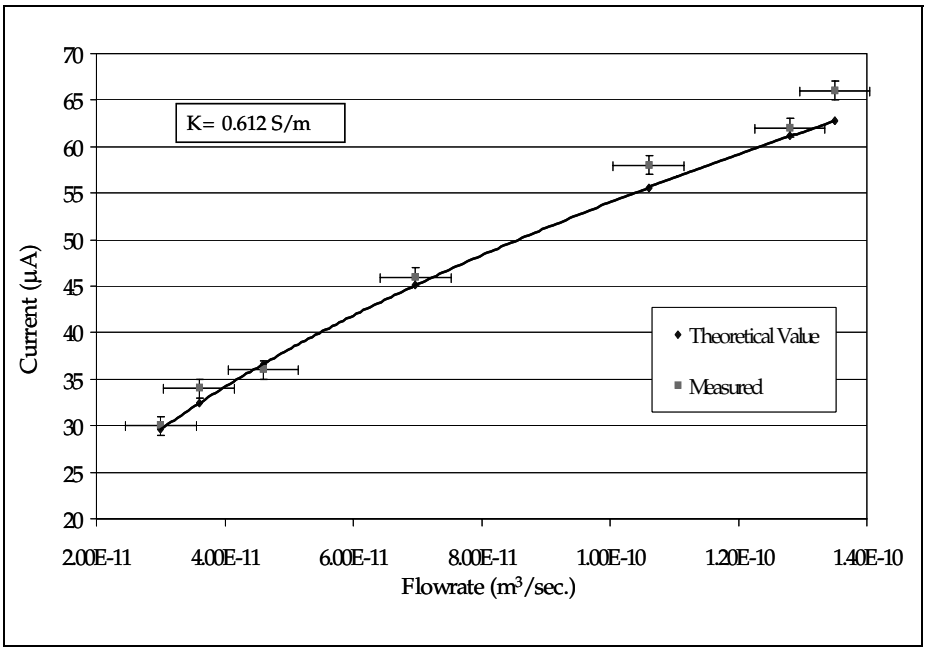

Figure 3.74 Experimental data points versus the theoretical model. The experimental data shows good agreement with theoretical model.

Divergence angle

For tests where steady emission was obtained the divergence angle is of the same magnitude (smaller) than what predicted by the reduced-order model, giving experimental corroboration of the uniform charge density inside the droplet fan and the non-thermalized ionization nature of the droplets. For cases of unsteady emission the divergence angle is substantially larger than what predicted by the reduced-order model, probably because of propellant transport on the electrode surface due to larger flowrates and smaller doping concentrations.

The model to estimate the fan divergence comes from the Ph.D dissertation of Dr. Lozano [Lozano, 2003]. The model predicts uniform charge density of a droplet fan where the droplet fan semi-angle, based on a Rayleigh charge limit of the emitted jet, is given by

$$\theta_B \approx \operatorname{atan}\left[\frac{9}{\sqrt{8\pi\sqrt{2}}}\sqrt[4]{\frac{f(\varepsilon)\cdot\varepsilon\cdot\gamma^2}{K\cdot V^3}\cdot\eta^3}\cdot\sqrt[8]{\frac{1}{\varepsilon_o\cdot\rho}}\right] \tag{3.42}$$

or

$$\theta_B \approx \operatorname{atan}\left[26.73\frac{\eta^{3/4}}{K^{1/4}\cdot V^{3/4}}\right] \tag{3.43}$$

The tests carried out with lightly doped propellant left cumulative uniform traces with divergence semi-angles substantially larger: 22° (Figure 3.68) and 47° (Figure 3.70).These values are larger than what expected from equation 3.32: 3.45° and 5.28° respectively. There are a number of reasons for the difference. Probably the two most relevant are:

- It is known that the reduced-order model underestimates the divergence angle [Lozano, 2003].
- Surface tension effects of the propellant on the electrode material made the propellant spread after it impacted the electrode. What is interesting is this convection does not preclude leaving sharp traces of the propellant on the electrode. The good wettability of the propellant, in any of its doping concentrations, with respect to the external electrodes was experimentally confirmed.

- In the case of the large divergence the engine functioned for substantially more time than in the other test, supplying more material that could be spread by surface tension.

For tests carried out with highly doped propellant it was possible to obtain steady - uniform impacts on the external electrode (Figure 3.71, Figure 3.72). The impacts closely resemble a circle. The sharp boundary of the electrode impacts evidences a sharp boundary of the droplet fan and thus uniform charge distribution. The divergence semi-angle is estimated from metrology at 4°. The reduced-order model predicts a divergence value equal to 8.06° for the largest flowrate used in the experiments ($\eta \approx 2.63$). These two values are of the same order Probably the difference is explained from the liquid vaporization and what we are seeing is the traces of salt left in the electrode (the propellant is about 30% in weight doped: a substantial part of the mass is propellant, susceptible to be evaporated from the vacuum chambers of the engine test facility and the SEM).

A simple model to support the last statements is proposed. The propellant would form on the electrode surface a meniscus with a contact angle θ_{ctct}. The meniscus can be described by a height h_d, an imprint diameter D_I, and an spherical radius R, as shown in Figure 3.75:

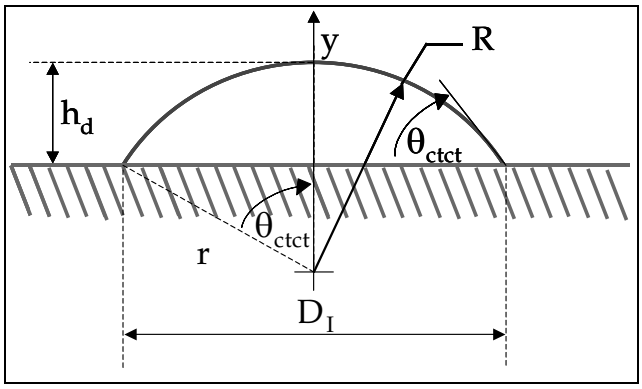

Figure 3.75 Schematic of a propellant imprint on the electrode surface.

The volume inside the meniscus is

$$V = \int_{(R-h_d)}^{R} \pi \cdot r^2 dy = \int_{(R-h_d)}^{R} \pi \cdot (R^2 - y^2) dy = \frac{\pi}{3} \cdot h_d^2 (3R - h_d) \tag{3.44}$$

or in terms of the contact angle

$$V = \frac{\pi R^3}{3} [\cos(\theta_{ctct}) - 1]^2 \cdot [2 + \cos(\theta_{ctct})] \tag{3.45}$$

Therefore, the imprint diameter can be expressed in terms of the contact angle and the volume as

$$D_I = \sqrt[3]{\frac{24}{\pi} \frac{V \cdot \sin(\theta_{ctct})^3}{[\cos(\theta_{ctct}) - 1]^2 \cdot [2 + \cos(\theta_{ctct})]}} \tag{3.46}$$

Equation 3.43 predicts that the spread footprint should be proportional to the cubic root of time for a fixed contact angle. Figure 3.76 illustrates the functional dependence of the imprint diameter with respect to the contact angle, normalized with respect to the imprint diameter when the contact angle is set at 90°.

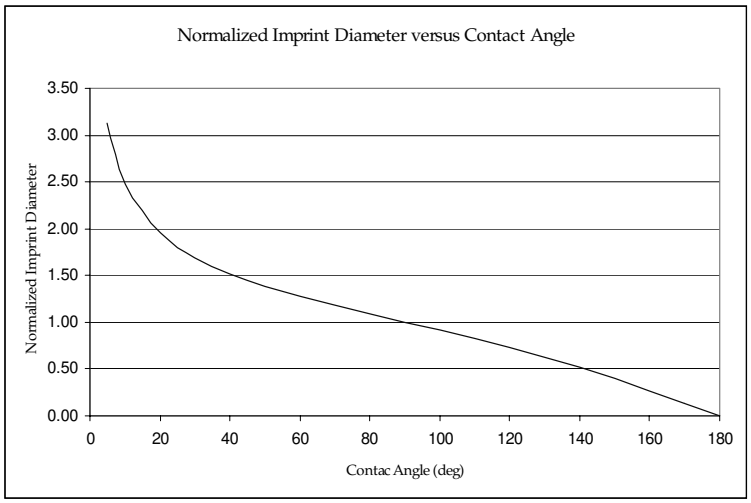

Figure 3.76 Normalized imprint diameter versus contact angle.

Spout problems

The engine from time to time is either emitting bursts of propellant or forming big drops at the spout exits, large enough to increase the pressure between the spouts and the electrode and produce arcing. This effect occurs when highly doped propellant is used. The explanation seems to be related with wettability issues and lack of closed-loop control.

The hydraulics, in particular the spouts, presently suffer from wettability problems when using formamide with doping concentrations such as to make the engine work steadily within the capabilities of the testing facility. These wettability issues do not refrain us from getting experimental curves that corroborate the steady-uniform emission of the engine, but have left us unable to obtain impact traces of the complete engine. The wettability problems are related with the profuse emission of propellant in an uncontrolled way because of non-ideal meniscus formation. To diagnose the problem the author presents three conceptual facts:

- From experimentation on channels carved in teflon substrates it is known that it is possible to fill in the channels made of non-wettable substrates, but these emitters show bursting-like starting transient [Lopez-Urdiales, unpublished work].
- Depending on how well the meniscus is defined at the spout exit, the same activation voltage can generate different meniscus deformations from the ideal Taylor Cone. To gain experience in this matter the author made a series of experiments with a metallic emitter that had an ID equal to 125 μm, using a syringe pump. For the same flowrate and activation voltage (~3.16 kV, electrode separation of several millimeters) one can get a Taylor Cone (Figure 3.77), a cycle of cone - meniscus that emits masses of liquid in a discrete way (Figure 3.78) or even emit large masses of propellant without forming a cone and in a non-axisymmetric way (Figure 3.79).The test was done with a propellant that was wetting well the channel material, but a well defined wetting front was present on the outside (Figure 3.80), indicating that the liquid was not creeping around the tip by capillarity.
- Sometimes the Taylor cones are formed misaligned with respect to the electrode normal. Because most of the voltage drop occurs within the Taylor Cone length [Carretero, 2003] the extractor cannot re-orient the droplet fan.

Therefore, it is possible to generate at the emitter end structures that emit far more than what is expected from stable Taylor Cones, with enough angular deviation to hit features that nor-

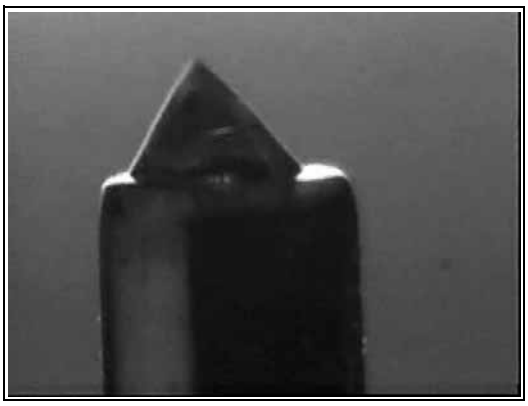

Figure 3.77 Ideal Taylor Cone.

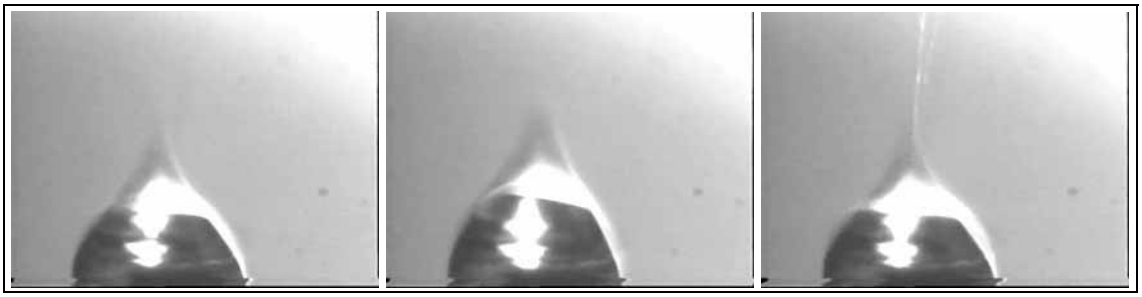

Figure 3.78 It is possible to generate a cycling between meniscus and cone where large droplets are emitted.

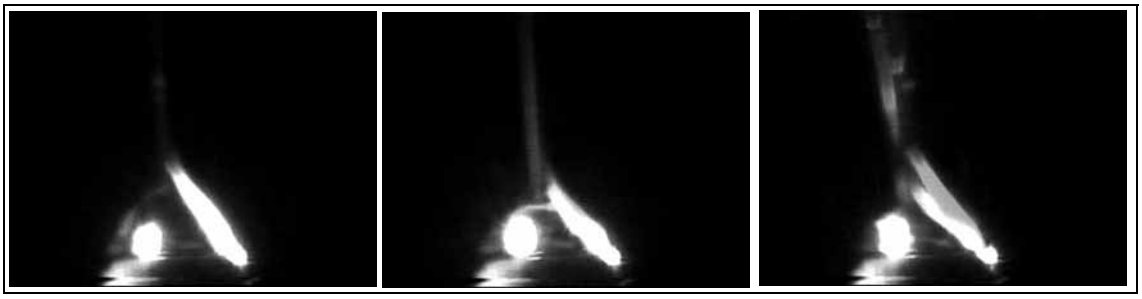

Figure 3.79 It is possible to generate a series of non-axisymmetric bursts, even without the cone formation like liquid dripping from a barely open faucet.

mally are not hit by a collimated fan. For the propellant used the jet formed at the Taylor Cone is of nanometer size; it is clear that flowrate orders of magnitude larger is being occasionally emitted in an uncontrolled fashion. The way one fixes this problem in single emitters

Figure 3.80 Picture of a meniscus before electrical activation. The wetting front of the meniscus is well defined and thus no wetting of the emitter lateral surfaces takes place.

is setting a closed-loop control where one sees the meniscus and based on that the voltage / pressure / flowrate is tailored to reach stable Taylor Cone emission.

The pressure between the electrode and the emitters can be diagnosed with the following model:

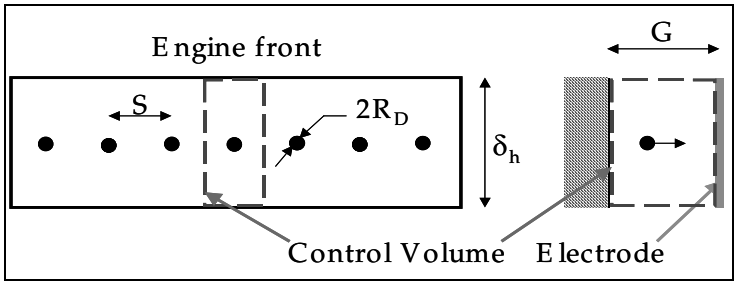

Figure 3.81 Schematic of the emitter-electrode space.

Figure 3.81 shows a large series of droplets of radius R_D separated a distance S crossing a gap G between the emitters and the collector. The engine has a thickness δ_h. To estimate the pressure between the engine and extractor a steady-state mass flow is assumed where the vapor production at the droplet surface and the vapor coming out from the gap sides are the same. The flowrate (molecules per second) on the liquid area, assuming a Maxwellian distribution, is

$$molecules/\sec. = \frac{P_{vap}}{\sqrt{2\pi \cdot m_v \cdot k_B \cdot T}} \tag{3.47}$$

The liquid area in the control volume is $4 \cdot \pi \cdot R_D^2$; the exhaust area in the control volume is $2 \cdot S \cdot G$. The molecule flux at the exit area is

$$molecules/\sec. = \frac{P}{\sqrt{2\pi \cdot m_v \cdot k_B \cdot T}} \tag{3.48}$$

where $P \le P_{vap}$. From mass conservation it is obtained the following relationship between the vapor pressure and the actual pressure in the emitter-to-extractor space:

$$\frac{P}{P_{vap(T)}} = \frac{2\pi \cdot R_D^2}{S \cdot G} \tag{3.49}$$

If the big drops are about the size of the spouts (40 μm) with S = 130 μm and G = 1 mm the fraction of the vapor pressure that is present in the space is about 8%. For G = 500 μm the fraction of vapor pressure increase to 15.5%. The upper limit is to have the engine wedge fully covered of propellant. In this case equation 3.49 becomes

$$\frac{P}{P_{vap(T)}} = \frac{S \cdot \delta_h}{2 \cdot S \cdot G} = \frac{\delta_h}{2 \cdot G} \tag{3.50}$$

For a typical engine δ_h is about 750 μm; therefore, for G equal to 1 mm the vapor pressure fraction gets increased to 37.5%, and for G equal to 500 μm the percentage value is 75%.

In the estimation of the breakdown conditions what is important is to determine how close the pressure at the emitter-to-extractor space to the pressure that produces the minimum of the Paschen curve. The curve is dependent on the actual gas that is used and it is expected that the presence of formamide modifies the curve for air. As a guideline 3.82 is the Paschen curve for air, using spherical electrodes. The minimum breakdown voltage falls near a pressure-gap equal to 7 μm-atm. [von Hippel, 1995]. From a reference the vapor pressure of formamide at 300 K is estimated at 9.5 Pa [Lide, 1995]. For G = 500 μm the minimum breakdown voltage falls in a blunt minimum centered at 1428 Pa. For G = 1 mm then the

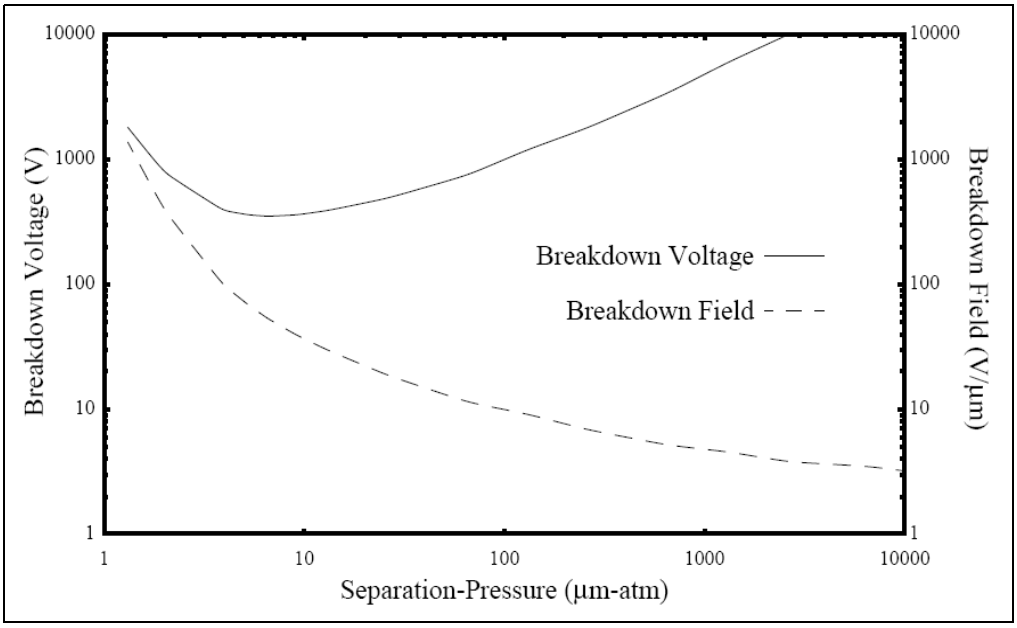

Figure 3.82 Paschen's curve for air [von Hippel, 1959].

pressure from minimum breakdown voltage fall to 714 Pa. In both cases the minimum breakdown voltage is about 300 V. For G = 500 μm a breakdown voltage above 2000 V needs a resident pressure smaller than 233 Pa, while for G = 1 mm for a breakdown voltage larger than 3.5 kV should be substantially smaller (this region is not shown in Figure 3.82), probably putting the pressure in the range on the vapor pressure magnitude. Nonetheless, the previous analysis in only preliminary because a true prediction should reflect the presence of sharp electrodes and formamide in the gas composition.

The author proposes that the arcing is produced by the following mechanism:

- The propellant does not wet well the engine interior, and comes in bursts to the emitter tips.
- The emitter tips cannot readily deliver these bursts as a steady electrified jet, and liquid spills from the emitters, at least intermittently. This effect is worsened by the lack of close-loop control and flooding can occur. Between bursts the emitters continue emitting single jets and current versus flowrate dependence of Taylor Cone emission mode is achieved.
- The excess material vaporizes due to the vacuum surrounding the engine, and the pressure between the engine emitters and the electrode increases up to

some fraction of the vapor pressure. This pressure fraction can be as small as 8%, or as large as 75%.

- The vapor pressure of the propellant is high enough to cause breakdown of the gap between the emitters and the electrode. The arcs use the emitted jets as conductive paths to reach the electrodes. This is evidenced by pictures like Figure 3.83, where the three major arcing points fall in the line that joins the two centers of the holes intended to avoid electrical interactions between the spring clusters and the electrodes, exactly the area of jet impact. Also one of the impacts seen in Figure 3.72 (the closest from the left) has enhanced brightness because its corresponding jet was used as conductive path for an arc, to eventually end in the same impact site of the stable jet. The major arcs match the flooding pattern of the corresponding engine (Figure 3.84).

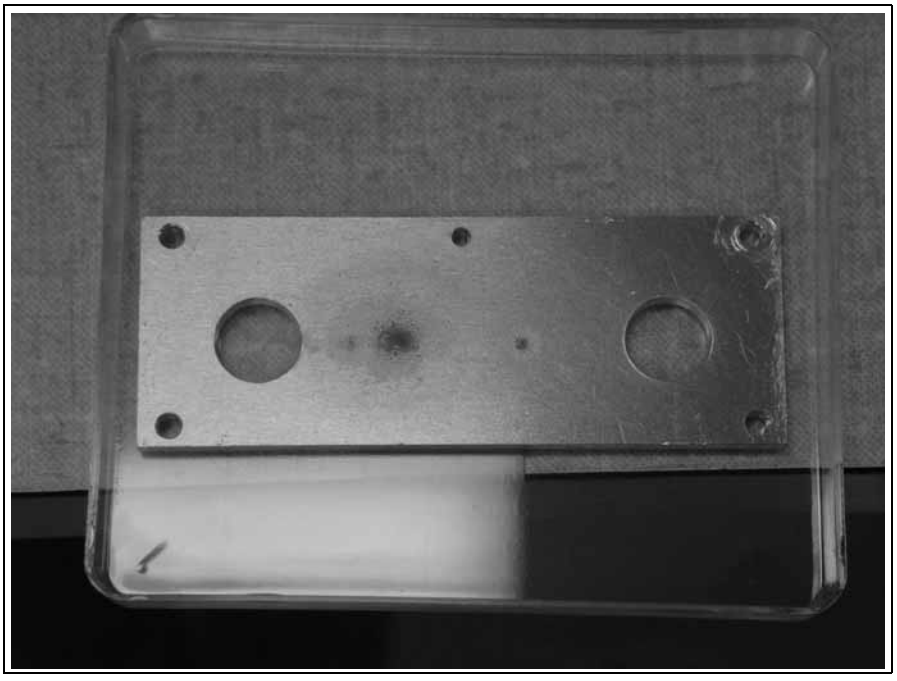

Figure 3.83 Electrode used in a test of the Linear Colloid Thruster Array where arcing events occurred. The arcs impacted the emitter using the jets, whose impacts lie in a line that joins the centers of the large electrode holes.

In a flooding case it is expected that the emitters will get covered of a propellant mass and the limit suggest by equation 3.50 (provided is smaller that unity) should hold. This would be a bad situation provided the pressure puts the system near the minimum breakdown value.

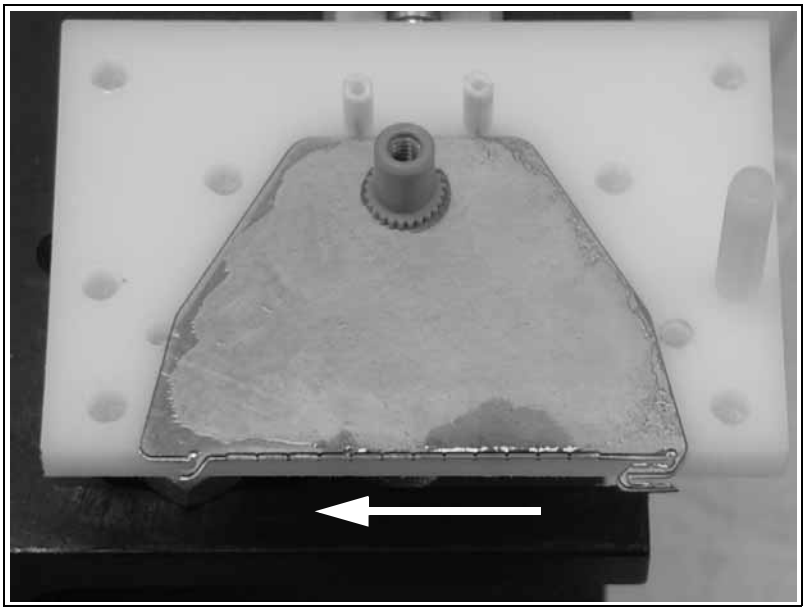

Figure 3.84 Picture of an engine that suffered propellant emitter coverage. See the two main propellant wetted sites compared to the main arcing points shown in Figure 3.83. The arrow shows the direction of the gravitational field while the test was carried out.

Chapter 4

PRELIMINARY DEVELOPMENT OF A PLANAR ELECTROSPRAY THRUSTER ARRAY

The natural extension of the work done in Linear Electrospray Thruster Arrays is to produce an engine that can have larger emitter densities without putting at risk the structural integrity of the engine, e.g., to have substantially smaller emitter-to-emitter separations. A clear improvement is then to have a planar array of emitters. This way the engine external surface is used more efficiently.

This chapter illustrates the development of an electrically controlled, externally fed Planar Electrospray Thruster Array that uses the ionic liquid $EMI-BF_4$ as propellant and sharpened tips as field enhancers. The engine operates in the ionic/mixed emission regime, and uses black silicon as wicking material.

This piece of research was done with a smaller budget and less time compared to the Linear Array; therefore, the proposed engine design was not brought to life to the extent the Linear Array was, but only a simpler version with external electrodes (i.e., the electrodes were not micro-fabricated) was implemented.

The exposition is concentrated in three key topics:

- Explanation of the engine design concept and design decisions.
- Device fabrication of the full and simplified Planar Array versions.
- Device fabrication and test results, analysis and discussion.

The conclusions arise from the validation of the proposed Planar Electrospray Thruster Array appear in Chapter 7.

4.1 Engine design concept

The proposed Planar Electrospray Thruster Array is the result of design considerations about the propellant selection, flowrate control, engine architecture, emission mode, and electrical issues. The following paragraphs will briefly comment each one of these design criteria.

4.1.1 Propellant selection

The engine uses $EMI-BF_4$ propellant. Ionic liquids are like molten salts where the liquid lacks a solvent and it is mainly composed of ionic species. The particular ionic liquid was selected because of its low vapor pressure, large electrical conductivity, stability to radiation [Marrese, 2003] and emission mode. $EMI-BF_4$ has a very small vapor pressure, unable to be measured to date, so open architectures can be implemented (the vapor pressure should be at most 10^{-9} Torr., the maximum vacuum obtained in the test vacuum chambers). The conductivity of ionic liquids is highly dependent on temperature [Fuller, 1997]. For $EMI-BF_4$ it is about 1.25 Si/m at room temperature, but at 55 $^{\circ}C$ is almost 3 Si/m. It is experimentally known that this liquid emits either solvated ions or ions+ droplets, allowing to reach higher I_{sp}'s than in droplet emission [de la Mora, 2003]. The state of the art of the models to predict the emission of Taylor Cones made of ionic liquids do not allow us to use more precise metrics to select the propellant.

4.1.2 Engine propellant feed and Electrical Control

In the case of the Planar Electrospray thruster Array the engine electrical control concept used for the Linear Array is still valid. A noticeable difference is the lack of stagnation pressure at the engine plenum, i.e., there is a zero external pressure difference between the plenum and the emitters; therefore, there cannot be propellant emission unless electrically

activated. In this sense the Planar Array is safer to propellant leak compared to the Linear Array. The following are a few complementary highlights of the feed system:

- The flow is driven by surface tension on the engine hydraulics exterior from the engine plenum to the emitter. This is obtained by having a wetting emitter surface and some emitter texture. This textured surface can be extended into a layer of wicking material.
- There is still flowrate match but in this case the system is more robust. The engine has a certain maximum pumping potential based on the interaction of surface tension pulling and viscous losses. This way the engine can deliver to the Taylor cones as much propellant as requested up to the maximum flowrate that can be delivered by the wicking material, i.e., when the internal pressure of the liquid reaches the maximum pressure produced by surface tension. In this sense the engine is flowrate self regulated where the two regulation variables are temperature and activation voltage.
- The flow field on the hydraulics surface is assumed to be fully developed, and is surface tension driven.
- It is required for the emitters to exceed the propellant level at the emitter modular units. Therefore, tall sharpened emitters are needed.
- Evaporation losses are not an issue in this engine.
- Clogging is not an issue in this engine because the propellant is not doped, it does not have a solvent component and the vapor pressure is virtually zero.

4.1.3 Engine architecture and structural considerations

This engine takes advantage of the quite low vapor pressure of the propellant by using an externally fed architecture, i.e., the propellant creeps along the emitter outside surface via surface tension effects. Thus, the hydraulics of the engine are substantially simpler to implement than in the Linear Array case, in particular the needle formation (no wafer bonding is needed). The engine is made of silicon wafers as substrates, while the electrical insulation is provided by thick CMOS-grade silicon oxide films and vacuum.

The proposed engine has a hydraulic system composed of a plenum, a set of pools were emitters raise from the pool floor, and a network of irrigation channels to connect the pools with the plenum. The pools play the same role as the manifolds in the Linear Array. Different modules could have slightly different spout configurations (emitter density, geometry, abso-

lute dimensions, thickness of the wicking material) to achieve I_{sp} variations within the same engine and thus being ideal for a broader range of missions. A layer of black silicon is used to efficiently distribute the propellant and supply hydraulic impedance to achieve flowrate matching. Black silicon was selected because it was the only CMOS-friendly material that was experimentally found to be wetted by the ionic liquid $EMI-BF_4$. A conceptual view of an emitter for this kind of engines is shown in Figure 4.1.

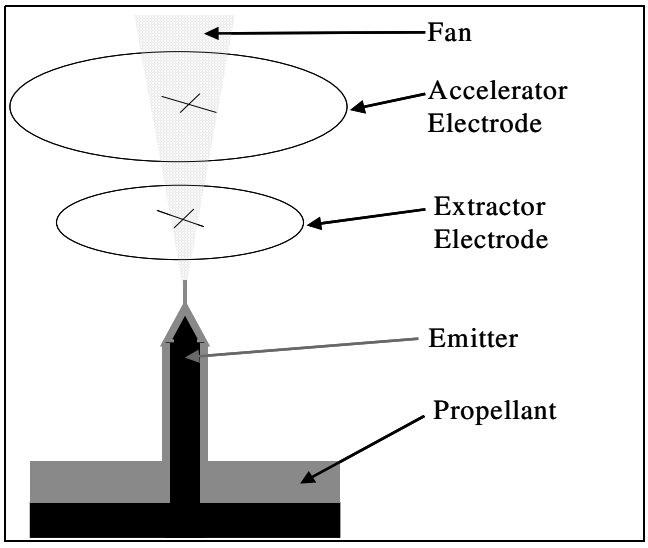

Figure 4.1 Schematic of an externally fed emitter.

As in the case of the Linear Array uniform time controlled etchings and segregation od the electrodes and hydraulics substrates were adopted.

The hydraulic system is carved on a single substrate because there is no need for wafer bonded hydraulics. The network of channels that communicate the pools with the plenum is not subject to alignment problems because are intended to work as open channels (no pressurization). The hydraulic system of the Planar Electrospray Thruster Array has the following architecture:

- A plenum or propellant tank that locally stores the propellant. The propellant tank is reachable from the exterior by an inlet.
- A set of irrigation channels that distribute the propellant from the plenum.

- A set of pools that receive the propellant from the channel network and provide propellant to the emitters that evolve from their bottom.
- A set of emitters that raise from the pool bottom level and face the electrode system.
- Black silicon covering the whole hydraulic system.

Grouping the emitters in sets allows us to leave pads of unperturbed surface to increase wafer bonding quality.

The electric system of the engine has the following architecture:

- An extractor electrode, responsible for generating the Taylor Cone from the propellant covering each emitter tip.
- An accelerator electrode, responsible for providing to the exit stream the intended velocity.

Two spout geometries are proposed as a trade-off of fabrication accuracy, field enhancement, and propulsive efficiency:

- *Volcano* emitters that have a blunt top and emit sideways (the rather large jet inclination reduces the propulsive efficiency and makes electrode design difficult). For this kind of emitter L_c (which characterizes the size of the Taylor's Cone base) is the radius of curvature of the transition between the flat top surface and the lateral surface.
- *Pencil* emitters that are fully sharpened and emit along their axis. For this kind of emitters L_c is the radius of curvature of the tip.

The spout geometries are shown in Figure 4.2. Judging from SEM pictures of the actual emitters L_c is of the same order of magnitude in both emitter kinds.

Both emitter geometries are formed by using the very same optical masks: they differ in the plasma etching sequence. The emitter-to-extractor separation is dominated by emitter type, jet divergence, and emitter density. Hydraulics and electrodes are joined using wafer bonding. Figure 4.3 is an concept schematic of the proposed Planar Electrospray Thruster Array.

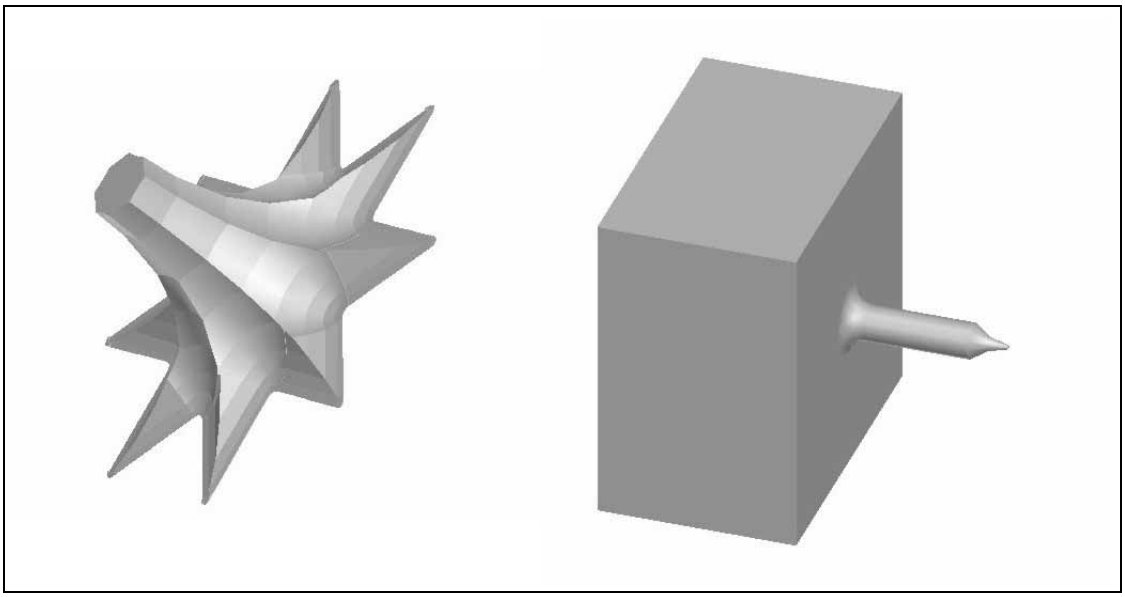

Figure 4.2 Schematics of the proposed spout geometries: sharpened spouts with blunt top -*volcanoes- (left)*, and fully sharpened emitters -*pencils- (right).*

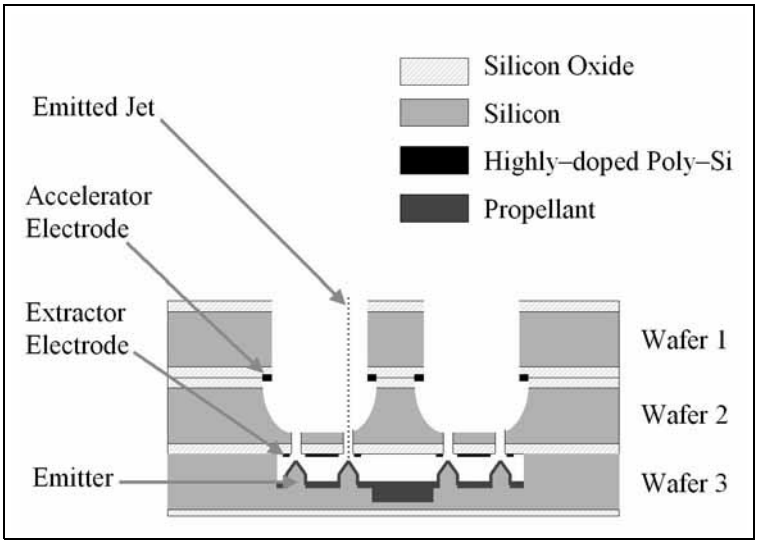

Figure 4.3 Conceptual schematic of the proposed Planar Electrospray Thruster Array.

4.1.4 Operational Mode

The engine is intended to operate in the single Taylor Cone mode because it has smaller beam divergence than the highly stressed regime. The engine is expected to emit mainly solvated ions.

High propulsive efficiency is obtained naturally from the types of emitted solvated ions [Lozano, 2003]. Substantially larger I_{sp} values compared to the droplet regime can be obtained. While for droplet emission mode specific velocity values up to 1000 sec. are feasible with ionic liquids up to 3500 sec. have been reported [Lozano, unpublished work]. The engine is expected from the experimental data that appears in the literature to emit mainly solvated ions where large propulsive efficiencies are feasible. If the engine emits in the mixed regime the propulsion efficiency may still be attractive for some missions, as a trade off for reaching a certain I_{sp}.

4.1.5 Electrochemical effects

Using ionic liquids as propellant can lead to electrochemical problems if the operation is in DC mode for more than a few hours. The counter-ions (ions of opposite polarity to those emitted) have to discharge at the interface between the liquid and the surface (the counter electrode). The resulting neutral molecules can either bubble out as a gas, accumulate as a solid residue, or react with the substrate. This happens in fact with any propellant but when there is a solvent, and operation is in the droplet mode, the recombination residues can be carried away as part of the emitted droplets.

Therefore, it is required to implement a bi-polar scheme that switches fast enough the sense of the voltage drop between the emitters and the electrodes to sequentially extract particles of both polarities and this way avoid/minimize electrochemical effects at the counter-electrode [Martinez-Sanchez, 2003; Lozano and Martinez-Sanchez, in preparation].

4.1.6 Engine Electric Field Enhancers

The Planar Array relies on spout area reduction / sudden spout slope change to effectively enhance the electric field at the emitter tips. The engine spouts were analyzed using Finite Element analysis of the electric field surrounding the emitters, using the commercial software Maxwell. For the numerical simulations the spouts and the extractor were considered equipotentials and the physical constraint that the field must decay away from the charge source was

also enforced. The conclusion from the Finite Element Analysis is that the spout system of the Planar Electrospray Thruster Array does a better job in increasing the electric field around the emitter compared to the Linear Array, and that the pencil geometry has better electric field enhancing capabilities compared to the volcano-like emitter. The constraints imposed by micro-fabrication methods do not allow to produce shadowing. The predicted activation voltages for the emitter-to-extractor separations that were implemented in the engine are sound, showing little variation for electrode-to-emitter separations larger than 500 μm (logarithmic saturation).

For both emitter types the finite element results and the values from equation 3.32 show good agreement, in particular for the case of the volcanoes. The starting voltage values from equation 3.30 are substantially smaller than what predicted by the other two methods.

The emitter roughness should not play a role in enhancing the electric field because the emitter is covered with propellant and the electric field that turns on the Taylor Cones surrounds the propellant free surface.

Pencil Emitters

The slope of the predicted starting voltage based on finite element analysis gets smaller the larger the emitter-to-electrode separation, and reaches an slow-varying limit value as a logarithmic behavior would suggest. The characteristic lengths used in equation 3.32 are L_c equal to 2.5 μm (the emitter tip radius) and L_c^o equal to 22 μm (the radius of the pencil body). The predicted starting voltage values from equation 3.32 are within 35% from the finite element results.

Figure 4.4 shows a typical electric field solution for electrode-to-emitter separations of 50 μm. The applied voltage between emitters and extractor is 1000 V. The summary of the numerical results is shown in Table 4.1 and it is contrasted to the prediction of equations 3.30 and 3.32 for the propellant $EMI-BF_4$, with a surface tension value equal to 0.0518 N/m [de la Mora, 2003]. The L_c used was equal to 2.5 μm (an estimate of the radius of curvature of the emitter at its tip from SEM pictures) and L_c^o was set at 25 μm (the radius of the pencil body).

Figure 4.5 is a plot of the starting voltage versus emitter-to-electrode separation using the finite element results and the values form equations 3.30 and 3.32.

TABLE 4.1 Starting Voltage versus Electrode Separation for the pencil geometry in the Planar Array.

Separation (μm)	Min. Electric Field (V/ m) @ 1000 V	Starting Voltage (V)	Equation 3.30 (V)	Equation 3.32 (V)
50	9.5×10^7	904	530	1277
150	5.7×10^7	1507	663	1697
250	4.0×10^7	2147	725	1893
500	2.7×10^7	3181	809	2158
750	2.4×10^7	3578	858	2313

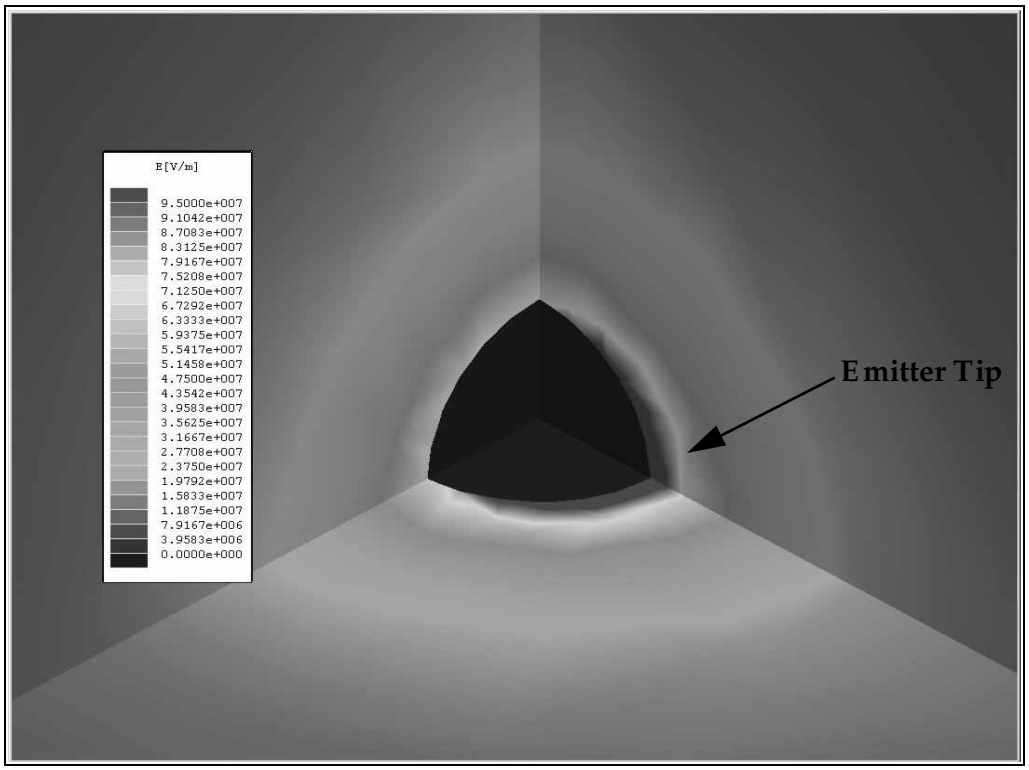

Figure 4.4 3-D Finite Element Analysis of the Planar Array emitters, pencil geometry, facing a flat electrode. Electrode-to-emitter separation in this case is 50 μm. The magnitude of the electric field is shown here for three planes surrounding the emitter tip. Total voltage drop = 1000 V.

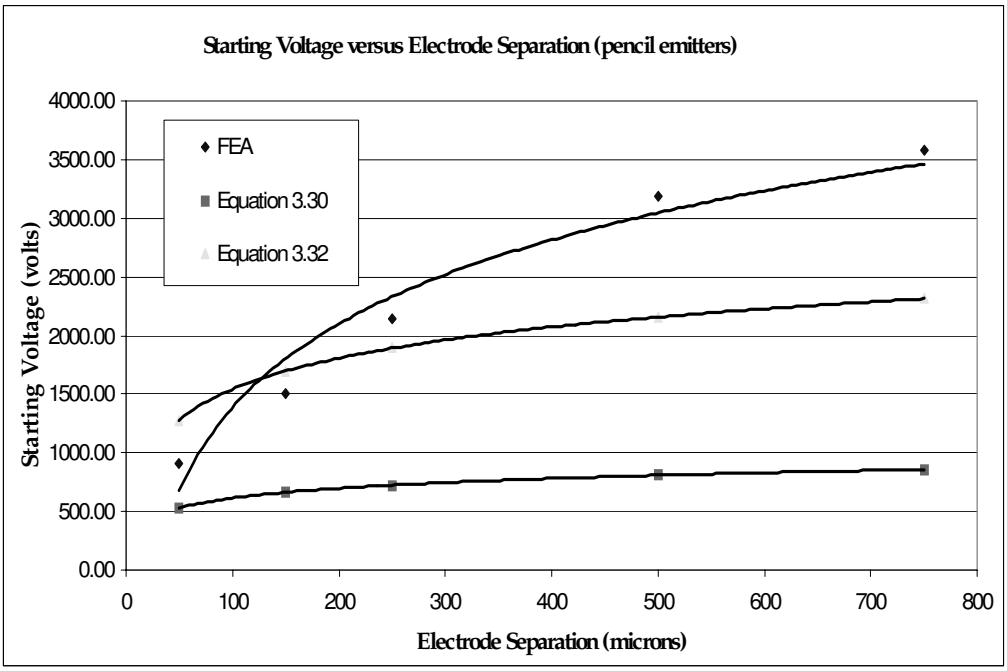

Figure 4.5 Starting Voltage versus Electrode Separation for the pencil geometry in the planar Electrospray Thruster Array from both FEA and equations 3.30 and 3.32. The fit done on the finite element data is logarithmic and evidences some saturation behavior when the electrode-to-emitter separation gets large. Agreement between finite element results and equation 3.32 is shown.

Volcano Emitters

The criterion adopted to interpret the results is the minimum electric field that surrounds the *vicinity* of a top sharp point. The predicted starting voltage based on finite element analysis shows logarithmic saturation and is in good agreement with the predicted values from equation 3.32 using as characteristic lengths L_c equal to 5 μm (an estimate of the sharp point radius) and L_c^o equal to 50 μm (the radius of the volcano body at its top). There is also a substantial difference between the starting voltage saturation value predicted from the numerical simulations compared to the saturation value from equation 3.30. Also, the volcanoes are less effective than the pencils in enhancing the electric field.

Figure 4.6 shows a typical solution of the electric field for electrode-to-emitter separation of 50 μm. The applied voltage between emitters and extractor is 1000 V. The diameter of the volcano top is 90 μm. The summary of the numerical results is shown in Table 4.2 and is

TABLE 4.2 Starting Voltage versus Electrode Separation for the volcano geometry for the Planar Array.

Separation (μm)	Min. E. Field (V/m) @ 1000 V	Starting Voltage (V)	Equation 3.30 (V)	Equation 3.32 (V)
50	8.50×10^7	505	631	1306
150	4.80×10^7	895	819	1860
250	2.50×10^7	1718	906	2118
500	1.90×10^7	2260	1025	2467
750	1.90×10^7	2260[a]	1094	2672

a. No substantial difference in the numerical results between 750 μm and 500 μm separation was found.

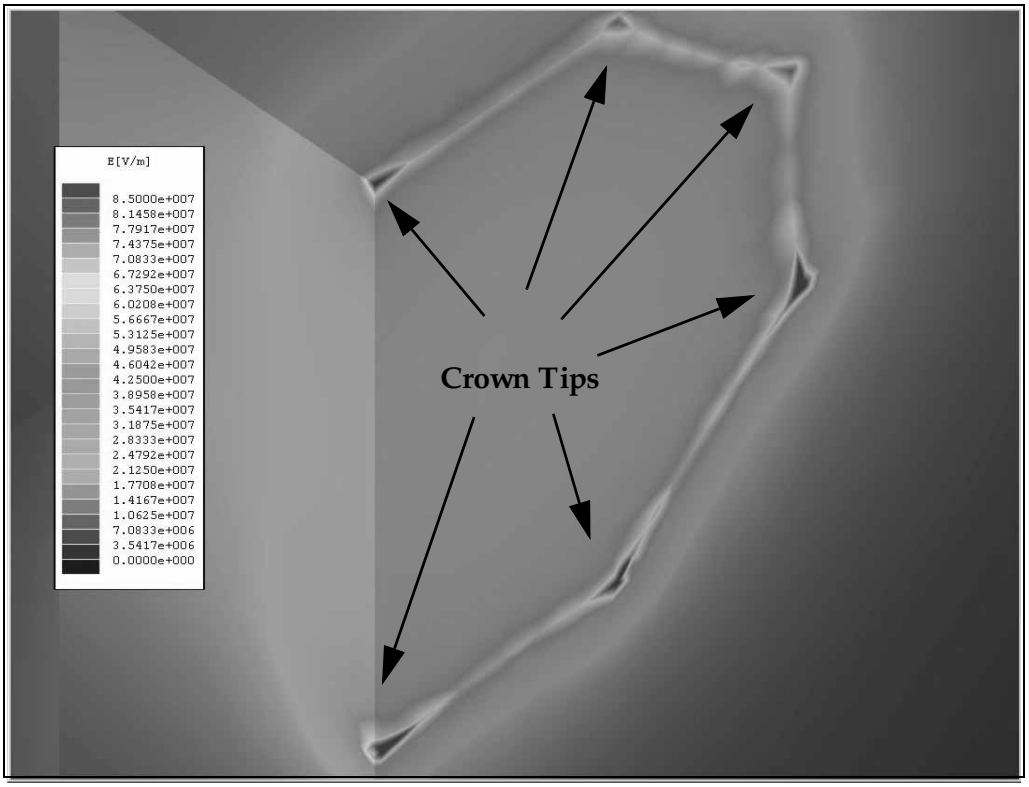

Figure 4.6 3-D Finite Element Analysis of the Planar Array emitters, volcano geometry, facing a flat electrode. Electrode-to-emitter separation is 50 μm. The bias voltage is 1000 V

compared to the predicted starting voltages from equations 3.30 and 3.32 for the ionic liquid $EMI-BF_4$. Figure 4.7 shows the starting voltage versus the emitter-to-electrode separation dependence for both the finite element results and values from equations 3.30 and 3.32.

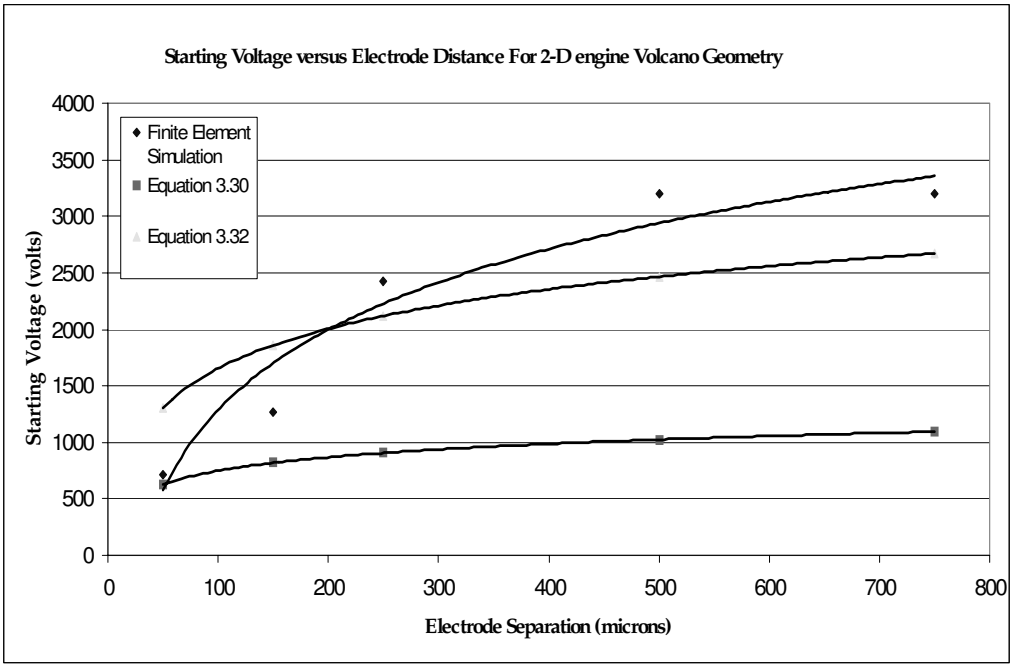

Figure 4.7 Starting Voltage versus Electrode Separation for the volcano-like geometry in the Planar Array. Good agreement between the finite element results and the values from equation 3.32 can be seen. Logarithmic saturation for large emitter separation -to- L_c ratios is also present.

Benchmarking of the Spout Electric Field Performance

Four series of finite element simulations were done to benchmark the proposed emitters: a finite element series to determine whether the influence of the pool edge on the electric field of the neighboring emitters was important, a finite element series to determine how close the emitters could be placed -based on micro-fabrication constraints-, and two series of finite element simulations to validate the claim that the electric field enhancing capabilities of the volcanoes does not depend on the size of the flat top. The numerical simulations show that the pool edge produces some shadowing to the neighboring emitters, the presence of a cavity on the volcano top surface does not influence the volcano emitter filed enhancing capabilities, the size of the volcano top surface influences the starting voltage, and emitter-to-emitter shadowing does not take place in the Planar Array.

Effect of the pool edge on the field

There was uncertainty whether or not the edge of the bucket will generate a perturbation of the electric field on the neighboring emitters, compared to the emitters in the bulk of the matrix. A series of finite element simulations using pencils, the emitters with higher clustering potential, was carried out.

The numerical results suggest that the pool edges produce some shadowing. This shadowing is not related to the number of pool edges surrounding the emitter (1, 2). The plausible solutions for this shadowing are

- Increase the emitter-to-edge separation.
- Place the pool edge *half* the emitter-to-emitter distance from the most external emitters, while increasing the height of the edge to make it act as a symmetry surface.

The analysis can be summarized in the following points:

- The electric field of two emitters neighboring to the pool edge was modeled. (Figure 4.8) The results of the finite element simulation are shown in Figure 4.9 for a potential drop of 1000 V. The result is that the electric field surrounding the emitter close to one pool edge is virtually identical to the electric field surrounding the emitter near two pool edges. The minimum magnitude of the electric field surrounding the emitter tip was found to be equal to 2.0×10^7 V/m.
- The electric field of nine emitters, without the presence of pool edges, was simulated using the same electrode-to-emitter separation distance (500 μm) and emitter-to-emitter separation distance (800 μm) (Figure 4.10). Periodicity boundary conditions were used. The electric field surrounding the emitter in the center of the set is shown in Figure 4.11. The minimum electric field surrounding this emitter is substantially larger: 2.7×10^7 V/m.

It is the opinion of the author that in principle the pool edges should not be a serious obstacle to the activation of the closest emitters because

- All the other evidence suggests that the emitters act independent of whatever is surrounding them (see *Coupling Effects*). Increasing the edge separation from the first row of emitters might actually be beneficial for wettability reasons (increase the non-wettable path to avoid spilling over).

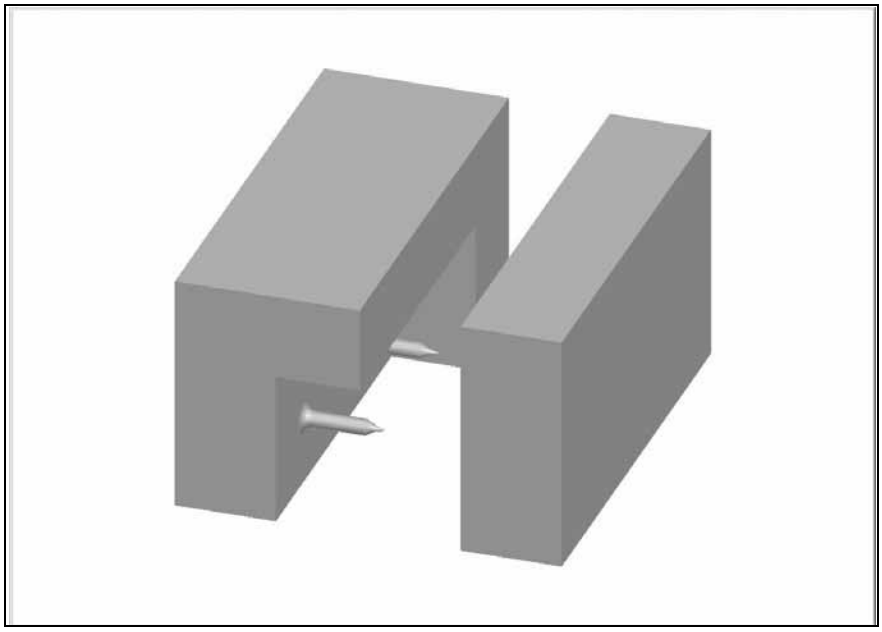

Figure 4.8 Schematic of a pencil matrix section where the fuel container edge is present. Appropriate periodicity boundary conditions were taken to make the finite element results useful for the comparison of edge influence in the electric field surrounding the emitters.

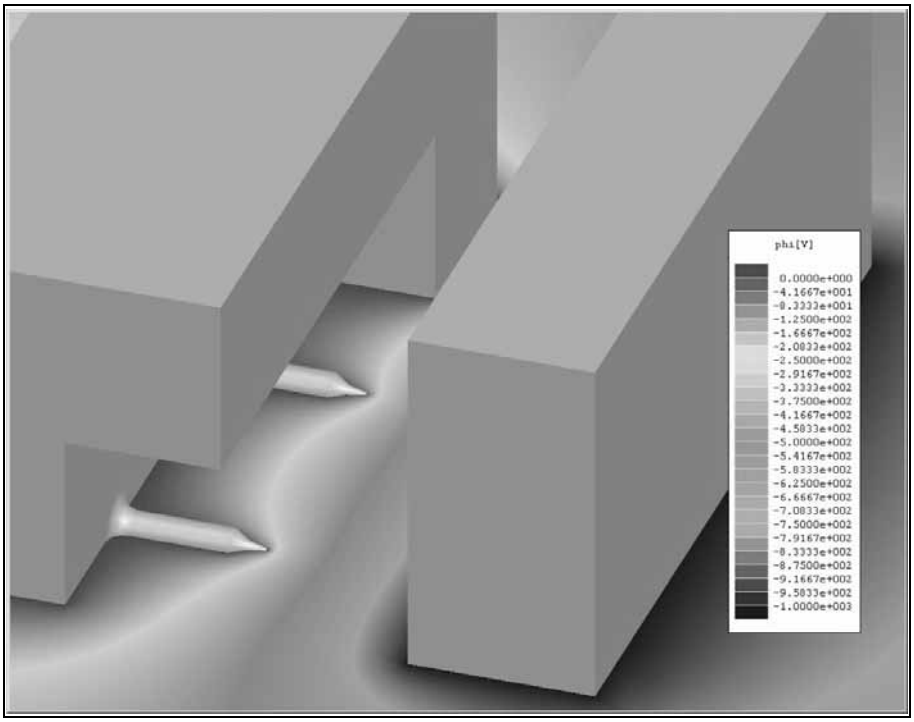

Figure 4.9 Finite element potential simulation in the space between the Planar Array emitters and the extractor, near the edge of the propellant container.

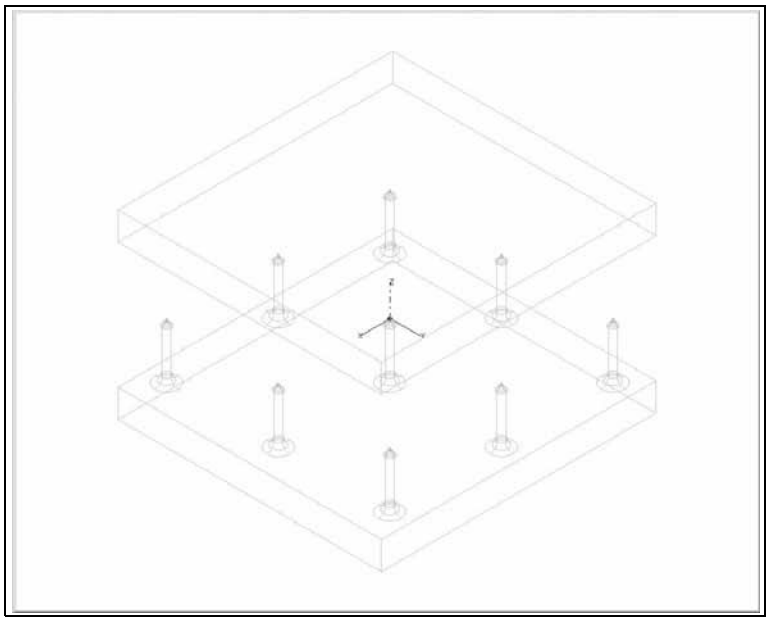

Figure 4.10 Schematic of a pencil matrix section without the container edge.

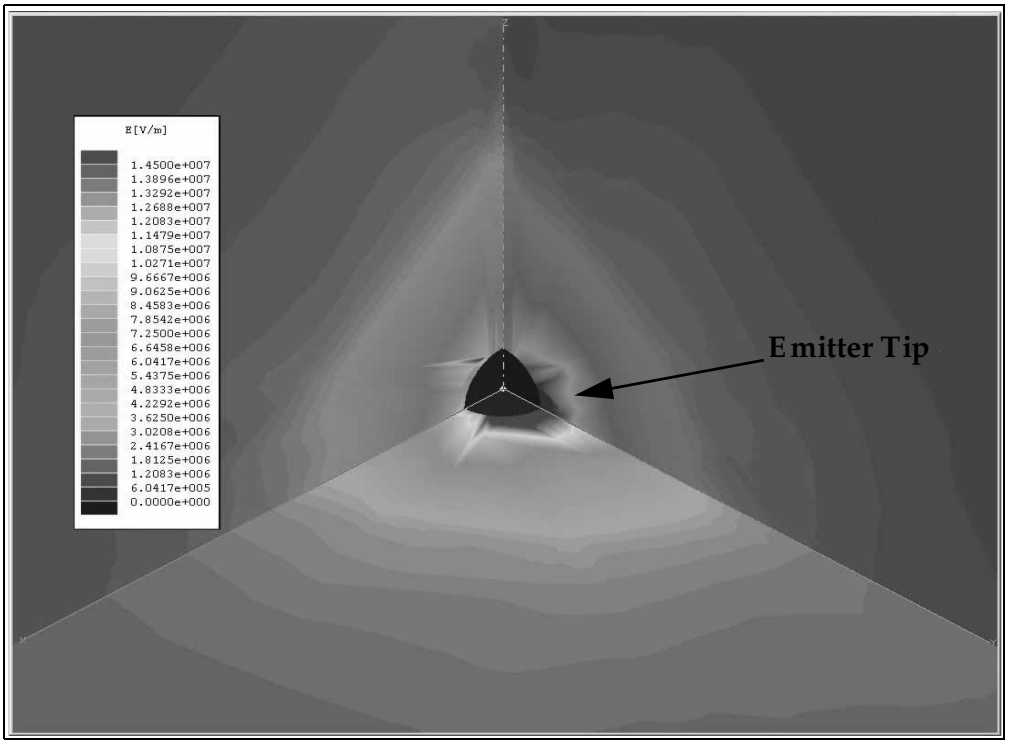

Figure 4.11 Finite element simulation in the space between the Planar Array emitters and the extractor, for an internal emitter, far from the propellant container edge. The magnitude of the electric field is shown here for three planes surrounding the emitter tip. Total voltage drop = 1000 V

- The real engine would provide electrical potential to each emitter via a concentric ring instead of a planar electrode. This way the effect of the surrounding should be damped.

Coupling effects

A series of finite element simulations were done to determine if the maximum emitter density, using the size of the starting etching mask, could produce emitter shadowing.

Based on the simulations it was determined that the emitters can be placed as close as possible and they would still have not shadowing effects. Specifically the electric field of a set of five pencil-like emitters was implemented (Figure 4.12). The emitter-to-emitter separation was set at 300 μm. The electric field surrounding one of the emitters is shown in Figure 4.13. The simulated electric field for both emitter-to-emitter separations are virtually identical: a minimum electric field of 2.7×10^7 V/m. surrounding the emitter is obtained. This result suggests the possibility of individual emitter control.

The result is explained by the fact that the electric potential decays a few L_c from the emitter tips and this L_c is far smaller than the emitter-to-emitter separation.

Influence of the top size on the field enhancement performance of volcanoes

A finite element simulation of the electric field for a volcano whose top surface has a bowl-like cavity (Figure 4.14). The results of the finite element simulation are shown in Figure 4.15. It is clear that even for edge thicknesses of the order of L_c the electric field is for practical purposes the same. Therefore, the volcano-like emitters enhance the electric field using the sharp points at the top surface as a local effect.

A series of finite element simulations were carried out with a 2:1 scale of the volcano parameterization used to benchmark the field enhancing capabilities of such emitters. Therefore, L_c was reduced to 2.5 μm and L_c^o was reduced to 45 μm. The same emitter-to-electrode separations was sampled. The results from the finite element simulations were compared to the values predicted from equations 3.32 and 3.30. Table 4.3 summarizes the results and Table 4.16

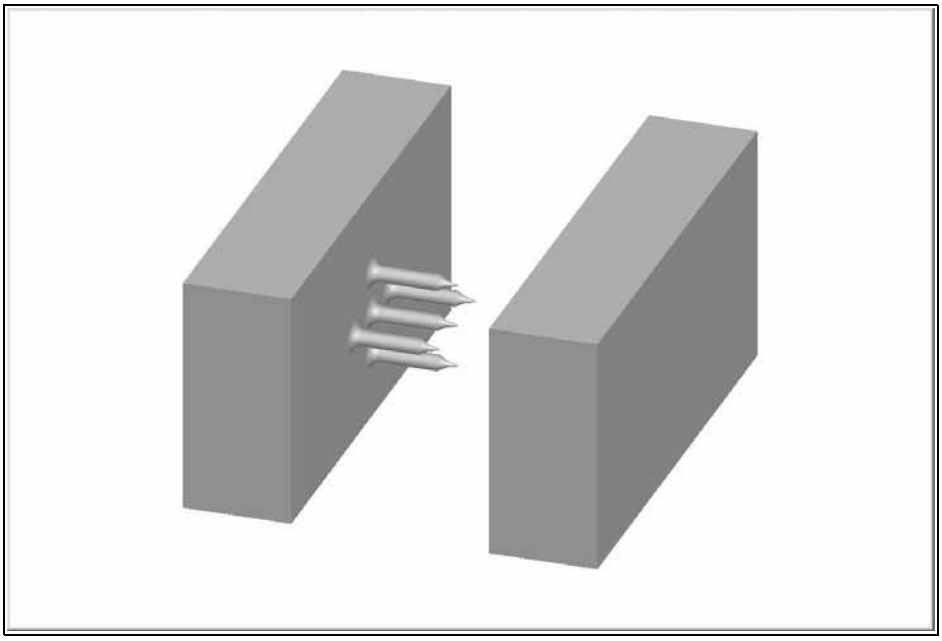

Figure 4.12 Schematic of the emitters in its densest packing from the optical mask layout.

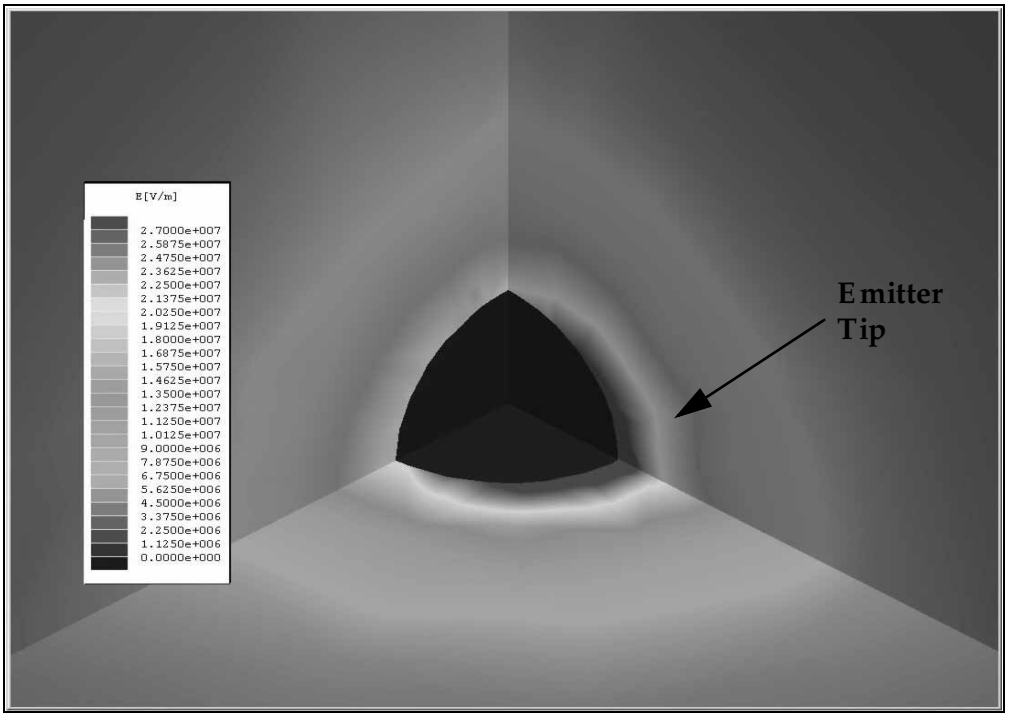

Figure 4.13 Electric field finite element simulation in the space between the Planar Array emitters and the extractor, for an inner emitter. The magnitude of the electric field is shown here for three planes surrounding the emitter tip. Total voltage drop = 1000 V.

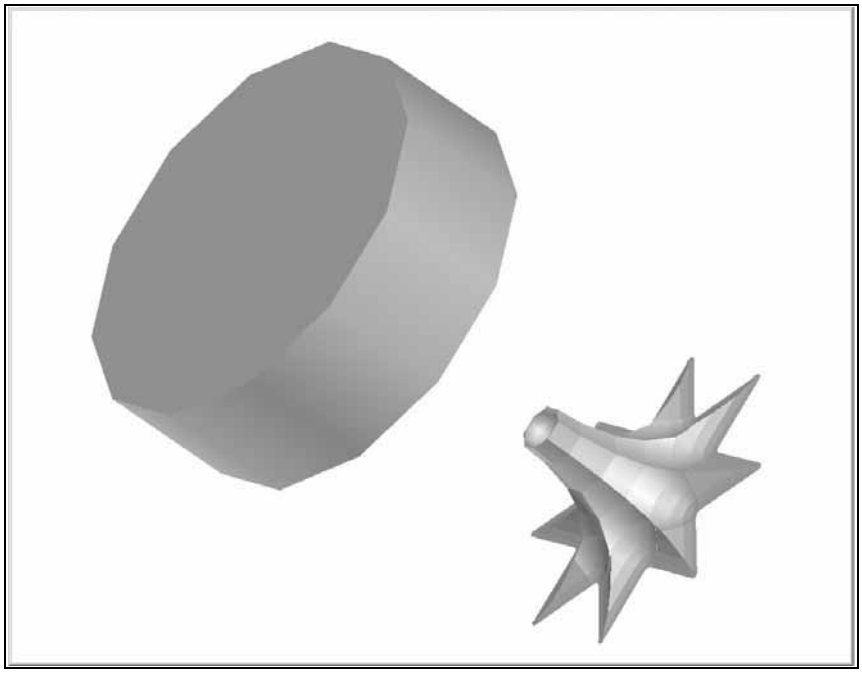

Figure 4.14 Schematic of a *volcano* emitter geometry, with the presence of a hollow *crown* on its top, facing a solid electrode.

graphically shows the findings. The conclusion of the series of finite element analysis is that the size of the volcano emitter influences the field enhancing capabilities and therefore, the starting voltage of the volcanoes.

4.1.7 Space Charge Considerations

The model developed in Appendix B can be applied to the emitters of the Planar array. Figure 3.21 and Figure 3.22 can still be useful to determine the threshold conditions to reach space charge saturation because the surface tension and conductivities of the propellant used in those graphics is similar to the values for $EMI-BF_4$.

Looking at those figures there is a small but possible window of emitter separations in the Planar Array that could generate space charge saturation conditions because of the larger emitter densities and smaller L_c compared to the Linear Array case. In the case of the Planar Array the minimum L_c is not set by clogging or electrical control considerations, but by etching taper, emitter height, and maximum emitter clustering.

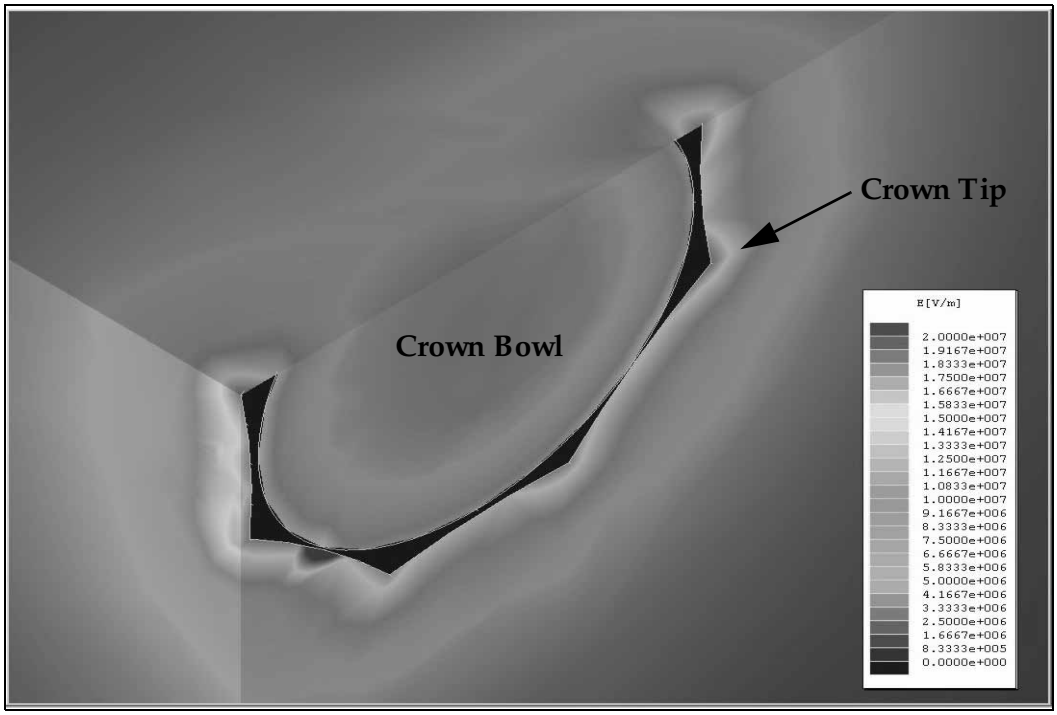

Figure 4.15 3-D Finite Element Analysis of the 2-D engine spout system with the crowned volcano geometry facing a flat electrode. Electrode-to-emitter separation 500 μm .

TABLE 4.3 Starting Voltage versus Electrode Separation for a volcano geometry for the Planar Array 50% of the size compared to the volcano emitter used in Table 4.2.

Separation (μm)	Min. E. Field (V/m) @ 1000 V	Starting Voltage (V)	Equation 3.30 (V)	Equation 3.32 (V)
50	1×10^8	859	530	1171
150	6.2×10^7	1385	663	1562
250	5.5×10^7	1561	725	1744
500	4.35×10^7	1974	809	1992
750	3.7×10^7	2321	858	2136

The problem would be then to make the emitters tall enough so they don't get immersed into the sea of propellant that surrounds them because all plasma etchings have etch taper and is strongly influenced by the degree of mask packing. Therefore, a minimum starting cross-section is needed. Based on micro-fabrication constraints the physical constraint line would be

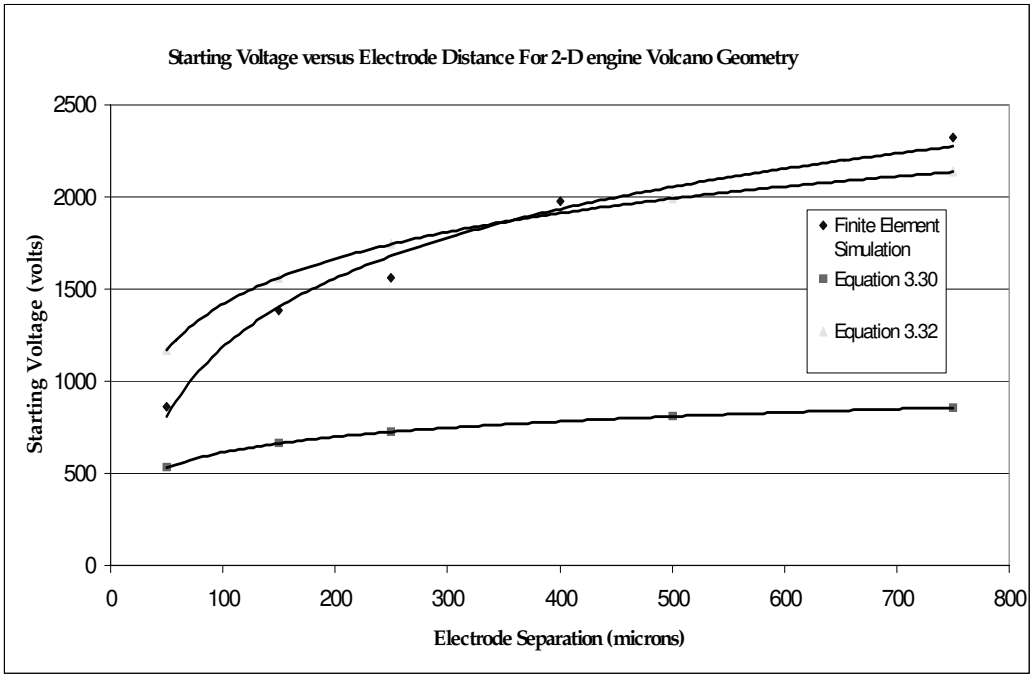

Figure 4.16 Starting voltage versus emitter-to-extractor separation for a volcano emitter scaled 50% from the absolute dimensions of the volcano emitter used in Figure 4.7.

for $R_c = 1\ \mu m\ \ S = 200 \cdot L_c$. This way the window of available spacings will substantially shrink, implying larger V_E.

The planar Array uses wafer bonding to join the hydraulics and the electrodes; therefore, it is better fit to have small emitter-to-electrode separations and larger thrust densities than ion engines can achieve.

4.2 Device Fabrication

Figure 4.17 shows a series of SEM pictures of a simplified version of a Planar Electrospray Thruster Array that uses external electrodes, composed of a 32×32 emitter array in one propellant pool; the two emitter kinds are shown as well. The conceptual engine uses silicon wafers: one for the hydraulics and one for each electrode. This engine would be entirely patterned using plasma etching using RIE and DRIE. The simplified engine was developed to preliminarily test the concept; therefore, no critical parts like the propellant plenum or the

channel network are present. As a result, the hydraulic system needs only 1 optical mask, 2 photolithographic processes, and about 20 fabrication steps to be implemented. The full version of the engine requires 8 optical masks, 8 photolithographic processes, and more than 88 fabrication steps. The emitters are made using thick layers of silicon oxide with the collimated stratified nested mask procedure developed for the Linear Array. A thin layer of black silicon covers the propellant pool and emitters, acting as a surface tension driven propellant pump. The electrodes of the full version of the engine would have a conductive path made of doped poly-Si to make them CMOS compatible for fusion wafer bonding; a thick silicon oxide layer is used as insulating layer. In this proposed electrode system the extractor electrode surround each emitter with a conductive ring to reduce non axisymmetric emission and lower the extraction voltage, while the accelerator electrode influences emitter sets. The electrodes and the hydraulics would be assembled using wafer bonding.

Section 4.2.1 briefly refers to the fabrication considerations and Section 4.2.2 explains the fabrication process flow. In order to gain a better knowledge of the micro-fabrication techniques the author advises to go to general references [Campbell, 1996; Madou, 2002], or the brief summary included in his Master of Science Thesis [Velásquez, 2001.

4.2.1 Fabrication Considerations

The following is a summary of the key fabrication choices made to implement the Planar Array fabrication:

- **Photolithography:** positive tone contact photolithography was selected as the photolithographic transfer method. The selection was mainly based on the need to build large enough Planar Electrospray Thruster Arrays, be able to use global alignment features, and achieve acceptable minimum feature size and resolution.
- **Etching and etch depth control:** Plasma time-controlled etching was selected to define the etch-depth of the features. Highly selective plasma etching recipes were favored in the fabrication tuning.
- **Nested Masks:** The engine hydraulics, in particular the emitters, are generated using a collimated stratified etching mask approach because sharp tips and tall emitters were intended.

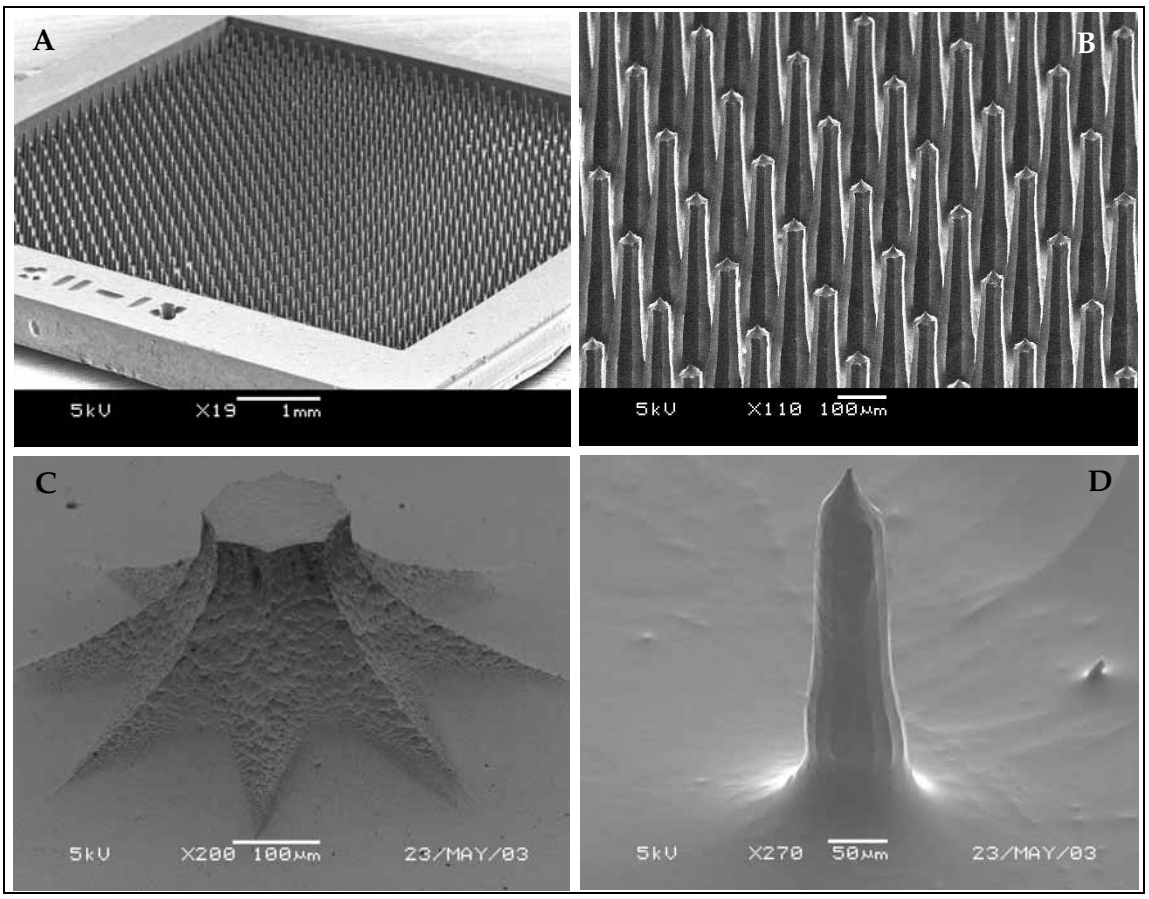

Figure 4.17 Series of pictures to describe a Planar Electrospray Thruster Array with external electrodes (not shown): isometric view *(A)*; emitter detail *(B)*; volcano emitter *(C)*; pencil emitter *(D)*.

- **Electrode assembly:** Fusion wafer bonding was selected as the method to join (in the future) the hydraulics to the electrodes and electrode to electrode. Other methods are not CMOS compatible of lack the precision required to make the electrode rings face individual emitters.
- **Highly doped DSP substrates:** The substrates chosen for the Planar Array are Highly doped (resistivities of the order of $0.5\Omega/cm$) because the hydraulics substrate back surface was used as electrode. The substrates are double side polished because both wafer surfaces are used to transfer optical mask patterns.

4.2.2 Fabrication Process Flow

Two process flows are illustrated: a fabrication process to implement the simplified Planar Arrays that were used to validate the concept, and the process flow of the full Planar Array. The latter process includes micro-fabrication of the electrodes, but was not implemented. In

key stages of the fabrication procedure of the simplified Planar Array pictures of the fabrication results are provided. In both cases 6" Si p<100> DSP, boron doped, 600 ± 5 μm thick substrates are used.

Fabrication process of the simplified Planar Array with external electrodes

The micro-fabrication procedure for these test arrays builds 100 hydraulic systems per wafer, spanning variations of emitter density, emitter starting diameter and emitter cross section shape. The engines are arranged in a 10×10 array. The process of the most complex engine, i.e., with pencil spouts, is provided here. In order to clarify the emitter formation a flow chart is provided. As will be seen in the full version of the Planar Array fabrication the key technologies to validate the engine concept are satisfactory performance of the wicking material and the fabrication of the emitters; the other hydraulics are not critical and can be implemented in different ways.

Hydraulics

- **Deposit on both sides of the substrate 11 μm of PECVD silicon oxide.**
- **Do photolithography on the top surface of the substrate transferring Mask ARRAY:** This mask has a collection of emitter modules of different emitter spacing, cross-section shape and inscribed diameter for a fixed pool area (8×8 mm).Appendix C summarizes the information of the available emitters in the mask.
- **Pattern the silicon oxide at the top surface.** This step generates the templates of the umbrella-like etching masks and the features to extract the emitters without die-sawing. The umbrellas usually are n-point stars.
- **Practice a series of DRIE steps to pattern the emitters:** Figure 4.18 is a flow chart of the emitter formation. A first isotropic DRIE is performed to sharpen the emitters while leaving in cantilever-like condition the etching mask *(a)*; then a DRIE step is used to deepen the emitters *(b)*; An isotropic DRIE / RIE finishes the desired emitter sharpening *(c)*; the remaining etching mask is removed *(d).* Figure 4.19 is an SEM picture of an emitter field after emitter deepening / before emitter full sharpening. Figure 4.20 shows a series of SEM pictures that morphologically characterize pencil emitters while Figure 4.21 shows a series of SEM pictures that morphologically characterize volcanoes.

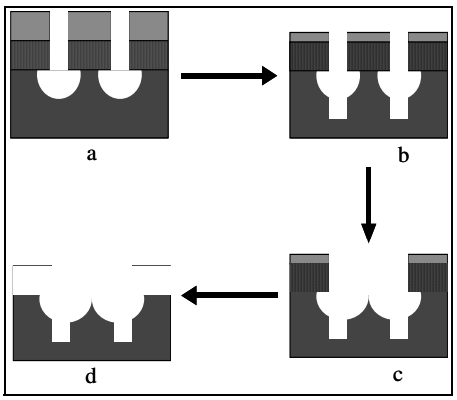

Figure 4.18 Micro-fabrication process used to pattern the emitters of the Planar Electrospray Thruster Array: the emitter formation starts with an isotropic DRIE step that starts to sharpen the emitters while leaving in cantilever-like condition the etching mask *(a)*; then a standard DRIE step is used to deepen the emitters *(b)*; then an isotropic DRIE/RIE step finishes emitter sharpening *(c)*; finally the etching mask left is removed *(d)*.

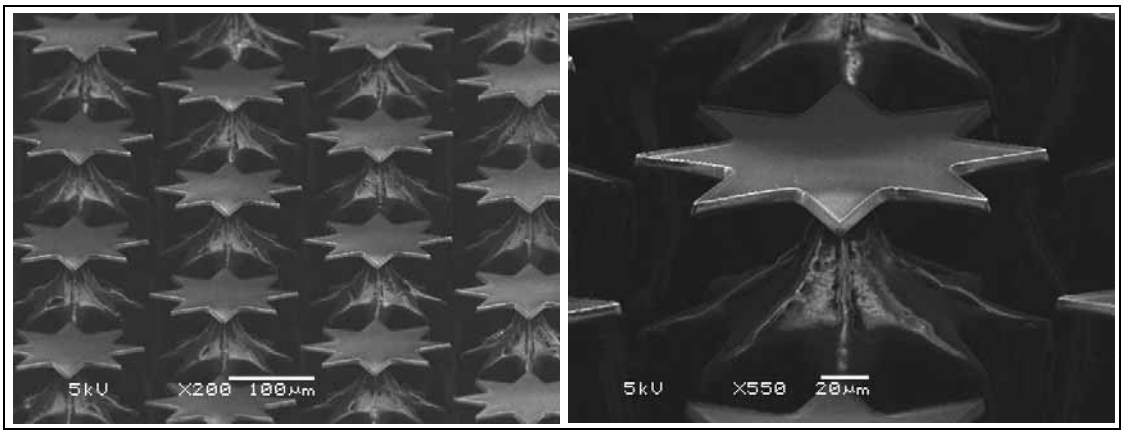

Figure 4.19 SEM picture of a Planar Array in progress of being formed *(left)* and emitter zoom (*right)*: the etching umbrellas, made of silicon oxide, about 6 μm thick, are visible. Some of the emitter sharpening and the emitter body have been formed. The excellent silicon oxide anisotropy of the etching umbrella is evident.

- **Generate everywhere on the top surface black silicon:** Depending on the etch time the black silicon morphology is different. Figure 4.22 is a summary of the preliminary morphology characterization of the wicking material.
- **Retrieve the engines by hand from the wafer:** the engine limits are carved from the emitter formation. A gentle cleavage releases the engines from the silicon wafer.

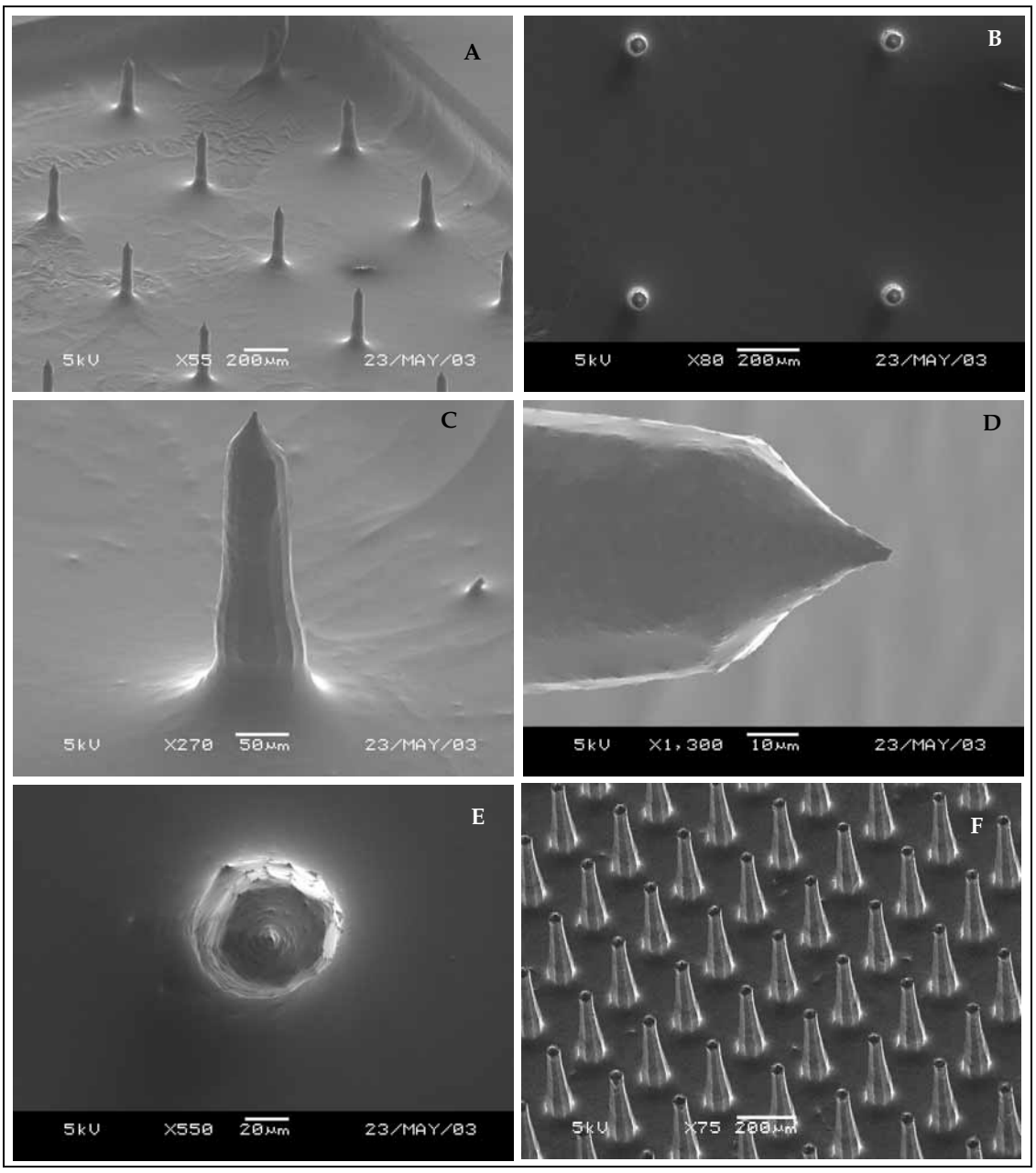

Figure 4.20 Series of SEM pictures to characterize the pencil emitter: sparsely packed pencil forest, where the pool edge can be seen *(A)*; top view of a set of sparsely packed emitters *(B)*; profile of a typical pencil *(C)*; emitter tip -the tip radius of curvature has been estimated at 2.5 μm *(D)*; top view on a pencil where small non-axisymmetry is visible *(E)*; highly packed pencil forest *(F)*.

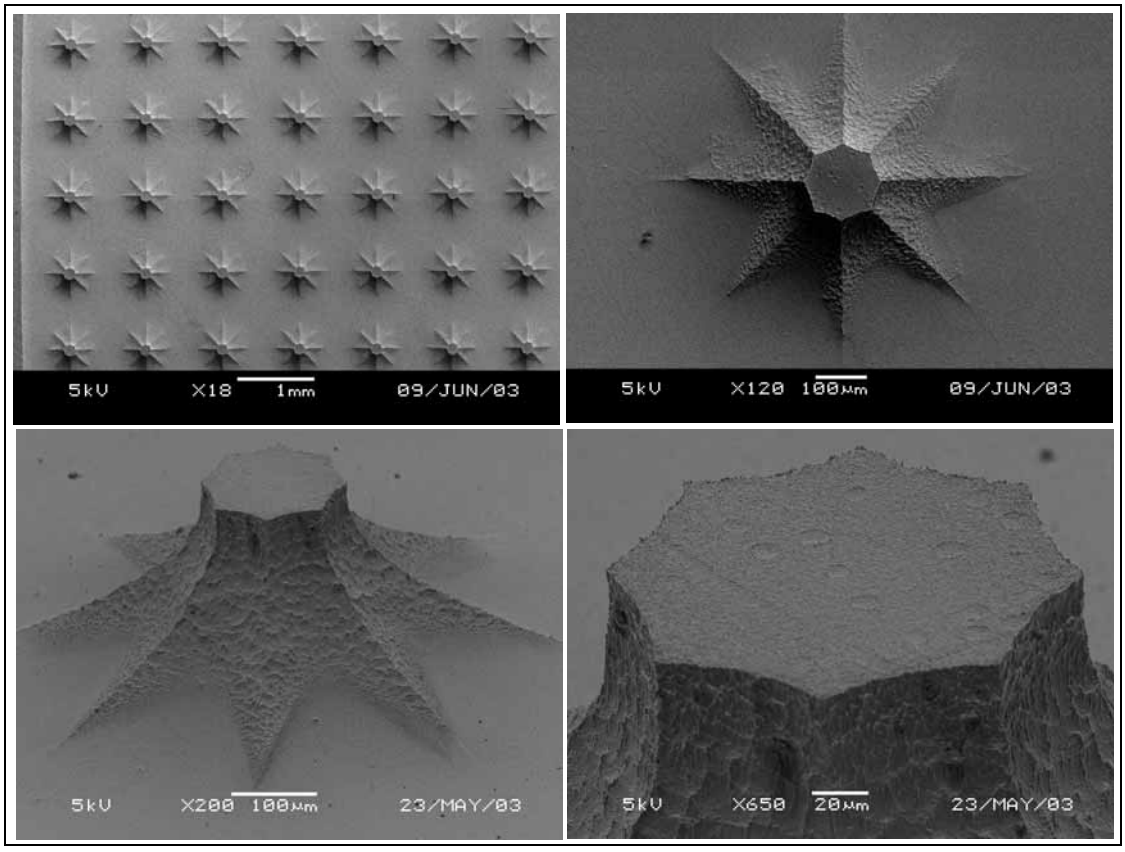

Figure 4.21 Series of SEM pictures to characterize the volcano emitter: volcano forest *(A)*; top view of a volcano *(B)*; profile of a typical volcano *(C)*; zoom of the flat emitter top with its evenly spaced sharp emitter tips - the tip radius of curvature has been estimated at 5 μm *(D)*. Volcanoes have better symmetry than pencils, and their fabrication is more robust. The angle between the lateral and top surface is virtually 90° .

Electrodes

The electrodes for the test arrays are externally provided, and not micro-fabricated. The author designed the setup, schematically shown in Figure 4.23. The fixture was build by an external vendor and the result is shown in Figure 4.24 (intended for a 4 volcano emitter array). The latter figure illustrates the fact that the clustering potential of the Planar Array is not adequately exploited by using external electrodes.

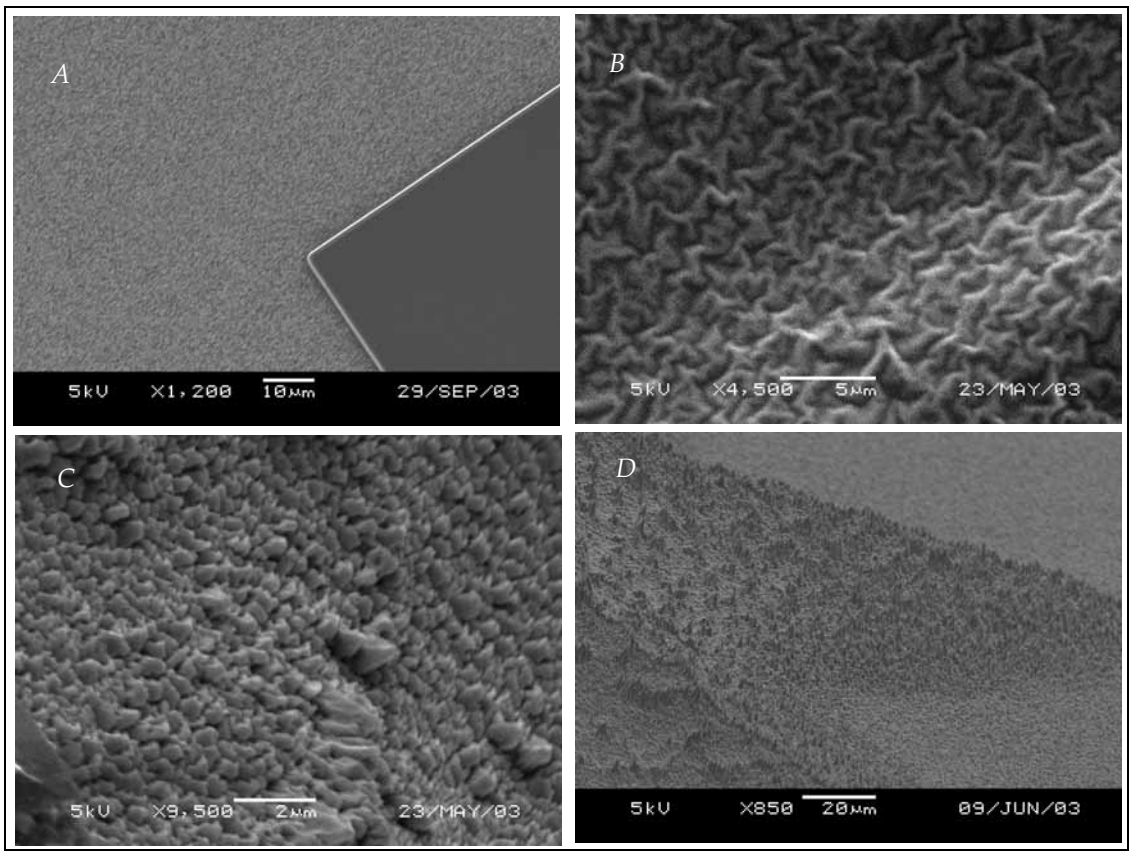

Figure 4.22 SEM picture of the morphology of a black silicon sample formed with different plasma etching times: 2 minutes -a fine grain is obtained- *(A)*; 5 minutes - wrinkled paper pattern ~1 μm deep is obtained *(B)*; 10 minutes -incipient pores 0.5 μm deep are formed *(C)*; 20 minutes - better defined pores are formed- *(D)*.

Full Version of the Planar array fabrication process

All the figures used to illustrate the process show the micro-fabrication of four emitter modules, each one composed of four emitters. Schematics of the optical masks are included for clarity because, unlike in the case of the Linear Array, a set of optical Masks was not produced. The convention used on them is black for the parts covered with chromium film and white for the open areas.

Hydraulics

- **Deposit on both sides of the substrate a thick layer of PECVD silicon oxide.**

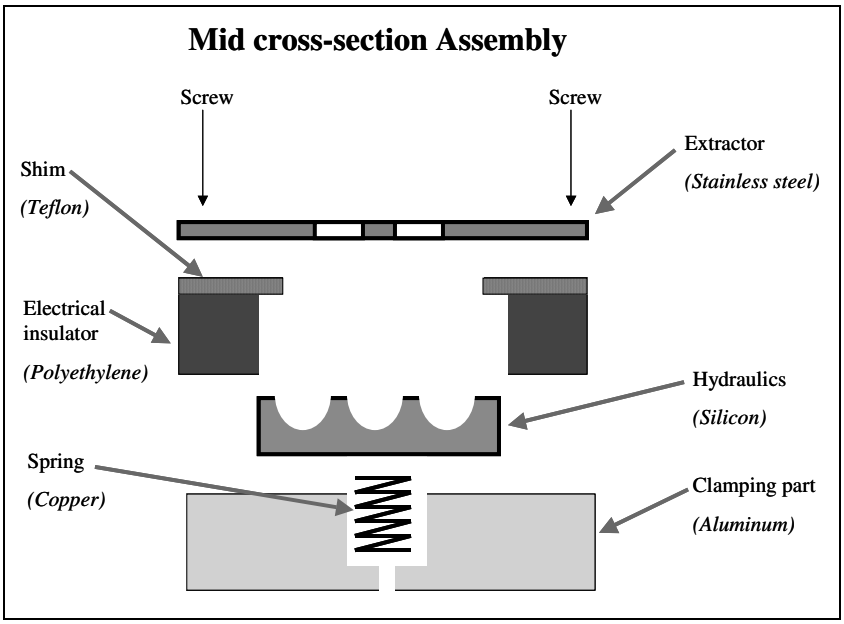

Figure 4.23 Schematic of the Planar Array with external electrodes. Only the Extractor is present in this drawing.

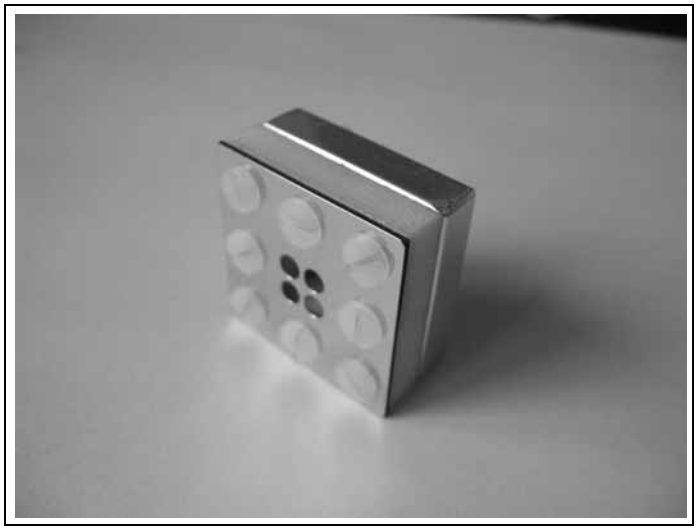

Figure 4.24 Picture of a fully assembled Planar Array with electrides. The engine is equipped with four volcano emitters.

- **Transfer the features of the irrigation channels and propellant plenum to the silicon oxide film on the top of the substrate using Mask 1 (Figure 4.25)**.

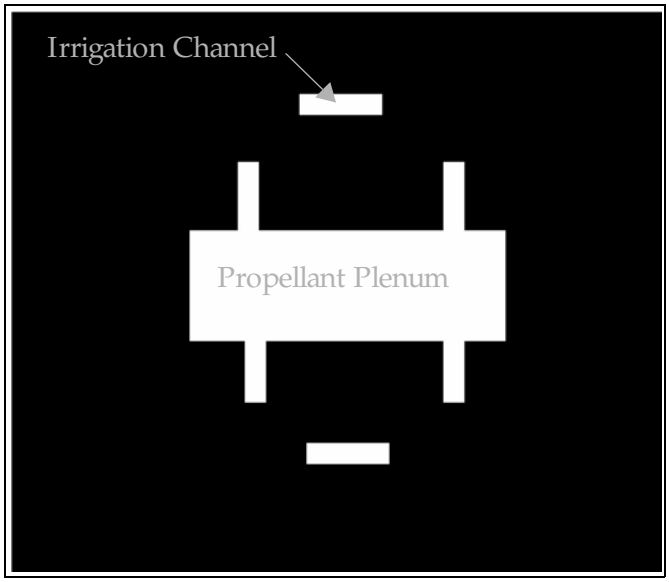

Figure 4.25 Concept view of Mask 1 for the Planar Electrospray Thruster Array.

- **Transfer the features of the electrode pad access bays and plenum inlet to the silicon oxide film on the bottom of the substrate using Mask 2 (Figure 4.26)**: Figure 4.27 is a cross-section of the hydraulics wafer at the place where the propellant inlet etching feature is placed.

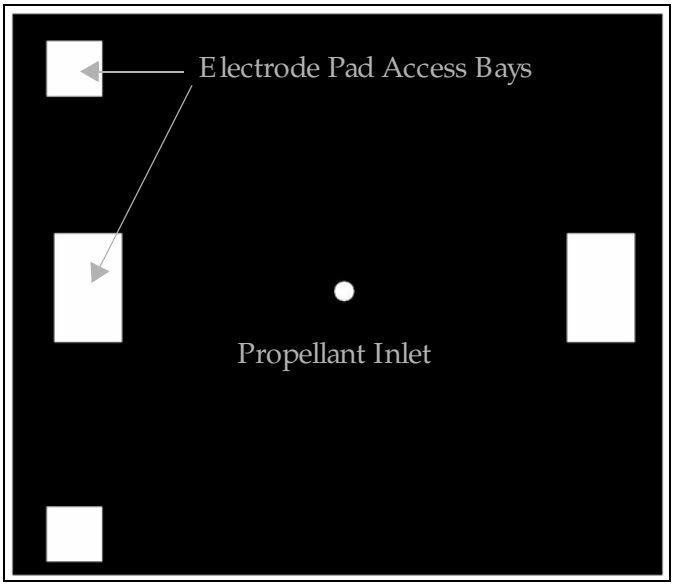

Figure 4.26 Concept view of Mask 2 for the Planar Electrospray Thruster Array.

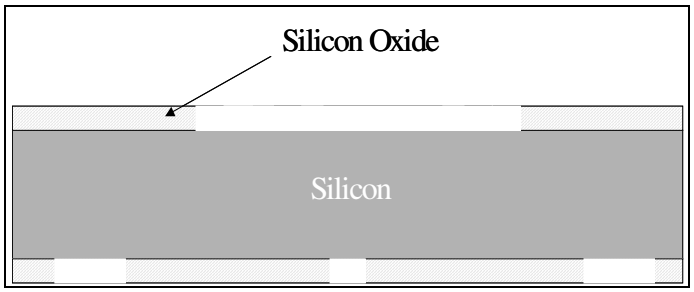

Figure 4.27 Cross-section of the hydraulics substrate after the bottom silicon oxide film has been patterned.

- **Do photolithography of Mask 3 (Figure 4.28) on the top surface of the substrate to complete a Nested Mask:** The layout contains the emitters and the propellant supply system; it also generates substrate gaps to avoid electrode breakdown.

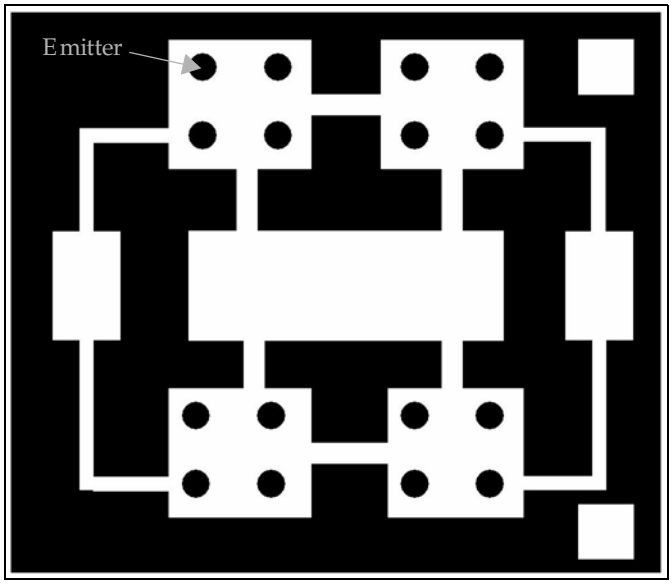

Figure 4.28 Concept view of Mask 3 for the Planar Electrospray Thruster Array.

- **Perform a DRIE step on the bottom surface to generate the fuel and parts of the electrode pad access bays.**
- **Perform two DRIE steps on the nested mask on top of the substrate to pattern the hydraulics and finish the electrode pad access bays:** Figure 4.29 shows a 3-D view of the top surface when all three DRIE steps are performed. The emitters are formed by the series of DRIE steps described in the simpler version of the Planar Array fabrication Flow.

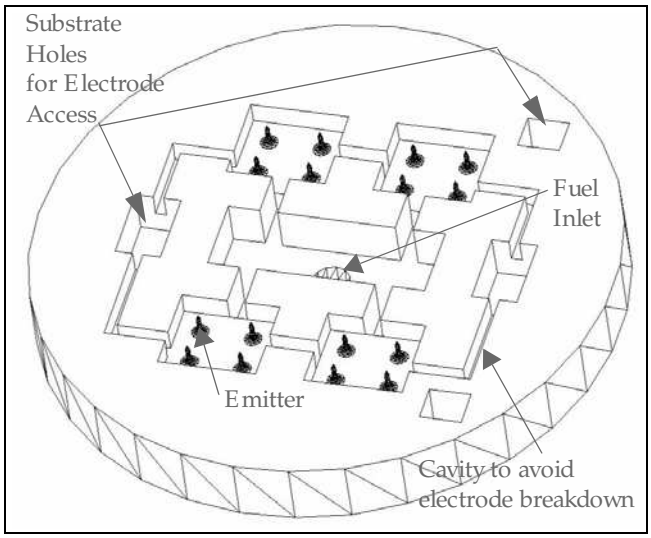

Figure 4.29 3-D view of the hydraulics substrate after the three DRIE steps have been carried out.

- **Wicking material generation**. Generate black silicon [Jansen, 1995] on the engine hydraulics.

Extractor Electrode

- **Generate a thick layer of thermal/ PEDCV silicon oxide on both sides of the substrate.**
- **Perform a CMP (Chemical Mechanical Polishing) to both surface sides of the substrate:** This step enhances the bondability of the substrate using fusion bonding.
- **Deposit a layer of LPCVD (Low Pressure Chemical Vapor Deposition) n-poly Silicon on the bottom surface.**
- **Pattern the extraction electrode conductive paths on the bottom of the substrate using the Mask 4 layout (Figure 4.30**).
- **Pattern the bottom silicon oxide layer on the bottom surface of the substrate to transfer Mask 5 (Figure 4.31):** The layout has the electrode perforations that let the emitted particles get through the extractor, and electrode pad access bays.
- **Practice a DRIE step to generate the features included in the layout of Mask 5:** A 3D view of the substrate after patterning the electrode holes from the bottom side is shown in Figure 4.32.
- **Pattern the silicon oxide film on the top surface of the substrate using Mask 6 (Figure 4.33):** The layout includes the electrode holes, the accelerator

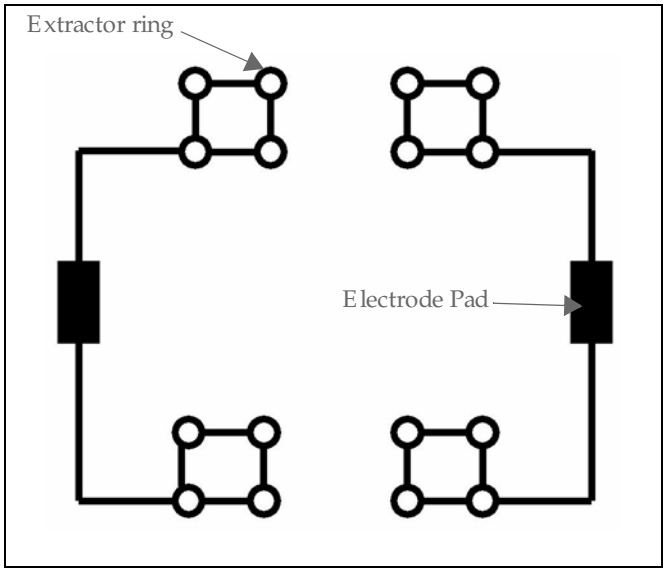

Figure 4.30 Concept view of Mask 4 for Planar Electrospray Thruster Array.

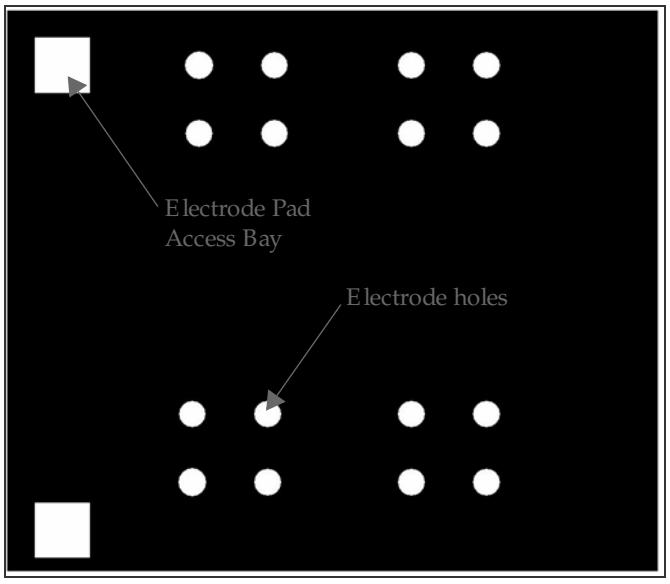

Figure 4.31 Concept view of Mask 5 for the Planar Electrospray Thruster Array.

pad access bays, and channels to avoid physical contact to the accelerator conductive paths.

- **Perform a DRIE step on the top surface to generate the features included in Mask 6**.

- **Perform a DRIE step without passivation on the top surface to generate the features included in Mask 6**: This step widens the electrode exit holes to generate a geometry like the one used in the Linear Array. Figure 4.34 shows a substrate cross section and 3D view of the extractor substrate after all the fabrication steps are carried out.

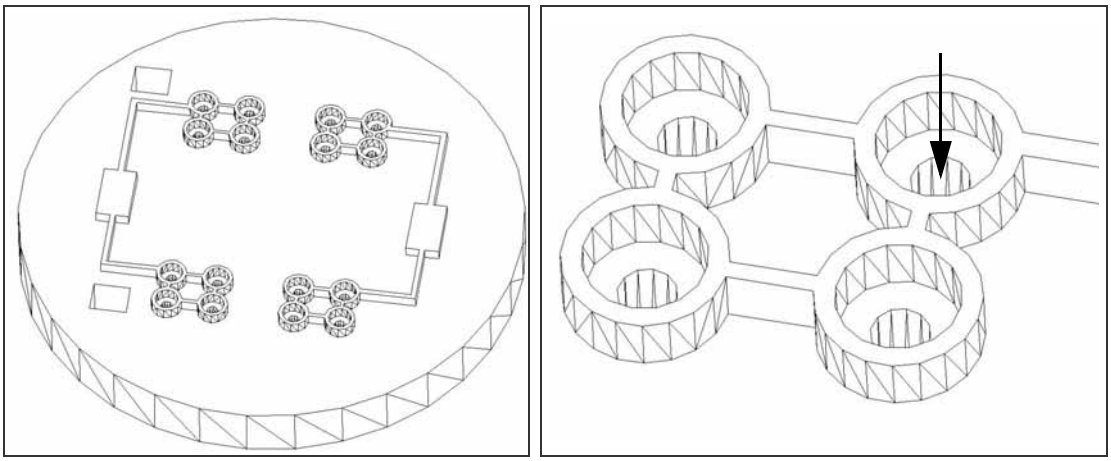

Figure 4.32 3-D view of the extractor substrate after electrode patterning and electrode holes (bottom surface portion) are formed, field view (*left*) and detail *(right*). The arrow indicates the flow direction. The electrode thickness has been exaggerated.

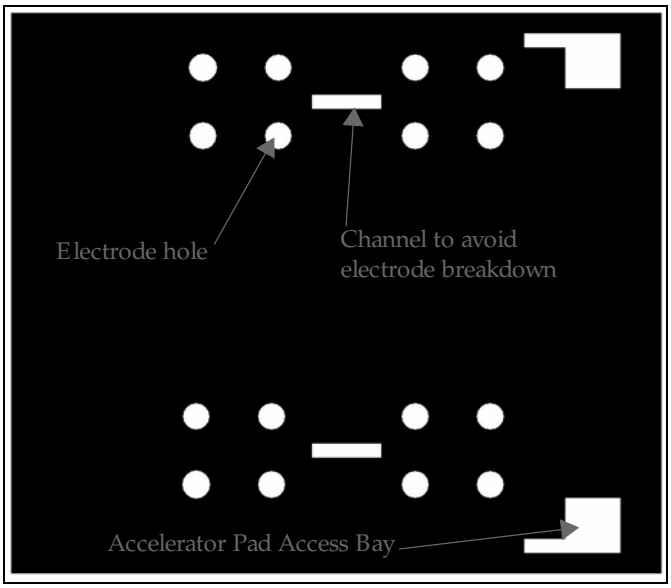

Figure 4.33 Concept view of Mask 6 for the Planar Electrospray Thruster Array.

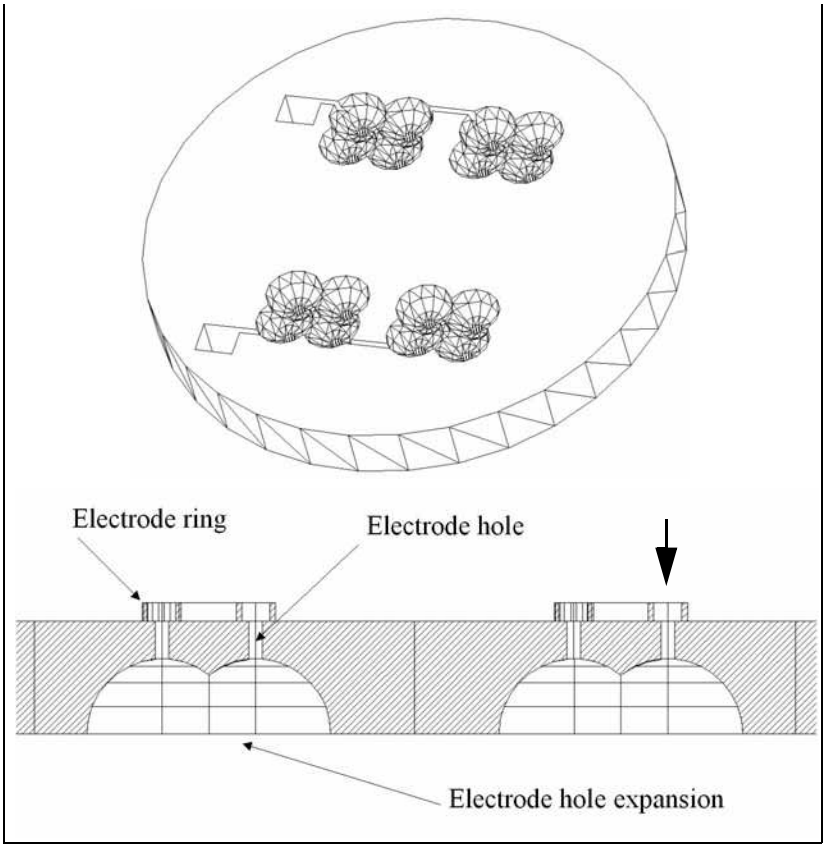

Figure 4.34 Extractor substrate 3D view *(above)* and cross-section *(below)*. The arrow symbolizes an emitter aligned to the extractor grid.

Accelerator

- **Generate a thick layer of thermal/ PEDCV silicon oxide on both sides of the substrate.**
- **Perform a CMP (Chemical Mechanical Polishing) to both surface sides of the substrate:** The step increases bondability of the substrate using fusion bonding.
- **Deposit a layer of LPCVD n-poly Si on the bottom surface.**
- **Pattern the LPCVD poly-Si film using Mask 7 (Figure 4.35):** This mask has the accelerator electrodes layout.
- **Pattern the silicon oxide film on the bottom of the wafer using Mask 8 (Figure 4.36):** The mask layout contains the accelerator electrode holes.
- **Practice a DRIE step to carve the exit hole features:** Figure 4.37 is a 3D view of the accelerator substrate after the fabrication process is completed.

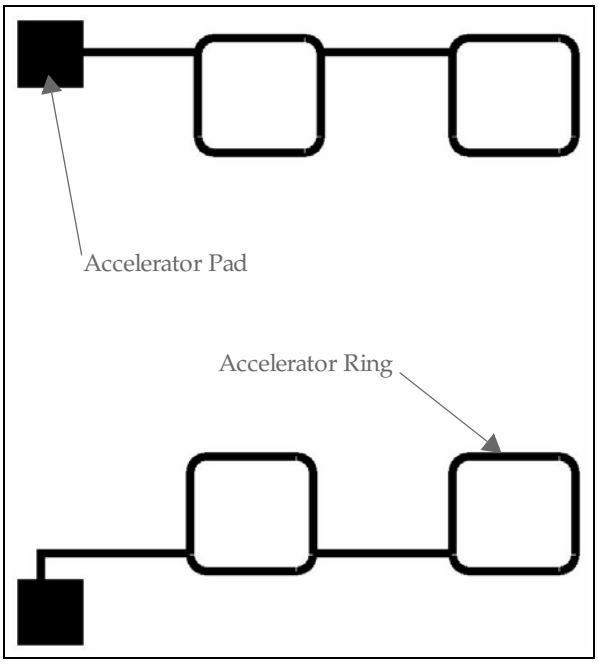

Figure 4.35 Concept view of Mask 7 for the Planar Electrospray Thruster Array.

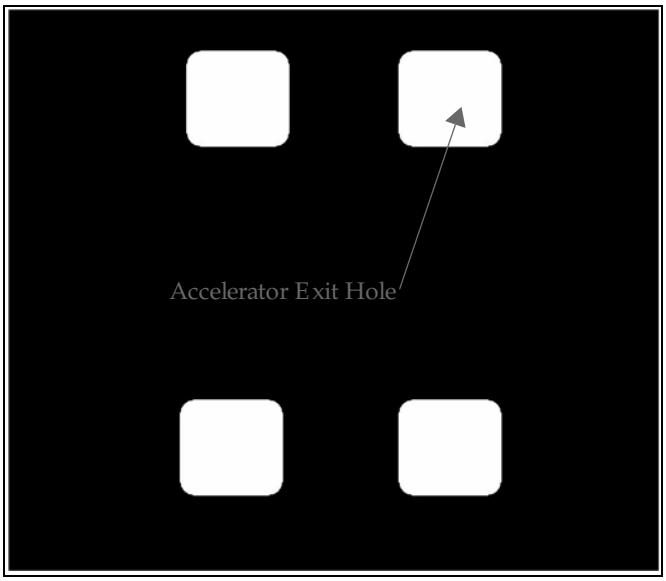

Figure 4.36 Concept view of Mask 8 for the externally fed Planar Electrospray Thruster Array. This optical mask patterns the accelerator electrode holes.

The three substrates the substrates are finally fusion bonded.

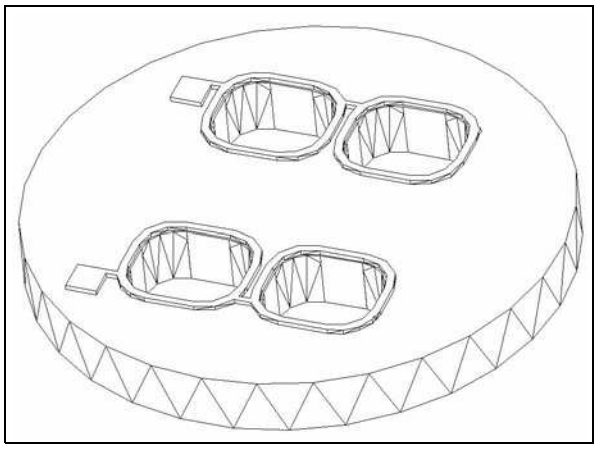

Figure 4.37 3D view of an accelerator substrate after fabrication is done.

4.3 Results of tests on the Simplified Planar Array

The feasibility of the Planar Array Concept was demonstrated through a series of tests. The goal was to demonstrate steady - uniform emission for arrays of emitters. All the tests were carried out in DC, using a polarity (negative emission) that would produce outgassing, but not deposition in the counter-electrode. The results from experimentation are

- Wettability tests validated the proposed external architecture concept.
- Cumulative uniform emission was demonstrated using the impact deposits on the Collector for several Arrays.
- Steady uniform emission was demonstrated from I - V measurements.
- An increase of the emitter current due to temperature increase demonstrates the possibility to implement temperature control. This fact allows to span a larger I_{sp} / thrust range.
- Starting voltages are in agreement with the finite element results and the values predicted by equation 3.32. Differences in the starting voltage for different runs of similar Planar Arrays are believed to be caused by differences in the electrode-to-emitter separation due to assembly.
- Emission from the Planar Arrays seems to be describable by a simple exponential fit. There is uncertainty on the power for the voltage dependence.

Developing a theoretical model of field emission using ionic liquids would probably need a strong effort because there are several effects that are not taken into account by the field emission models developed for electrons:

- The emission is of solvated ions and the liquid has finite conductivity, viscosity and dielectric permittivity.
- There is a strong variation of the electrical conductivity and the viscosity for ionic liquids with respect to temperature.

Nonetheless, there are fairly good models about ion emission from metals [Mair, 1991] and they can probably be extended and adapted to ionic liquids.

In the ion regime there is a direct proportionality between the emitted current and the propellant expelled. In other words, key features such as flow rate matching might be needed to be taken into account to accurately describe the emission phenomenon.

4.3.1 Testing facility

A setup to provide the hydraulics of the Planar Array with a collector has been designed and built by the author, taking advantage of the fact that the implemented Planar Array has non-micro-fabricated electrodes. The experiments were done in a vacuum chamber equipped with two 70 liters/sec. turbo-pumps, providing ultimate pressures under 10-7 Torr; experiments were carried out starting at about 5×10^{-5} Torr.

The emitter-to-collector separation was set at 250 μm. The engine received propellant at the moment of being assembled to the testing facility. Measurements of current using both a current meter (current collected by the external electrode) and the potential drop of a $102 K\Omega$ resistor in series with the engine (current emitted from the power supply) were carried out while spanning a voltage range. The facility included a distributed heater and a thermocouple to allow temperature-controlled experiments. Figure 4.38 shows the schematic of the testing facility where a brief description of its constitutive parts is available, and Figure 4.39 shows a picture of a fully assembled testing facility (engine is inside).

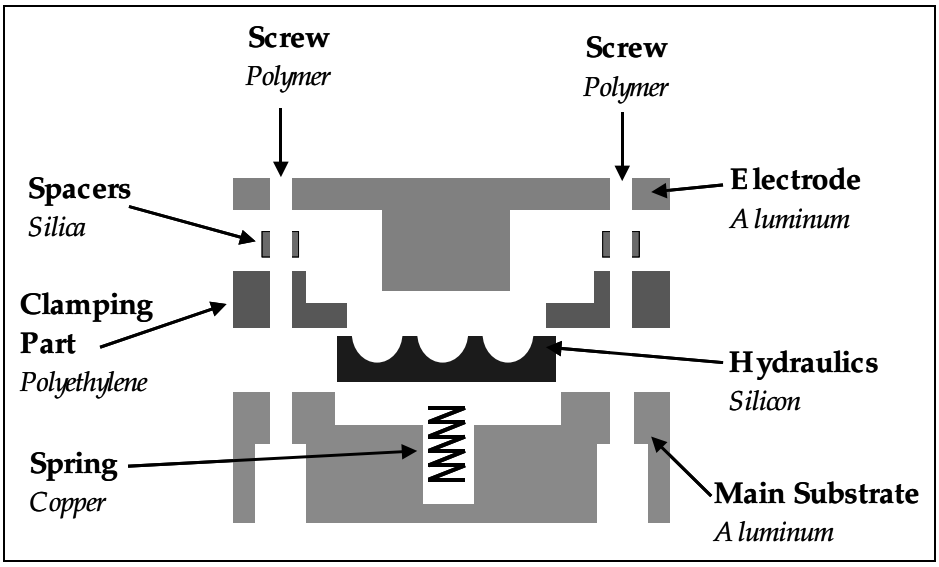

Figure 4.38 Cross-section of testing facility used to characterize the externally fed Planar Electrospray Thruster Array.

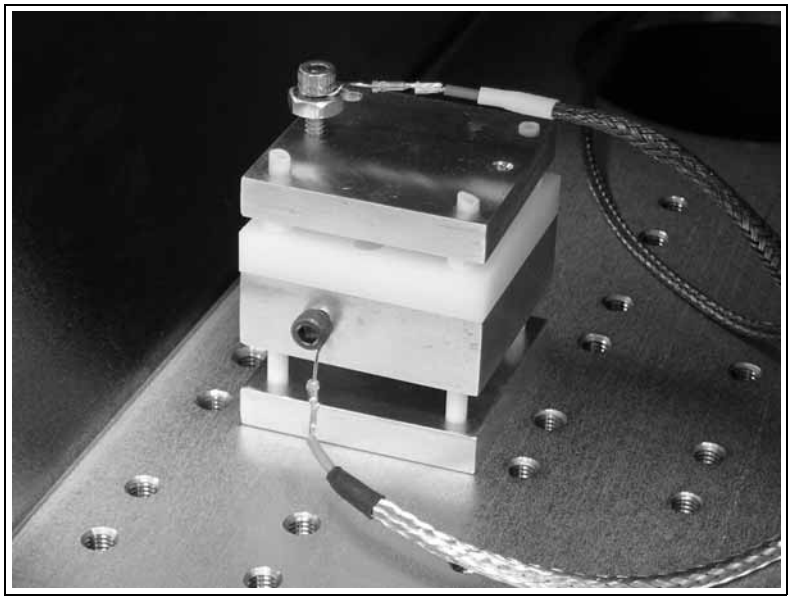

Figure 4.39 A fully assembled Planar Array Testing Facility.

4.3.2 Results and discussion

The following is an overview of the experimental results obtained to validate the proposed Planar Array. Appendix D can be found useful to better understand the I-V behavior obtained experimentally.

Wettability tests

A series of tests were done as a preliminary exploration about the optimal roughness/porosity using the black silicon layer as a wicking material in the Planar Array. The optimum morphology should depend on two counteracting effects:

- A larger wicking material free surface will pull more liquid, provided it does not severely interfere with itself, i.e., it is mainly open.
- A larger free area is related with pore growth and thus more hydraulic impedance.

A simple test method was implemented to diagnose the wettability of black silicon: to use a fixed liquid size (3 μL), use a long narrow capillary to put it in the center of a treated surface, and see what happened during a small period of time. A battery of tests with different black silicon formation times was made. The tests demonstrated that $EMI-BF_4$ wets well black silicon, and that there is an optimal formation time to achieve maximum wettability. The tests were qualitative (wetted / non-wetted status change), i.e., no estimates of the flowrate moved by surface tension were made.

Figure 4.40 (A) shows a section of a forest of *bottles* (under-sharpened pencils) before supplying the propellant. Figure 4.40 (B) is a picture of the same region 2 minutes later, after the propellant has completely wetted the emitter pool.

The following are the conclusions on the preliminary characterization of the wettability properties of black silicon for different formation times:

- **Black silicon with 5 minutes of formation time:** Bulk front substantially lags wetting front (Figure 4.41, left).

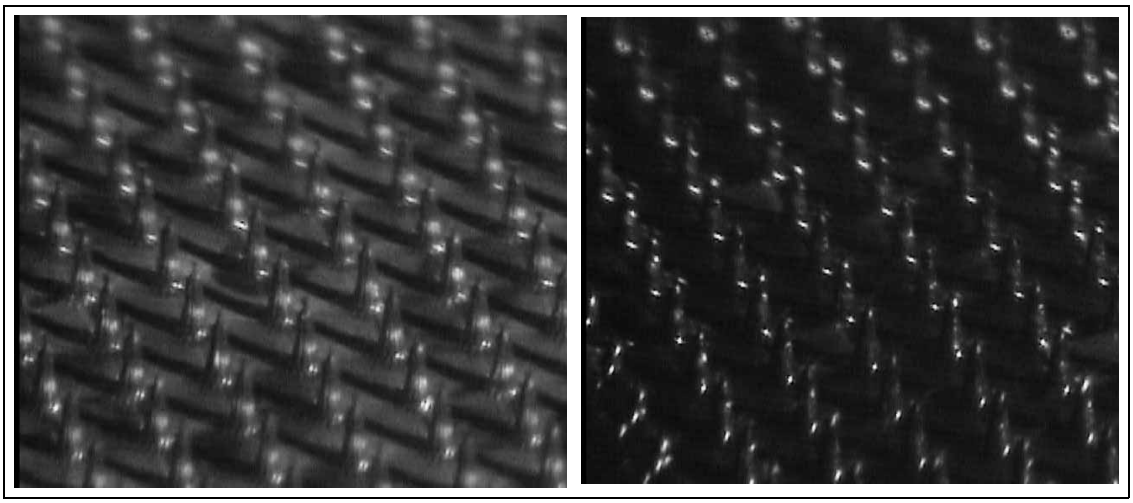

Figure 4.40 Series of pictures to demonstrate the wettability of black silicon with $EMI-BF_4$: Picture of a bottle forest before placing the ionic liquid sample in the middle of the array *(A)*; Picture showing the same set of emitters a couple of minutes after placing the propellant droplet in contact with the black silicon surface.

- **Black silicon with 10 minutes of formation time:** The advance of the wetting front and liquid bulk were far faster than in the previous case. The two speeds were indistinguishable. This sample proved to have the best characteristics for wetting the surface (Figure 4.41, center).
- **Black silicon with 20 minutes of formation time:** The liquid still wetted well the surface but both the liquid bulk and the wetting front moved far slower than in the case with 5 minutes of formation time. The bulk liquid and the wetting front moved at about the same speed (Figure 4.41, right).

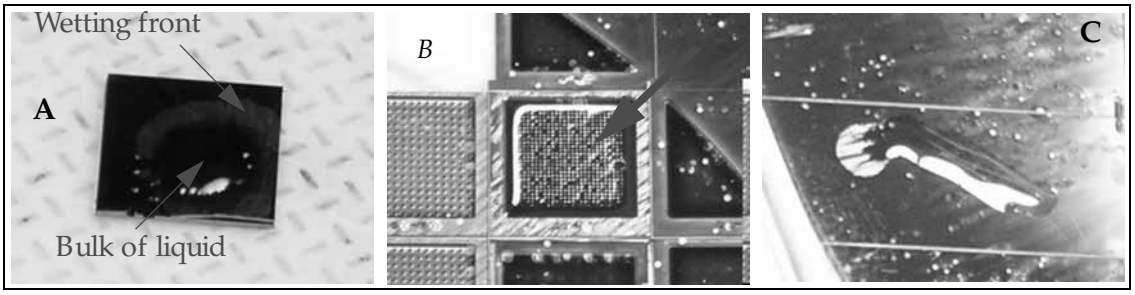

Figure 4.41 Series of pictures to characterized the wettability of black silicon with $EMI-BF_4$ for different black silicon formation times: 5 minutes *(A), 10 minutes (B)*, 20 minutes *(C)*.

Emission uniformity

A series of four room temperature tests using the testing facility described before were carried out to validate the mission uniformity of Planar Arrays with different emitter densities. The cumulative deposits on the Collector were used as evidence of uniform emission. The small fluctuations in the current measurements are evidence of steady operation. The current fluctuations might be caused by gas generation by the propellant due to electrochemical effects. Also, two tests were carried out using Planar Arrays with the same emitter kind but with different emitter numbers (2×2, 8×8).

A comparison of the current per emitter vs. extraction voltage suggests uniform emission and the existence of some transition region. Some unusual effects were found while obtaining the experimental curves, probably due to momentary propellant starvation caused by propellant bursts: it was possible for the measured current to fall and maintain a smaller value; after decreasing the extraction potential, waiting for a while and then increasing the extractor voltage again, the current reading was back to normal. Nonetheless the curves obtained were repeatable outside of these transients and varied little between identical emitters made on the same batch.

A fan divergence equal to $14°$, with an axis inclined about $41.4°$, was obtained for the volcano emitters. An untitled axis fan and a divergence angle equal to $9.5°$ was obtained using metrology of the collector impacts of pencil emitters. It was also established experimentally that the emission points of volcano emitters are the sharp points at the top surface - lateral surface interface.

Figure 4.42 is an optical picture of the collector electrode after the test of a 2×2, 8-tip volcano emitter Planar Array (emitter-to-emitter separation is 4000 μm).

Each of the dots shows a blank zone (area without visible deposits) surrounded by a corona, presumably made of propellant. Minor differences in the corona size and morphology between different emitters are perceived. This corona is substantially larger than the top sur-

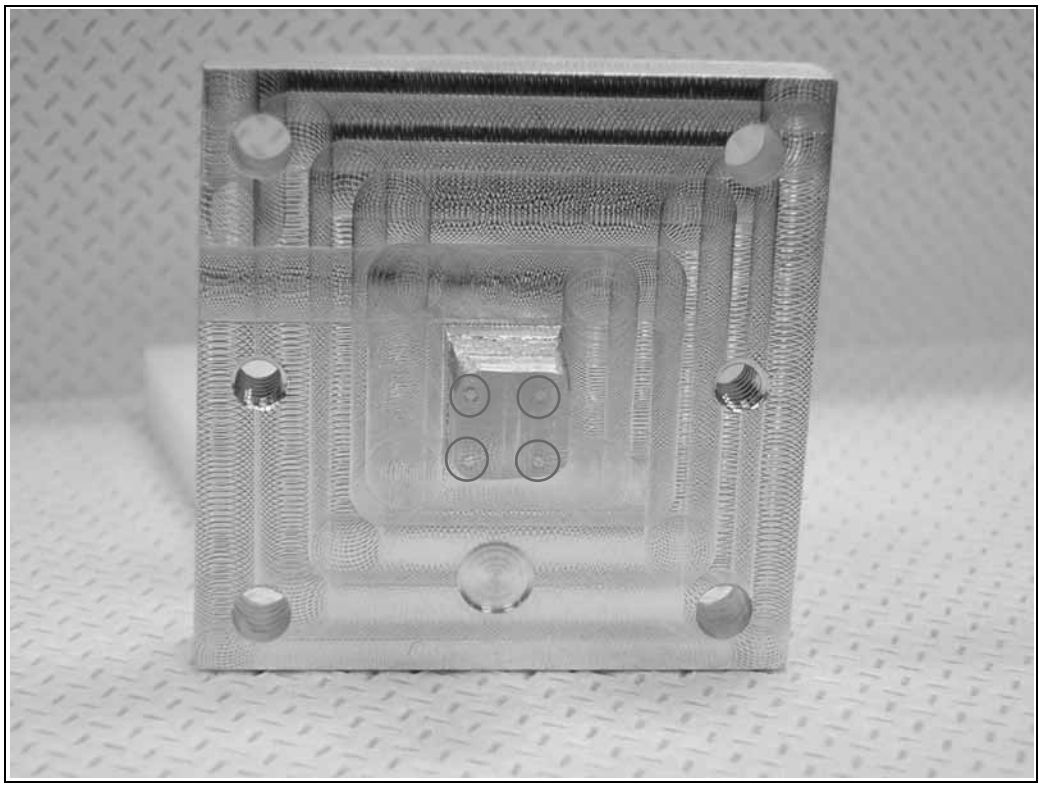

Figure 4.42 Optical picture of the collector electrode impact pattern after the first Planar Array test. The impact sites are surrounded by drawn circles. This pattern demonstrates good emitter-to-emitter uniformity.

face of an emitter (the corona diameter is about 260 μm, the emitter top surface diameter is about 90 μm), evidencing beam tilting & fan divergence (see Figure 4.46).

Figure 4.43 shows the impact pattern left on the external electrode when using a 4×4 8-point volcano emitter Planar Array. There are visibly eleven impacts, as expected because the electrode area is smaller than the engine emitter area (6.8×6.8 mm versus 8×8 mm). The impacts are still fairly uniform, evidencing emitter-to-emitter uniform emission. Two key results compelled us to take a SEM picture of the Planar Array used in the test:

- The corona marks were substantially smaller than in Figure 4.42.
- One of the emitters directly under the external electrode collecting area did not leave any pattern.

From Figure 4.44, a SEM picture of the Planar Array used in the experiment, it is clear what happened: the emitters were overetched volcanoes (~pencils) and one of them was missing.

This particular engine was part of a wafer that was processed with the intention to get volcano arrays with an starting cross-section larger than the starting cross-section of the emitters of this array. The fact that this Array needed a substantially larger starting voltage corroborates that the volcanoes were overetched.

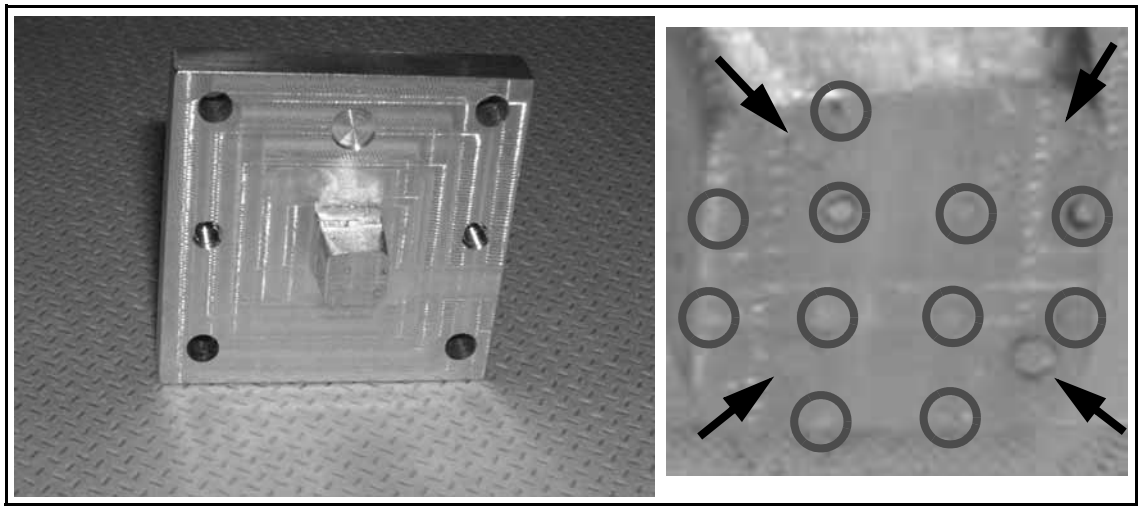

Figure 4.43 Propellant impacts on the external electrode after testing a 8-point volcano 4X4 emitter array *(left)* and zoom *(right)*. Eleven impacts are clearly visible showing good uniformity (encircled by drawn circles). The previous 2X2 emitter pattern is visible to some extent after cleaning the electrode for the second test (arrows).

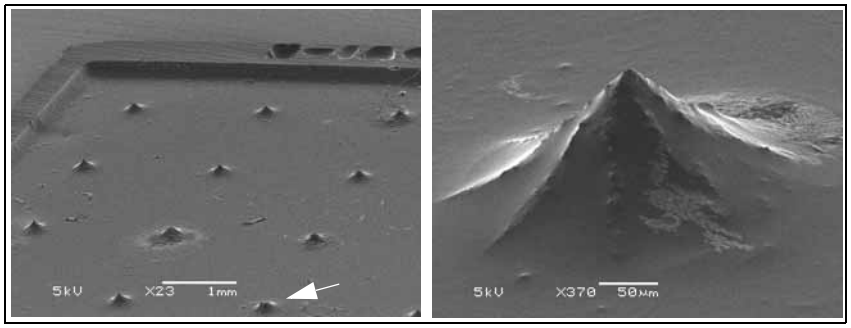

Figure 4.44 SEM pictures of a 4X4 Planar Array used in the second test *(left)* and emitter zoom *(right)*. The volcano emitters were over-etched and thus their emitter-to-electrode separations increased. One of the emitters is missing as evidenced from the impact data (arrow).

Figure 4.45 is a collage (it became common practice to reconstruct macro electrode pictures based on partial SEMs) of SEM pictures of the collector electrode surface after a test of an

8×8 8-point volcano emitter array with exactly the same emitter dimensions of the Planar Array used in the first test, emitter-to-emitter separation equal to 1000 μm. A 6×6 impact array is present, as expected from the area difference between the collector and the emitter pool. There are also about ten impact points, at the spacing sites expected from the emitter array configuration, that are partially visible on the collector area because their fan fell outside the coverage range (only portions of the fan are visible).

The structure of the coronas is now revealed with more detail: even though they look roughly axisymmetric, there is clarity in the way the coronas are transferred: there are eight equally distributed preferential directions, suggesting the eight sharp points the emitters have at the top surface edge, implying that this kind of emitters develop, as expected, Taylor cones at each sharp point. The impacts also suggest that the emission is tilted a certain angle with respect to the flat top normal. The existence of a blank spot at the center of the corona implies that this area is not reached by the charged particles; assuming the divergence of each of the charged particle fans to be describable by a single divergence angle around a certain tilted axis, then the conclusion is that this axis is tilted some quantity with respect to the emitter top surface (which is parallel to the collector surface). Using the last figure for in-plane metrology and knowing that the emitter-to-collector separation was about 250 μm, the semi-angle for each individual fan is equal to $14°$, with an axis inclined about $41.4°$, as shown in the schematic of Figure 4.46. The author was expecting a value around $45°$ for the tilting angle because that is the original orientation angle of the edge sharp points; some deviation from this value might be due to the electrical field that pulls the emitter fans upwards.

Structural integrity of the emitters after a few hours of operation was verified with SEM pictures after the tests (Figure 4.47). This picture shows an emitter with complete physical integrity, covered with ionic liquid (it does not vaporize in vacuum). The absence of emitter structural damage is understandable because the propellant covers the emitter and protects it from impacts up to penetration depths of the order to the propellant film thickness.

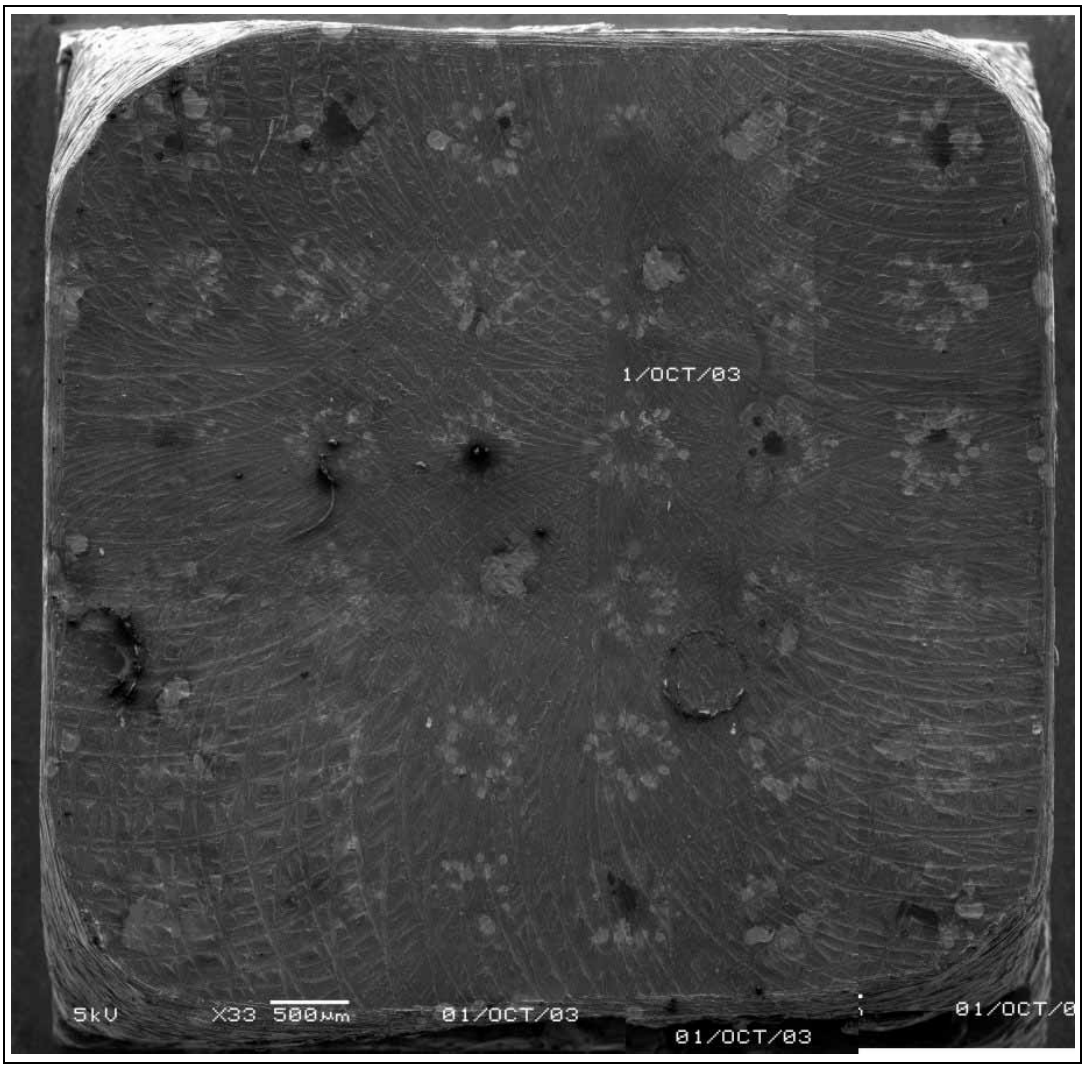

Figure 4.45 Collage of SEM pictures that map the impacts on the collector electrode for a 8×8 Planar Array. Traces of the previous two tests are visible, but fortunately are mild enough to allow appreciation of the latest emitter pattern.

Finally, Figure 4.48 is a collage of SEM pictures of a 32×32 pencil emitter array. There is a second pattern superimposed to the clean impact dots that resemble the emitter array. This secondary pattern is not well arranged and may have two possible sources:

- Surface creep of the propellant because of the roughness of the external electrode. This explanation is supported by SEM pictures such as Figure 4.50 where the secondary traces follow the machining strokes.

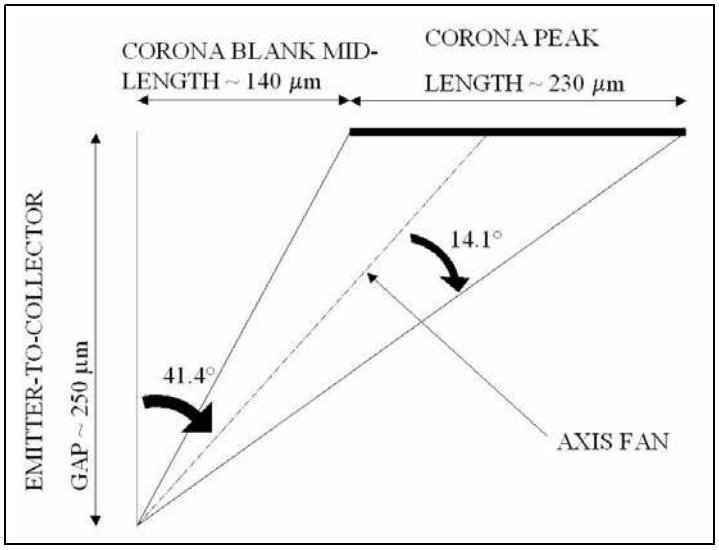

Figure 4.46 Schematic to illustrate the fan semi-angle and the fan axis tilting angle, based on the corona peaks.

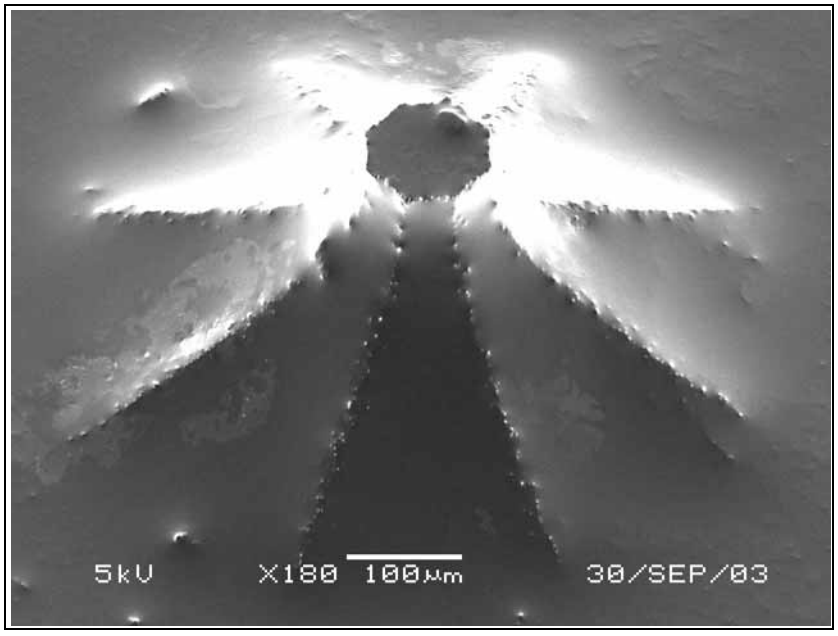

Figure 4.47 SEM picture of a tilted volcano after testing the emitter array it is part of. The glowing at the surface is due to the conductive behavior of the ionic liquid completely covering it.

- Some emitters might have secondary emitter tips and maybe expelled some propellant in disagreement with the emitter array pattern. There can be other sharp tips at the emitter top surface, not directly aligned with the main pencil

direction (Figure 4.49): they might get activated, specially at the largest extraction voltage values used when obtaining the characterization curves.

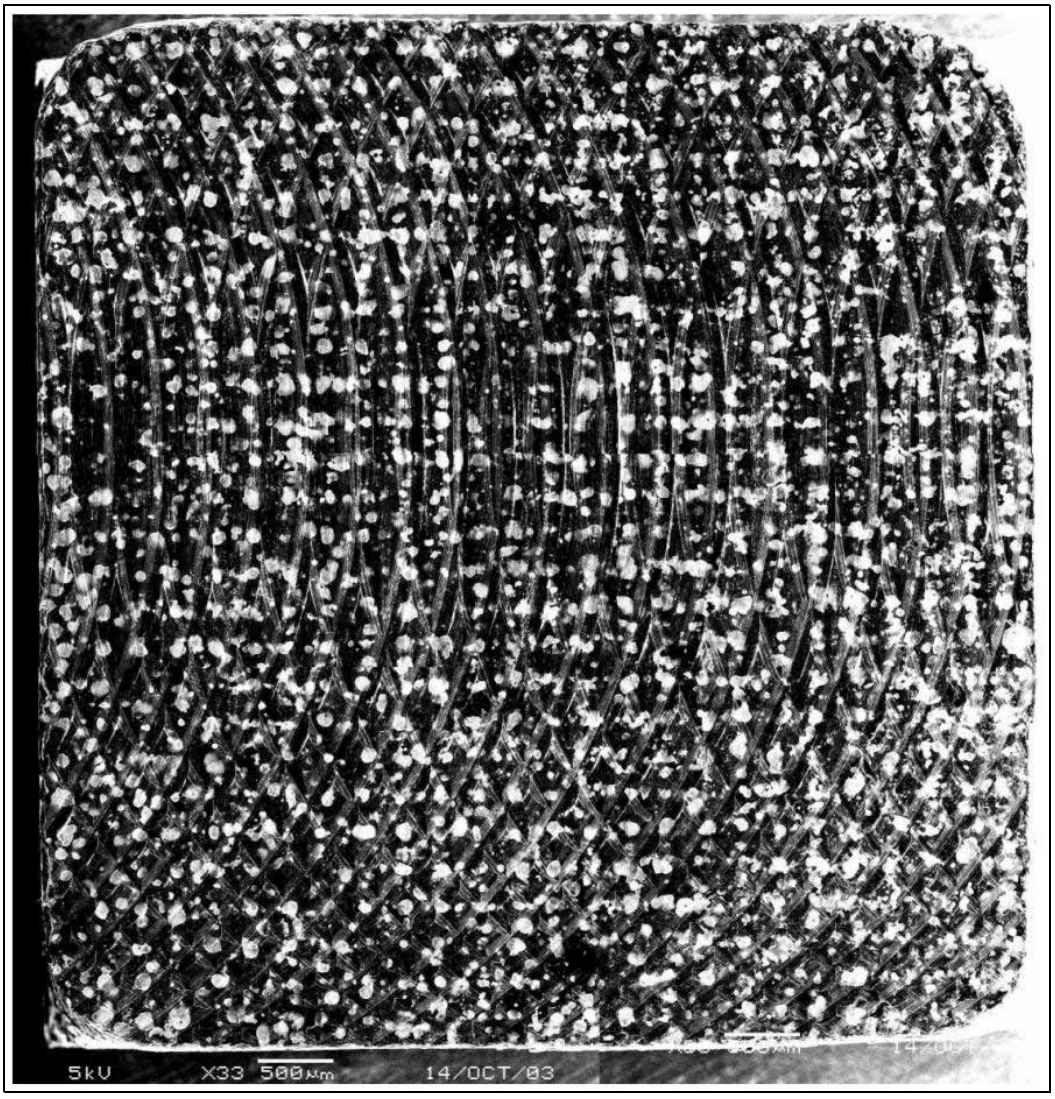

Figure 4.48 Impact pattern of the external electrode used to test a 32×32 pencil emitter array. Good emitter to emitter uniformity is evidenced for this highly packed emitter array. Some propellant was displaced because of surface tension driven flows at the electrode surface due probably to the inherent machining roughness.

Figure 4.51 is a SEM picture of one of the impacts. The imprint is fairly axisymmetric. The impacts also suggest uniform space charge distribution and a sharp fan edge. The divergence semi-angle was found equal to $9.5°$. This divergence value is of the same order of the divergence angle obtained for volcano emitters, and experimental results reported in the literature

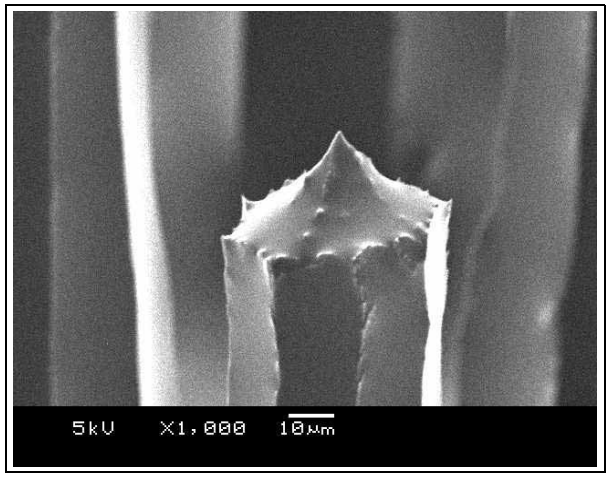

Figure 4.49 Emitter tip zoom of a 32×32 Planar Array. Some secondary emission points are present at the base of the emitter top surface.

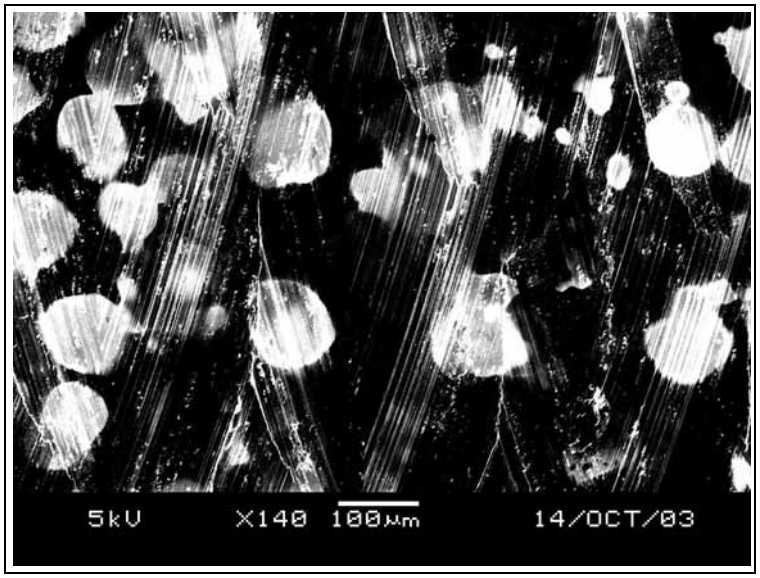

Figure 4.50 SEM zoom picture of the impact pattern on a 32×32 pencil emitter Planar Array used in the last uniformity test. The emitter-to-emitter separations are in excellent agreement with the emitter-to-emitter distances in the array. This picture makes it evident that a substantial propellant surface transport takes place along the end mill traces. This material transport explains a good portion of the secondary pattern seen in the external electrode.

($\sim 14°$). A possible explanation for the small divergence angle is the stronger electric field surrounding the pencil emitter tip (stronger electric fields focalize the beam). It is also possible that the macro-sized solid needles that are used in most of the experiments have more than

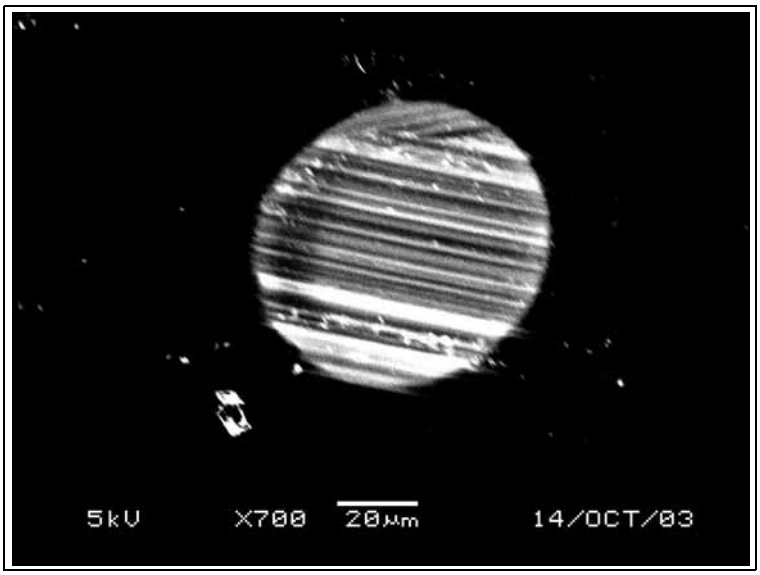

Figure 4.51 Typical emitter impact of the principal impact pattern. The individual impact mark evidences good axisymmetric emission, uniform emission and an divergence semi-angle equal to 8.5°

one emission point because they have a less sharpened tip and local roughness might be able to initiate propellant emission.

Figure 4.52 shows the experimental data obtained from a 2×2 8-tip volcano emitter Planar Array. The starting voltage was 1567 V; the maximum emitted current was 1.176 μA @ 3000 V. The estimated current-per-emitter at the largest extraction voltage is equal to 294 nA (36.75 nA per sharp point of the volcano emitter).

Figure 4.53 shows the experimental data obtained from a 8×8 8-tip volcano emitter Planar Array. The activation voltage was equal to 1350 V. The maximum emitted current @ 3337 V was 14.7 μA. For an estimated emitter population of 40 emitters (36 complete coronas and 10 half-coronas are seen on the electrode) gives a current-per-emitter equal to 367.5 nA, and 46 nA per sharp point at this voltage, values in the same range as the ones obtained with externally fed single emitters, made of tungsten [Lozano, 2003].

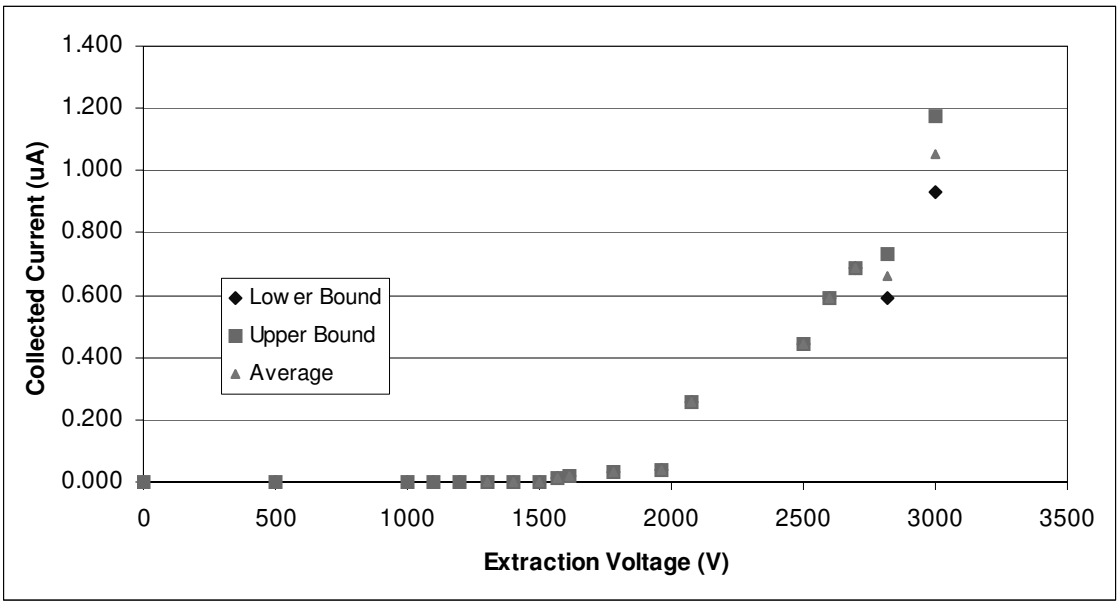

Figure 4.52 I - V plot for a 2×2 8-tip volcano emitter Planar Array, Electrode Separation equal to 250 μm.

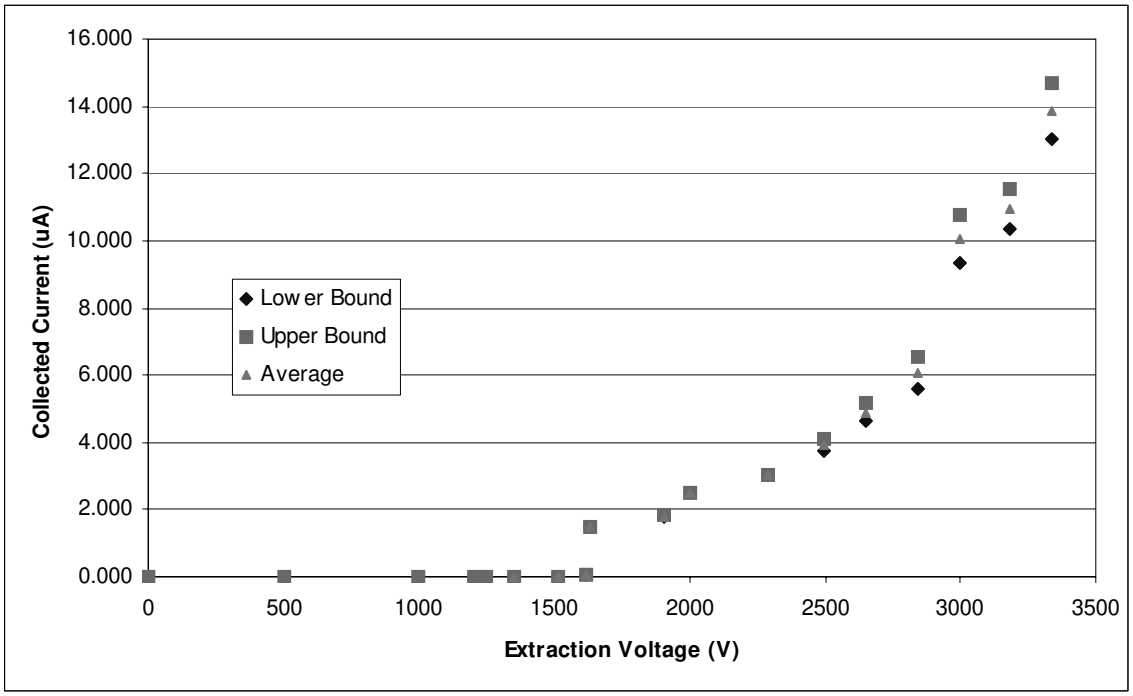

Figure 4.53 I - V plot for a 8×8 8-tip volcano emitter Planar Array, Electrode Separation equal to 250 μm.

Figure 4.54 and Figure 4.55 show the I - V per-emitter characteristic plot. The emissions from equal emitters coming from different emitter array densities do agree, except of a preliminary *transition region*. There is a region near the starting voltage that is believed to contain the transition from a fully off engine to a fully on. The transition region might be related with the starting of emitter sets due to electrode-to-emitter separation differences.

Based on the field emission models briefly discussed in Appendix D we expect some experimental behavior of the type

$$I = I_o \cdot e^{A \cdot V^n} \tag{4.1}$$

Where n is some real exponent. In particular three n-values were considered: 0.5, 1 and -1, respectively for Schottky-like, Poole Frenkel -like and Fowler Nordheim -like emission:

- For n = 1 a regression fit predicts the I- V dependence with a correlation of 0.9895 as

$$I = I_o \cdot \exp(V/V_o) \tag{4.2}$$

- where V_o is equal to 712.12 V and I_o is equal to $3.43 \times 10^{-3} \mu A$ (Figure 4.54).
- For n = 0.5 a regression fit predicts the I- V dependence with a correlation of 0.9864 as

$$I = I_o \cdot \exp([V/V_o]^{0.5}) \tag{4.3}$$

  where V_o is equal to 52.41 V and I_o is equal to $1.12 \times 10^{-4} \mu A$ (Figure 4.55).
- Figure 4.56 show the data assuming n = -1. In this plot it can be seen that the data are not as well described by this model compared to the two previous cases.

Starting Voltage

Based on the finite element simulations the starting voltage should be about 2400 V for an emitter-to-electrode separation equal to 250 μm; the value predicted by equation 3.30 for $EMI-BF_4$ predicts a starting voltage equal to 906 V for the same electrode-to emitter separation; equation 3.32 for the same liquid and configuration predicts a starting voltage of about 2000 V. The experimental value for the 2×2 Planar Array test described before falls midway

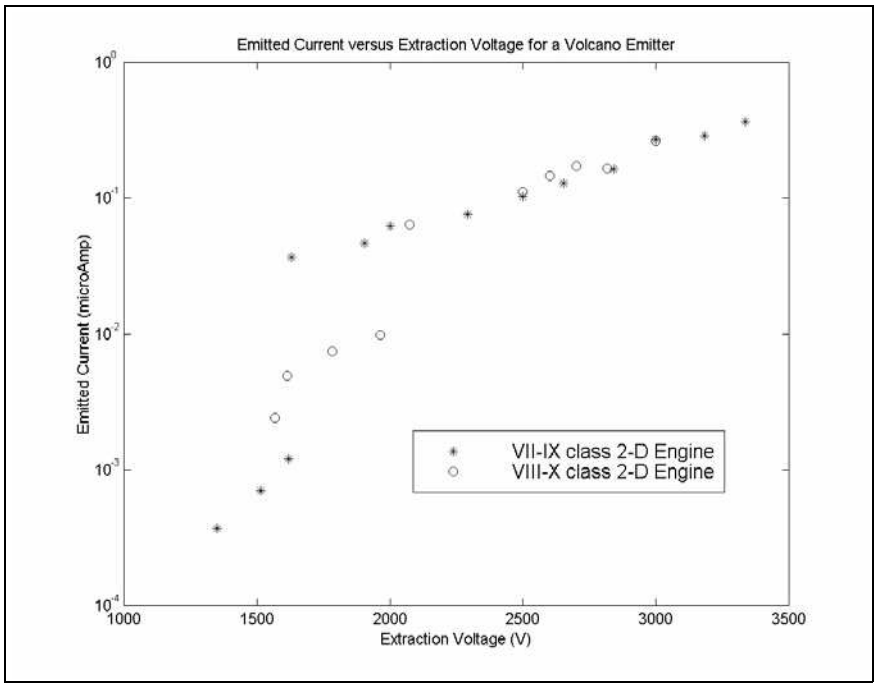

Figure 4.54 Semi-log plot of the per-emitter collected current versus extraction voltage for an 8-points volcano emitter. For the engine labeling system please see Appendix C.

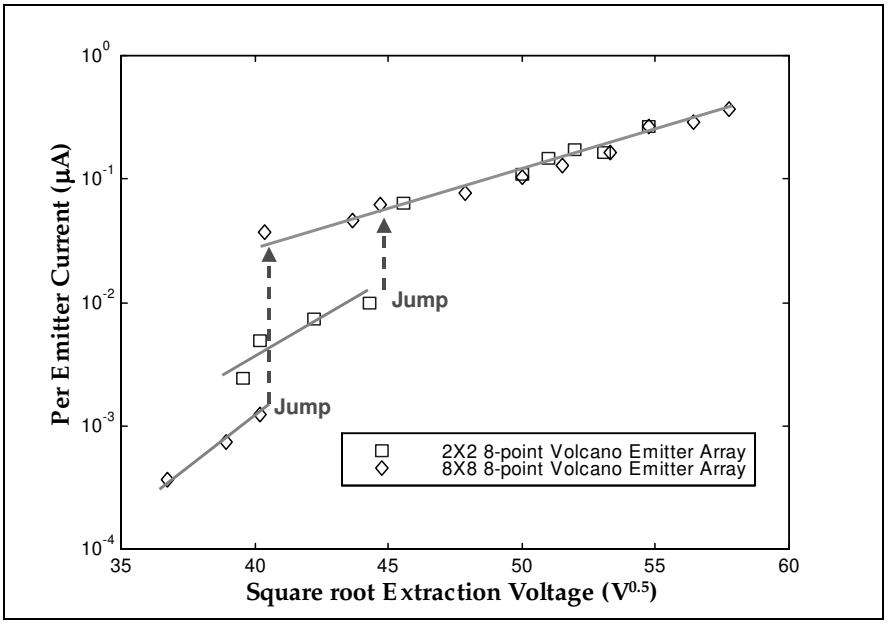

Figure 4.55 Semi-log plot of the per-emitter collected current versus the square root of the extraction voltage for an 8-points volcano emitter.

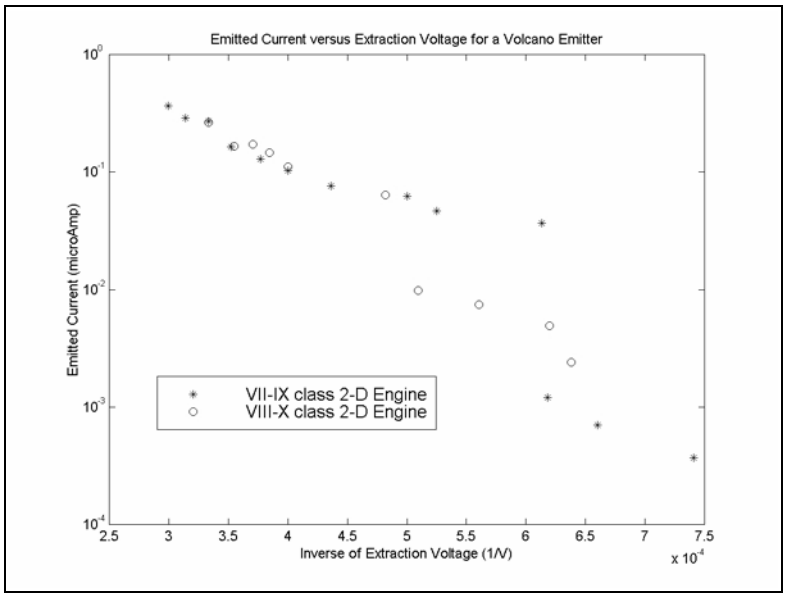

Figure 4.56 Semi-log plot of the per-emitter collected current versus the inverse of the extraction voltage for an 8-points volcano emitter. For the engine labeling system please see Appendix C.

between the two estimates. The experimental values fall within 30% from the starting voltage value predicted by equation 3.32, which is of the same order of the finite element results. The voltage drop in the engine due to electrical conduction is estimated at less than 1 V. It is known from the finite element analysis that the emitters are not shadowing each other. The mild disagreement between experiment and model might be based on three effects:

- Wrong estimation of the radius of curvature: the radius of curvature might increase because of the presence of the propellant film; if the radius of curvature is selected as 10 μm, then the predicted starting voltage from finite element results and equation 3.32 predict the experimental values.
- There is uncertainty in the true emitter-to-electrode separations because this distance is dependent on the particular test assembly. Based on the Finite Element Analysis done the used emitter-to-collector separation has substantial sensitivity to separation differences. The separation uncertainty is expected to vary the results by up to 20%, depending on the selected characteristic length. The fact that experimental starting voltages oscillated between 1350 and 1550 V supports this point.
- The model assumes two radii of curvature of identical value and axisymmetry in the emitter. The emitting points for a volcano are substantially different from these assumptions.

Effects of Temperature variation

A controlled temperature experiment was carried out using a 2×2 8-tip volcano emitter Planar Array. The temperature was set to 51.3 $\pm 0.1°C$ and monitored with a k-type thermocouple. It was demonstrated that it is possible to vary by orders of magnitude the emitted current for the same extraction voltage. The starting voltage (1450 V) was almost equivalent to the starting voltages of room temperature tests. Oscillations in the emitted current were obtained, larger than in the room temperature case, but still smaller enough than the average value. Unlike the room temperature tests, no transition region was obtained suggesting that the transition region is related to insufficient propellant supply when the extraction potential is small, or to some energetic threshold condition. Experimental data contradicts the temperature dependence of the emission predicted by the models in Appendix D. The increase of orders of magnitude of the emitted current for the heated experiment compared to the room temperature experiments could be related to the fact that the electrical conductivity of $EMI-BF_4$ increases orders of magnitude, and its viscosity decreases orders of magnitude, for a rather small temperature change [Fuller, 1997].

Figure 4.57 is a composition of several SEM pictures of the impact pattern on the collector surface. Propellant surface creep using the machining strokes is evident.Figure 4.58 shows the experimental data obtained in the test (compare to Figure 4.52).

Nonetheless, the oscillations were rather small and do not affect the zeroth order statement that the engine operation is steady.

Figure 4.59 is a semi-log plot of the emitted current versus extraction voltage for the experimental data collected in the temperature-controlled experiment. Voltage drops inside the engine, assuming the voltage drop occurred mostly at the tips, were estimated to be smaller than 10 V in the highest emitted current case.

Using equation 4.1 with n = 0.5 the correlation is 0.9899 and the two fit coefficients are V_o equal to 5.8898 V and I_o equal to $1.76 \times 10^{-2} \mu A$. In other words, the slope of the semi-log plot

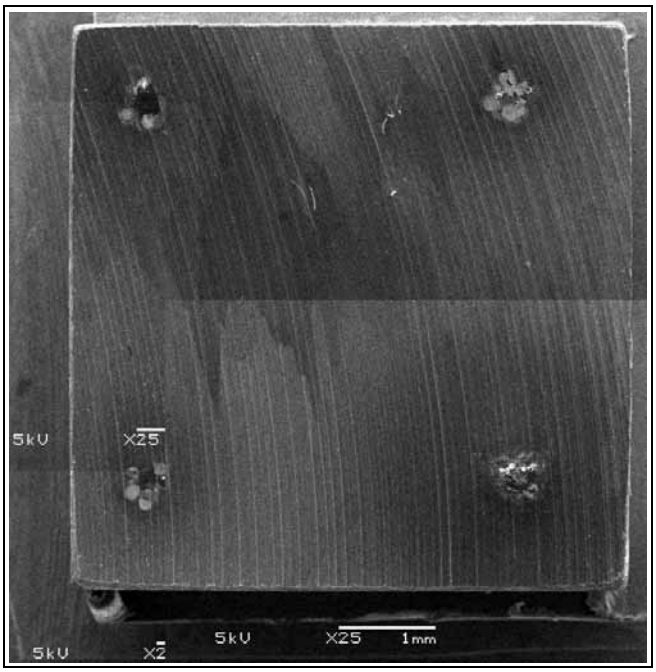

Figure 4.57 Collage of SEM pictures of the external electrode after the temperature-controlled test was carried out. Uniformity in the emission is demonstrated from this figure. Also, propellant surface transport due to the electrode surface roughness is visible, as noted before.

is increased compared to the room temperature case (V_o equal to 52.41 V at room temperature) and the intercept refers to a higher value (I_o equal to $1.12 \times 10^{-4} \mu A$ at room temperature). This is in contradiction with all the variable-temperature models discussed in Appendix D because they predict that the higher the temperature, the smaller the slope of the experimental data in a semi-log plot. Some of the models briefly explained in Appendix D, in particular the Schottky model, predict an increase in the constant I_o proportional to the square of the temperature times the exponential of the effective work function divided by the temperature. In principle larger temperatures should imply larger I_o, but because we do not have available the work function of the ionic liquid it is not possible to tell if I_o follows a known reduced-order model.

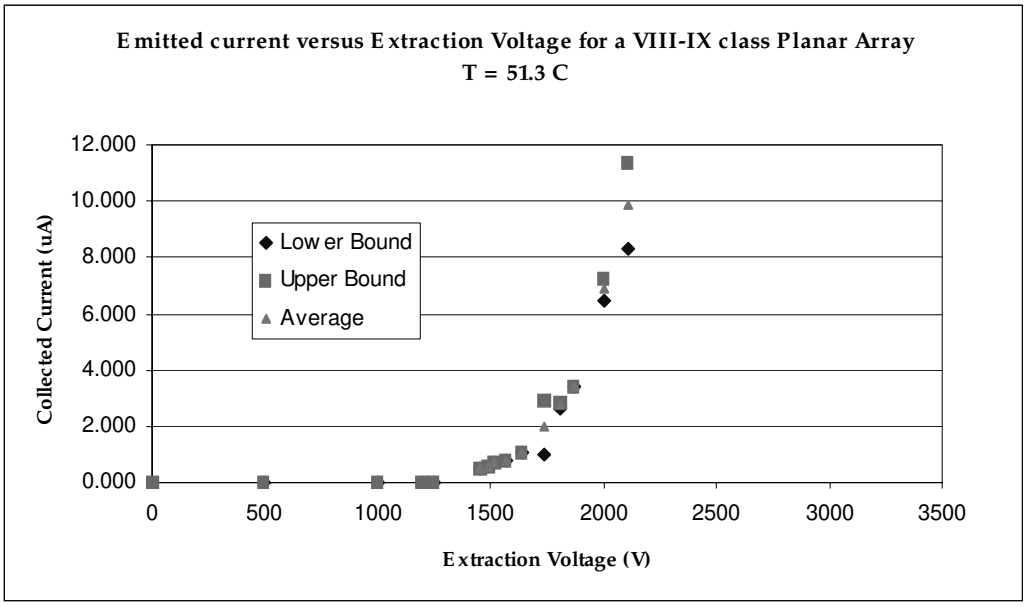

Figure 4.58 Emitted current versus Extraction Voltage for a 2×2 8- point volcano emitter Planar Array. Electrode Separation is 250 μm ; temperature is 51.3 $°C$. Compare to room-temperature data of Figure 4.52. For the engine labeling system please see Appendix C.

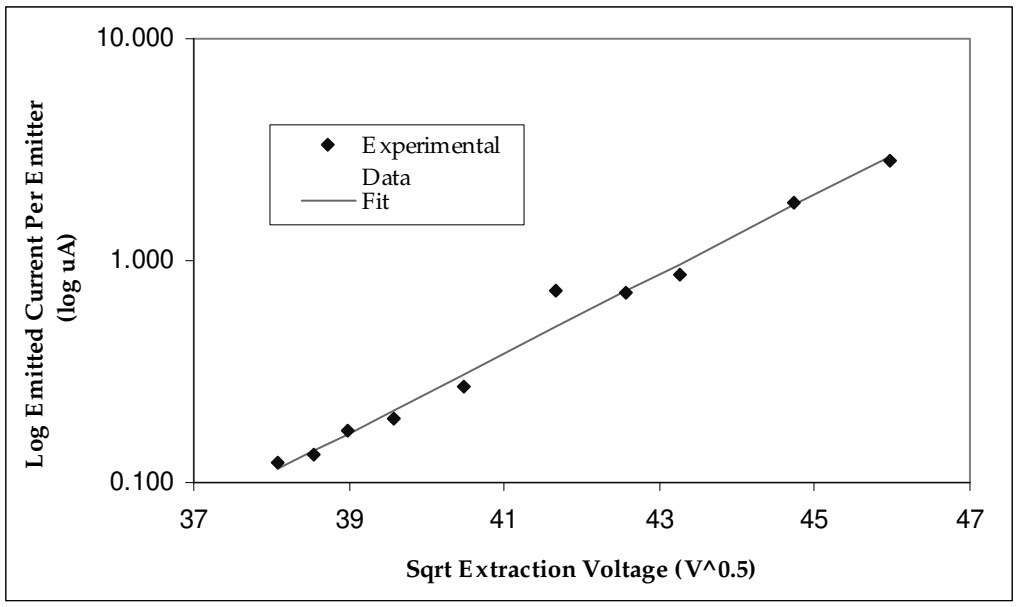

Figure 4.59 Per-emitter emitted current versus square root of the extraction voltage for a 2×2 8-tip volcano emitter Planar Array at 51.3 $°C$.

Chapter 5

PERFORMANCE ESTIMATION FOR BOTH PROPOSED ENGINES

5.1 Performance estimates on the Linear Colloid thruster Array

Given the model for single Taylor Cone droplet emission [de la Mora, 1994] and work done by MIT's Space Propulsion Laboratory on the poly-dispersity of the droplet specific charge for highly conductive formamide [Lozano, 2003] it is possible to estimate several of the performance parameters of the Linear Array, using the conductivity values of 0.6 S/m and 2 S/m for a total voltage drop of 5000 V. The smaller conductivity value is included because the flowrate versus current characterization was achieved with a propellant with a similar value. The larger electrical conductivity value is included to get an idea of the upper bound in I_{sp} values that can be obtained using formamide: to use formamide with larger electrical conductivities requires to effectively address wettability issues of the spouts, something that requires some work but looks feasible.

Figure 5.1 graphically shows the specific charge, I_{sp}, thrust and power consumption for the Linear Array using formamide with an lectrical conductivity equal to 0.6 S/m while Figure 5.2 is calculated for formaide with an electical conductivity equal to 2 S/m. The propulsive efficiency is estimated to be larger than 90% because o f the small specific charge spread [Lozano, 2003]. Taking into account extration losses this efficiency goes down to 85%. From this set of plots it is clear that the engine can provide an I_{sp} range from 200 to 350 seconds, a thrust level from 100 to 450 micro-Newtons and a power consumption from 0.1 to 0.4 Watts while using formamide with K = 0/6 S/m; using formamide with K =2 S/m then

the I_{sp} range goes from 350 to 700 seconds, a thrust level from 25 to 250 micro-Newtons and a power consumption from 0.1 to 0.4 Watts. For this kind of engines the main throtability variable is the flowrate.

This engine then has an I_{sp} range is equivalent to the reange that monopropellant or super-heated hydrazine thrusters can deliver. The missions that can be carried out with this engine should not stress on mass savings because of the rather low I_{sp} value. The engine is a better match for precisely throttled low-thrust time-limited changes in the position or orbit of small satellites. Most of the propellant lost in vaporization comes from the vapor emisison from the Taylor Cones. The fraction f_v of propellant lost as vaporization losses are estimated [Velasquez, 2001] as

$$f_v = \frac{L_c^2 \cdot K \cdot P_v(T)}{2 \cdot \gamma \cdot \varepsilon \cdot \varepsilon_o \cdot \sin(\alpha_T) \cdot \eta^2 \cdot \sqrt{\frac{8 \cdot K_b \cdot T}{\pi \cdot m_v}}} \tag{5.1}$$

where m_v is the mass of the vapor molecules and P_v is the vapor pressure. Using vapor pressure values of the literature [Lide, 1995] and common η value (~1.5) the fraction of propellant lost using formamide at 300 K with an electrical conductivity equal to 0.6 S/m is 0.05%; for formamide with an electrical cinductivity equal to 2 S/m the fraction increases to 0.16%. The more flowrate the smaller the vaporization loses, but in any case it is expected to have most of the propellant making part of the propulsive stream.

5.2 Performance estimates on the Planar Colloid Thruster Array

It is known that $EMI-BF_4$ emits two kinds of particles: a mixture of dimers whose specific charge is about 310000 C/Kg m (309 amu), and a monomer whose specific charge is 870000 (111 amu) C/Kg [Lozano, 2003]. Based on the measurements it is possible to estimate the propulsive efficiency, and the losses due to extraction are estimated to be low. (Figure 5.3) and I_{sp} range (Figure 5.4). From these figures it is clear that the Planar Array is more efficient than the Linear Array. Also, the I_{sp} range goes from 3800 sec. to 8500 sec. This engine is far

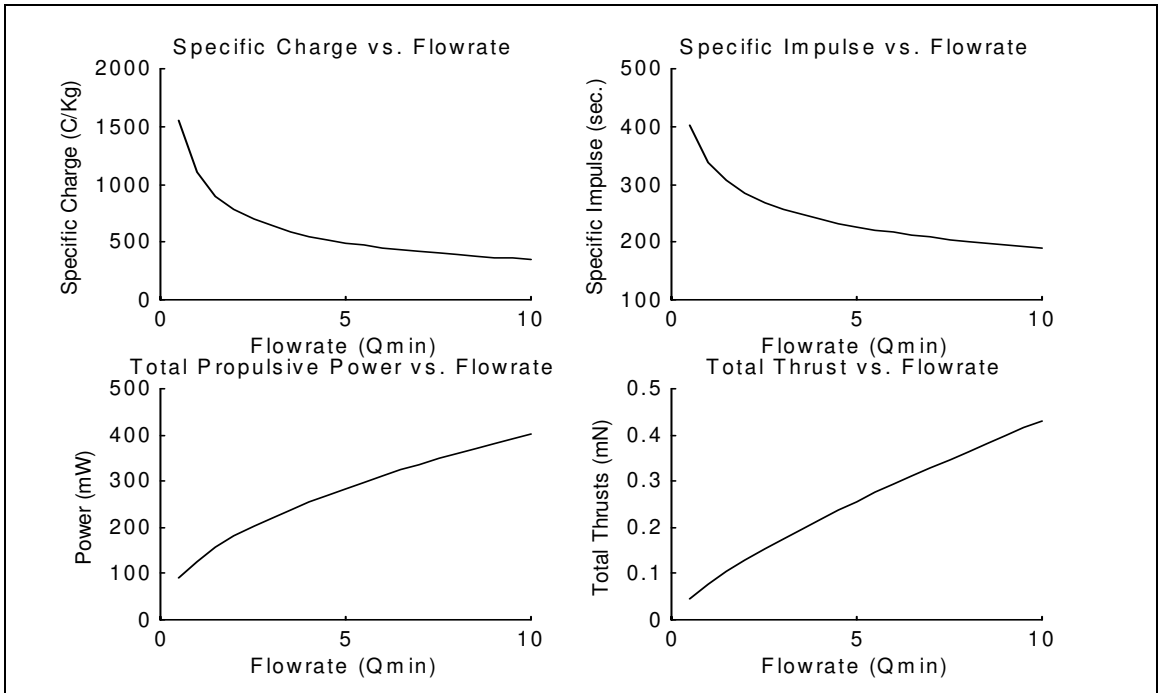

Figure 5.1 Specific charge, Specific Impulse, Power Consumption, and Thrust versus flow rate for the Linear Array using formamide with an electrical conductivity of 0.612 S/m and 5000 V of total potential drop.

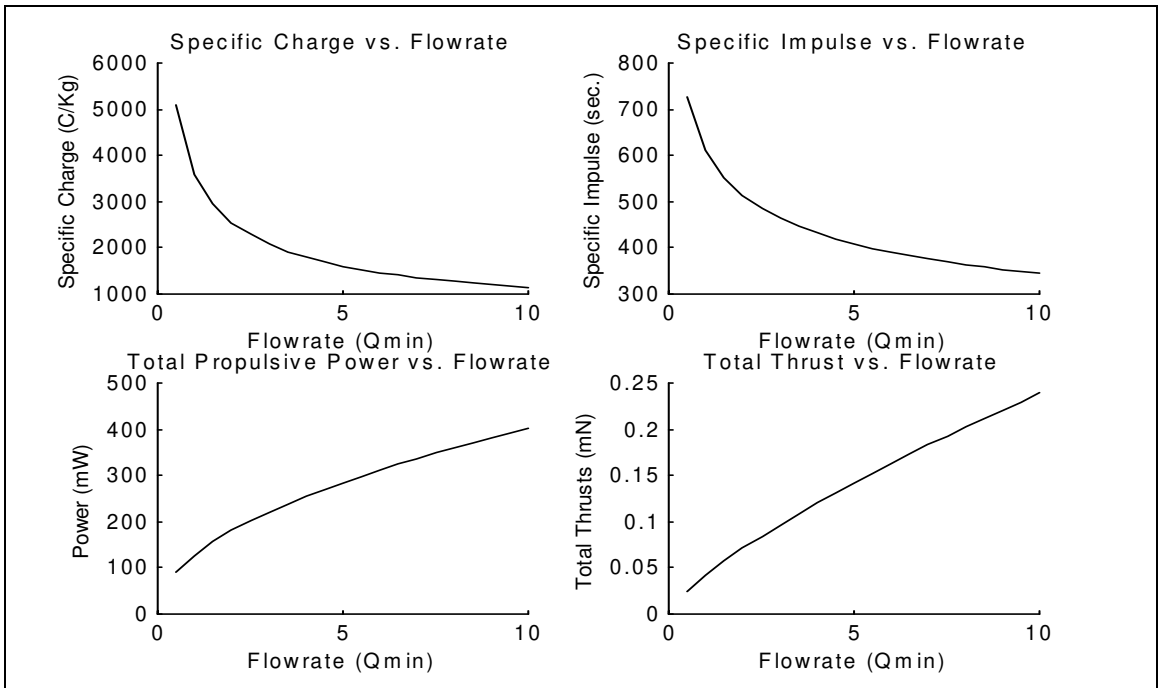

Figure 5.2 Specific charge, Specific Impulse, Power Consumption, and Thrust versus flow rate for the Linear Array using formamide with an electrical conductivity of 2 S/m and 5000 V of total potential drop.

more efficient in using the propellant than the Linear Array and therefore, it can be used as main engine for micro-satellites in missions such as deep space and non-time limited orbital maneuvers. For this kind of engine the main throtlability variable is the extraction voltage.

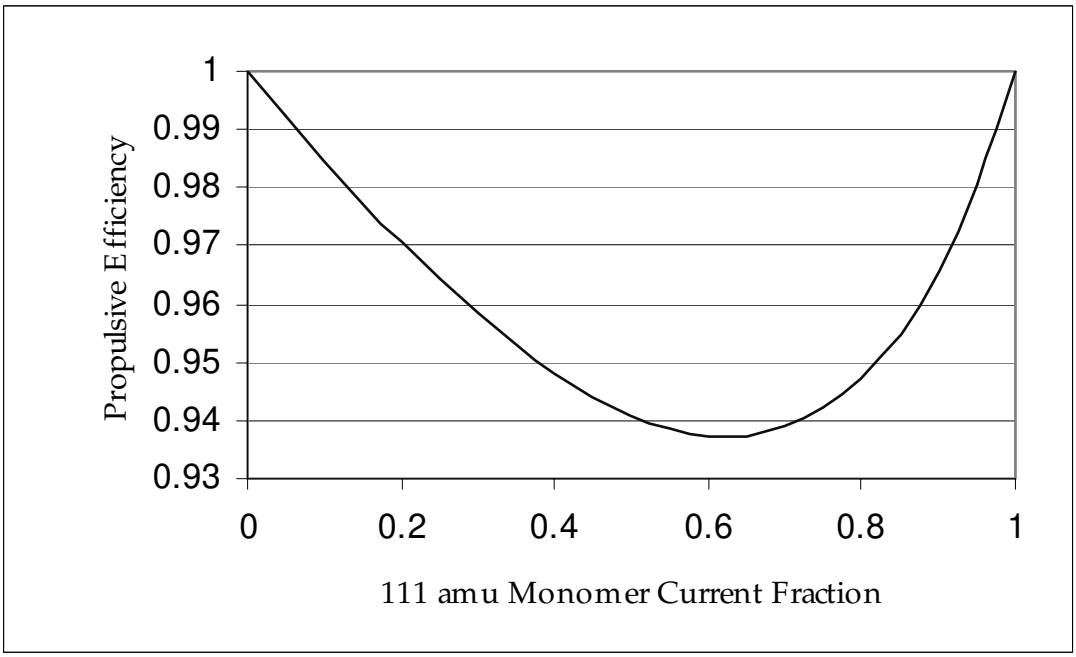

Figure 5.3 Propulsive Efficiency versus Monomer current fraction. The propulsive efficiency has a lower bound set at about 93%.

Figure 5.5 shows an estimate of how much thrust could be obtained from a 32×32 pencil Planar Array based on the I_{sp} estimates and the current versus total voltage data obtained for heated 8-point volcanoes @ $51.3\ ^{\circ}C$. In this estimate is assumed that the volcanoes uniformly emit from each of the eight tips and that the current emitted per sharp point is similar to the current emitted by a pencil. It is also clear that the Planar array, even in one of its densest emitter configurations, can provide only a fraction of the thrust provided by the linear Array (comparison of thrust is done per emitter, which is per unit of emitte-to-emitter separation).

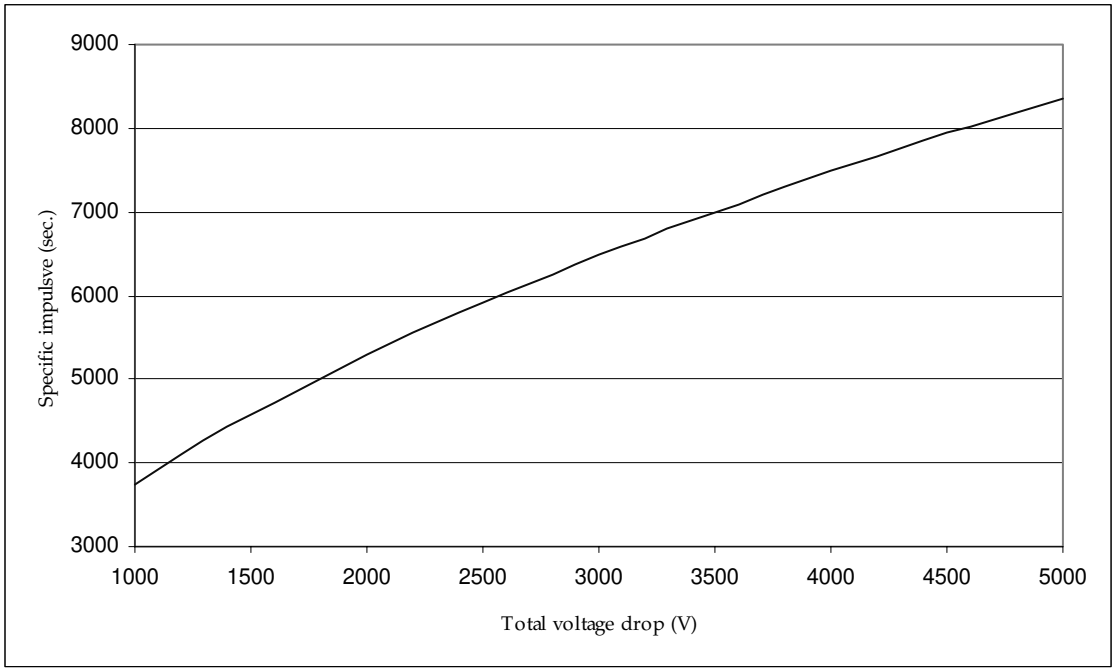

Figure 5.4 I_{sp} versus total voltage frop for an electrospray engine using $EMI-BF_4$ as propellant. The used mix ratio of the two species is closer to the one that gives the smallest propulsive efficiency.

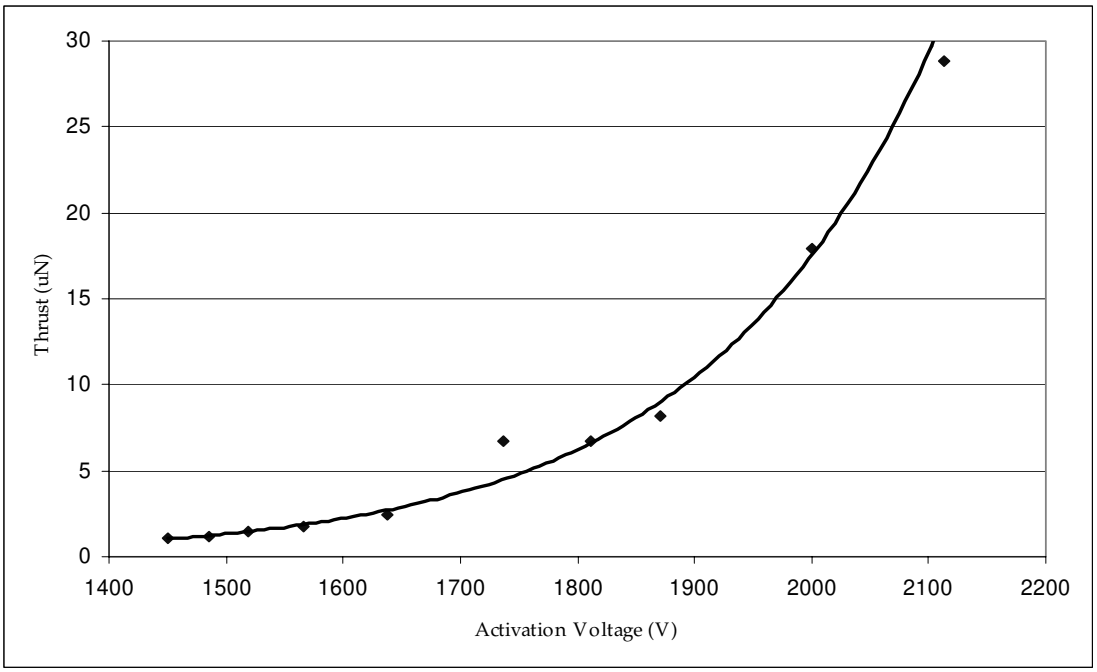

Figure 5.5 Estimated total thrust versus activation voltage for a 32×32 pencil Planar Array @ 51.3 $°C$. An exponential fit precisely maps the values based on the I-V data.

Chapter 6

A PLANAR ELECTROSPRAY THRUSTER ARRAY CONCEPT WITH WICKING MATERIAL

This chapter presents a tentative design of an internally fed Planar Electrospray Thruster Array that uses a porous material to achieve its hydraulic impedance. The engine is internally fed to keep the door open to doped solvents and other propellants with substantial non-zero vapor pressure. This engine would also work with a pressure difference, as in the case of the Linear Electrospray Thruster array documented in this work.

6.1 A word on Porous Materials

Wicking materials are appealing for Electrospray Thruster applications because they have advantages for batch processing and scaling-down:

- Many emitters can be put in a small surface. Emitters defined using photolithography have a practical minimum characteristic length of the order of one micron if resolution, uniformity and absolute dimensional uncertainty are taken into account. Emitters that come from the morphology of a porous material do not have this limitation because the pore size and pore spacing can be defined by molecular-size mechanisms. Nanometer-size pores with excellent uniformity and repeatability can be obtained with some electrochemical procedures.
- The smaller the emitter ID the smaller the starting voltage, with the corresponding savings in electronics and the reduction of break-down for a fixed emitter-to-extractor electrode separation.
- The hydraulic system can provide redundancy: the porous material can perform as a multiply-connected network where the clogging of a branch does not imply that an emitter will not receive its share of propellant. This is achieved if the emitter ID is larger than the pore diameter.

The key idea behind wicking materials is to obtain a physical mechanism that ensures the flow self-regulates in a steady way. The analogy is a candle where the reservoir is the upper portion of wax that is melted and the wicking material transfers fuel from this reservoir to the flame: the wicking material regulates the fuel flow based on the flame demand. This flow range goes from zero up to the maximum pumping capacity of the material set by surface tension and viscous loss balance.

For a porous medium the fluid velocity is modeled by Darcy's equation, that for an isotropic medium is defined as [Adler, 1992]

$$\bar{v} = -\frac{1}{\mu} K^* \vec{\nabla} P \tag{6.1}$$

where $\bar{v}$ is the bulk velocity inside the pores of the medium, μ is the liquid viscosity and K^* is the permeability of the medium. Inside the porous material it is reasonable to assume that the flow is locally fully developed and laminar. For a Newtonian fluid with a flowrate Q through a pore modeled as a circular cylinder with some axial dimension L and characteristic pore diameter $\varnothing$ the bulk velocity is given by the well known Hagen-Poiseuille equation

$$\bar{v} = \frac{4Q}{\pi \cdot \varnothing^2} = \frac{\varnothing^2 \cdot \Delta P}{32 \cdot \mu \cdot L} \tag{6.2}$$

By comparison of equations 6.1 and 6.2 it is clear that the permeability is inversely proportional to the *square* of $\varnothing$. Equation 6.1 can be used to determine the effective permeability if all the other parameters are known or estimated. There is a useful semi-empirical equation to determine the permeability (the Carman-Kozemy equation):

$$K^* = \frac{\Xi \cdot \widehat{\Lambda}^2}{K_k} \tag{6.3}$$

where Ξ is the porosity, i.e., the ratio between void volume and total medium volume, $\widehat{\Lambda}$ is a kind of characteristic length equal to the void volume divided by the wetted area, and K_k is the so called *Kozemy constant*: it has a value of 2.0 for uniform capillary-like pores while it has a

value of 4.8 for randomly porous media. It is stated in the literature that equation 6.3 works quite well for predicting the permeability of a porous material. On the other hand Ξ can be estimated from gravimetric experiments and $\widehat{\Lambda}$ is related to the structure of the porous material: if the wicking material is uniform a characterization of a sample would be representative.

Vafui (2000) points out that even though the pores are modeled as circular channels it is ideal to make the pore cross-section have sharp corners because this enhances the surface tension pulling. A micro-fabricated channel with small cross-section dimensions would benefit from this fact as well.

The structures of the porous materials relevant to Electrospray Thruster applications can be arranged in two categories:

- **Parallel capillaries:** it would work fine provided $\varnothing$ is substantially smaller than the emitter internal diameter L_c, because it would provide hydraulic redundancy by feeding L_c in parallel.
- **Branches/ random/ 3D pores:** it would work fine but non-parallel capillary wicking substrates have stagnation zones due to the sudden change in the direction of the flow. Therefore, clogging zones are inherent to this morphology. A rather mild limit for this clogging effect would be for a material of this kind to become one that resembles a material of the first category (independent channels running disconnected) via cancellation of stagnation zones, an unlikely scenario nonetheless.

The same reference from Vafui points out that even in the case of 3D porous materials the 1D models suggested in this chapter give good agreement with the actual performance of the wicking material. Also, for wetting fluids the effect of the contact angle in the permeability can be neglected if this angle is less than $60°$.

Finally what is intended in a hydraulic system that uses a porous material to obtain hydraulic impedance is to minimize the capillarity number Ca

$$Ca = \frac{\mu \cdot \bar{v}}{\gamma} = \frac{\varnothing^2 \cdot \Delta P}{32 \cdot L \cdot \gamma} \tag{6.4}$$

because for a fixed L and pressure difference a smaller diameter and larger surface tension allows to transport more flow through the pores.

The velocity of a flow that moves in steady state through a pore of diameter $\varnothing$ is given by the Washburn equation

$$\bar{v} = \frac{\varnothing^2 \cdot (\Delta P + P(\gamma))}{32 \cdot \mu \cdot L} \tag{6.5}$$

Equation 6.5 is the same equation 6.2 where the available pressure is both the hydrostatic pressure difference between the channel ends and the surface tension pulling. $P(\gamma)$ is the equivalent pressure exerted by surface tension means,

$$P(\gamma) = \frac{4 \cdot \gamma \cdot \cos[\theta_{ctct}]}{\varnothing} \tag{6.6}$$

where θ_{ctct} is the contact angle. Figure 6.1 is an schematic to better clarify the variables involved in the last equations.

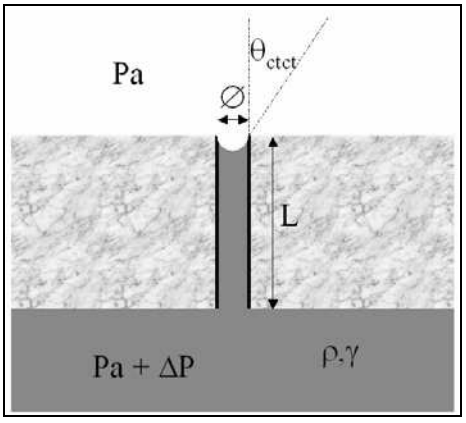

Figure 6.1 Schematic of a pore of axial length L, diameter $\varnothing$ and contact angle θ_{ctct} that can convect flowrate through it both by hydrostatic pressure difference and surface tension.

The use of a porous medium to achieve the hydraulic impedance for a Planar Array has several advantages compared to more standard approaches, such as

- $\varnothing$ can be small enough to make the surface tension effects do most of the pumping of the propellant to the emitters.
- A porous system could become *leak safer* than the traditional engine implementations if the need of a pressure difference is eliminated. No flow will be produced unless electrically assisted, even for a wide variation of propellant physical properties due to doping concentration or temperature.
- It is possible to achieve redundancy in the propellant supply to the emitters if the hydraulic diameter of the porous material is substantially smaller than that of the emitter (Figure 6.2). This way clogging concerns are substantially reduced.

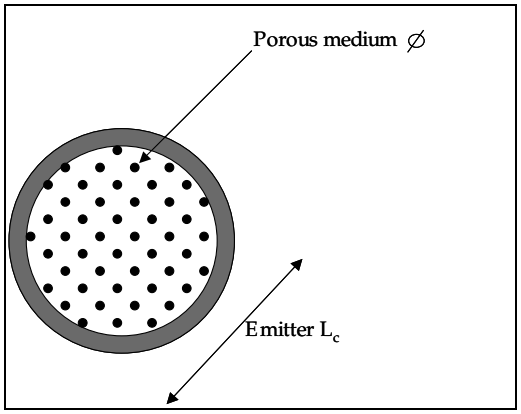

Figure 6.2 Top view of an emitter fed by a porous material where feeding redundancy takes place.

- The Clustering potential advantages of Planar Arrays over Linear Arrays are applicable to this kind of engines: based on the electrical characterization of the Planar Array spouts done in Chapter 4 it is safe to use emitter-to-emitter separations as small as 5 hydraulic diameters without producing interference between emitters.
- A system of emitter modules where each module boundary acts as a point of contact between the electrode and the engine main substrate substantially reduces the free length of the electrodes, thus increasing by orders of magnitude the resistance of the electrodes to collapsing due to electrostatic suction. This modular system will allow us to selectively grow porous material in patches with the consequent improvements in engine stiffness and resistance to external loads. If the porous material is produced from the main substrate then thermal mismatch can be reduced to a minor role, thus increasing the engine resilience to harsh environments.

- This scheme might also allow us to implement a system of stand-off posts to reduce the number of points of contact between the electrodes and the ground substrate, as a strategy to reduce electrical breakdown hazard.

6.2 Material Selection

The best candidate for substrate material from the standpoint of micro-fabrication is silicon. On one hand most micro-fabrication technologies have been developed for silicon substrates (as a spin off of semiconductor industry), while on the other hand silicon is arguably an excellent substrate candidate from the physical point of view. For a more in-depth discussion of this selection please see the Master of Science Thesis of the author [Velásquez, 2001].

Given the silicon selection as main substrate it is natural to look for porous substrates of *proven* compatibility with this material. Questions on wafer bonding quality, resistance to harsh environments, chemical attack from the propellant and maybe breakdown voltage would arise if a porous material without well-known micro-fabrication history is proposed. Fortunately, there is a porous material technology that can achieve pore diameters smaller than a fraction of a micron on channels that can perfectly span the whole silicon substrate thickness: *porous silicon*. Some other porous materials were taken into consideration, such as naturally porous materials ($CaCO_3$), micro-sphere beds (probably made of polymer) and ceramic powder sintering. Some of them have clear flaws (such as chemical resistance, uncertainty in the pore characterization and bulk uniformity) while others remain as open questions as alternative paths for achieving a porous media for Electrospray Thruster applications.

Porous silicon is produced by anodic etching of silicon. The porous material is produced by putting the silicon substrate into a 1% - 49% HF bath while biasing some voltage (Figure 6.3). The wafer side that is not intended to be etched is in contact with a KCl solution in water, allowing proper connection of the wafer in an electrical circuit (power supply - KCl - wafer - HF - power supply). A set of o-rings separates the two wet environments where the wafer serves as interface wall. Current is passed through using platinum wires; the current density is of the order of $10\text{–}100\ mA/cm^2$. A film of sputtered aluminum can be deposited on the wafer back to increase electrical contact. Sputtered aluminum is also the etching mask applied on

the top surface; the actual pore size is *not* defined by some etching mask (like patterned dots) but by the actual bath concentration, current density and doping concentration of the silicon substrate. A teflon coated magnetic stirrer inside the HF bath is ideal to keep the bath uniform and remove bubbles that appear at the top surface. For more information on reaction chamber setups please see [Anderson, 1991].

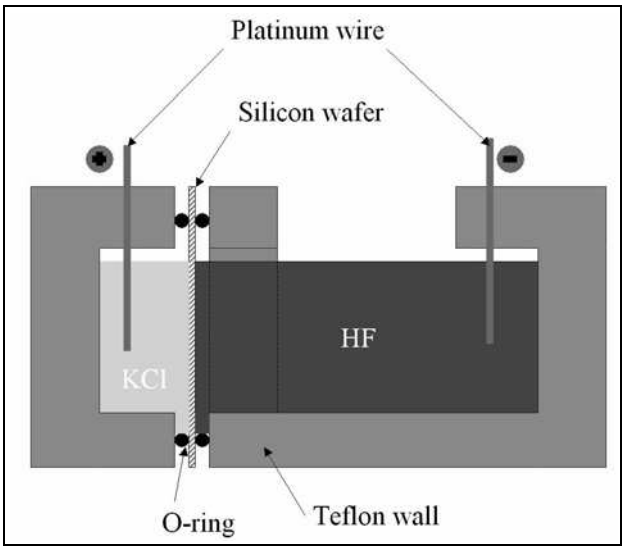

Figure 6.3 Porous silicon reaction chamber.

It is also possible to make pores with a certain inclination with respect to the top surface normal. For pores running in-plane, current densities of the order of $100mA/cm^2$ are needed with <111> substrates. In this case the current direction and the etched preferential direction don't line up. The preferential etching direction is <100>; therefore, <100> wafers will produce vertical pores (parallel to the top surface normal). For pores of random orientation low current densities and highly doped silicon are needed. For a deeper exposition on this subject please see [dos Santos, 1998].

6.3 Fabrication process flow of a Planar Electrospray Thruster Array based on porous silicon

The proposed internally fed Planar Electrospray Thruster Array is shown in Figure 6.4. It is composed of three DSP lightly doped p-Si <100> substrates: *Wafer 3* contains the propellant tanks and the irrigation network that feeds the emitter modules; *Wafer 2* has patterned blocks of porous silicon to provide hydraulic impedance to the emitters, while on the other side of the wafer the emitter tips are carved; *Wafer 1* contains both the extractor and the accelerator electrodes. The electrical insulation is provided by vacuum gaps and silicon oxide. The conductive paths of the electrodes are made of highly doped Poly silicon to make the fabrication process CMOS compatible.

The following micro-fabrication process is intended as a guideline for an actual fabrication implementation. Almost for sure several details will need to be tuned along the way, in particular the actual parameters used in the porous silicon formation. The process flow includes a set of conceptual optical masks, pointing out some of their key lengths. All the fabrication sketches refer to a set of four modules, each one having four emitters. The modules play the same role as the manifolds in the Linear Electrospray Thruster Array. Only the extractor electrode fabrication appears in this process; the acceleration electrode and the electrode pads fabrication procedures are analogous to the ones described in Chapter 4 for the proposed Planar Array. The convention used on the sketches is that chromium-covered surfaces appear black.

The procedure is as follows:

Wafer 2

- **Do photolithography on the top surface of the substrate using Mask A (Figure 6.5).** The mask layout includes the emitter sharpening features and the module divisions.
- **Etch isotropically the top surface of the substrate:** The etching is rather shallow, enough to keep the planarity of the top surface Figure 6.6 shows a cross section of the substrate after this step.

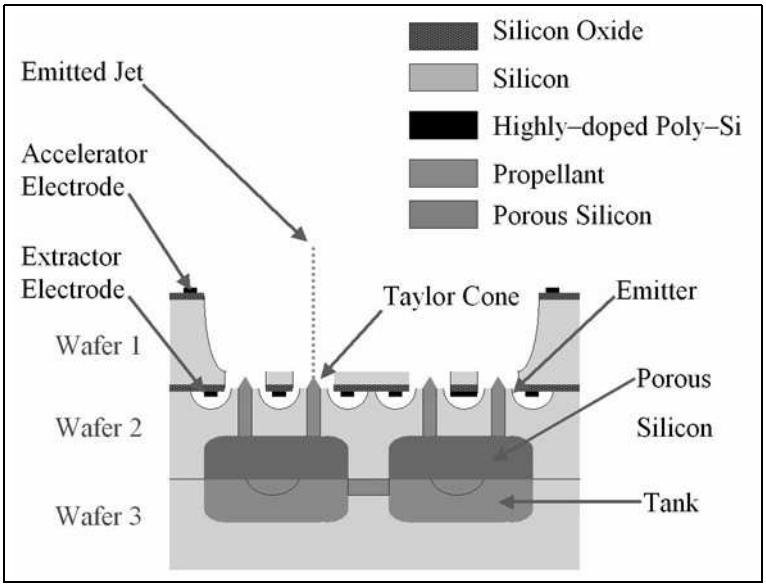

Figure 6.4 Cross-section of the proposed Planar Electrospray Thruster Array with porous silicon as wicking material.

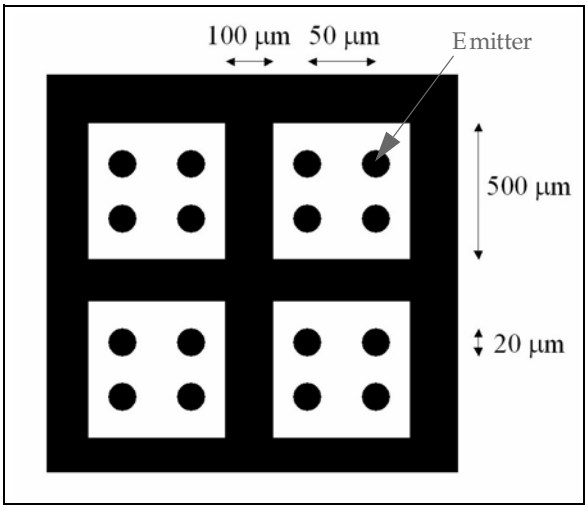

Figure 6.5 Mask A. The 50 μm emitter-to-emitter separation is suggested for the spout geometry as the minimum separation to have decoupled emitters.

- **Do photolithography of the top surface of the substrate using Mask B (Figure 6.7):** The mask layout includes the internal geometry of the emitters. This internal geometry has sharp corners to enhance the wetting and thus facilitate the propellant convection to the spout tip.

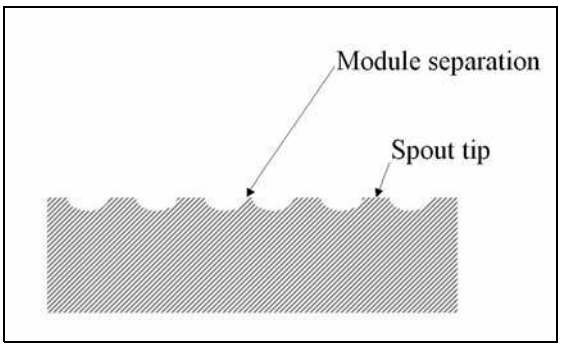

Figure 6.6 Cross-section of *Wafer 2*.

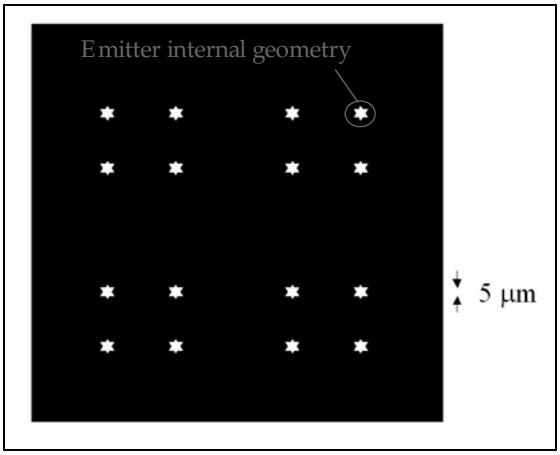

Figure 6.7 Mask B. The emitter internal cross section has a diameter of 5 μm and has sharp corners to enhance wetting.

- **Practice a DRIE to pattern the top surface of the substrate:** Figure 6.8 is a cross section of the substrate after this step.

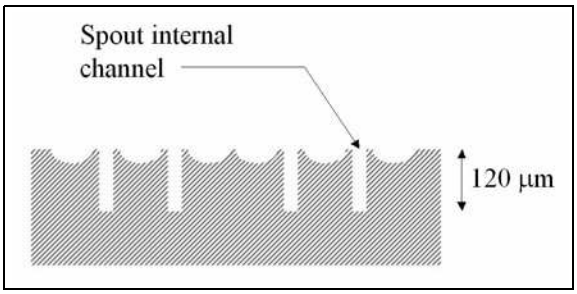

Figure 6.8 Cross-section of *Wafer 2*.

- **Deposit on the bottom surface of the substrate 0.5 μm of sputtered aluminum.**
- **Do photolithography on the bottom surface of the substrate using Mask C (Figure 6.9):** The mask layout defines the porous material pads and the module-to-module separations.

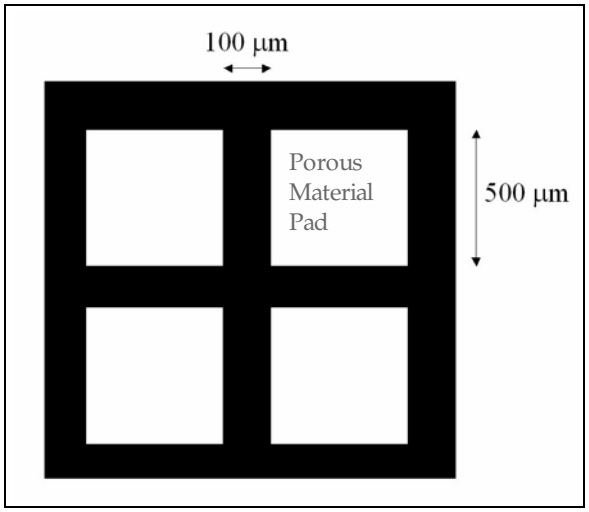

Figure 6.9 Mask C.

- **Pattern the aluminum layer.**
- **Generate the porous silicon layer on the bottom surface of the substrate.** A cross section of the substrate after this step is complete is shown in Figure 6.10.

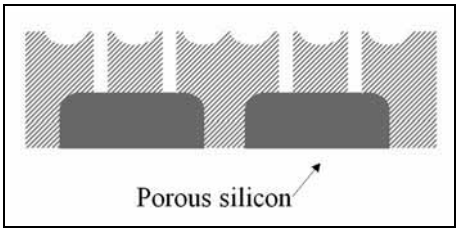

Figure 6.10 Cross section of *Wafer2*, after porous silicon is created. Notice the porous material and exit channels communicate. The liquid will need an extra pressure to flood the bigger channel to achieve filling in.

Wafer 3

- **Deposit a layer of PECVD silicon oxide on the top surface of the wafer.**
- **Do photolithography on the top surface using Mask C.**
- **Pattern the silicon oxide on the top of the wafer.**
- **Do photolithography on the top surface of the wafer using Mask D (Figure 6.11):** A nested mask is implemented. The mask D layout contains the irrigation network and the propellant plenum.

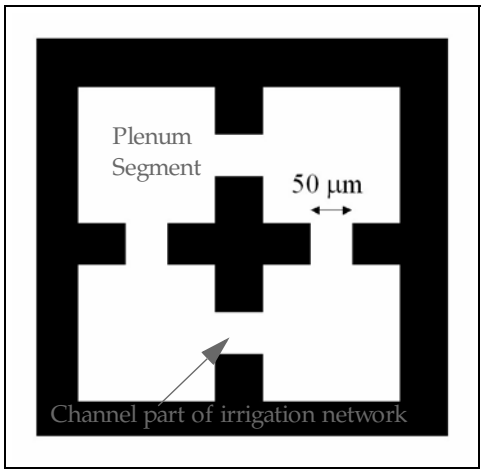

Figure 6.11 Mask D. Module tank to module tank communications are intended as propellant supply redundancy; their hydraulic impedance is negligible.

- **Practice two non-passivated DRIE steps to transfer the features included in the nested mask:** Figure 6.12 is shows an actualized substrate cross section.

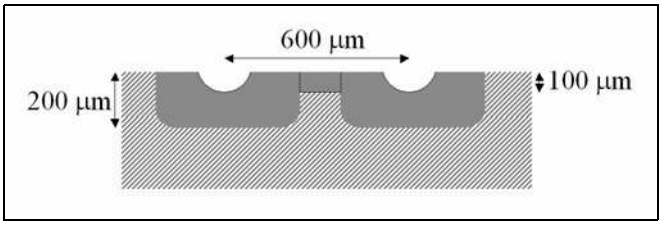

Figure 6.12 *Wafer 3* cross-section after complete processing.

Wafer 1

- **Deposit on both sides a thick layer of thermal / PECVD silicon oxide.**

- **Perform CMP to the silicon oxide films to planarize it for wafer bonding.**
- **Do photolithography on the top surface of the substrate using Mask C.**
- **Pattern the top silicon oxide layer.**
- **Deposit a layer of W/ Ti (both evaporated) on the bottom surface of the wafer.**
- **Do photolithography on the bottom surface of the wafer using Mask E (Figure 6.13).**

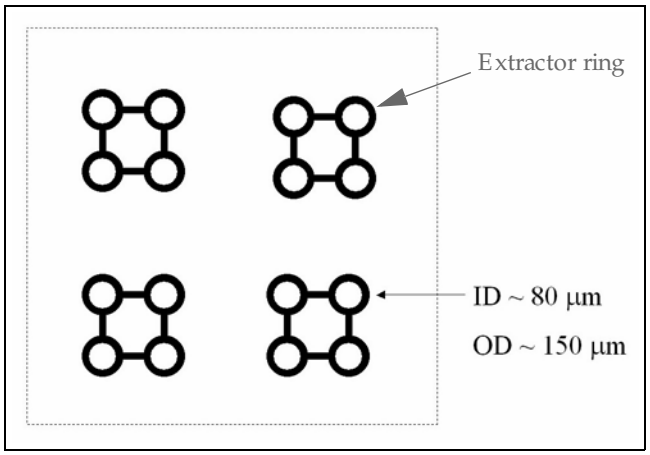

Figure 6.13 Mask E. This mask has the pattern of the conductive paths that provide the electrical signal to the engine.

- **Pattern the metal layer on the bottom surface of the substrate.** This step patterns the extractor electrodes.
- **Do photolithography on the bottom surface using Mask F (Figure 6.14).**
- **Perform a DRIE step without passivation on the top surface of the wafer:** This step generates the electrode hole exit expansions to avoid particle hitting.
- Pattern the silicon oxide and silicon on the bottom surface using RIE/DRIE. Figure 6.15 is a substrate cross section of *wafer 1* after processing.

Finally the three substrates are fusion bonded: Titanium melts at about $1668°C$ and tungsten at about $3422°C$; therefore, the electrodes should survive the bonding (oxidation does not take place because the atmosphere is nitrogen).

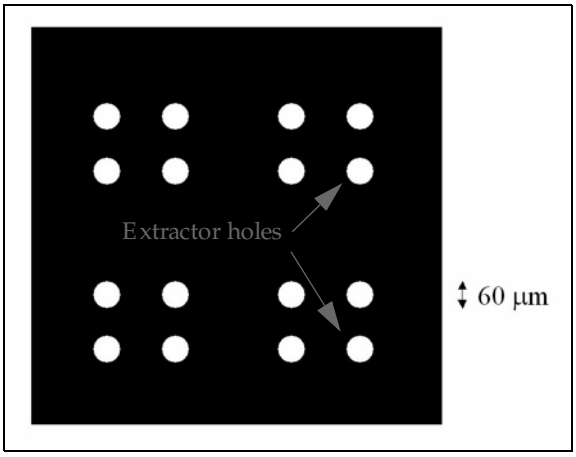

Figure 6.14 Mask F. This mask has the pattern of the holes that allow the charged particles to pass through the electrode substrate without hitting it.

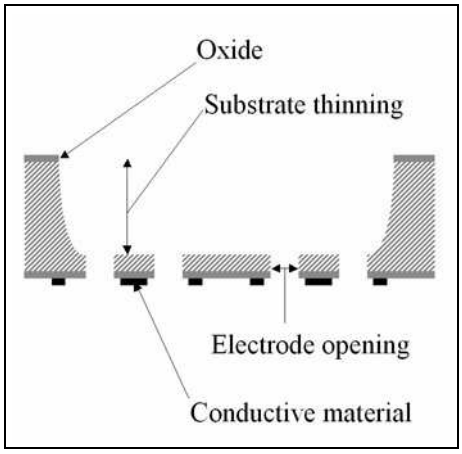

Figure 6.15 Cross-section wafer TOP.

Chapter 7

CONCLUSIONS OF THE RESEARCH; THE FUTURE

7.1 Conclusions

The achievements of this research work are:

- The preliminary development of a micro-fabricated silicon-based Linear Array of Colloid Thrusters that uses a doped solvent as propellant, and is appropriate for a range of specific impulses from 200 to 350 seconds with thrust levels from 100 to 450 micro-Newtons.
- The preliminary development of a hybrid micro-fabricated/macro-fabricated silicon-based Planar Array of Colloid Thrusters that uses $EMI-BF_4$ as propellant, appropriate for a range of specific impulses from 3800 to 8500 seconds and thrust levels from 1 to 30 micro-Newtons.
- The demonstration of the feasibility of high clustering for the proposed engine concepts.
- Demonstration of uniform-steady operation of the modular units: a manifold in the Linear Array, and a propellant pool in the case of the Planar Array.
- Novel micro-fabrication techniques were successfully developed to implement the proposed designs:
    - Collimated Stratified Nested Masks.
    - Deep Cycled RIE Silicon.
    - Deep cycled RIE Silicon Oxide.
    - Black Silicon Cl_2-based.
- Demonstration of the possibility to vary the emission characteristics of the Planar Array using temperature control. This behavior seems to be related to the

fact that the electrical conductivity of $EMI-BF_4$ increases orders of magnitude, and its viscosity decreases orders of magnitude, for a small temperature change.

- Demonstration of small emission fan divergence in both engines, in agreement with reported values in the literature and reduced-order model.
- The spouts of the Linear Array do not have a well defined wetting front. This translates in emission of propellant bursts. A tentative solution involving closed-loop feedback and surface treatment of the engine interior / spout exterior is proposed.

7.2 The Future

The following is a brief list of topics that the author considers will play an important role in the future research of micro-fabricated Colloid Thrusters. It is divided in three sections:

- Some improvements for the Linear Colloid Thruster Array.
- Some improvements for the Planar Electrospray Thruster Array.
- Emitter damage and life issues on Colloid Thrusters.
- Technology breakthroughs.

7.2.1 Some improvements for the Linear Colloid Thruster Array

The optical masks that are used to build the colloid thruster array can be improved in several ways. The most relevant improvement deals with enhancing the DRIE uniformity by keeping a rather constant etching window cross-section. In other words, to fill in the space not needed by the engine with decoy features that force the etching window be of about the same width everywhere. This strategy will lead to more uniform DRIE because on one hand it will make all etching areas similar and plasma depletion (microloading) will not take place. Also the sidewall slope will be improved because this strategy calls for narrowed etching windows and, as it was demonstrated in Chapter 3, that there is a dependence of the etching sidewall angle with respect to the etching window cross-section. Narrower etching windows via added decoy features would enhance the alignment capabilities of the clip system and can also lead to better emitters.

Another possibility is to build the clip system in one or two different substrates and bond the Engine Main Substrate to the clip substrates. On one hand it will enhance the engine yield because less critical features would be attached to a given substrate; on the other hand wafer bonding might get trickier. Also it is important to make sure the clip system does not get mechanically over-constrained to the point where it can fail under its own influence.

7.2.2 Some improvements for the Planar Colloid Thruster Array

It would be desirable for any version of the Planar Array to provide as much electrical safety as possible. Therefore, the electrode substrates should physically contact any other substrate in a few points: for example, the electrostatic grids of ion engines make physical contact in a few places were ceramic insulators are placed. In the designs shown in Chapters 4 and 6 this issue is not stressed. One possibility to achieve this is to pattern the silicon oxide layers into *bays* or short posts to reduce as much as possible the contact area. This solution might be too sensitive to gap clogging from external debris because silicon oxide films of more than a few tens of microns cannot be deposited without some fancy stress control approach. The natural extension of this idea then would be to provide the physical connection between electrodes and hydraulics using standoff posts, as shown in Figure 7.1.

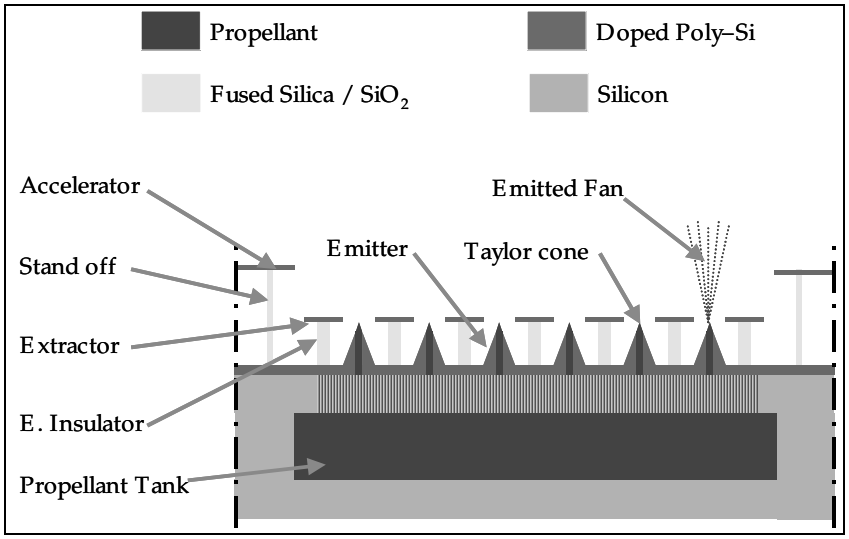

Figure 7.1 Cross section of a Planar Array implementing a standoff system to provide physical contact between the electrodes and the hydraulics.

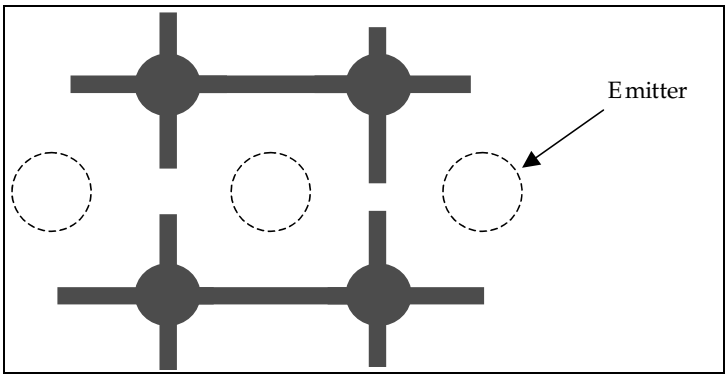

Figure 7.2 Standoff schematic for the hydraulics-to-extractor interface.

The standoff layout for the extractor electrode is shown in Figure 7.2. The standoff layout could be micro-fabricated and precisely aligned by either processing it as a whole piece, or filling in the standoff layout using micro-fabricated silica posts assembled using flat display techniques [Browning, 1997]. Figure 7.3 shows the kind of post density and post aspect ratio that can be obtained (the posts are 350 μm tall and 25 μm wide).

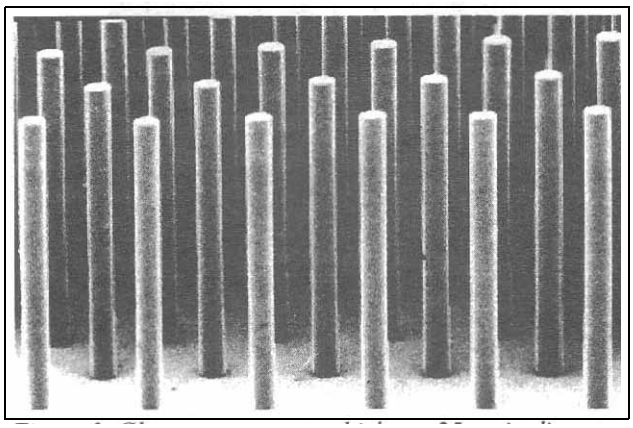

Figure 7.3 A silica post forest to implement the electrode assembly in a Planar Array electrode system.

Another strategy to increase the electrical breakdown safety factor but get the emitter tips as close as possible to the extractor rings is shown in Figure 7.4. In this figure the electrode is formed as a by-layer of some conductive material (silicon is an option) By placing the electrodes at about the emitter tip height will maximize the electric field enhancing capabilities of

the spouts [Akinwande, 2002]. To produce the electrodes in a stratified way allows to decouple the emitter-to-extractor distance and the electrical insulation thickness, optimizing the distances the way is needed: small distance in the activation part and large distance in the potential breakdown paths.

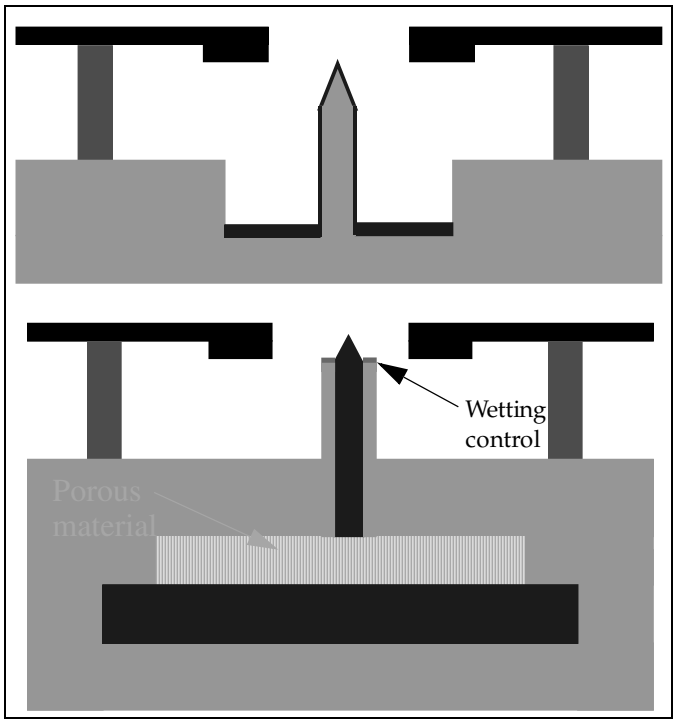

Figure 7.4 Cross section of a Planar Array implementing a stand-off system and a stratified electrode: externally fed emitters (*above*), internally fed emitters (*below*).

It is important to reduce as much as possible the extractor to electrode distance to allow rather small activation voltages, of the order of 1.5 kV. Therefore, alignment of the extractor grid with respect to the emitter is critical. There are two clear ways to obtain this alignment, both using macro-scale features with micro-sacale precission:

- The spring system used in the Linear Array can be extended to the Planar Array: the spirng clusters made in the hydraulics substrate could be made of silica and allow lo align the hydraulics substrate to the extractor. This way the two electrodes of the Linear Array will become the hydraulics and extractor sub-

strates of the Planar Array. The system would require at least three sets of spring clusters to reach robust - repeatible alignment.

- A lego-like pattern can be formed using the electrical insulation layer nad the hydraulics substrate (Figure 7.5). The features are deep enough and large enogh to allow manual assembly, while precise enough to provide good alignment. The strategy would contemplate to provide interference of the constitutive parts by precise tuning of the sidewall slopes, the use of some maleable material (gold) as bonding material of the union, or the formation of displacement springs if one of the constitutive parts.

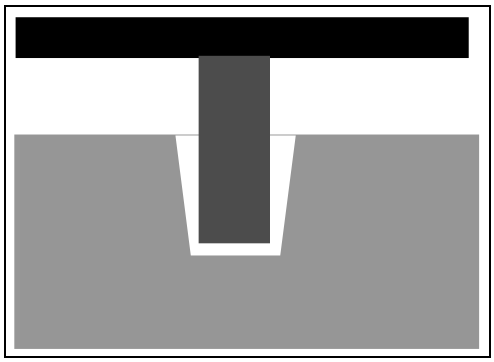

Figure 7.5 Schematic of a lego-like assembly system

7.2.3 Emitter damage and life issues

Emitter damage has not been considered in this work and would make up a Ph.D. thesis by itself. The few statements the author can make about this particular issue are:

- The highly-stressed regime should be avoided to enhance the engine life. Colloid thrusters operated with high extraction voltages will most certainly generate multiple cone emission with the consequent larger divergence angles. This can be an issue if accelerator electrodes are omitted.
- Recalling the work on Colloid Thrusters done in the 1970's it might be viable to contemplate the addition of a surrounding shield to reduce the possibility of negative particle backstreaming (positive polarity), in particular secondary electrons.
- The single cone regime is characterized by small divergence angles and no thermalized particles. In other words the space charge density in the particle fan is uniform and has a sharp edge, unlike the plumes of plasma-based electric engines. This is critical because this allows the ion optics to do a better job of focusing the beams emitted from the engine.

- To neutralize the engine by bipolar operation is an asset because it would remove the need of an external source of electrons than can backstream to the emitters and damage it. Backstreaming is a known limitation of the operational range of gridded ion engines.
- Another possible electron source could be from collisions in the spray plume. What is needed for these collisions to happen is some poly-dispersity in the emitted stream, and it seems even for single cone regime of charged droplets this is present [Lozano, 2003]. In the ionic regime the existence of two or more ionic species might trigger negative particle creation from the plume.
- It is a good idea to use zero vapor pressure propellants to avoid supply clogging by formation of solid deposits, because two conditions are required for deposit formation: Electron backflow and mass supply, i.e., deposition of materials (like vapors) from the space surrounding the surface in question.
- Externally fed geometries have the advantage that the propellant continuously covers the emitter structures, acting as a protective film. This film most certainly will be thicker than what any charged particle would travel before giving up its kinetic energy (the penetration depth of a 1kV electron beam into the liquid is of the order of 0.1-0.2 μm only). Also the protective film is renewed all the time because of the propellant flow towards the emitter tip. This clearly implies longer engine life.
- If the engine achieves neutralization by bipolar operation with time-modulation, the emitters will be negatively biased for half of the thruster lifetime. Electron bombardment cannot occur during such periods (but positive ion bombardment can). If electron bombardment is the main factor that limits the thruster life the lifetime would be at least doubled with respect to a positive-polarity concept with an electron neutralizer source.
- In the case of non-zero vapor pressure a key question is what is going to happen to the engine while off, because an exposed propellant area without forced emission will imply unnecessary propellant losses. A solution can be to freeze the propellant by using thermal control, taking advantage of the low thermal inertia of silicon. Another solution would be to provide the engine with valves to avoid propellant exposure. To implement a fabrication process for a valve in an already complex fabrication process is not an easy task but nonetheless might have to be contemplated to develop a realistic engine in terms of life-related issues. Of course, this issue is avoided if ionic liquids are used.

7.2.4 Technology Breakthroughs

The neutralization problem for Colloid Thrusters: Spatial bipolar mode, Time-dependent bipolar mode. Electrochemistry issues with ionic liquid as propellant

Colloid Thrusters, like any other kind of electric thrusters, need to maintain current neutrality because otherwise charge will continue to build up to a point where the engine cannot emit more. If the jets are not neutralized at some point, they will come back because of energy conservation to were they were created, in an oscillatory-like mode. Also, the spacecraft will change to high potential, and probably arcs or sparks will intermittently discharge it. It is clear then that the engine needs some sort of neutralization in real applications: in vacuum chamber tests this neutralization current, at least when positive charged particles are extracted, can be assumed by the vacuum chamber itself in the form of secondary electron emission. Colloid Thrusters have the advantage that they can emit both polarities, so in principle they can be self-neutralizing. This is specially important in this kind of engine because of the small absolute power involved in propulsive mechanisms and the rather large thermal losses created by common thermionic neutralizers (compared to the propulsive power). Therefore, it is clear that a good strategy would be to force the engine to emit both polarities. There are several options:

- To have a fraction of the emitters emit positive charge in DC, the rest emit negative charge. The connections should be such as to force *zero* net current emission.
- To have all emitters emit alternatively positive and negative charge, with *zero mean* current. Charge does accumulate temporarily, but if the rate of cycling is high enough, the capacitance of the spacecraft may limit voltages sufficiently. This probably requires prohibitively high frequencies.
- Operate at any time in a bipolar mode as in the first idem, but periodically reverse the polarities so that the engine mildly oscillates around the zero charge condition.

The latter option is more attractive because it also solves the problems created by localized *electrochemical effects*, which might be severe with ionic liquids.

Ionic liquids do not have a solvent but are completely made of ions of both polarities. When you operate in the pure ionic mode, one loses the capacity of the solvent to absorb the neutralized residue of the counter-ions and still emit it as part of the extracted droplets. Depending on the polarity of the engine if DC-energized for the case of $EMI-BF_4$ the emitters will either outgass or form a deposit that damages irreversibly the emitters. The solution then would be to avoid the electrochemical effects. From the work of the MIT Space Propulsion Laboratory [Martinez-Sanchez, 2003; Lozano and Martinez-Sanchez, in preparation] a solution has been offered that implies cycling the signal faster than what it takes to build up charge up to the point to trigger the electrochemical reactions. Experimentally it was demonstrated for a simple one-needle configuration that one can cycle the signal with a frequency equal to 1 Hz and have emitters that showed problems within one hour function cleanly for a week [Lozano, unpublished work].

The only drawback of a time-modulated neutralization is that it is inherent lossy. To charge/discharge a capacitor through a non-zero resistor implies to lose half the stored energy [Senturia, 2000]. However, because it only needs to be done at low frequency, the fractional energy loss could be overall very small.

Temperature control in Colloid Thrusters

The results from the experimentation done in Chapter 4 with the simplified version of the proposed black silicon based Planar Array are quite encouraging. The fact that it is possible to increase by one order of magnitude the emitted current by moderately increasing the engine temperature enables us to predict that temperature control is called to play an important role in the engine control dynamics. Silicon is a good heat conductor and does not have large specific heat inertia; therefore, it should be feasible to implement a reliable temperature control system.

On the other hand if the power density in the engine is large enough one may need to evacuate, instead of adding, heat to keep the engine working. In other words if the emitter density is large enough the losses per-emitter will build up to the point where some sort of cooling sys-

tem should be contemplated. The natural selection for an space application would be radiative heat transfer but it might need a different (at least locally) approach if the temperature difference is not specially favorable for this type of heat transfer mechanism.

Maybe the only drawback of increasing the engine temperature to increase the thrust is the fact that a certain amount of power needs to be spent in heating the engine. Because the deltas of temperature involved are very modest, good thermal design, with appropriate radiative shielding, should make this a non-issue.

Polymer based Emitters

One of the most exciting new directions for engine development is the fact that polymer substrates can be used to make the emitters. Polymers have several attractive properties:

- They are likely to naturally solve wettability issues at the emitter exterior (for example using teflon as substrate material will likely imply non-wettability).
- Polymers can be spun, molded and in general be processed in a high throughput/low cost scheme[1]. Potential polymer candidates are mylar, kapton, teflon, PDMS and SU-8.
- If the polymer has a small electrical permittivity the column of propellant (internally fed engine) will act as a conductive thin rod and enhance the electric field. Experimentally was found that emitters can be started with moderate voltage drops [Lopez-Urdiales, unpublished work; Lozano and Martinez-Sanchez, unpublished work] where the extra starting voltage is paid in terms of fabrication simplicity (no need to build field enhancers).

Polymers could be also patterned with laser, ultrasound, water and several other processing techniques that relax the clean-room constraints usually related to micro-fabrication. Also, because of the lack of sharpening, the emitters should be more robust (at least geometrically) to life-related damage. An improvement in this direction would be to use ceramics as substrate materials to create the hydraulic impedances, at least in the most external portion of the channels, so the sputtering mechanisms do not face a soft material (as any polymer is). The

1. This is an advantage for rapid prototyping, modular assembly and engine redundancy.

fabrication techniques would be different, mainly heat treatment of ceramic tubes or sintering. This idea is expanded in the following sub-section.

Holey fibers and improvements for uniform hydraulic impedance sources

One of the key problems in the development of the Linear Array was how to provide a uniform array of high aspect ratio hydraulic impedances. The proposed solution was to plasma pattern the channels by time controlling the etch, and to wafer-bond two substrates, with the consequent yield limitations that this procedure implies. There is a remarkable source of high hydraulic impedance that was recently proposed by Joseph Bango, form Connecticut Analytical. The idea is to borrow some of the latest technology in photonics: holey fibers. Holey fibers are optical fibers that contain inside many continuous air cavities, as shown in Figure 7.6.

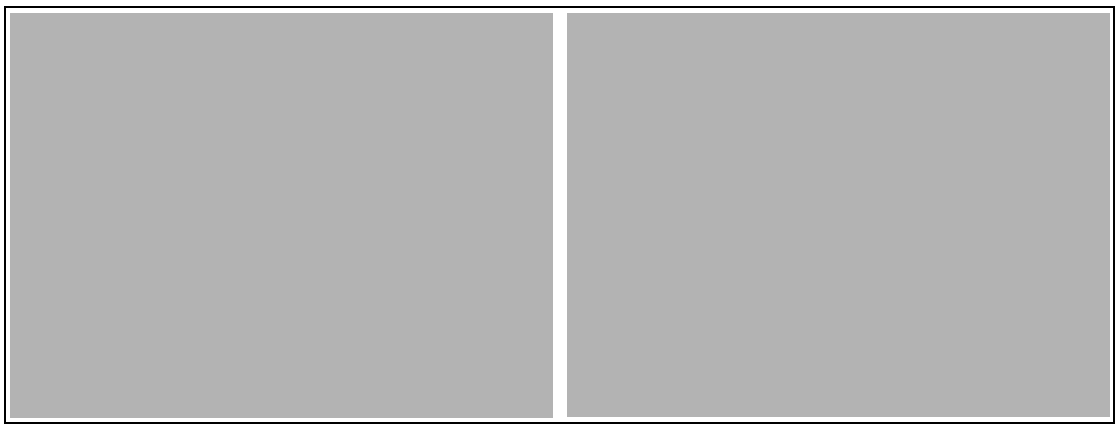

Figure 7.6 Cross-section of an optical fiber (*left*) and zoom (*right*). Notice the uniform, equally spaced channels that would be ideal as parallel hydraulic impedance source (courtesy of Joseph Bango).

For photonics applications the cavities play a role in improving the transmission capabilities of the optical fibers, but for our purpose they will provide highly uniform high hydraulic impedances with diameter-to-axial length ratios as large as desired. Surface treatments at the channel exits would make them non-wettable to the propellant (Bango has successfully used the ionic liquid $EMI-BF_4$ with the fibers in both filling the cavities and avoiding wetting of the exit).

The author believes that this is a key technology for the development of Colloid Thrusters because it removes two of the technological challenges of Colloid Thruster fabrication: generation of uniform, high hydraulic impedance arrays, and the need of external field enhancers, by using a commercial product from photonics companies, who care far more than us about cavity uniformity. The engine can then be composed of a propellant reservoir, a set of *straws* that would provide hydraulic impedance arrays, and electrodes. The electrical permittivity of fused silica, the raw material for these fibers, is low enough to allow us drop any special structural field enhancers in the engine (see the sub section *"Polymer-based E mitters"*) because the propellant columns will act themselves as field enhancers; therefore, a flat holey fiber exit would be good enough to avoid wetting problems if such surface is properly treated.

Each fiber would have its own electrode system. This can be implemented in two ways: each fiber could have a global electrode set, or a micro-fabricated electrode set that provide independent signal for each fiber cavity. If the electrode-to-emitter separation is large enough then to first order all fiber cavities are placed at the same location and a global ring, that takes care of the fan divergence, would be enough to give signal to the overall emitter set in each fiber. The micro-fabricated version would imply smaller extraction voltages because it could be placed closer to the emitters, but it would imply some clever alignment structure to take full advantage of the per-emitter control that it provides.

The author feels that this technology can substantially reduce the costs in developing Colloid Thrusters (you can get 1 meter fibers with the specifications pointed out at US $2.000 or less -prices of January 2004-; you need only about 15 mm per engine straw), reduce the fabrication times (no more wafer bonding, long plasma etchings, reservation times) and accelerate the generation of improved engine versions (quick iteration and validation of conceptual designs).

Appendix A

A MODEL OF THE ELECTROSTATIC PULL-IN IN A COLLOID THRUSTER

In this analysis the electrode structure is acting within its linear regime and the ability to recover from deflections is to first order constant if the deflections are small compared to the thickness of the beam that is acting as spring. The simple model that is proposed in this analysis is a doubly clamped beam where its lower surface is experiencing pulling due to the presence of an electric field between the beam and the substrate directly below it, as shown in the following figure:

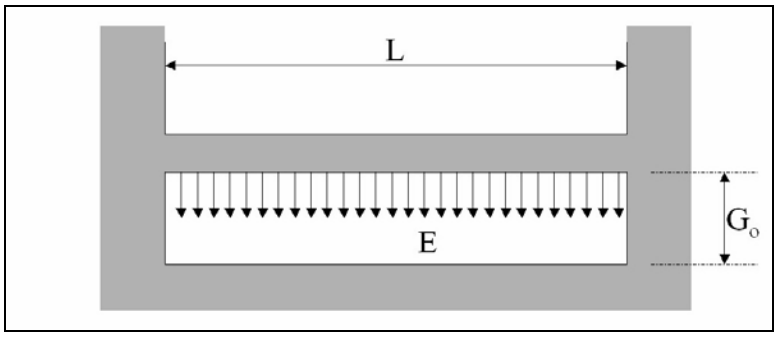

Figure A.1 Schematic of the model to predict the threshold conditions to generate an collapse of the electrode-emitter configuration. G_o is the unperturbed gap size.

There is space charge between the electrode and the substrate; therefore, the electric field between the beam and the bottom is not constant. If the gap G is smaller than the characteristic length of the frontal area of the electrode (the area that is facing the substrate) then an

space charge saturation 1-D model can be assumed to describe it. In this model the electric potential ψ, electric field E and charge flux J are

$$\psi = -V_E \cdot \left(\frac{x}{G}\right)^{4/3} \tag{A.1}$$

$$E = \frac{4}{3} \cdot \left(\frac{V_E}{G}\right) \cdot \left(\frac{x}{G}\right)^{1/3} \tag{A.2}$$

$$J = \frac{4\sqrt{2}}{9}\varepsilon_o\sqrt{\delta} \cdot \sqrt{\frac{V_E^{\,3}}{G^4}} \tag{A.3}$$

where V_E is the magnitude of the extractor potential and G is the distance between the plane where the particles are emitted at zero potential and the plane where the extractor voltage is applied, δ is the specific charge. To better illustrate all this analysis Figure A.2can be helpful.

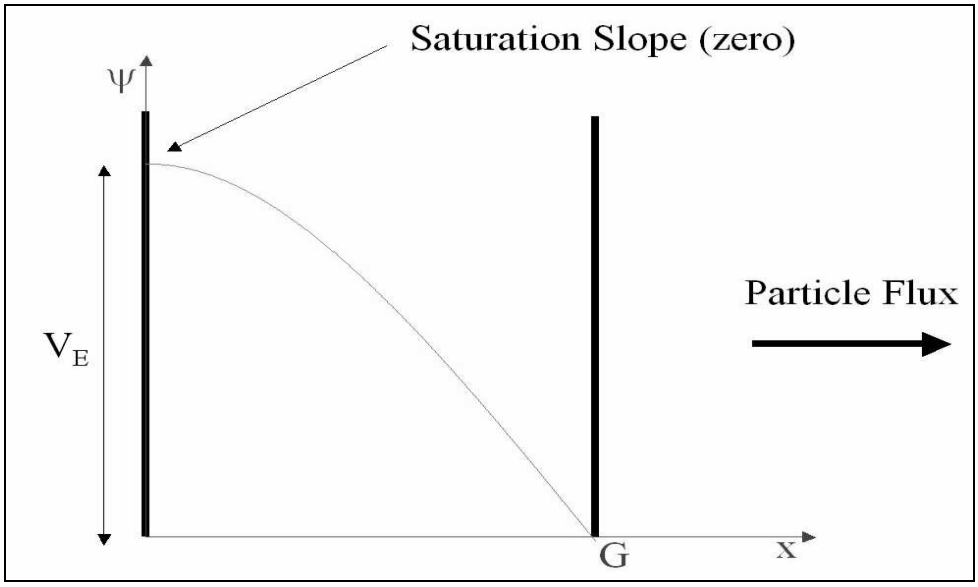

Figure A.2 Scheme to illustrate the Space Charge Saturation 1-D model.

The magnitude of the electric field at the electrode distance is given by

$$E_M = \frac{4}{3} \cdot \left(\frac{V_E}{G}\right) \tag{A.4}$$

The electrostatic pressure acting uniformly on the electrode is equal to

$$\frac{1}{2} \cdot \varepsilon_o \cdot E_M^2 = \frac{8}{9} \cdot \varepsilon_o \cdot \left(\frac{V_E}{G}\right)^2 \tag{A.5}$$

The electrostatic pressure at the substrate distance is zero: the particles in flight are pulling the electrode and their concentration is large enough to change the electric field.

The force acting on the electrode is

$$F_{pull} = \frac{8}{9} \cdot A \cdot \varepsilon_o \cdot \left(\frac{V_E}{G}\right)^2 \tag{A.6}$$

where A is the electrode side area. When the elastic properties of the electrode are taken into account then G has a dependence on the applied voltage; this way

$$G = G_o - x \tag{A.7}$$

where x describes the elastic displacement due to the electrostatic force

$$F_{pull} = x \cdot k_{stiff} \tag{A.8}$$

From equations A.6 and A.8 the net restoring force F_{NR} is

$$F_{NR} = k_{stiff} \cdot (G_o - G) - \frac{8}{9} \cdot A \cdot \varepsilon_o \cdot \left(\frac{V_E}{G}\right)^2 \tag{A.9}$$

which must be zero in equilibrium. The net stiffness is

$$\frac{\partial F_{NR}}{\partial(-G)} = k_{stiff} - \frac{16}{9} \cdot A \cdot \varepsilon_o \cdot \frac{V_E^2}{G^3} \tag{A.10}$$

and this should be positive for stability. The instability threshold is therefore

$$k_{stiff} = \frac{16}{9} \cdot A \cdot \varepsilon_o \cdot \frac{V_E^2}{G^3} \tag{A.11}$$

Replacing this stiffness value into the force balance shows that the maximum deflection before collapse is

$$G^* = \frac{2}{3} \cdot G_o \tag{A.12}$$

This is the same criterion for a parallel capacitor without charge inside the gap [Senturia, 2000]. The spring constant for doubly clamped beam of axial length L, area moment of inertia I^*, made of an isotropic material with Young's modulus E, and under uniform load is

$$k_{stiff} = \frac{384 \cdot E \cdot I^*}{L^3} \tag{A.13}$$

The condition found in equation A.11 implies that the maximum potential that can be applied across the gap is

$$V_{max} = \sqrt{\frac{64 \cdot E \cdot I^* \cdot G_o^3}{L^3 \cdot A \cdot \varepsilon_o}} \tag{A.14}$$

The area moment of inertia for a rectangular cross section is

$$I^* = \frac{b \cdot H^3}{12} \tag{A.15}$$

where H is the cross-section height and b is the cross-section width. For purposes of electrostatic pull determination the electrode side area A is not the full area facing the emitters but, as a first approximation, the metallized area of the conducting path: the other portions of the front area are covered with dielectric and there the electric field is not normal to the surfaces, but has a rather large tangential component to force a constant potential on the metallic parts. Because tangential fields produce electromagnetic pressure opposite to the electromagnetic pressure produced by normal fields, this is an effect on our side to avoid structural collapse.

Roughly speaking the conductive path is formed by two strips of length L and width υ. Taking into account this information equation A.15 is simplified into

$$V_{max} = \sqrt{\frac{8 \cdot E \cdot b \cdot H^3 \cdot G_o^3}{3 \cdot L^4 \cdot \upsilon \cdot \varepsilon_o}} \tag{A.16}$$

Appendix B

A MODEL ON SPACE CHARGE SATURATION FOR COLLOID ENGINE

The following analysis combines the equations that describe the current emitted by single Taylor Cone emitters in droplet mode with the Child-Langmuir space saturation model to determine the necessary conditions for space charge limitation in Colloid Thruster Arrays. The current emitted by Taylor Cones operating in droplet mode is [de la Mora, 1994]

$$I = f(\varepsilon) \cdot \sqrt{\frac{\gamma \cdot K \cdot Q}{\varepsilon}} = \rho \cdot \delta \cdot Q \qquad \text{(B.1)}$$

where γ is the surface tension of the liquid, K is its electrical conductivity, Q is the volumetric flowrate expelled from the Taylor cone, ρ is the liquid density and ε is its relative electrical permittivity; $f(\varepsilon)$, is an empirically determined quantity that roughly speaking is described by the following set of equations

$$f(\varepsilon) = \begin{cases} \frac{\varepsilon}{2}, \varepsilon < 40 \\ 20, \varepsilon \geq 40 \end{cases} \qquad \text{(B.2)}$$

The flowrate can be expressed as

$$Q = \eta^2 \cdot \frac{\gamma \cdot \varepsilon \cdot \varepsilon_o}{\rho \cdot K} \qquad \text{(B.3)}$$

where η is a dimensionless parameter, equal to the square root of the ratio between inertial and capillary forces evaluated at the characteristic radius r^*, where r^* scales with the jet diameter. The current carried by a Taylor cone is then

$$I = f(\varepsilon) \cdot \eta \cdot \gamma \cdot \sqrt{\frac{\varepsilon_o}{\rho}} \tag{B.4}$$

the jet will break up into droplets at some downstream distance due to instabilities. The current that is expelled from a Taylor Cone will eventually distribute itself over an area that increases as the droplets get farther from the cone apex. The highest average current density occurs when the charged droplets of the array of Taylor cones first meet. For a Linear Array the charge is distributed in an area that scales with the square of the emitter spacing S; in the case of a Planar Array the area scales with the square of the characteristic length S times some geometrical factor ζ that takes into account the emitter packing and their relative distribution. For the case of a squared Planar Array the ζ factor is equal to 1. Therefore, the current flux from a Taylor Cone as part of an array is

$$J = \frac{f(\varepsilon) \cdot \eta \cdot \gamma}{\zeta \cdot S^2} \cdot \sqrt{\frac{\varepsilon_o}{\rho}} \tag{B.5}$$

To obtain the saturation current we equate the average current density in the Colloid Thruster array and the Child-Langmuir current density, and we obtain that the gap to emitter spacing ratio at saturation is

$$\frac{G}{S} = \sqrt{\frac{4\sqrt{2} \cdot \zeta}{9 \cdot f(\varepsilon) \cdot \eta \cdot \gamma}} \cdot \sqrt[4]{\varepsilon_o \cdot \delta \cdot \rho \cdot V_E^{\,3}} \tag{B.6}$$

The extraction potential V_E for a meniscus not interacting with its neighbors can be calculated using an axisymmetric asymptotic model [Martinez-Sanchez, 2001]. If the radius of Curvature R_c is far smaller than the electrode-to-emitter distance then the minimum voltage to create the electrical instability that generates the Taylor cone in a meniscus is

$$V_E = \sqrt{\frac{\gamma \cdot R_c}{\varepsilon_o}} \ln\left(\frac{4 \cdot G}{R_c}\right) \tag{B.7}$$

Or in general for a given geometry

$$V_E = \sqrt{\frac{\gamma \cdot L_c}{\varepsilon_o}} \ln\left(\frac{4 \cdot G}{L_c}\right) \tag{B.8}$$

where L_c is to first order the hydraulic diameter of the emitter. The meniscus needs to be outside the confining cross-section; therefore, only positive R_c values are allowed. The upper bound of the R_c magnitude is ∞, corresponding to a flat meniscus. The lower bound of the R_c magnitude is proportional to L_c. To assume a R_c value around the lower bound is a good idea because it characterizes a worst-case scenario.

If equation B.8 is replaced into equation B.6 we get

$$\frac{G}{S} = \sqrt{\frac{4\sqrt{2} \cdot \zeta}{9 \cdot f(\varepsilon) \cdot \eta \cdot \gamma}} \cdot \sqrt[4]{\varepsilon_o \cdot \delta \cdot \rho \cdot \left[\sqrt{\frac{\gamma \cdot L_c}{\varepsilon_o}} \ln\left(\frac{4 \cdot G}{L_c}\right)\right]^3} \tag{B.9}$$

The droplets are not monodisperse but an average δ value from the de la Mora's model can be used.

Appendix C

SUMMARY OF THE CONVENTION USED TO LABEL THE PLANAR ARRAYS

TABLE C.1 Compendium of the different emitter module configurations available in the mask *ARRAY*. *Emitter separation* is defined as the distance between emitter centers and *internal diameter* is defined as the diameter of the maximum circle that fits inside the emitter cross-section. The *OD* label refers to the external diameter when the emitter cross-section is a star. The first number refers the column number from the upper left corner of the optical mask, while the second number refers the row number from the same reference point.

LABEL	NUMBER OF EMITTERS	EMITTER SEPARATION	CROSS SECTION	INTERNAL DIAMETER
I-I, II-I, III-I	16X16	500 μm	square	100 μm
II-II, II-II, III-II	16X16	500 μm	hexagon	100 μm
I-III,II-III,III-III	16X16	500 μm	octagon	100 μm
I-IV, II-IV, III-IV	16X16	500 μm	circle	100 μm
I-V, II-V, III-V	16X16	500 μm	5-point star	100 μm (OD 200 μm)
I-VI, II-VI, III-VI	16X16	500 μm	6-point star	100 μm (OD 200 μm)
I-VII, II-VII, III-VII	16X16	500 μm	16-point star	100 μm (OD 200 μm)
I-VIII, II-VIII, III-VIII	16X16	500 μm	16-point star	100 μm (OD 125 μm)
I-IX, II-IX, III-IX	32X32	250 μm	8-point star	100 μm (OD 200 μm)
I-X, II-X, III-X	8X8	1000 μm	8-point star	100 μm (OD 200 μm)
IV-I, V-I, VI-I	8X8	1000 μm	square	200 μm
IV-II, V-II, VI-II	8X8	1000 μm	hexagon	200 μm
IV-III, V-III, VI-III	8X8	1000 μm	octagon	200 μm

TABLE C.1 Compendium of the different emitter module configurations available in the mask *ARRAY*. *Emitter separation* is defined as the distance between emitter centers and *internal diameter* is defined as the diameter of the maximum circle that fits inside the emitter cross-section. The *OD* label refers to the external diameter when the emitter cross-section is a star. The first number refers the column number from the upper left corner of the optical mask, while the second number refers the row number from the same reference point.

LABEL	NUMBER OF EMITTERS	EMITTER SEPARATION	CROSS SECTION	INTERNAL DIAMETER
IV-IV, V-IV, VI-IV	8X8	1000 μm	circle	200 μm
IV-V, V-V, VI-V	8X8	1000 μm	5-point star	200 μm (OD 525 μm)
IV-VI, V-VI, VI-VI	8X8	1000 μm	6-point star	200 μm (OD 395 μm)
IV-VII, V-VII, VI-VII	8X8	1000 μm	16-point star	200 μm (OD 395 μm)
IV-VIII, V-VIII, VI-VIII	8X8	1000 μm	16-point star	200 μm (OD 255 μm)
IV-IX, V-IX, VI-IX	16X16	500 μm	8-point star	200 μm (OD 390 μm)
IV-X, V-X, VI-X	4X4	2000 μm	8-point star	200 μm (OD 390 μm)
VII-I, VIII-I, IX-I	4X4	2000 μm	square	400 μm
VII-II, VIII-II, IX-II	4X4	2000 μm	hexagon	400 μm
VII-III, VIII-III, IX-III	4X4	2000 μm	octagon	400 μm
VII-IV, VIII-IV, IX-IV	4X4	2000 μm	circle	400 μm
VII-V, VIII-V, IX-V	4X4	2000 μm	5-point star	400 μm (OD 1050 μm)
VII-VI, VIII-VI, IX-VI	4X4	2000 μm	6-point star	400 μm (OD 785 μm)
VII-VII, VIII-VII, IX-VII	4X4	2000 μm	16-point star	400 μm (OD 785 μm)
VII-VIII, VIII-VIII, IX-VIII	4X4	2000 μm	16-point star	400 μm (OD 507 μm)
VII-IX, VIII-IX, IX-IX	8X8	1000 μm	8-point star	400 μm (OD 775 μm)
VII-X, VIII-X, IX-X	2X2	4000 μm	8-point star	400 μm (OD 775 μm)

TABLE C.1 Compendium of the different emitter module configurations available in the mask *ARRAY*. *Emitter separation* is defined as the distance between emitter centers and *internal diameter* is defined as the diameter of the maximum circle that fits inside the emitter cross-section. The *OD* label refers to the external diameter when the emitter cross-section is a star. The first number refers the column number from the upper left corner of the optical mask, while the second number refers the row number from the same reference point.

LABEL	NUMBER OF EMITTERS	EMITTER SEPARATION	CROSS SECTION	INTERNAL DIAMETER
X-I, X-II	25X25	320 μm	16-point star	150 μm (OD 295 μm)
X-III, X-IV	20X20	400 μm	16-point star	150 μm (OD 295 μm)
X-V, X-VI	10X10	800 μm	16-point star	150 μm (OD 295 μm)
X-VII, X-VIII	8X8	1000 μm	16-point star	150 μm (OD 295 μm)
X-IX, X-X	5X5	1600 μm	16-point star	150 μm (OD 295 μm)

Appendix D

A CRASH COURSE ON FIELD EMISSION

The author decided to make a few remarks on field emission because of the experimental results discussed in the following sections. The intention with this small introduction is by no means to address the field emission topic with substantial depth but to provide some guidelines to the reader.

There are a number of field emission mechanisms with different voltage-to-current dependences, mostly based in the quantum nature of charge interactions. In this brief summary the theory behind thermionic emission, Saturated current emission, Child-Langmuir emission, Fowler-Nordheim emission and cold emission will be explored. Some other emission mechanisms are not discussed because the author considers they are not relevant to explain the emission observed in the Planar Electrospray Thruster Array. For a deeper exposure on the different emission mechanisms the author of this work recommends in particular two references: [Jenkins, 1966] and [Gomer, 1993].The following conceptual views are useful to better understand the physical models of the different emission mechanisms.

D.1 Electrons in solids

Electrons can be represented as being inside a potential well representing the minimum energy that an electron needs to leave the material. These solids can be either conductors, insulators or semiconductors.

Metals are modeled as ideal conductors. In this scheme the atoms are assembled into a crystal lattice and they lose their valence atoms. This group of electrons move freely through the metal, and are the *conduction* electrons, similar to a highly densified electron gas. The statistics that describe the conduction electrons is the Fermi-Dirac distribution. There is a maximum energy level occupied by the valence electrons named the *Fermi* level. The *work function* is the difference between the vacuum energy level and the Fermi level.

In the case of insulators and semiconductors the assumption that valence electrons are free to move through the solid is no longer valid. In order to describe the physical behavior of these materials the band theory should be used. In a few lines this can be stated as follows:

- The electrons of a single atom have some discrete allowed energy levels.
- When these atoms form part of a lattice the energy levels are perturbed and become bands in order to allocate the electrons to the allowed energy levels without violating the exclusion principle.
- The regular arrangement of the solid causes a periodic field distribution.
- electrons with some energies are able to propagate through the solid while those with other energies don't, creating a set of bands separated by energy gaps. In particular the gap between the highest energy of bound electrons and the lowest conduction energy is large in an insulator. In a semiconductor this gap is smaller and can decrease even more if impurities place *hop* middle energy levels that make the crossing feasible.

For the band scheme the conductivity increases rapidly with increasing temperature, because the higher energy tail of the distribution of valence electrons spills into the conduction band as the temperature increases.

D.2 Surface barrier and Schottky Emission

There is a surface barrier that prevents easy escape of electrons from conductive surfaces. One of the simplest models was suggested by Schottky. This model postulates that for an electron to leave a smooth surface of a metal the material has to be polarized and the force between the material and the charged particle can be seen as the attraction between the departing particle and its mirror image. The energy to separate the electron from its mirror

image, starting at the atom size distance is inversely proportional to the atomic radius. The work function is the sum of this escape energy and the energy implied in moving the electron from zero position to the atomic radius (this energy is also inversely proportional to the atom radius); therefore denser metals (smaller atoms) have substantially larger work functions than less dense ones. this also means that the work function depends on the anisotropic lattice packing. The work function can be modified by the presence of impurities at the metal surface. The Schottky emission can be seen as a field-enhanced thermionic emission where the bias voltage is responsible of perturb the barrier the electrons need to surpass to exit the emitter surface. When the applied voltage exceeds the value necessary to draw the total emission to the anode a positive field is established that makes the work function barrier to be reduced. This is known as *Schottky effect*. The corrected Richardson-Dushman emission equation is then

$$I = I_o(T^2) \cdot e^{\frac{-\tilde{\phi}}{k_B \cdot T}} \cdot e^{\sqrt{\frac{V_E}{V_o(T)}}} \tag{D.1}$$

This means that beyond the saturation regime the current continues to rise with an exponent proportional to the *square root* of the applied voltage.

D.3 Thermionic Emission (clean metals)

Thermionic emission, the electron emission from heated solids, is by far the most used type of emission mechanism in engineering devices. This mechanism is the explanation of the *Edison effect* that is present when a vacuum tube is working. The *Richardson-Dushman* equation gives the current density emitted by a body at temperature T with a work function $\tilde{\phi}$

$$I = \frac{4\pi \cdot m \cdot k_B \cdot T^2}{h_p^3} \cdot e^{\frac{-e \cdot \tilde{\phi}}{k_B \cdot T}} \tag{D.2}$$

If the constants are piled up as I_o and V_o we obtain the generic equation that describes thermionic emission from semiconductors as well

$$I = I_o(T^2) \cdot e^{\frac{-\tilde{\phi}}{V_o(T)}} \tag{D.3}$$

The thermionic model is not of relevance for the modeling of the emitted charge of the 2-D Colloid Thruster Array because the substrate temperatures are far too low for it to be activated.

D.4 Saturated emission

The model of thermionic emission can be extended to the *saturated emission diode* regime where the presence of a bias voltage is taken into account. In this case the current is expressed as

$$I = I_o(T) \cdot e^{\frac{-V_E}{V_o(T)}} \tag{D.4}$$

where V_E represents a bias voltage. In the event of a negative bias voltage this emission mode will produce an exponential increase in the emitted current.

D.5 Child-Langmuir Emission

When the bias voltage becomes positive the current gets limited by the emitted electrons forming a space charge region. Therefore, the current density obeys the Child-Langmuir law that can be generically stated as

$$I = I_o \cdot V_E^{3/2} \tag{D.5}$$

where I_o is in particular a function of the inverse of the square of the space charge region length, called the *perveance*.

D.6 Fowler-Nordheim Emission

This emission theory applies in emitters at low temperatures, with high surface electric fields. In the thermionic emission model, the classical assumption was made that electrons without

energies larger than the well energy barrier cannot escape the well. In the quantum mechanics picture the wave function ψ can have a non-zero value at portions outside the potential well, making it possible for the electrons to tunnel through the barrier. It is reported in the literature that this tunneling mechanism is common for electric fields of the order of $4 \times 10^9 V/m$ or more. The result of a model that takes into account quantum tunneling is the *Fowler-Nordheim* relationship, where the resulting current density is given by

$$I = \frac{q}{2\pi \cdot h_p} \cdot \frac{\frac{h_p^2}{2 \cdot m}\left[\frac{3 \cdot n}{8\pi}\right]^{1/3} \cdot E^2}{\left[\tilde{\phi} + \frac{h_p^2}{2 \cdot m}\left[\frac{3 \cdot n}{8\pi}\right]^{2/3}\right] \cdot \sqrt{\tilde{\phi}}} \cdot e^{-\frac{4}{3} \cdot \sqrt{\frac{8 \cdot \pi^2 \cdot m}{h_p^2}} \cdot \frac{\tilde{\phi}^{3/2}}{q \cdot E}} \tag{D.6}$$

where q is the electron charge, h_p is Plank's constant, m is the electrons mass, E is the electric field at the emitter tip, and n is the electron number density. The electric field near the surface is proportional to the applied electric field divided by a characteristic length. The equation D.6 can be generalized as

$$I = I_o \cdot V^2 \cdot e^{-\frac{V_o}{V_E}} \tag{D.7}$$

Nomenclature

GREEK

α_T	Taylor Cone semi-angle, equal to 49.3 [°]
β	In a Stable Single Taylor cone, Fraction of the Total Current that is delivered by the Ion Stream in an ion/Droplet Stream [-]
β_1	Scaling factor of the volume that produces most of the viscous disipation [-]
β_2	Scaling factor of the distance that produces most of the viscous disipation [-]
Ξ	Porosity [-]
δ	Specific Charge, i.e., charge per unit of mass [Coulomb/Kg]
δ_D	Droplet Specific Charge [Coulomb/Kg]
δ_I	Ion Specific Charge [Coulomb/Kg]
δ^*	Ratio between the Droplet Specific Charge and the Ion Specific Charge [-]
δ_h	Hydraulics thickness [m]
ε_o	Free-space Electrical Permittivity, $8.85 \cdot 10^{-12}$ [Farads/m]
ε	Relative Electrical Permittivity [-]
γ	Surface Tension coefficient [N/m]
μ	Viscosity [Pa.s]
μ_{eff}	Effective Viscosity [Pa.s]
ζ	Area Factor, Area = $s^2 \cdot \zeta$ [-]
θ_{ctct}	Contact Angle [rad]
$\tilde{\phi}$	Work Function [V]
υ	Electrode Conductive Path Thickness Width [m]
η	Dimensionless ratio of inertial forces over capillary forces at the point of maximum normal electric field [-]
η_{min}	Minimum η value for stable single cone droplet operation [-]
η_P	Propulsive Efficiency [-]
Λ	Void Volume to Wetted Area Ratio [m]
ρ	Mass Density [Kg/m^3]
ψ	Electrostatic Potential [V]
ψ	Wave Function [m^{-1}, 1D]
Δ_j	Misalignment in the j-axis [m]
ΔV	Velocity Delta [m/sec.]
$\Delta\psi$	Delta of Electrical Potential [V]
$\varnothing$	Characteristic pore diameter [m]
Γ	Particle Flux [particles/m^2]

A

A	Electrode Frontal Area [m^2]
$A_\perp$	Cross-sectional Area [m^2]

B

b	Beam base dimension (i.e., width) [m]
B	Channel Width [m]

C

c	Final charged particle speed [m/sec.]

Ca	Capillarity number [-]
D	
D^*	Critical hydraulic diameter to enable electrical control [m]
D_I	Imprint Diameter [m]
D_{gas}	Nitrogen Tank Channel diameter (C.T. Linear Array propellant supply) [m]
D_{interm}	First Stage Exit Channel diameter (C.T. Linear Array propellant supply) [m]
D_{inlet}	Diameter of Propellant channel connected directly to the C.T. Linear Array (C.T. Linear Array propellant supply) [m]
D_{pump}	Pump channel diameter (C.T. Linear Array propellant supply) [m]
E	
E	Electric Field [V/m], Young's Modulus [Pa]
$\tilde{E}_{min}$	Minimum Energy to produce Thermionic Emission [N.m]
E_{tot}	Total Energy [J]
E_{TH}	Minimum Electric Field to produce Taylor Cone threshold condition [V/m]
E_M	Electric Field @ Electrode Surface [V/m]
F	
$f(\varepsilon)$	de la Mora's experimental fit for the flowrate versus emitted current dependence in a single cone droplet regimen Taylor Cone emission [-]
F	Thrust [N]
F_{pull}	Electrostatic pulling force acting on the electrode [N]
G	
G	Emitter-to-extractor Gap [m]
G_o	Unperturbed Gap size [m]
G^*	Threshold Gap for Collapse [m]
g	Gravity Constant [m/sec./sec.]
H	
h_p	Plank's Constant [N.m.sec]
h_d	Propellant deposit height [m]
H	Beam Height [m]
I	
I	Current [Coulomb/sec.]
I_o	Field Emission Base Current [Coulomb/sec.].
I_{sp}	Specific Impulse, i.e., Thrust per unit of weight flowrate [sec.]
I^*	Cross-sectional Area Inertia Moment [m^4]
J	
J	Current Flux [A/m^2]
K	
k_B	Boltzmann's Constant [V/Coulomb]
K_n	Knudsen Number [-]
k_{stiff}	Equivalent Spring constant [N/m]
K	Electrical Conductivity [Si/m]
K_k	Kozemy Constant [-]
K^*	Permeability [m^2]
K_{th}	Thermal Conductivity [W/K/m]
L	

L	Axial Dimension (e.g., beam length) [m]
L_o	Undeformed Length [m]
L_c	Hydraulic diameter [m]
L_c^o	External spout characteristic cross-sectional length [m]
L_{gas}	Nitrogen Tank Channel Length (C.T. Linear Array propellant supply) [m]
L_{interm}	First Stage Exit channel Length (C.T. Linear Array propellant supply) [m]
L_{inlet}	Length of the Propellant Channel connected directly to the Linear C.T. Array (Linear C.T. propellant supply) [m]
L_{pump}	Pump channel length (Linear C.T. Array propellant supply) [m]
M	
m	Mass [Kg]; Counter [-]
m_v	vapor molecule mass [kg]
$\dot{m}$	Mass flowrate [Kg/sec.]
N	
n	Number Density [particles/m3]; Counter [-]
$\dot{N}_n$	Production Rate of the n-species Particle [particles/sec.]
O	
P	
P	Mechanical Pressure [N/m^2]
P_w	Power in [W]
P_{gas}	Pressure at the Nitrogen Tank (C.T. Linear Array propellant supply) [Pa]
P_{interm}	Pressure at the first exit stage (C.T. Linear Array propellant supply) [Pa]
P_{po}	Pressure at the external propellant tank (C.T. Linear Array propellant supply) [Pa]
P_{pump}	Pump Inlet pressure (C.T. Linear Array propellant supply) [Pa]
P_o	Engine Tank Stagnation pressure (C.T. Linear Array propellant supply) [Pa]
P_{out}	Power out [W]
P_{vap}	Vapor Pressure [Pa]
Q	
q	Particle Charge [Coulombs]
Q	Flowrate [m^3 /sec.]
Q_{min}	Minimum flowrate for single Taylor Cone stable operation [m^3 /sec.]
R	
R_Ω	Ohmic Resistance [Ohms]
R	Spherical radius [m]
R_c	Radius of Curvature [m]
R_D	Droplet Radius [m]
R_j	Jet Radius [m]
r*	Characteristic length in aTaylor Cone that scales with the jet radius [m]
S	
S	Emitter-to-emitter separation length [m]
T	
t	Time [sec.]
T	Temperature [°C , K]
T_o	Reference Temperature [°C , K]

U

U	Unperturbed Jet Velocity [m/sec.]
$\tilde{U}$	Internal Potential Energy [J]

V

v	Velocity [m/sec.]
v_{rad}	Irrotational Sink Velocity [m/sec.]
$\bar{v}$	Bulk velocity [m/sec.]
V	volume [m^3], Total Voltage Drop [V]
V_o	Unperturbed Volume [m^3], Field Emission characteristic voltage [V]
V_E	Extraction Voltage [V]
V_A	Acceleration Voltage [V]
V_{max}	Maximum Electric potential through the gap before pull-in collapse [V]

X

x	Coordinate parallel to the gap normal [m]

REFERENCES

[Adler, 1992] Adler, P., *"Porous Media"*, 1992.

[Akinwande, 2001] Akinwande, A. I., *"Analytical Electrostatic Model of Silicon Conical Field Emitters-Part I"*, IEEE Transactions of Electron Devices, Vol 48, No 1, January 2001.

[Akinwande, 2001-2] Akinwande, A. I., *"Analytical Electrostatic Model of Silicon Conical Field Emitters-Part II: Extension to Devices with Focusing Electrode"*, IEEE Transactions of Electron Devices, Vol 48, No 1, January 2001.

[Akinwande, 2002] Akinwande, A. I., *"Double-gated Spindt Emitters with Stacked Focusing Electrode"*, J. Vac. Sci. Technol. B 20(1), American Vacuum Society, 2002.

[Anderson, 1991] Anderson, C., *"Investigations of the Electrical Properties of Porous Silicon"*, Journal of the Electrochemical Society, v 138, n 11, Nov. 1991, p 3406-11.

[Bailey, 1975] Bailey, A., *"Temperature Effects and Capillarity in an electrostatic Thruster"*, 75A434, AIAA 11th Electric Propulsion Conference, New Orleans, LA, 1975.

[Browning, 1997] Beowning, J , *"Scaling of Field Emission Display Technology"*, F-42 - F-46, International Display Research Conference, Toronto, Canada, 1997.

[Campbell, 1996] Campbell, S., *"The Science and Engineering of Microelectronic Fabrication"*, Oxford University Press, 1996.

[Carretero, 2003] Carretero, J., *"Modelling Developments on Colloid Thrusters"*, 28th International Electric Propulsion Conference, Toulouse, France, 17-21 March, 2003.

[Lide, 1995] Lide, D., *"Handbook of Chemistry and Physics"*, CRC, 1995.

[de la Mora, 1994] de la Mora, J., *"The Current Emitted by Highly Conductive Taylor Cones"*, J. Fluid Mech., vol 260 pp 155 - 184, 1994.

[de la Mora, 2003] de la Mora, J., *"A Source of Heavy Molecular Ions Based on Taylor Cones of Ionic Liquids Operating in the Pure Ion Evaporation Regime"*, Journal of Applied Physics, vol. 94, No. 6, September 2003.

[dos Santos, 1998] dos Santos, M., *"Aligned Pipe Arrays Formation by Silicon Anodic Etching"*, J. Vac. Science Technology B, 16 (4) 1998.

[Dressler, 2003] Dressler, R., *"Mass Spectrometric Analysis of Ion Emission for Selected Colloid Thruster Fuels"*, 39th AIAA/ASME/SAE/ASEE Joint Propulsion Conference and Exhibit, 2003.

[Fenn, 1989] Fenn, J.,*"Colloid Ionization for Mass Spectrometry of Large Biomolecules"*, Science, 246, 64-71, 1989.

[Fife, 2002] Fife, M., *"A Colloid Engine Accelerator Concept"*, AIAA 2002-3811, 38th AIAA Joint Propulsion Conference, Indianapolis, Indiana, 2002.

[Fuller, 1997] Fuller, J, *"The room Temperature Ionic Liquid 1-ethyl-3-methylimidazolium Tetrafluoroborate: Electromechanical Couples and Physical Properties"*, J. Electrochem. Soc., 144, 3881-3885, 1997

[Gilbert, 1600] Gilbert, W., *"De Magnete, Magneticisque Corporibus"*, London, 1600.

[Gamero, 2001] Gamero, M., "*Colloid as a Source of Nanoparticles for Efficient Colloid Thrusters",* J. of Propulsion and Power, Vol 17., No 5., 2001.

[Gomer, 1993] Gomer, R., *"Field Emission and Field Ionization"*, American Institute of Physics, 1993.

[Hall, 1949] Hall, R., *"The Application of non-Integral Legendre Functions to Potential Problems"*, Journal of Applied Physics, Volume 20, October, 1949.

[Hendricks, 1966] Hendricks, C., *"Parametric Studies of Electrohydrodynamic Spraying"*, 66A252, AIAA 5th Electric Propulsion Conference, San Diego, CA, 1966.

[Hruby, 2001] Hruby, V., *"Micro Newton Colloid Thruster System Development"*, IEPC-01-281, 27th International Electric Propulsion Conference, Pasadena, CA, 2001.

[Hunter, 1965] Hunter, R. E., *"Exploring the Feasibility of the Electrodeless Colloid Thrustor"*, Ph.D. Dissertation, Ohio State University, 1965.

[Jansen, 1995] Jansen, H., *"The Black Silicon Method: A Universal Method for Determining the parametric Setting of a Fluorine-Based Reactive Ion Etcher in Deep Silicon trench Etching with Profile Control",* Journal of Micromechanics and Microengineering, V5, No. 2, June 1995, p115-20

[Jenkins, 1966] Jenkins, R., *"Electron and Ion Emission from Solids"*, Dover Publications Inc.,

1966.

[Khayms, 2000] Khayms, V., *"Advanced Propulsion for Microsatellites"*, Ph.D. Dissertation, Massachusetts Institute of Technology, September 2000.

[Kenneth, 1969] Kenneth, W., *"Research and Development in Needle and Slit Colloid Thrusters"*, NASA TN D-5305, Goddard Space Flight Center, Greenbelt, MD, 1969.

[Leonomand, 1981] Leonomand, ?????????????????? *"Libro que habla de como calcular tension superficial en un tubo de seccion cuadrada"*

[Lozano, 2003] Lozano, P., "*Studies on the Ion-Droplet Mixed Regime in Colloid Thrusters"*, Ph.D.Thesis, Massachusetts institute of Technology, 2003.

[Madou, 2002] Madou, M., *"Fundamentals of Micro-fabrication"*, Second Edition, CRC Press LLC, 2002.

[Mair, 1991] Mair, G. L., *"Link Focused ion beams from liquid metal ion sources"*, Wiley, 1991.

[Marrese, 2003] Marrese, C., *"Colloid Thruster Propellant Stability after Radiation Exposure"*, 39th AIAA/ASME/ASEE Joint Propulsion Conference and Exhibit, 2003

[Martínez-Sánchez, 1999] Martínez-Sánchez, M., *"Research on Colloid Thrusters"*, 26th International Electric propulsion Conference, Kitakyushu, Japan, 1999.

[Martínez-Sánchez, 2001] Martínez-Sánchez, M., Class notes of the course *Space Propulsion*, Massachusetts Institute of Technology, Spring 2001.

[Martínez-Sánchez, 2003] Martínez-Sánchez, M., Pending patent on the method to eliminate electrochemical effects on Colloid using ionic liquids, 2003.

[Mueller, 1997] Mueller, J., *"Thruster options for Microspacecraft: A Review and Evaluation of Existing Hardware and Emerging Technologies"*, AIAA 77-3058, 1997.

[Mueller, 2002] Mueller, J., *"JPL Micro-Thrust Propulsion Activities"*, AIAA-2002-5714, Nano-Tech 2002, "At the Edge of the Revolution", Houston, Texas, 2002.

[Paine, 1999] Paine, M., *"Design Study for Micro-fabricated Colloidal Thrust"*, MS THesis, Massachusetts Institute of Technology, 1999.

[Paine, 2001] Paine, M., *"A Micro-fabricated Colloid Thruster Array"*, AIAA 2001-3329, 37th AIAA/ASME/SAE/ASEE Joint Propulsion Conference and Exhibit, Salt Lake City, Utah, 2001.

[Perel, 1967] Perel, J., *"Research on a Charged Particle Bipolar Thrustor"*, 67A728, AIAA Electric Propulsion and Plasmadynamics Conference, Colorado Springs, CO, 1967.

[Perel, 1970] Perel, J., *"Analytical Study of Colloid Annular Thrusters"*, 70A1113, AIAA 8th Electric Propulsion Conference, Stanford, CA, 1970.

[Perel, 1970-2] Perel, J., *"Experimental Study of Colloid Annular Thrusters"*, 70A1112, AIAA 8th Electric Propulsion Conference, Stanford, CA, 1970.

[Perel, 1973] Perel, J., *"Colloidal Annular Array Thruster Development"*, 73A1077, AIAA 10th Electric Propulsion Conference, Lake Tahoe, Nevada, 1973.

[Perel, 1978] Perel, J., *"Mechanisms of Emitter Surface Damage During Electrohydrodynamic Colloid Particle Generation and Acceleration"*, AFOSR TR 78 - 1026, Work performed under AFOSR Contract F44620-75-C-0056, 1978.

[Pranajaya, 1999] Pranajaya, F., *"Progress on Colloid Micro-thruster Research and Flight Testing"*, 1999.

[Rayleigh, 1882] Lord Rayleigh, Phil. Mag., V., 14, pp. 184, 1882.

[Reichbach, 2001] Reichbach, J., *"Micropropulsion System Selection for Precision Formation Flying Satellites"*, 37th AIAA/ASME/SAE/ASEE Joint Propulsion Conference & Exhibit, Salt Lake City, Utah, 2001.

[Rice, 1981] Rice, W. R., *"The Effect of Grinding Direction on Flaw Character and Strength of Single Crystal and Polycristaline Crystals"*, J. Mater. Sci., Vol 16, 853 - 862, 1981.

[Senturia, 2000] Senturia, S., *"Microsystem Design"*, Kluwer Academis Publishers, 2000.

[Shtyrlin, 1996] Shtyrlin, A., *"State of the Art and Future Prospects of Colloidal Electric Thrusters"*, AIAA, 96A29967, 1996.

[Slocum, 1992] Slocum, A., *"Precision Machine Design"*, Prentice Hall, 1992.

[Smythe, 1939] Smythe, W., *"Static and Dynamic Electricity"*, McGraw-Hill, 1939.

[Spearing, 2000] Spearing, M, *"Controlling and Testing Fracture Strength of Silicon on the Mesoscale"*, J. Am. Ceram. Soc., 83 [6], 1476 - 1484, 2000.

[Tang, 2001] Tang, K. *"General of Multiple Colloids Using Micro-fabricated Emitter Arrays for Improved Mass Spectrometric Sensitivity"*, Analytical Chemistry, Vol. 73, No. 8 April 15, 2001.

[Taylor, 1964] Taylor, *G. I., "Disintegration of Water Drops in an Electric Field", Proc. R. Soc. London A 280, 1964."*, 1964.

[Thompson, 1984] Thompson, S. P., *"The Dynamics of Liquid Metal Ion Sources"*, J. Phys D: Appl. Phys. 17 (1984) 2305 - 2321.

[Vafui, 2000] Vafui, K., *"Handbook of porous Media"*, Dekker, 2000.

[Varian, 2004] Varian Company, *"Vacuum Technology Seminar"*, IAP Course, Massachusetts Institute of Technology, January 2004.

[Velásquez, 2001] Velásquez, L. F., *"A Micro-fabricated Colloid Thruster Array"*, M.S. Thesis, Massachusetts Institute of Technology, June 2001.

*[*Velásquez*, 2002]* Velásquez, L. F., *"Micro-fabrication of a Colloid Thruster Array"*, 6th International Symposium: Propulsion for Space Transportation of the XXIst Century, Versailles, France, 2002.

[Velásquez, 2002-2] Velásquez, L. F., *"A Micro-fabricated Colloid Thruster Array"*, Joint AIAA/ ASME /SAE Propulsion Conference, Indianapolis., Indiana, USA, 2002.

[Velásquez, 2002-3] L. F. Velásquez, Ph.D. General Examination, Massachusetts Insitute of Technology, December 2002.

[Velásquez, 2003] Velásquez, L. F., *"Development of a Micro-fabricated Colloid Thruster Array"*, International Joint Propulsion Conference, Toulouse, France, 2003.

[Velásquez, 2003-2] L. F. Velásquez, *"The Concept and Development of a Micro- fabricated Colloid Thruster Array"*, Joint AIAA/ASME /SAE Propulsion Conference, Hunsville, Alabama, 2003.

[Velásquez, 2003-3] L. F. Velásquez, solutions Homework Set No. 4, as part of the TA work in the course 6.777: Design and Fabrication of MicroElectroMechanical Devices; Massachusetts Institute of Technology, Spring 2003.

[von Hippel, 1959] A. von Hippel, *"Molecular science and Molecular Engineering"*, MIT Press, 1959.

[Xiong, 2002] Xiong, J., *"The designing, Fabrication and Test of a MEMS Colloid thruster"*, Proceedings of SPIE Vol 4928, SPIE 0277-786X /02, 2002.

[Xiong, 2002-2] Xiong, J., *"A Colloid Microthruster System"*, Microelectronic Engineering, 61-62, pp. 1031-1037, 2002.

[Zafran, 1969] Zafran, S., *"Colloid Microthruster Test Stand"*, 69A314, AIAA 3rd Flight Test, Simulation and Support Conference, Houston, TX, 1969.

[Zafran, 1970] Zafran, S., *"Colloid Microthruster System Life Test"*, 70A1110, AIAA 8th Electric Propulsion Conference, Stanford, CA, 1970.

[Zeleny, 1914] Zeleny, J., *"The Electrical Discharge from Liquid Points an a Hydrostatic Method to Measure Electric Intensity at their Surface"*, Phys. Rev., 3, pp 69-91, 1914.

[Zeleny,1915] Zeleny, J., *"On the conditions of Instability of Liquid Drops, with Applications to the Electrical Discharge from Liquid Points"*, Proc. Comb. Phil. Soc., 18, pp. 71-93, 1915.